
Site U1347¹

Expedition 324 Scientists²

Chapter contents

Background and objectives	1
Operations	3
Sedimentology	4
Paleontology	9
Igneous petrology	10
Alteration and metamorphic petrology	20
Structural geology	22
Geochemistry	23
Physical properties	25
Paleomagnetism	26
Downhole Logging	28
References	32
Figures	36
Tables	103

Background and objectives

Background

Integrated Ocean Drilling Program Site U1347 (proposed Site SRS3-3B) was the second site completed during Expedition 324, after a quick switch in plans to avoid the track of passing Typhoon Choi-Wan. The site was planned as one of three sites to be drilled on Tamu Massif and was envisioned as the deepest penetration into basement. This site is at the center of a north–south transect across the massif and was intended to sample near the summit of this large volcanic edifice (Fig. F1).

Tamu Massif is the largest volcanic construct within Shatsky Rise, with a volume of $\sim 1.8 \times 10^6$ km³ (Sager, 2005). It may have formed over a geologically short period of time (<1 m.y.) with a high effusion rate, similar to those of flood basalt eruptions (Sager and Han, 1993; Mahoney et al., 2005). In the context of the plume head hypothesis, Tamu Massif appears to represent the initial plume head eruptions. With this massive eruption, the Pacific-Izanagi-Farallon triple junction jumped eastward by 800 km to the location of Tamu Massif. Subsequently, the melt anomaly that formed the rise appears to have “captured” the triple junction, which should have moved northwestward relative to the Pacific plate according to kinematic analysis, but instead followed the axis of Shatsky Rise to the northeast (Sager et al., 1988). After the voluminous Tamu Massif eruption, volcanism declined as two smaller volcanoes formed to the north, Ori and Shirshov massifs, which were followed in turn by lesser output forming Papanin Ridge on the northeast end of the rise (Sager et al., 1999).

Magnetic lineations surrounding Tamu Massif indicate that it formed on lithosphere of latest Jurassic to earliest Cretaceous age. Anomaly M21 brackets the southwest flank, whereas Anomalies M19–M17 cross the northeast flank (Nakanishi et al., 1999) (see Fig. F3 in the “Expedition 324 summary” chapter). The spacing between these lineations is larger than that in adjacent basins, which implies that the lithosphere upon which Tamu Massif erupted was captured from the Farallon plate by a northeastward ridge jump. Because of the complete isostatic compensation (Sandwell and McKenzie, 1989) and the close relationships between the morphology of the rise and past ridge positions shown by magnetic anomalies, Tamu Massif appears to be the same age as the surrounding lithosphere (Sager et al., 1999; Nakanishi et al., 1999). This idea is supported by the age of basalts cored at

¹Expedition 324 Scientists, 2010. Site U1347. In Sager, W.W., Sano, T., Geldmacher, J., and the Expedition 324 Scientists, *Proc. IODP, 324*: Tokyo (Integrated Ocean Drilling Program Management International, Inc.).
doi:10.2204/iodp.proc.324.104.2010
²Expedition 324 Scientists’ addresses.



Ocean Drilling Program (ODP) Leg 198 Site 1213 on the southwest flank of Tamu Massif. These igneous rocks were radiometrically dated at 144.6 ± 0.8 Ma (Mahoney et al., 2005), a date consistent with Anomaly M19 in the geomagnetic polarity timescale (GPTS) (Ogg et al., 2008) and close to the Jurassic/Cretaceous boundary. The sediments directly above these igneous units are Berriasian in biostratigraphic age (Shipboard Scientific Party, 2002b, 2002c), which is also consistent with formation in the earliest Cretaceous.

Tamu Massif appears to be a large, central volcano dissected by faulting on its north side (Sager et al., 1999). The southern and western flanks appear to be normal, largely unfaulted volcanic flanks, whereas the north and east sides show linear troughs and ridges that may represent ridge-related faulting. The Tamu Massif summit has a large, rounded dome shape caused mainly by a cap of pelagic sediments as thick as 1.2 km (Sliter and Brown, 1993). Beneath these sediments, the center of Tamu Massif contains a bowl-shaped minibasin bounded by volcanic basement ridges on the west and east sides (Sager et al., 1999). The western ridge (“Toronto Ridge” of Sager et al., 1999) is tallest, protruding 500–1000 m above the rest of the summit (Sager et al., 1999). The eastern ridge is completely buried and has a subdued, rounded shape.

Site U1347 is on the east flank of Tamu Massif on the upper slope where the volcanic basement is ~800 m deeper than the top of the buried eastern ridge. This location was selected for several important reasons. Because it is ~30 km downslope from the nearby buried eastern summit ridge, it is thought that the site was far enough from a potential volcanic center that it is less likely to have been inundated by a large thickness of lava during any one eruption. This would potentially allow coring to sample several eruptive sequences. In addition, the seismic signature at the site suggests that layers within volcanic basement can be sampled with reasonably shallow coring (Fig. F2). Over much of Tamu Massif, igneous basement is characterized by a curious “layered” appearance. At Site 1213, igneous material with this signature was cored and found to be sills or sheet flows interbedded with sediment (Shipboard Scientific Party, 2002a). In most places, this layered basement is ~0.1 s two-way traveltime (TWT) thick on seismic reflection profiles (~200 m assuming a seismic velocity of 4 km/s) and thus too thick to drill through in a short time. In contrast, at Site U1347, this layer is only ~0.03 s TWT thick (~60 m) on the seismic reflection profile and yet the layer can be followed upward into the basin on the Tamu Massif summit, where it is much thicker. Thus, at Site

U1347 coring through this transition was considered an achievable objective. Another reason for coring at Site U1347 is that the sediments are thin at this location, estimated before drilling at 154 m thick. By targeting such a location, the time spent drilling through sediment to get to igneous basement is minimized. At 154 m thick, the sediments are just thick enough that the bottom-hole assembly (BHA) can be surrounded and supported by sediment before the drill bit makes contact with igneous rock.

At Site U1347, the original plan was to drill ~300 m into igneous basement (i.e., ~454 meters below seafloor [mbsf]). This was predicated on an estimate of igneous rock penetration at a rate of 2.5–3.0 m/h, a value based on previous experience with drilling seamounts (Shipboard Scientific Party, 2002a) and oceanic plateaus (Shipboard Scientific Party, 2001). At this rate, it was expected that the total penetration could be achieved with two drill bits and a single drill bit change using a free-fall funnel (FFF). Unfortunately, Shatsky Rise did not read any of these reports and the formation was harder than expected. The overall penetration rate was about half of the planned value with the result that only a little more than half of the planned igneous basement penetration was achieved before time ran out for this operation.

Scientific objectives

Sampling the summit of Tamu Massif was an important objective because this volcano is the main edifice within Shatsky Rise and Site U1347 is closest to its center. As with most Expedition 324 sites, the operational goal for the site was to drill through the sediment overburden, core the oldest sediment overlying igneous basement, and then core as deeply into the igneous formation as possible with the time allowed.

Scientific objectives of Expedition 324 sites are similar (for more details and rationale, see the “[Expedition 324 summary](#)” chapter). Coring of igneous rock was planned to determine the age of igneous basement so that the age progression and duration of volcanism at Shatsky Rise can be constrained. A critical objective at Site U1347, and indeed all Expedition 324 sites, was to core enough igneous rock of suitable freshness and composition to allow at least one reliable radiometric date to be established. Igneous rocks were also critical to geochemical and isotopic studies, the goals of which are to establish the elemental compositions, variations in compositions, and isotopic characteristics of the rocks. Such data are crucial for determining the source of magma, inferring its temperature and depth of melting and crystallization, deducing the degree of partial melt-

ing, and tracking its evolution over time. Operationally, this meant that at Site U1347 the goal was to core a representative suite of igneous units that was fresh enough to provide reliable geochemical and isotopic measurements. In addition, with the three-hole transect across Tamu Massif, it is hoped that questions of age trends and geochemical and isotopic variations within a single large volcanic edifice can be addressed.

Expedition 324 also sought to constrain the evolution of Shatsky Rise by collecting samples for a host of nongeochemical studies focusing on varied aspects of rise geology. Physical volcanologists, structural geologists, and logging geophysicists will use cores and logs to infer the eruption style, igneous products, and physical structure of Shatsky Rise. Given its size and inferred eruption rate, Tamu Massif is likely to be an example of an unusual volcanic construct, the development which is poorly understood. Shatsky Rise core samples will also be used to study the submarine alteration of igneous rock and its effect on other analyses. Studies of sediments overlying igneous basement are planned to better understand the paleontological age of Shatsky Rise sediments and the processes and rates of Cretaceous sedimentation atop the rise volcanoes. Moreover, sediment types and paleontological environment data will indicate the paleodepths of sediment deposition, information that is important for understanding the eruption and subsidence history of the volcanic edifices. Paleomagnetic study of the samples recovered during Expedition 324 seeks to determine the magnetic polarity of basement for comparison with surrounding magnetic lineations and the GPTS as well as the paleolatitude of the rise and its plate tectonic drift. Tamu Massif samples are important in this effort because they were likely formed farthest south and are the oldest, thus, they should show the maximum tectonic drift. Physical properties of Shatsky Rise core samples will be measured to better understand the nature of the rocks that make up the rise and to constrain fundamental physical properties that affect geophysical imaging and remote sensing. Such data will be useful for constraining seismic and gravity studies in particular.

Operations

Times in this chapter are given in local ship time. During transit to Site U1346, shipboard clocks were advanced 1 h, resetting local ship time to Sydney Standard Time (Universal Time Coordinated + 10). No further adjustments to the clock were made during the expedition.

After a 370 nmi transit from Site U1346, the R/V *JOIDES Resolution* came to position at Site U1347 at 1730 h on 21 September 2009. The average speed during the transit was 8.0 kt. The slow pace was a result of heavy seas kicked up by passing Typhoon Choi-Wan.

After the driller tagged seafloor at 3461.0 m drilling depth below rig floor (DRF) (Table T1), Hole U1347A was spudded with the rotary core barrel (RCB) at 0710 h on 22 September. The hole was drilled with a wash barrel in place to 71.0 m drilling depth below seafloor (DSF) where rotary coring was initiated. While coring the interval from 71 to 109 m DSF, the average recovery was ~5% because of chert fragments jamming in the core catcher. As the hole was extended beyond this depth, chert became much less prevalent and recovery and penetration rate improved. We reached basaltic basement at ~158 m DSF. Coring into basement continued until 2145 h on 25 September when operations were suspended in order to change to a fresh bit after the initial rotary bit had accumulated 60 rotating hours. After flushing the hole with a 50 bbl mud sweep, the drill string was pulled back to 155 m DSF and the hole displaced with 57 bbl of heavy mud.

A FFF was made up and deployed at 0130 h on 26 September. The vibration-isolated television (VIT) camera was then launched to monitor the extraction of the bit through the FFF. As the VIT frame was suspended ~10 m above the FFF, a hydraulic supply hose to the VIT winch ruptured resulting in the TV camera frame rapidly descending and coming into contact with the lip of the deployed FFF. The rig mechanic spent 1 h replacing the defective hose. Once the repairs were concluded, the VIT camera was raised into position to image the FFF and the bit was pulled off the FFF at 0515 h. After the VIT camera was recovered, an inspection of the camera assembly indicated no obvious damage except for a slightly bent compass arm.

While coring with the first bit, heave frequently exceeded 3 m making it difficult to keep the bit on the bottom of the hole. An inspection of the recovered bit indicated that the bit body was under gauge by ~3/8 inch. With the exception of two chipped teeth, the cutting structure was intact as well as the cone seals. There was some noticeable shirt tail wear, but overall the bit was in remarkably good condition for the accumulated hours.

A new RCB C-4 bit with a refurbished mechanical bit release was quickly affixed to the rotary drilling assembly and run back in the water column. Hole U1347A was successfully reentered at 2250 h on 26

September after 2 h of maneuvering against a strong current. The drill string was advanced to the bottom of the hole where the driller found only 1 m of soft fill. At 0500 h on 27 September, coring resumed but was suspended after cutting the first core with the new bit. The core barrel containing Core 324-U1347A-21R could not be recovered for 5.75 h because the core winch motor had shorted field windings and had to be replaced. Once the new motor was mounted and tested, coring resumed.

From 1530 h on 27 September to 1230 h on 30 September rotary coring deepened the hole from 242.7 m DSF to a final depth of 317.5 m DSF in routine fashion with no hole problems. Operations were concluded when the last core was able to advance only 1 m in 3 h (rate of penetration [ROP] = 0.3 m/h), possibly caused by either a worn bit, an extremely hard formation, or a combination thereof. Because the time allotted for drilling at Site U1347 was nearly expired, it was decided to terminate drilling.

Total penetration into basement in Hole U1347A was 159.9 m DSF, cored at an average ROP of 1.5 m/h (Fig. F3). While coring basement, the ROP for individual cores ranged from a lethargic 0.7 m/h to a more energetic 4.1 m/h. The average recovery for basement coring was 64.2%. The drilled/washed interval was 71.0 m, and the total average recovery for the entire hole was 47.1%.

The hole was prepared for logging with three mud flushes and a wiper trip to 86 m DSF. Once the bit was released at the bottom of the hole, the bore was displaced with 83.5 bbl of 10.5 ppg mud. The drill string was pulled back in the hole and placed at the logging depth of 131.5 m DSF. The first logging run was made with the triple combination (triple combo) tool string, which succeeded in reaching within 2 m of the bottom of the hole. A preliminary analysis of the results of the first logging run indicated that the hole was in good condition and suitable for the additional measurement runs planned for this site. The second tool string deployed was the Formation MicroScanner (FMS)-sonic tool string, which was also successfully run (two complete passes) to within 2 m of the bottom of the hole. The third planned logging tool suite included the Ultrasonic Borehole Imager (UBI), but this run was cancelled because of hardware problems.

After the logging equipment was secured, the drill string and beacon were retrieved in routine fashion. Once the drilling equipment was secured, the vessel departed for Site U1348 at 0400 h on 2 October. The total time on site for Site U1347 was 10.4 days.

Sedimentology

One hole was drilled at Site U1347 on the eastern flank of Tamu Massif (water depth = 3450 meters below sea level [mbsl]). A total of 17.7 m of sediment was recovered in Cores 324-U1347A-1W through 11R over a stratigraphic interval of ~88 m before entering basaltic basement at 157.6 mbsf. The recovered sediments at Site U1347 are dominated by radiolarian-rich volcanoclastic siltstones with varying proportions of glauconite. Minor intervals of chert and claystone are also present. Bioturbation is often pervasive in the silty facies, with rip-up clasts and erosional contacts as common features suggestive of turbulent and transient depositional events. Sediments are also present as relatively thin interbeds between the massive basaltic flows and pillow basalt units within the igneous complex. These sediments are similar in character and composition (e.g., predominantly radiolarian-bearing siltstones) to the sediments above basement, although some show features consistent with thermal alteration caused by subsequent basalt emplacement.

Unit descriptions

The overall stratigraphy of the sedimentary material recovered from Site U1347, including the sedimentary beds between basaltic units, is shown in Figure F4. Three stratigraphic units were identified at Site U1347 in the sedimentary pile above the sediment/basement contact (Fig. F5).

- Unit I: brown, black, and dark gray cherts with occasional fine-grained nannofossil cherts or porcellanites present as thin coatings (71–80.6 mbsf).
- Unit II: glauconitic radiolarian-rich silicified limestones and calcareous sandstones, with volcanoclastics (80.6–99.8 mbsf).
- Unit III: radiolarian-rich sandy siltstones and silty sandstones, with volcanoclastics and glauconite (99.8–157.6 mbsf).

Four additional stratigraphic units interbedded with the igneous units below 157.6 mbsf were identified. These units are divided based on their role in separating the established igneous units, rather than sedimentary-lithologic differences (Fig. F4).

- Unit VI: radiolarian-bearing sandy siltstones (186.7–187.2 mbsf). Original bedding is disturbed.
- Unit VIII: dark homogeneous claystones, overlying laminated radiolarian-bearing sandy siltstones (200.8–205.83 mbsf).
- Unit XI: radiolarian-bearing sandy siltstone and volcanoclastic limestone, with interbedded vesicular basalt (258.3–258.8 mbsf).

- Unit XIII: low-density altered volcanoclastic sandstone (278.1–278.2 mbsf).

Other small pieces of sedimentary material are present within the igneous units, mainly forming baked contact rinds at pillow surfaces. However, these fragments make up such a small proportion of the cores that they do not warrant unit divisions of their own. See “[Site U1347 visual core descriptions](#)” in “Core descriptions” for location of these sediment fragments.

Unit I

Interval: 324-U1347A-1W through 3R

Depth: 71–80.6 mbsf

Only fragments of chert with chalk coatings were recovered in Cores 324-U1347A-1W through 3R, with the exception of 9 cm of light gray pumice at the top of Core 1W. This unit is from 71 to 80.6 mbsf stratigraphically, although the majority of this unit is unrecovered, presumably because of the interbedding of well-indurated cherts with unlithified calcareous sediments. The pumice at the top of the wash core is considered to be “fall-in” from the unrecovered section above and is possibly Cenozoic in age, although no biostratigraphic age constraint is possible. The chert and chalk sequence recovered at this site on Tamu Massif appears superficially similar to stratigraphic Unit I at Site U1346 on Shirshov Massif, although little else can be deduced from the available material. The chert is very dark brown to black with circular porcellanite spots (probably recrystallized radiolarian “ghosts”) and faint laminations in places. Evidence of bioturbation in the chert layers appears as indistinct burrow structures visible in some places. The minor chalk coatings are often silicified and/or recrystallized with poor preservation of the presumed original nannofossil composition.

Unit II

Interval: 324-U1347A-3R through 4R

Depth: 80.6–99.8 mbsf

The recovered portion of Unit II, which begins at interval 324-U1347A-3R, 1.13 cm, and ends at the base of Section 4R-1, spans 10.3 m. Unit II consists of silicified radiolarian-bearing glauconitic limestones and sandstones with occasional cherts. Sedimentary rocks in the lower portion of Section 3R-1 are light brownish gray heavily silicified limestone with abundant rounded glauconite grains, streaks of grey chert, and some small opaque mineral grains. The large concentration of radiolarians and degree of silicification in these limestone pieces warrants naming them porcellanites, or even radiolarites in some cases. The matrix is generally a mixture of micritic

calcite and/or radiolarians with secondary silica cement.

A sharp contact exists between the first porcellanite and the last black chert in Section 324-U1347-3R-1. One black chert nodule was recovered at the top of Section 4R-1. The remaining sedimentary rocks in Section 4R-1 are less heavily silicified, greenish gray glauconitic sandstones with volcanoclastics. Radiolarians are very common throughout and are likely the source of the secondary silica cement found in this unit. These sandstones also contain some dark clasts, many of which are subangular, that appear volcanic in origin and probably represent weathered basaltic fragments. Green glauconite clasts are a major constituent and comprise the majority of the grains in the sandstones. These grains often have a rounded appearance, because of the replacement of circular radiolarian tests, and in some cases display yellowish limonitic alteration halos. Where the glauconite has replaced radiolarians, fine netlike biogenic structures are often preserved (Fig. F6). These glauconitic grains are mostly composed of very well preserved whole radiolarian tests, but a few are fragmented or fractured and show possible evidence of reworking. Secondary pyrite, often as clusters concentrated in voids, is common throughout. Much of the sandstone shows cross-bedding (Fig. F7). A large (~2 cm) scalloped shell fragment is present at interval 324-U1347A-4R-1, 36 cm.

Unit III

Interval: 324-U1347A-5R through 11R

Depth: 99.8–157.6 mbsf

From the top of Core 324-U1347A-5R at 99.8 mbsf to the middle of Core 11R at 157.6 mbsf, a thick sequence of indurated, dark gray, radiolarian-rich sandy siltstones with volcanoclastics and glauconite was recovered. The bulk of these sediments is composed of dark brown clay minerals. The clay composition, as determined by X-ray diffraction (XRD) analysis, is a mixture of altered zeolitic clays (heulandite, fedotovite, and phillipsite) with montmorillonite in some samples (Table T2). As expected, calcite is present in all samples, along with orthoclase, glauconite, albite, talc, and pseudomalachite in certain intervals.

The siltstones have a large radiolarian component. Preservation of the microfossils is variable, from very good to poor (Fig. F8). In some of the coarser intervals, many radiolarians are replaced by secondary calcite leaving only circular “ghosts” in the silty matrix. Radiolarians are, however, well preserved in other horizons (Fig. F9). Other rare biogenic constituents such as fish teeth can also be observed in certain intervals, especially in smear slide preparations.

Altered plagioclase laths, small basaltic clasts, and volcanic glass are also present throughout the cores and occur in especially high abundance in Cores 324-U1347A-6R through 10R (Fig. F10). The volcanic origin of much of the fine material is evidenced by the dominance of certain zeolites that are commonly associated with the breakdown of mafic volcanic material.

The majority of the material in Unit III is fine grained, ranging from clay to silt, although coarser intervals are present. Sediments generally coarsen upward from the base of the unit to the top. Clay-sized material dominates in Cores 324-U1347A-9R through 11R near the base of the unit, and sandy siltstones with coarse sand interbeds become more common in Cores 5R through 6R at the top of the unit. Two thin, black, coarse sandstone beds consisting of calcite-cemented volcanic (basaltic) clasts and glass were found at intervals 324-U1347A-5R-1, 27.5–41 cm, and 6R-1, 73–77 cm. These beds were within the radiolarian-bearing sandy siltstone intervals but were recovered as isolated pieces because of drilling disturbance. Interestingly, adjacent to the sandstone bed in Section 324-U1347A-6R-1, a small but very coarse bed of glassy volcanoclastics containing very dark gray spherical grains between 0.5 and 7 mm in diameter was recovered (Fig. F11). Some of these glass spherules have a core of coarser material with a finer grained rim. No concentric rings are observed within this rim. Large pieces of brown volcanic glass are also present outside of the spherules.

Although the overall trend within this unit is coarsening upward, we observe many smaller graded and fining-upward sequences. These are often marked by sandy siltstones at the base followed by siltstones, with laminated claystones at the top. In some cases, the fine clay at the top of these sequences is bioturbated with *Chondrites* ichnofossils and then truncated by an erosional contact with a coarser horizon (e.g., interval 324-U1347A-8R-2, 41–48 cm). Structures such as scour marks, sharp erosive contacts, lenses of coarser material, churned strata, and rip-up clasts are common throughout in the upper part of the unit, especially in Cores 324-U1347A-6R through 8R (Fig. F12).

Much of this unit contains evidence of bioturbation. Well-defined trace fossils (ichnofossils) are present in some cores. The character, pervasiveness, and ichnofacies change from the base of the unit to the top. In Cores 324-U1347A-5R through 6R, mottled textures in some intervals suggest minor to moderate bioturbation including some *Planolites*-like structures, occasionally with reduction halos. The degree of bioturbation increases through Cores 7R and 8R, reaching moderate to intense levels. In Core 8R, the

bioturbation reaches a peak. Large, U-shaped, vertical burrows (*Teichichnus*?) can be seen in Section 324-U1347A-8R-1, and *Chondrites* is present in the clay-rich parts of Sections 8R-2 and 8R-3 (Fig. F13).

Whereas the unit is mostly devoid of bioclasts, occasional calcitic shelly fossils are present, such as the small bivalve fragments found in Sections 324-U1347A-8R-CC and 6R-1 to 6R-2. A poorly defined small (1.5 cm) ammonite impression was found in interval 324-U1347A-8R-5, 92 cm.

Basalt was first encountered in Core 11R at 157.6 mbsf. The location and summary of these beds can be seen in Figure F4 (see “Igneous petrology” for a more detailed account of the igneous units). Description of the sedimentary rocks, which interbed with the basaltic flow and pillow units, follows below.

Unit VI

Interval: 324-U1347A-15R-1

Depth: 186.7–187.2 mbsf

Within Section 324-U1347A-15R-1, a 50 cm long section of sandy siltstones separates two massive basalt flow units. Logging data suggest the actual thickness of this unit is ~4.5 m. These sediments are composed of two distinct lithologies with differing coloration: a greenish gray radiolarian-bearing sandy siltstone and a very dark gray sandy siltstone.

Traces of original bedding can be seen, although the bedding is inclined and there are signs of soft-sediment deformation. The siltstones are well indurated, brittle, and display hackly fractures. At interval 324-U1347A-15R-1, 50–57 cm, a feature interpreted as a gas or fluid escape pipe can be seen cutting across remnant bedding planes. Sedimentary interbeds are also present in Core 13R within the Unit IV basaltic flow, although they are not extensive enough to warrant a unit division of their own. One piece, at interval 324-U1347A-13R-7, 19.5–21.5 cm, consists of a sandy siltstone with a diverse, well-preserved radiolarian assemblage.

Unit VIII

Interval: 324-U1347A-16R-5 through 17R-1

Depth: 200.8–205.83 mbsf

In Sections 324-U1347A-16R-5 and 17R-1, ~2.2 m of sediments were recovered, which are thought to be part of a 4.5 m thick sedimentary package between two massive basalt flows. In Section 16R-5, 72 cm of black homogeneous silty claystones was recovered. In Section 17R-1, 143 cm of dark greenish gray radiolarian-bearing sandy siltstones are located stratigraphically above the massive basalt of Unit IX. Sediments from both of these intervals are brittle, with hackly fractures and waxy textures.

Unit XI

Interval: 324-U1347A-22R-5

Depth: 258.3–258.8 mbsf

Between the upper and lower pillow lavas in Section 324-U1347A-22R-5, small pieces of sedimentary material spanning ~50 cm in the core were found. Logging data suggest these pieces represent a largely unrecovered, ~5 m (logging Unit VIIIb) sedimentary interbed. A piece of dark gray silty claystone with some color banding was recovered between 18 and 39 cm. Heavily recrystallized radiolarians are visible in this piece as well. Between 39 and 68 cm a piece of fine-grained basalt with a chilled margin on the upper surface separates the claystone from a small piece of sandy volcanoclastic-bearing limestone, 5 cm in length.

Unit XIII

Interval: 324-U1347A-24R-5

Depth: 278.1–278.2 mbsf

A pale gray low-density altered volcanoclastic sandstone is found in Section 324-U1347A-24R-5, between the upper and lower pillow lavas (stratigraphic Units XII and XIV). This small rock has a medium-grained sandstone texture and is noncalcareous and porous. XRD data reveals that it is composed solely of quartz and cristobalite (see Table T2). As both the upper and lower contacts were not recovered, it is difficult to determine whether this piece represents a highly altered in situ volcanic rock or redeposited sedimentary material of volcanogenic origin.

Sedimentary carbon content

Thirty-seven samples were taken from Cores 324-U1347A-3R and 4R in Unit II, Cores 5R through 10R in Unit III, and Cores 15R through 17R in the basaltic interbeds. Both total carbonate (CaCO_3) content and total organic carbon (TOC) content in weight percent were determined (Table T3). The amount of carbonate in the samples overall is low, averaging 6.04 wt% (± 14.79 wt%, 2σ). Carbonate contents range from 0.98 to 37.65 wt%. Most values, especially within the Unit III siltstones, are below 10 wt% CaCO_3 with the majority clustered between 1 and 5 wt%. A silicified limestone from interval 324-U1347A-3R-1, 15–16 cm, has the highest carbonate content.

TOC percentages at Site U1347 are generally low, ranging between 0.07 and 1.28 wt%, with most samples containing <0.5 wt%. One sample from the dark homogeneous claystone in interval 324-U1348A-10R-1, 53–55 cm, has a relatively high TOC value of 1.28 wt%. The TOC from the basaltic-interbedded sediments is low, from 0.10 to 0.53 wt%, although

the dark coloration of Section 324-U1347A-16R-5 hints at possible higher organic matter content prior to alteration.

Interpretation

A relatively thick sequence of sedimentary material was recovered at Site U1347 before entering basaltic basement at 157.6 mbsf. Three stratigraphic units are identified in these sediments, representing three distinct depositional environments. Unit I consists of interbedded cherts and carbonates and was probably deposited in a fairly deep pelagic environment with high calcareous nannofossil and radiolarian fluxes and little terrestrial influence. Little else can be deduced about the nature of this unit because of poor core recovery. Unit II consists of silicified limestones and sandstones with copious glauconite clasts and radiolarians and occasional shell fragments. These suggest relatively shallow water conditions in a high-productivity marine setting. The trough cross-bedding structures are suggestive of very shallow water, possibly an upper shoreface environment above wave-base. The high zeolite content and presence of basaltic volcanoclastics, including glass, suggests Unit III was deposited close to a large volcanogenic source. Abundant radiolarians in this unit suggest high-productivity conditions. The coarsening observed from the bottom of Unit III to the top, coupled with the changing style of bioturbation, suggests sequential shallowing within this unit.

The change in lithology and structural indicators between Units III and II, suggestive of shallowing, presents certain problems when considering the classic model of a subsiding volcanic edifice (e.g., Winterer and Sager, 1995) and certainly merits further investigation. It may be that the deposition of Unit III was sufficiently rapid, through the emplacement of sequential turbidites, to outstrip the rate of subsidence, thus allowing progradation of the siltstones to occur. This would account for the shallowing-upward sequence without requiring the entire massif to be uplifted. However, as neither the sedimentation rate nor paleodepth of this unit is known, it is difficult to evaluate the feasibility of this scenario. The overall change from Unit III to Unit I, however, does suggest a deepening sequence (nearshore marine to pelagic), which is supported by changes in benthic foraminifer assemblages (neritic to bathyal) across the same interval (see “Paleontology”).

Unit I

The interbedded chert and chalk at this site on Tamu Massif is very similar to that recovered in stratigraphic Unit I at Site U1346 on the Shirshov Massif. The depositional environment was therefore proba-

bly very similar: a pelagic environment with deposition occurring above the carbonate compensation depth on a bathymetric high created by the subsidence of the volcanic edifice of Shatsky Rise. The age of these cherts, and indeed all the sedimentary units at Site U1347, has been constrained to the Berriasian to late Valanginian (Early Cretaceous) based on calcareous nannofossil biostratigraphy and preliminary investigation of the radiolarians. This age range places Unit I in the same broad age range as Site U1346 Unit I. The dark color of the cherts at both sites also suggests the two units may have a similar mode of deposition. Although the recovery of Unit I at Site U1347 is very poor, the dark coloration of the cherts suggest a nonoxidizing environment, possibly related to a relatively high sedimentation rate compared to a red chert facies depositional mode (e.g., Fontile et al., 2006).

Unit II

The silicified limestones and sandstones in Unit II have a high radiolarian content. Preservation of biogenic silica in marine sediments is indicative of a high-productivity marine setting, most likely related to equatorial upwelling. The carbonate component, although now extensively recrystallized, looks to be fine grained, and therefore probably was originally sourced from calcareous marine plankton or inorganic carbonate muds. The large concentration of glauconite in these rocks is suggestive of postdepositional reducing conditions and relatively low sedimentation rates in water <500 m. The replacement of biogenic components with glauconite is a common feature and can be seen in the replacement of radiolarians in Cores 324-U1347A-3R and 4R. The glauconite-replaced microfossils do not appear to be broken or transported a great distance, suggesting in situ formation within the siliceous limestones and sandstones. The cross-bedding, which is so prevalent in this unit, suggests agitated shallow water. Although cross-bedding can also be generated in deeper settings by contour currents, the packages of cross-bedded laminations seen in these cores most closely resemble structures normally seen in depths corresponding to the offshore–shoreface transition (Davis, 1985).

Unit III

The clear volcanogenic origin of much of the material in Unit III strongly suggests that this unit represents the altered weathering products of a proximal basaltic volcanic source. Altered volcanic glass and occasional plagioclase laths are found throughout the sequence, as are zeolites, such as phillipsite and heulandites, commonly associated with the weather-

ing and alteration of mafic igneous materials. The fine grain size and lack of large igneous clasts suggests transportation some distance from the source. This is further supported by the degree of hydraulic sorting seen in several of the cores. The presence of rip-up clasts and scour marks suggests that, at least in some cases, the emplacement of the material was by rapid lateral movement. In the lower cores (324-U1347A-9R through 11R), the dark coloration, slightly elevated TOC, fine-grained matrix, and lack of bioturbation except for *Chondrites* indicate a quiet dysoxic environment. In the middle to upper Cores 5R through 8R the brownish gray coloration, slightly coarser material, increased bioturbation, and large burrow structures suggest a higher energy oxic environment. The coarse band of spherical glass grains in Section 6R-1 has a clear volcanogenic origin. The lack of clear concentric rings with the rims suggests that these structures do not represent accretionary lapilli and more closely resemble glass spherules, probably related to explosive emergent volcanism in the vicinity.

One model to explain the sedimentary sequence observed in Unit III is progradation where products from a weathering basaltic volcanic edifice infill a local basin, thereby creating a shallowing-upward sequence within the siltstone complex. The basin infill is then capped by a radiolarian, carbonate-rich, shallow-water lithology with fewer volcanoclastics (Unit II). Several lines of evidence seem to support shallowing upward from Unit III to II. Eventual subsidence of the volcanic massif would lead to pelagic conditions and the deposition of chalk and chert (Unit I).

Basalt interbeds

The sedimentary beds in between the basalts are generally composed of similar material to Unit III, radiolarian-bearing siltstones, although they have clearly been altered by proximity to the basalts during emplacement. In some cases, thermal alteration of the sediments has resulted in a waxy texture. The stratigraphic thickness of these beds is difficult to determine because of fracturing during drilling and poor recovery, but logging data suggest Units VI, VIII, and XI are each 4.5–5 m thick (see “[Downhole Logging](#)”). Unit XIII is not visible on the logging data, suggesting a different origin for this interval.

If the sedimentation rate within these interbeds could be measured, some estimate of the time between basaltic emplacements at this exact location could be made, although this would not necessarily be indicative of a hiatus in eruptive activity over the entire massif. However, no shipboard estimate of biostratigraphic age was possible in these beds, mak-

ing sedimentation rates impossible to constrain. It should be noted, however, that greater age constraint from radiolarian biostratigraphy may be possible with further study. The disturbed bedding in Unit VI (Core 324-U1347A-15R) suggests soft-sediment deformation, possibly related to slumping or disturbance caused by emplacement of the upper basalt flow (Unit V). If mass sediment transport occurred, the thickness of the unit gives no useful estimate for hiatus duration. In contrast, the sediment in Unit VIII has 1 m of undisturbed fine laminations throughout Section 324-U1347A-17R-1, suggesting in situ deposition of sediments and possibly a longer period between emplacements of the basaltic flows of Units IX and VII than between those of Units VII and V. The presence of a small altered limestone bed in Unit XI suggests higher carbonate flux relative to volcanoclastics during the hiatus between emplacement of basalt Units XII and IX. The origin of the silica-rich rock in Unit XIII is unknown and warrants further investigation. It may be a highly altered in situ volcanic deposit, which has developed a sedimentary texture because of high temperature thermal alteration and remobilization of silica.

Paleontology

Sediments from Site U1347 (Cores 324-U1347A-1W through 11R) are generally carbonate-poor in lithology and comprise bioturbated siltstones and sandstones (stratigraphic Units II and III) with overlying chert and chalk fragments (stratigraphic Unit I) (see “[Sedimentology](#)”). Shipboard calcareous microfossil studies were performed on Unit II and III sediments (mudstones only for foraminifers) as well as on chalks from Unit I. Further, investigations of calcareous microfossils were extended into the underlying basement basaltic lava section, in which interbedded mudstones occurred at several levels (Units VI, VIII, XI, and XIII).

In general, calcareous nannofossils and foraminifers of Units I–III are moderate to poor in preservation and low in abundance and diversity. Intercalated sediments in the underlying basement section are almost barren of both microfossil taxa. Fortunately, the ages of four samples from Cores 324-U1347A-2R and 10R (Units I–III) are assignable to the Berriasian–Valanginian based on calcareous nannofossils. The foraminifer assemblage is marked by the absence of a planktonic group. Though the total number of specimens is limited, benthic foraminifers obtained from Units I–III most likely represent a neritic assemblage (Cores 6R through 8R) and subsequent bathyal faunal elements upsection (Cores 1R and 2R). There-

fore, an overall deepening trend from <200 mbsl (Unit III) to 200–2500 mbsl (Unit I) is inferred (note lack of foraminifer data for Unit II).

Washed foraminifer samples are to a large extent dominated by volcanogenic lithic fragments and minerals. Radiolarians consistently occur throughout the sediment and basement sections, with peaks in size, abundance, and diversity in Cores 6R through 8R. A highly abundant, diverse radiolarian assemblage is observed in Sample 324-U1347A-13R-7, 19.5–21.5 cm (Fig. [F14](#)).

Calcareous nannofossils

Calcareous nannofossils in the sediments of Site U1347 are moderately preserved and occur in high abundance in the topmost interval (Unit I). Preservation declines to poor and abundance decreases to rare around Core 324-U1347A-324-6R and further downhole. The sediments recovered from between the underlying basaltic units are barren of calcareous nannofossils.

The presence of zonal marker species *Crucellipsis cuvillieri* together with *Axopodorhabdus cylindratus*, *Creতারhabdus striatus*, and *Speetonia* sp. allows for the assignment of stratigraphic Unit I (Sample 324-U1347A-2R-1, 12 cm; encrusting limestone on a chert piece) to the Berriasian to Aptian (see “[Paleontology](#)” in the “[Methods](#)” chapter; Bown, 2005). Of these taxa, *C. striatus* is assumed to be a contaminant from RCB drilling, which often causes soft-sediment mixing. Hence, the proposed biostratigraphic range of Sample 324-U1347A-2R-1, 12 cm, is from Zone NK1 to Subzone NK3b (Berriasian–upper Valanginian) (Table [T4](#)). Likewise for Unit III, the presence of *C. cuvillieri* together with *A. cylindratus* (Samples 324-U1347A-6R-2, 97 cm; 7R-3, 65 cm; and 10R-1, 66 cm) indicates a biostratigraphic range from Zone NK1 to Subzone NK3b (Berriasian–upper Valanginian) (Table [T4](#)).

It should be noted that the majority of examined samples show a low-diversity assemblage, which is often solely composed of Watznaueriaceae occasionally together with the small proportion of Chiastozygazeae (Core 324-U1347A-3R through Section 6R-1, Sections 7R-CC through 9R-1, and Cores 10R through 17R [except for Sample 324-U1347A-10R-1, 66 cm]). The absence of primary zonal marker species in these intervals hinders the chronostratigraphic interpretation.

The above-described calcareous microfossil zonation translates to a numerical age interval of 140–133 Ma for Units I–III. Accordingly, the estimated age of the basaltic basement section immediately below would be 140–133 Ma or older.

Foraminifers

Foraminifer abundance and diversity are low through the examined interval at Site U1347. No planktonic foraminifers were encountered during the course of shipboard study, as was the case at Site U1346. Benthic foraminifer specimens exhibit good to moderate preservation, and they tend to be broken or fragmented with increasing burial depth (Table T5).

Though present only in trace amounts, benthic foraminifers recorded from stratigraphic Unit I belong to the genera *Dorothia*, *Glomospirella*, and *Ramulina* (Table T5). In general, these taxa are ubiquitous in the bathyal setting (200–2500 mbsl) (e.g., Sliter and Baker, 1972; Koutsoukos and Hart, 1990; Holbourn et al., 2001).

Downhole, Unit III yields such benthic foraminifer genera as *Dentalina*, *Lenticulina*, *Planularia*, and *Conorboides*. The former three are nodosariids and the same faunal elements as those of the Site U1346 assemblage at the neritic–upper bathyal depth (largest number of specimens collected from Sample 324-U1347A-7R-4, 50–52 cm). The occurrence of *Conorboides* (Sample 324-U1347A-8R-2, 49–51 cm) is important, as its Cretaceous bathymetric distribution is considered to have been narrowly restricted to the neritic setting (e.g., Koutsoukos and Hart, 1990; Jones and Wonders, 1992). Taking into account the lack of taxa typical of the bathyal setting, the water-depth estimate for Unit III is most likely <200 mbsl, though further effort to increase the number of specimens is critical.

Several intercalated mudstone layers in the basaltic basement section (stratigraphic Units VI, VIII, XI, and XIII) are almost barren of foraminifers, although they all disaggregate well by means of the kerosene method (see “Paleontology” in the “Methods” chapter). Two levels (Samples 324-U1347A-15R-1, 70–72 cm, and 17R-1, 41.5–43.5 cm) are marked by a few small and/or fragmented specimens of nodosariid benthic foraminifers, which are difficult to interpret in terms of paleowater depth.

Igneous petrology

Stratigraphic unit description and volcanology

In this site report the stratigraphic units are given Roman numbering (stratigraphic Units I–XVI), whereas the small-scale lithologic units identified during core description are given Arabic numbering (lithologic Units 1–82). We identified these lithologic units on the basis of sedimentological changes or, in the case of volcanologic units, criteria includ-

ing the presence of chilled margins or contacts, identifiable flow tops, vesicle distribution, and the occurrence of intercalated volcanoclastic or sedimentary horizons. When considered together these criteria define the various sizes of individual volcanic inflation units. Accordingly, in the volcanic context, the term “stratigraphic unit” is used to combine smaller consecutive inflation units of similar character into lava packages or single eruptive sequences (see “Igneous petrology” in the “Methods” chapter).

Hole U1347A was drilled on the upper southeastern flank of Shatsky Rise on Tamu Massif (Fig. F1). The top of the drilled succession (Figs. F15, F16) commences with ~18 m of Lower Cretaceous sediment, including a chert-chalk series (Unit I), radiolarian-bearing glauconite-rich sandstones, and silicified limestones (Unit II) and a sequence of laminated volcanoclastic glauconite-rich sand- and siltstones (Unit III). Igneous basement was reached 157.6 mbsf in Section 324-U1347A-11R-1, after which drilling continued for 159.5 m into a volcanic succession dominated by five massive (~8–23 m thick) basalt flows and pillow basalt units. The massive flows appear in two eruptive sequences separated by a volcanically more complex ~75 m thick sequence of pillow basalt with individual inflation units ranging in size from 0.2 to 5.6 m. Based on the macroscopic core descriptions the volcanic units are thus divided into three groups (Fig. F15). In order of increasing depth, these are:

1. Group 1 is the top basement sequence and consists of four massive lava flows (stratigraphic Units IV, V, VII, and IX), which together have a combined thickness of ~60 m.
2. Group 2 comprises a ~75 m thick lava stack sequence of pillow basalt inflation units (Units X, XII, and XIV) interspersed with thicker, more massive basalt units (typically 1–2 and rarely >3 m).
3. Group 3 is a succession of very thick (~23 m), massive lava flows (Units XV and XVI), located toward the base of the hole. The hole terminated ~2 m into the top of the second massive lava flow in this group; its true thickness is therefore unknown.

The core also revealed that the volcanic units are interbedded by four ~5 m thick, mostly undeformed sedimentary intervals (Units VI, VIII, XI, and XIII) (see “Sedimentology” for a more detailed description of these interbeds). A fifth interbed in Unit X was not recovered but has since been recognized in the downhole logging measurements as a ~5 m sedimentary interval of low resistivity and high natural gamma readings (see “Downhole Logging” for more details). The following is a description of the vol-

canic units and a preliminary assessment of the physical volcanology of the eruptive sequences drilled at Site U1347.

Group 1

First massive basalt flow (stratigraphic Unit IV, lithologic Unit 4)

Unit IV is a single 16.6 m thick (19.5 m in downhole logs) massive aphyric basalt flow (recovery = ~70%) with microcrystalline chill zones toward the upper and lower contacts, becoming coarser (fine-grained basaltic texture) toward the core. Thin section analyses of this coarser material reveal microphe-nocrysts of plagioclase intergrown with clinopyroxene and some traces of (pseudomorphed) olivine. Magnetic susceptibility readings are observed to increase concomitantly with grain size (Fig. F16), with the highest readings toward the lowermost region of Unit IV.

The lower chilled zone is somewhat thinner than the upper and is demarcated by a series of small pipe vesicles. Both the upper and lower contacts of the flow are well preserved, with a large proportion of fresh basaltic glass that surrounds and supports small blocks of basaltic rubble in what may be interpreted as an original brecciated flow top crust (interval 324-U1347A-11R-1, 21–28 cm). Vesicles are concentrated in both the upper chilled zone and uppermost part of the flow core but become sparse or absent in its middle and lower part. However, within the lower part of the flow core vertical arrangements, or zones, of small vesicles (i.e., pipe vesicle structures) are common and typically contain material of slightly darker color, subsequently identified as melt segregations. Geochemical analysis of these segregation materials reveals them to be of slightly different composition to that of the bulk flow (i.e., elevated K_2O and Ni and lower MgO, V, and Cr) (Hartley and Thordarson, 2009), whereas diktytaxitic texture, indicative of elevated volatile content (Goff, 1996) is more common in the middle and lower core regions (see “Geochemistry”).

Interestingly, preliminary data indicate a magnetic reversal may occur in the top half of the unit, with downhole logs revealing a decrease in resistivity at a similar interval (see “Paleomagnetism” and “Downhole Logging”). If confirmed, these data indicate that this massive flow unit actually represents the incomplete upper and lower portions of two separate inflation units.

Second massive basalt flow (stratigraphic Unit V, lithologic Unit 5)

This second massive flow is 12.5 m thick, has a very similar aphyric character to that of the overlying

Unit IV, and also contains microphe-nocrysts of plagioclase intergrown with clinopyroxene together with traces of pseudomorphed olivine. Abundant fresh volcanic glass is preserved at the upper surface and reveals a pahoehoe-like flow-top structure (Figs. F17, F18). Fragments of radiolarian-rich sediment were also recovered within this surface and have apparently been baked by the lava flow; these are interpreted as part of a flow-top breccia. A good example is shown in Figure F19, where the contact between the lava and sediment clast is glassy and represents a narrow zone (~1 cm) of lava chilling and a profound baking of the mudstone clast. Moreover, a small but significant total natural gamma ray anomaly is apparent in the downhole logs; this most likely represents a thin sediment layer or lens of more than ~10 cm thick intervening between the two flows at this location (see also “Physical properties” and “Downhole Logging”).

Beneath the uppermost ~1 m thick chilled zone, the top ~3 m of the second massive flow is highly vesicular (~15%–20%). However, because recovery in Unit V is poor, details of the internal structure of this massive basalt flow cannot be recorded. Again, on the basis of downhole logging data, this unit may be divided into three zones, with a less fractured and more massive middle zone yielding higher resistivity readings apparently bracketed by regions of lower resistivity. The lower contact of the second massive flow is defined by a sand–siltstone succession (Unit VI; Fig. F15) that appears as a ~4.5 m thick intercalation in the downhole logging data (of which only ~50 cm was recovered in the core).

Third massive basalt flow (stratigraphic Unit VII, lithologic Units 7–9)

The third massive flow of Group 1 in the downhole logging measurements is apparent as a ~8 m thick interval that follows beneath the sedimentary interbed of stratigraphic Unit VI (see “Sedimentology”). This flow contains <3% plagioclase microphe-nocrysts, only a trace of clinopyroxene, and no olivine, and thus it is the most aphyric of all basalts cored at Site U1347. Recovery is relatively good (>60%) with the topmost ~3 m being highly vesicular (20%–30%), passing down into ~2–3 m of nonvesicular basalt in the flow core. However, unlike the overlying unit, the lower part of this flow is absent.

Geochemical analyses reveal that the lower (nonvesicular) part of this unit is characterized by high TiO_2 and Ni abundances compared to the top part and the overlying massive lava flows of Units VI and IV (see “Geochemistry” for more details). Such a difference could be interpreted as a compositional break reflecting different magma sources. If correct, this flow

“unit” may actually represent juxtaposed portions of two separate flows (Fig. F15), which in downhole logging measurements may be evident from a pronounced decrease in resistivity at or near the level of their contact (see “[Downhole Logging](#)”). In addition, the lower flow is also characterized by high magnetic susceptibility, which diminishes significantly toward its base (Fig. F16). Unit VII is underlain by a well-bedded 4–5 m thick radiolarian-bearing clay-sandstone (Unit VIII; Fig. F15). This is of finer grain size than sediment of Unit VI and contains abundant signs of bioturbation (see “[Sedimentology](#)”).

Fourth massive basalt flow (stratigraphic Unit IX, lithologic Unit 11)

The fourth and lowermost of the massive basalt units of Group 1 follows beneath the sedimentary intercalation of stratigraphic Unit VIII; it is ~12 m thick, moderately vesicular (especially in its upper part), and plagioclase-pyroxene phyric with phenocryst abundances of as high as 20% (Fig. F16). These petrographic characteristics distinguish it from the overlying three flows. Despite moderate recovery (<50%), many volcanic features are observed, including the baking of sediment at the upper contact, a well-defined chilled upper zone, a sparsely vesicular core, and a chilled lower margin at its base. This fourth massive flow is obviously much less vesicular than the flows above, but its core contains well-developed vertical vesicle pipes and associated small segregation zones containing darker melt material.

Group 2

Heterogeneous stack of pillow lavas and minor flow units (stratigraphic Units X, XII, and XIV)

The heterogeneous lava stack comprising Units X, XII, and XIV is 75 m thick and consists primarily of pillow lava inflation units with glassy margins and massive aphanitic to plagioclase-phyric interiors (Figs. F20, F21). Inflation units within the pillow lava-dominated sections have glassy margins 1–3 cm thick; these consist of plagioclase and pyroxene in sideromelane and display a transition to spherulites at the edge of the margin (Fig. F21). Unaltered glass is present in all of the chilled pillow unit margins throughout the pillow lava succession. Irregular tube- and drop-shaped vesicles (or amygdules) are present along the inside of some pillow margins. Most of the vesicles in the pillow lava succession are filled with secondary minerals. The interiors of pillows are relatively free of macroscopic features but rarely preserve megavesicles, cooling joints, or sparse spherical vesicles (<1 mm in diameter). The groundmass of the pillow lavas varies from cryptocrystalline

on the margin, to very fine grained in the interiors with sparse tabular and glomerocrystic plagioclase phenocrysts.

Since pillow lava inflation units are typically sub-spherical or oblate, it is important to note that the curated thickness may, in some instances, only represent marginal sections through these pillow units and thus represent a significant underestimation of the individual pillow thicknesses; however, we deduce that these types of inflation units generally have individual thicknesses ranging from ~0.2 to 1.2 m (Fig. F22). From the recorded curated size distribution, ~1 m appears to be the modal maximum thickness for individual pillow inflation units in this stack. Examination of individual unit thicknesses within the stack as a whole indicates a broader size distribution including three larger (~3–6 m) massive units, nine or ten medium-sized inflation units (~1–2 m), and the intervening successions consisting of numerous small pillow inflation units (~0.2–0.8 m). The pillow units are intercalated with sediments ranging from sandy siltstone to volcanoclastic limestone, in some cases bedded sediment layers are as thick as ~5 m (e.g., Units XI and XIII), and in other instances they occur as small interpillow sediment pockets (e.g., intervals 324-U1347A-19R-3, 57–78 cm, and 22R-5, 19–30 cm).

For ease of description, Group 2 has been arbitrarily divided into upper, middle, and lower sections on the basis of the intervening sedimentary intercalations (Units XI and XIII).

Upper pillow lava stack (stratigraphic Unit X, lithologic Units 12–42)

This upper lava stack follows beneath the fourth massive flow of Group 1, lacks any (cored) intervening sedimentary bed, and consists predominantly of small pillow inflation units less than ~1 m thick. In total, >20 small pillow inflation units can be identified ranging in recovered thickness from 0.15 to 1.35 m, yielding a total recovered thickness of ~40 m. Vesicularity within these pillows is variable, with only rare development of well-defined concentric vesicle zones, and chilled margins often lack visible radial cracking and the associated vesicle concentrations. Petrographically, these pillow lavas are composed of massive aphyric, sparsely phyric, and plagioclase phyric basalt, with plagioclase phenocryst abundances of <1%, 3%–5%, and 10%, respectively. Plagioclase “phenocrysts” often occur in the form of anhedral plagioclase laths arranged into glomerocrysts of ~2–3 mm in size. Groundmass textures vary from cryptocrystalline through microcrystalline to very fine grained (and rarely to medium grained) groundmass sizes from chilled margins into flow interiors.

Thicker inflation units of 1–2 m occur toward the lower part. Much larger units of 3–5 m thickness (lithologic Units 37 and 42) form the base of this section but are themselves separated by four or five successions of larger pillow units. The thickest of these larger units (lithologic Unit 42) lies directly upon a thin sedimentary intercalation of silty claystones and a coarse-grained volcanoclastic limestone (stratigraphic Unit XI; Fig. F15), which defines the boundary between the upper and middle lava stack sections.

Middle pillow lava stack (stratigraphic Unit XII, lithologic Units 46–58)

This middle lava stack consists of ~10 small pillow inflation units, ranging in thickness from ~0.2 to 1.5 m, and is intercalated with a single thick flow unit of ~5.6 m, giving it a total recovered thickness of ~20 m. Vesicularity in the pillow units is variable, with only rare development of well-defined concentric vesicle zones, and chilled margins often lack visible radial cracking and associated vesicle concentrations. Petrographically, these pillow lavas are composed of massive aphyric, sparsely phyric, and plagioclase phyric basalt. The core of the larger unit contains pipe vesicles and segregation features. Downhole logging indicates low resistivity throughout much of this section, probably due to the stacking pattern of the small pillow units; by contrast, the 5.6 m thick flow in the middle of Unit XII is characterized by a consistently higher resistivity. The middle lava stack is underlain by a thin ~15 cm (~50 cm by downhole logging) sedimentary intercalation of highly altered volcanoclastic sandstone (stratigraphic Unit XIII; Fig. F15), which defines the boundary between the middle and lower lava stack sections.

Lower pillow lava stack (stratigraphic Unit XIV, lithologic Units 60–80)

This lower section consists of ~10 large inflation units typically ranging in recovered thickness from ~0.5 to <2.0 m, and which are intercalated with a few much smaller pillow units of ~0.1–0.2 m, giving a total recovered thickness of ~14 m. This is close to the true thickness since recovery throughout this lava stack approached 100%. Vesicularity in the larger inflation units typically occurs as weakly concentrated accumulations of vesicles within the upper chill zone but increases in density (~1%–2%) toward the top glassy contact. Pipe vesicles and magmatic segregation features occur within the core of the units. The lowermost units of this stack are a succession of particularly small pillows (~0.1–0.2 m thick) containing thin intercalations of highly baked sedi-

mentary material. These small pillows lie directly upon the top of the massive flow units of Group 3.

Group 3

Fifth and seventh massive basalt flows (stratigraphic Units XV and XVI, lithologic Units 81 and 82)

The largest of the volcanic units recovered in Hole U1347A occurs immediately below the lowermost pillow basalts of Group 2. The uppermost lava flow (Unit XV) is ~23.1 m thick and is itself immediately underlain by Unit XVI, which is similar in character but only cored to a depth of ~2 m before drilling was terminated at the site. Based upon observable internal characteristics in the recovered core this is likely to have been of a similar “massive” dimension. Both flows have well-developed chilled zones at the top (glassy to microcrystalline in the topmost ~1–2 m), with a somewhat thinner one (<0.5 m) at the base of the upper flow. By comparison with the overlying lava stack, relatively little glass formed at these flow contacts, but intense sediment baking effects were observed to have occurred where a thin sandstone or mudstone had intervened between the two flows (interval 324-U1347A-29R-4, 70–82 cm). Vesiculation is confined to the upper 2–3 m, below which the flows become very homogeneous and largely nonvesicular. Moreover, pipe vesicles and associated magmatic segregation features are less well developed compared to the four thick units (IV, V, VII, and IX) that occur in Group 1 at the top of this volcanic succession.

Texturally, these units consist of thick, homogeneous, and very fine grained flow cores, progressively passing into microcrystalline and ultimately cryptocrystalline patches through the chilled zones and at the chilled margins. Within the massive flow of Unit XV, several 30–70 cm thick zones of marginally coarser texture may be identified; these may reflect cooling (and crystallization) heterogeneities or multiple injections during inflation (see “**Petrography and igneous petrology**” for more details).

Preliminary assessment

It is known that the stacking and horizontal arrangements of lava successions are complex, though such studies are largely restricted to continental examples (e.g., Jerram and Widdowson, 2005). From these studies, the hierarchical organization of lava units may be described in terms of lava flow-fields, lava flows, and lava lobes (Self et al., 1997). The term “flow-field” designates the entire product of an eruption event and may consist of one or multiple lava flows. The term “flow” refers to a lava body formed by the solidification of a single outpouring of lava and represents a single episode of magma effusion

during the eruption event. However, lava flows rarely form a laterally continuous stretch of lava; instead they consist of successions of lobate segments or inflation units, which can occur on several scales. Continual inflation of such lobes (or coalescence of several lobes) produces a broad lava body with a very flat upper surface that could be identified as a “sheet” lobe (Hon et al., 1994). Meter- or kilometer-scale sheet lobes can themselves be found to be composed of centimeter- to meter-scale lava lobes in the field. The term “toe” is given to small, centimeter- to decimeter-sized budding lava lobes. Importantly, in marine eruptions, these toes typically form glassy rinds, inflate, and often separate from the main lobes to produce pillow lava units. All these different scales of inflation units are analogous to those of the different unit types recovered in Hole U1347A.

Pillow lava stacks

Pillow lava units of Group 2 are similar in dimension to those cored in Hole U1346A, but they differ in key respects. For instance, the pillows cored in Hole U1347A are much less vesicular, with only rare development of concentric vesicle zones or banding, and they often lack visible radial cracking around their margins. In addition, they are highly remarkable for their well-developed chilled margins and dark glassy rinds (~1–3 cm thickness), in which fresh basaltic glass (showing vitreous, conchoidal fractures) is commonly preserved (Figs. F20, F21). Structures within the glassy chilled margins also reveal details of deformation that resemble those of typical pahoehoe-like crusts, such as cross-sections through wrinkled and folded lava crusts. In other cases these chilled margins provide evidence for the coalescence of adjacent pillow units, occurring between lobes at the centimeter to meter scale (e.g., Sections 324-U1347A-19R-2 and 20R-2). Most basalts in Group 2 appear petrographically similar. However, inspection of the stacking pattern, together with differences in the sizes of the inflation units and the positioning of intercalated sedimentary horizons (Fig. F15), reveals a repetitive pattern. For example, the pillow basalt sequences all appear to begin with larger massive units, pass upward into predominantly medium-sized inflation units, and then finally pass into an overlying succession of small, closely packed pillow lava units before the cycle is repeated. This stacking pattern may indicate several eruptive pulses, each producing separate flow-fields, during which the rate of lava effusion diminishes over time. In such a scenario, the thicker, larger units (>3 m) would be produced at the onset, followed by the production of progressively thinner units (1–2 m), and concluding with a more prolonged but reduced-magmatic-flux

eruptive phase producing the smaller pillow units. Hiatuses between the eruption of these putative flow-fields are indicated by the occurrence of sedimentary intercalations.

Flow-field organization of the massive sheet flows

The thicker massive flows of Groups 1 and 3 have well-developed upper chill zones and thinner ones developed at their lower contacts. They also have thick homogeneous cores with the degree of crystallinity increasing subtly away from their margins. These petrographic changes define a broadly tripartite internal structure that divides each flow into a vesicular upper crust, a massive core, and a sparsely vesicular basal zone. The upper crust has glassy folds and concentrations of vesicles (and amygdules) in the top 1–3 m (10–30 vol%). The massive core of each unit is typically homogeneous, sparsely vesicular with rare megavesicles, and often incorporates well-developed pipe vesicle zones containing dark melt segregation material. Vesicle density in these unit interiors is usually negligible (<2%), and these vesicles are randomly distributed, rounded, sub-rounded, or sometimes coalesced. A large proportion of the vesicles are filled with secondary minerals (calcite and clay minerals); however, the diktytaxitic vesicles remain open. Contacts between the large units typically reveal a glassy margin, sometimes with brecciated basalt clasts. The upper crust exhibits folds and stretched vesicles typical of inflated pahoehoe sheet flows (e.g., Hon et al., 1994) with glassy margins containing spherulites (Figs. F17, F18). These crusts display several alternating horizontal layers of larger and smaller vesicle horizons and rare large (>5 mm) vertically elongate, irregularly shaped vesicles.

Petrographically, the massive interiors of the larger flows are composed of a microcrystalline to very fine grained, typically aphyric to sparsely plagioclase phyrlic basalt, with groundmasses consisting of plagioclase and clinopyroxene microlites and altered glass (see “**Petrography and igneous petrology**”). Phenocrysts occur either as 2–3 mm clots and/or intergrowths of two distinct generations of plagioclase. These plagioclases are either characterized by cores of individual tabular plagioclase crystals, of up to 2 mm, surrounded by later acicular microlites, or else they appear as smaller 0.3–0.6 mm glomerocrysts composed entirely of plagioclase microphenocrysts. Only occasionally does the tabular plagioclase occur independently as separate crystals.

Ubiquitous development of segregation features associated with pipe vesicles in the four upper massive flows of Group 1, and in the larger inflation units of the underlying Group 2 succession, indicates em-

placement and subsequent inflation through continued high-rate magma supply, followed by stagnation, cooling, degassing, and solidification. These thick units are comparable in both dimension and internal structure with those commonly observed in continental flood basalt provinces (Thordarson and Self, 1998); accordingly, it may be deduced from their thickness dimension that they are also likely to be laterally extensive sheet flows.

Volcano-sedimentary relationships

The sediments lying above, and intercalated within, the volcanic succession recovered from Hole U1347A are indicative of the availability of basalt-derived material both during and after the eruptive episodes. Sedimentary structures, extensive bioturbation, and macro- and microfossil content indicate that moderate-depth to shallow-marine depositional conditions were established during noneruptive periods (see “[Paleontology](#)” and “[Sedimentology](#)”). To better understand how the sedimentary record may have responded to lava eruption, it is useful to briefly outline the dynamics of lava flow emplacement and the evolution of a lava field or pile. Lava fields evolve continually over periods of years to decades. During their development, different areas will become active due to changes in the supply of magma from the vent sources to the propagating tips of individual lava flows that constitute the evolving lava field. Accordingly, areas of an active lava field become periodically abandoned and elsewhere rejuvenated over the period of active volcanism. These changes can result in a highly dynamic physical environment across the surface of a single lava field, which will have profound effects upon the distribution of coeval sedimentation. For instance, until the whole of the lava field becomes inactive, the development of sedimentary deposits will be localized and patchy. Once eruption does cease altogether, the whole of the volcanically generated surface becomes a potential site for alteration and/or deposition. Development of sedimentary deposits is far more likely in a submarine environment, compared with subaerial flows. The intra- and supra-volcanic deposits recovered in Hole U1347A can thus be respectively interpreted as patchy, localized, volcanically coeval deposits, developing into a more continuous post-eruptive sedimentary succession in a shallow- to off-shore-marine environment.

Petrography and igneous petrology

Variably porphyritic plagioclase-clinopyroxene basalt pillows and larger inflation units were recovered in Hole U1347A. Polished thin sections of rims and interiors of 73 of these flows were prepared, includ-

ing all instances where inductively coupled plasma-atomic emission spectroscopy (ICP-AES) analyses were made. The chemical analyses reveal that a variety of distinctive and fairly differentiated rocks were obtained ($\text{TiO}_2 > 1.5\%$; $\text{Mg\#} < 60$), all of incompatible element depleted tholeiitic character (see “[Geochemistry](#)”). Fresh glass was recovered at many locations, readily enabling identification of the microphenocrysts and phenocrysts preserved within it. From these exterior portions of flows and pillows, general crystallization histories could then be traced into their interiors.

Based on lithology, units of the basalt succession were divided into three groups (Fig. [F15](#)). The distribution of these groups and lithologic units, together with a summary of the relative abundances of phenocrysts and the presence of glass, is shown in Table [T6](#), and more precise visual estimates based on thin section descriptions are plotted in Fig. [F23](#). The occurrence of fresh glass has been logged in 324GLASS.XLS in LOGS in “[Supplementary material](#).” The following gives a summary of the petrographic description of the major lithologic groups using thin sections. A discussion follows of the crystallization histories based on rock textures and mineralogy as illustrated by photomicrographs.

Group 1 upper massive basalt flows (stratigraphic Units IV, V, VII, and IX)

The petrography of the upper massive basalt lava flow units (four massive flow units: IV, V, VII, and IX) is based on 28 thin sections from all identified flow units. These are of low to moderate vesicularity (1%–15%), are aphyric to sparsely plagioclase-phyric (1%–5%), and commonly contain glomerocrystic plagioclase and/or clinopyroxene. Plagioclase is the most abundant phenocryst phase, usually present as glomerocrysts forming aggregates as large as 5 mm. Relatively high abundances (5%–7%) of plagioclase phenocrysts occur in lower Unit IX (Figs. [F16](#), [F23](#)). Olivine and clinopyroxene are observed as microphenocrysts. Although olivine is typically pseudomorphed by brown clay (see “[Alteration and metamorphic petrology](#)”), a few unaltered olivine microphenocrysts are included in the more glassy parts of Units IV and V. Some are skeletal in form and as large as 0.7 mm. Olivine microphenocrysts commonly contain rare inclusions of altered glass and (only) one olivine crystal contains Cr spinel. Clinopyroxene microphenocrysts usually subophitically enclose acicular microcrysts of plagioclase. In groundmasses of the larger massive flow interiors, intersertal to subophitic textures predominate. Unaltered glass is present in the marginal areas of massive flow units. The unaltered glass in the rims merges

within centimeters to zones of dark brown coalesced spherulites (e.g., Fig. F24).

Group 2 pillow lava stack (stratigraphic Units X, XII, and XIV)

The petrography of pillow lavas (Units X, XII, and XIV) is based on 36 thin sections from 19 of the 57 inflation units identified (see 324UNIT.XLS in LOGS in “[Supplementary material](#)”). These have 0%–3% vesicles that range in size from 0.1 to 1 mm in the glassy rims but are larger in pillow interiors, except the lowermost massive flow of Unit X (Fig. F15), which has a higher vesicularity (7%–15%). The basalts are aphyric, sparsely plagioclase-phyric (0%–5%), and sparsely plagioclase-clinopyroxene phyric (5%–20%). Plagioclase phenocrysts are commonly glomerocrysts forming aggregates as large as 3 mm. On the other hand, pyroxene and olivine occur only as microphenocrysts (<1 mm diameter) throughout the pillow lava stack. Most pyroxene microphenocrysts are intergrown with acicular or tabular plagioclase. Olivine microphenocrysts are rare in most thin sections (several grains per thin section) and are almost completely replaced by secondary minerals. With the exception of the upper pillow lava succession of Unit XII, the relatively thick inflation units (>1.5 m) within the pillow lava successions have no olivine, whereas many of the thinner inflation units (<1.5 m) contain olivine (Table T6). Many glassy margins of pillow tops, sides, and bottoms are preserved as fresh glass, most usually mantling basaltic rock with spherulitic textures (see 324GLASS.XLS in LOGS in “[Supplementary material](#)”). Groundmass minerals of flow interiors are microcrystalline to very fine grained and are composed of acicular plagioclase, dendritic clinopyroxene, and tiny skeletal titanomagnetite. Textures around pipe vesicles or gas blisters, as well as around magmatic segregations, are aphyric and cryptocrystalline, darker in color, and contain more titanomagnetite than surrounding rock.

Group 3 lower massive basalt flows (stratigraphic Units XV and XVI)

The petrography of the lowermost massive basalt flows (Units XV and XVI) is based on nine thin sections. These are aphyric to sparsely plagioclase-phyric (<3%) and commonly contain both plagioclase pheno- and microcrysts and olivine microphenocrysts. Clinopyroxene phenocrysts are not present. Plagioclase is the most abundant phenocryst phase, usually present as glomerocrysts forming aggregates as large as 3 mm. Individual tabular phenocrysts of plagioclase reach as large as 2 mm. Olivine occurs as microphenocrysts and is typically pseudo-

morphed by brown clay (see “[Alteration and metamorphic petrology](#)”). Some of it is skeletal in form, and as large as 0.5 mm in diameter, but it also forms glomerocrystic aggregates with plagioclase phenocrysts and microphenocrysts. Groundmasses in the massive flow interiors have coarsely spherulitic to intersertal and subophitic textures (e.g., Fig. F25). The grain size of intergrown groundmass plagioclase and clinopyroxene in Unit XV (0.2–0.4 mm) is greater than Unit XVI basalt below it (0.1–0.2 mm).

Crystallization history of basalts

Figures F24, F25, F26, F27, F28, F29, F30, F31, and F32 depict the crystallization histories and many other attributes of the basaltic rocks in Units IV–XVI. Captions in all cases identify the curated depths and the stratigraphic unit (I–XIV) of the thin sections, including their main characteristics (flow unit, pillow succession, etc.) and positions (rim, top, upper, middle, etc.) within the sampled stratigraphic unit or interval.

In hand specimen, many rocks were deemed aphyric, whereas in thin sections even the glassiest samples were observed to contain tabular/elongated to partly skeletal crystals of plagioclase, with variable proportions of these plagioclases intergrown with anhedral pale brown clinopyroxene. These crystals could be termed “microphenocrysts” because they are tiny (<1 mm). The two-phase intergrowths are either isolated pairings of the minerals or crowded multicrystal clumps and clusters and are of different grain sizes both within and between samples. Many thin sections contain (a few) much larger phenocrysts, megacrysts, and glomerocrysts of the plagioclase/clinopyroxene aggregates, in some cases including small amounts of olivine. Except at extreme glassy margins, the crystals are usually mantled with dark brown spherulitic overgrowths that consist chiefly of needles of plagioclase and intergrown fibers of dendritic clinopyroxene. The crystallization histories of the rocks, therefore, can be considered in two stages: (1) a preeruptive interval crystallizing larger crystals (and aggregates) and (2) a syn- and posteruptive interval with smaller crystals growing in the melt at the time of eruption. Synchronicity between plagioclase and clinopyroxene crystallization in the preeruptive stage is indicated by their combined nucleation on the planar surfaces of faceted plagioclase, whereas spherulitic overgrowths imply a sudden and abrupt increase in cooling rate at the point of eruption.

The presence of up to several percent of tabular plagioclase crystals (e.g., within and adjacent to glassy material) intergrown with well-formed anhedral clinopyroxene, the rarity of olivine, and the almost

complete absence of Cr spinel distinguishes these rocks from their less differentiated counterparts at Sites 1213 and U1346 elsewhere on Shatsky Rise. Evidently, eruption did not change the identity of the crystallizing minerals because during every stage of crystallization the basalts appear to be saturated in both clinopyroxene and plagioclase. The rocks were, therefore, in a condition of low-pressure plagioclase-clinopyroxene cotectic crystallization during their entire cooling and differentiation history. Olivine was a minor (trace to 1%) coprecipitating mineral during only the earliest stages. It was later supplanted by titanomagnetite, which only is visible between crystals of the silicate minerals in the rapidly cooled spherulitic portions of pillows and flows and within intersertal patches in their interiors.

Crystallization history of pillow and flow units following eruption

Pillow basalts in Hole U1347A are restricted to a central stack of ~75 m in the middle of the basalt sequence (Group 2) and occur in packages sandwiched between thicker flow units of up to ~23 m thick. In general, the pillows recorded the same pattern of crystallization, from rims to interiors, as those of pillows in Hole U1346A, with the exception that olivine is rarely present and Cr spinel is absent (except for a single tiny crystal in one thin section). The rocks become increasingly crystalline away from glassy rims, progressing from the outer zones dominated by spherulites of plagioclase toward the interior of pillow inflation units, where branching acicular plagioclases are intergrown with smaller grains of dendritic to subhedral clinopyroxene and skeletal titanomagnetite. The rocks in Hole U1347A, however, are significantly less altered than those in Hole U1346A, and, therefore, the textures and morphologies of all the minerals can be easily observed with the microscope. The modal proportion of fresh rock as seen by crystallinity in reflected light (percentage of polished mineral surfaces) is never <50% and, in some examples, is as high as 95%.

More information about crystallization can be determined from the thicker flows. Figures F24 and F25 depict the crystallization of two of the five thickest cooling units in Hole U1347A. These, respectively, are the third massive basalt flow (Unit V; Flow 3; ~8 m thick based on logging) near the top of the basalts in Group 1 and the fifth massive basalt flow (Unit XV; Flow 5; ~23 m thick based on logging and curated coring depths) in Group 3 near the base of the cores (see Fig. F16 for locations).

In both of these massive flows, general increases in grain size (e.g., plagioclase observed in photomicrographs) and crystallinity are apparent through the

flow interiors. Grain size and crystallinity increase from both tops and bottoms but not in the same way. For instance, the degree of crystallinity, and the average grain size of Flow 3 at 4 m from its base, is far less than that observed in Flow 5 at only 1.5 m from its base. This is probably because Flow 3 is much thinner and therefore cooled more efficiently from its top than from its insulated base (Kirkpatrick and Hodges, 1978). The stubbiness (width to length ratio) of plagioclase crystals in Flow 3 is also greater throughout. Along with a lower degree of crystallinity, this may be a consequence of a more differentiated composition, or else the melt of Flow 3 was simply more viscous on eruption and thus less prone to form elongate and acicular plagioclases (Kirkpatrick, 1975).

Flows 3 and 5 also can be distinguished in another way. Many subaerial basalt flows tend to crystallize in frameworks of minerals (Jerram et al., 2003). Isolated crystals and clumps at their margins continue to grow in both length and width in interiors until they touch and form interlocking aggregates and networks. At this point, because the delicate networks are rarely broken, almost no motion of interstitial liquid is present and the networks will continue to crystallize in situ. In submarine tholeiitic pillow lavas, two types of networks can be distinguished, even in the centers of small pillows: (1) those consisting mainly of interlocking acicular plagioclase (e.g., Kirkpatrick, 1979; Natland, 1979) and (2) those consisting of aggregates or networks of intergrown plagioclase and clinopyroxene, forming a so-called “sieve texture” around much finer grained dark intersertal patches.

In these terms, Flow 3 is more clearly allied with the first type, with plagioclase crystals first touching and then forming a weakly linked network in its interior (Fig. F24D). Flow 5 exhibits clumps or clusters of intergrown plagioclase and clinopyroxene that touch and form sieve textures in its interior (Fig. F25B–F25F). Similar sieve-textured plagioclase-clinopyroxene networks separating intersertal patches are also well developed in Flows 1 and 4. Some portions of the interior of Flow 5, however, are not nearly so coarsely crystalline as most other flows in Hole U1347A, nor do they have well-developed sieve texture. This is partly evident in Figure F25D, whereas Figure F25E clearly shows two zones of different crystallinity, crystal size, and network characteristics on the left and right. In these zones, the finer grained material is evident as darker splotches and streaks consisting of dark glass, finely crystalline dendritic clinopyroxene, and elongate skeletal titanomagnetite, suggesting they likely are more differentiated than the bulk of the rock. The patches and streaks of finer grained and darker material within

Flow 5 do not appear to have separated from the rest of the rock and created an internally hybrid lava flow.

Finally, further support for this cooling history for these thick massive lava flows comes from variations in magnetic susceptibility measured within Flow 5 (see “**Physical properties**”). This is controlled by the quantity of titanomagnetite in the rock, which, in submarine basalts, depends on crystallinity. Those rocks in which all glass has been crystallized into minerals (including all vestiges of intersertal glass) have the most titanomagnetite (corresponding to the coarsest crystalline portions of the core). Accordingly, the glass in quenched pillow rims should have the least titanomagnetite and thus have a lower magnetic susceptibility. On this basis, the nearly continuously recovered Flow 5 records the least magnetic susceptibility at its “quenched” top, fluctuations thereafter, and a general increase toward its base, below which the susceptibility again decreases toward the contact (Fig. F33). These data support petrographic inferences that the flow cooled asymmetrically, is coarsest grained and most crystalline toward its base, has chemical variability, and thus has intrinsically different proportions of titanomagnetite within it. A similar increase in magnetic susceptibility with depth occurs in Flow 1 (~19 m thick) but without the fluctuations (Fig. F33).

Phenocrysts, megacrysts, and glomerocrysts

Large crystals in these basalts are tabular, equant, or irregularly shaped and are significantly larger than the smaller tabular plagioclases and intergrown clinopyroxenes that are plentiful in the glass (Fig. F26). These larger crystals were all formed prior to eruption. Some have skeletal or sievelike interiors or occur as broken zoned fragments, or occur within multicrystalline aggregates and glomerocrysts. They are variously present in glass, in spherulitic portions of pillows and flows, and in their coarse-grained interiors, and their proportions can vary from one thin section to the next, between hand specimens, and within individual cooling units. In many cases, grain size is sufficiently small that the phenocrysts and microphenocrysts were more readily discerned in thin sections than during visual description of the core. However, special aspects of their crystal morphologies (in particular zoning, skeletal morphologies, or broken outlines) permit them to be distinguished from posteruptive crystals of similar size.

Table T6 shows the estimated presence and relative abundance of phenocrysts as estimated using thin sections. Most notable are the abundance of plagioclase phenocrysts in Flow 4 and the rarity or absence of clinopyroxene phenocrysts in the lower pillow

stack (stratigraphic Units IX and XIV, respectively), as well as their absence in Flows 5 and 6 (stratigraphic Units XV and XVI). Olivine is persistent in trace abundances throughout the core.

Olivine: This rare mineral is almost always replaced by pale brown clay minerals (Fig. F27A–F27C), calcite, or both (Fig. F27D). Despite alteration, its crystal outlines are usually maintained even if the crystals have delicate dendritic extensions (Fig. F27A, F27B). Some olivine is intergrown with tabular plagioclase (Fig. F27C), and some grains have broken edges (Fig. F27D). Small dark brown circular areas within the crystals (Fig. F27B) are probably altered glass inclusions. Very rarely, some relict fresh olivine remains (Fig. F27E), with even rarer inclusion of Cr spinel (the only grain of this mineral seen). Overall, the few olivine phenocrysts appear to have crystallized mainly before extrusion but continued to crystallize with dendritic extensions afterward.

Plagioclase: Plagioclase displays the most varied crystal morphologies. Here we consider only the larger crystals and glomerocrysts that formed prior to eruption. Some crystals are tabular but have a skeletal interior, often with a nonskeletal mantle or normally zoned exterior (Fig. F28A). Others are elongate syneusis aggregates of several crystals, each having a central twin plane (Fig. F28B), or else they appear as moderately complex multicrystalline aggregates made up of several crystals bounding each other along portions with skeletal interiors (Fig. F28C). All of the above crystals appear to be a single array of exterior oscillatory and normal zones. Finally, some glomerocrysts are complexly multicrystalline, with melt inclusions within and between crystals and grains exhibiting complex sequences of skeletal growth and oscillatory zoning (Fig. F28E, F28F). Oscillatory zoning observed in a single crystal (Fig. F28F) reveals the different rates of growth along different crystal facets when it still was isolated in the melt. The crystal then became attached to the glomerocryst (Fig. F28E), after which the oscillatory zoning continued to develop in the aggregated crystal. Many of the observed glomerocrysts exhibit similar complex patterns of growth. The path from simple faceted and tabular morphologies to a complex aggregate of crystals can be readily observed, even in megacrysts approaching 0.5 cm (Fig. F29), and some glomerocrysts preserve unaltered glass inclusions both within and between crystals (Fig. F30). These inclusions may record the degassing histories of these rocks that, on the basis of their vesicularity and characteristics of interbedded sediments, appear to have erupted in a shallow-water environment.

Clinopyroxene: Figure F31 shows typical attributes of the larger clinopyroxene population. The most usual

occurrence in the glassy portions of the flow is as small crystals intergrown with tabular or at least faceted plagioclase. Some of the pyroxenes have a somewhat lumpy but mostly faceted outline (Fig. F31A), whereas others are intergrown with skeletal plagioclase (Fig. F31B). Toward flow interiors, in the more finely spherulitic portions of the rocks, the intergrowths shown in Figure F31A combine into loosely strung aggregates (Fig. F31C), which seem to be precursors to the network sieve structure described earlier. In coarser grained rocks, the clinopyroxene grains also are larger, and these aggregates become fully interlocking (Fig. F31D). Examples of truly coarse grained aggregates can be found with clinopyroxene that subophitically enclose angular plagioclase fragments (Fig. F31E). These examples suggest a substantial period of cotectic crystallization of clinopyroxene and plagioclase in a slowly cooled magma prior to eruption. Euhedral clinopyroxene phenocrysts occur only in a few glassy samples. Examples from flow tops are shown in Figure F31F and F31G, where clinopyroxene appears as isolated small crystals.

Titanomagnetite

Titanomagnetite has importance in determining certain rock magnetic properties such as magnetic susceptibility. Many of the rocks are fresh enough to preserve detailed crystal morphologies of this mineral (Fig. F32). Glass rims from pillow units typically have no titanomagnetite, which is confirmed after a close inspection of the glassy chilled margins, which reveal swirling spherulitic patterns of fibrous plagioclase and brighter dendritic clinopyroxene containing only a very few titanomagnetite grains (Fig. F32A, F32B).

However, within ~2–3 cm of these glassy outer rims, the spherulitic swirls of plagioclase and dendritic clinopyroxene become populated with hundreds of tiny titanomagnetite grains (Fig. F32C). In high-magnification reflected light, these titanomagnetite grains reveal incipient skeletal morphologies, whereas coarser titanomagnetite with better developed skeletal morphology can be seen in the menisci of segregation vesicles despite the high degree of alteration (Fig. F32D). Intersertal patches in the coarser grained portions of the flows and pillows also tend to be altered, but not so extensively that the alteration destroys the titanomagnetite crystals. In Figure F32E, an elongate skeletal titanomagnetite grain spans a large portion of basaltic rock (more reflective, white), with interlocking clinopyroxene-plagioclase (light gray) and two altered (nonreflective, dark gray) intersertal patches into which the crystal grew lengthwise. In Figure F32F, many of the titanomag-

netite grains (small, less reflective grains) are completely enclosed by intergrown plagioclase (dark gray) and clinopyroxene (light gray), yet none appears in the altered intersertal portions of the rock (nonreflective). In Figure F32G, an intergrowth of titanomagnetite and plagioclase is shown next to an altered space with clay minerals. Typically, titanomagnetite has alteration pits and cracks, but on the whole its morphology is well preserved.

Finally, Figure F32H shows an unusual cross section through a partially crystalline glass inclusion in a plagioclase crystal. The dark crystals are a trellis of dendritic titanomagnetite, with the larger crystals and their pointed tops representing a larger “trunk” and smaller orthogonal crystals being “branches.” The mineral is set in glass that, in this thinned out view, is only pale brown. The tiny clear crystals are dendritic clinopyroxene. There is no acicular plagioclase evident.

Preliminary assessment

From their compositions, Shatsky Rise basalts in Hole U1347A are more differentiated than basalts in either Hole 1213B or Hole U1346A (see “[Geochemistry](#)”). In petrographic terms, this is evident from the predominance of plagioclase-clinopyroxene intergrowths at all stages of crystallization, the scarcity of olivine phenocrysts, and the almost complete absence of Cr spinel. These phenocryst assemblages and the character of intergrowths compare well to those of rather evolved, low-temperature gabbros that formed in “shallow” crustal magma chambers (such as those occurring beneath superfast spreading ridges). The fastest spreading ridge currently is the East Pacific Rise, yet basalts there are almost always aphyric, whereas basalts of ridges spreading at slow and intermediate rates, such as the Mid-Atlantic Ridge and Costa Rica Rift, are often porphyritic (e.g., Hekinian and Morel, 1980; Bryan, 1983; Natland et al., 1983). Natland and Dick (2009) attribute this aphyric nature to a filtration effect occurring in the nearly consolidated gabbros beneath the East Pacific Rise and the necessity to drive only eruptive liquids through this and into a steady-state “melt lens” at the top of these gabbros; importantly, this lens is not seen on slowly spreading ridges (Sinton and Detrick, 1992). This melt lens collects only evolved residual liquids that happen to work their way buoyantly through a dense filtration network or series of flow channels in the gabbros. Whereas melt leaks into the lens, the phenocrysts are instead retained as textural relics in the gabbros. Eruption then taps the aphyric magma in the melt lens. In the case of Shatsky Rise basalts, the high abundances of cotectic plagioclase and clinopyroxene phenocrysts present makes it

probable that there was no melt lens present beneath Site U1347, or beneath Sites 1213 and U1346, despite the postulated high spreading rates for the spreading surrounding Shatsky Rise.

Experimental petrology on mid-ocean-ridge basalt (MORB) (e.g., Stolper 1980; Fujii and Bougault, 1983; Kinzler and Grove, 1992), and on rocks from the Ontong Java Plateau (OJP) large igneous province (LIP) (Sano and Yamashita, 2004), indicates that precursor magmas only have olivine on the liquidus at low pressure. This is then followed by plagioclase and finally clinopyroxene at lower pressures and a temperature interval of only $\sim 50^\circ\text{C}$. The rocks in Hole U1347A are multiply saturated in these minerals, with plagioclase and clinopyroxene predominating, suggesting that these minerals have crystallized at similar temperatures, but at very low pressures upon eruption in a shallow submarine environment. The basalts in Holes 1213B and U1346A were only slightly different in their crystallization sequence, as they had both olivine and plagioclase phenocrysts when they erupted, soon followed by clinopyroxene. The supposition that primitive MORB and LIP liquids always have olivine alone on the liquidus, and thus must always be picritic, has been questioned previously (e.g., Kushiro and Thompson, 1972; Natland et al., 1983; Fisk, 1984). Shatsky Rise now appears to be an additional location where this conventional wisdom may be questioned.

Primitive basaltic liquids that are multiply saturated in several silicate phases raise two other petrogenetic problems. First, experimental petrology (Fisk, 1984) suggests that they originated by partial melting at low pressure, at depths perhaps only 10–20 km in the mantle. Alternatively, computer simulations suggest that low to moderate H_2O content in the magma may have caused phase boundaries to converge at low pressure (Almeev et al., 2008), especially in enriched basalts that have higher concentrations of K_2O and related incompatible elements. This raises the question: did Shatsky Rise basalts result from partial melting of either “dry” or fairly “wet” mantle at shallow depths? Second, along spreading ridges, multiply saturated and fairly primitive rocks exist along portions of the Central Indian Ridge, where gabbroic and ultramafic rocks have been dredged from many fracture zones (e.g., Engel and Fisher, 1975). They also occur in Deep Sea Drilling Project Hole 504B on the Costa Rica Rift (Natland et al., 1983), where the seismically measured thickness of ocean crust is only ~ 4 km. In a similar fashion to the rocks in Hole 504B, the rocks of Shatsky Rise are depleted and have low concentrations of elements such as Zr, Y, and TiO_2 (see “**Geochemistry**”). Indeed, the concentrations of these elements are low

even within the MORB spectrum, and this may also mean that the rocks are dry. However, if this interpretation is correct, why, then, should rocks that are depleted, and which cotectically crystallized plagioclase and clinopyroxene, occur at Shatsky Rise where the crust is relatively thick?

Alteration and metamorphic petrology

The entire section of basaltic rocks (massive and pillow lavas) recovered from Hole U1347A has been affected by slight to moderate low-temperature water-rock interactions, resulting in almost complete replacement of glassy mesostasis and complete replacement of olivine. In contrast, plagioclase and clinopyroxene are generally well preserved throughout the hole, either in the groundmass or as phenocrysts. The overall alteration of the basalt pieces ranges from slight to moderate (from 5% to 50%), with the majority of the rocks showing $\sim 15\%$ alteration, estimated visually using binocular microscope on the archive half and optical microscope on discrete thin section samples, without taking veins and vein halos into account. Fresh glass was observed in some slightly altered basaltic sections and at pillow margins (Fig. F34).

Clay minerals, together with calcite, are the most abundant secondary minerals in Hole U1347A, replacing primary phases, glassy mesostasis, and filling vesicles and veins. As a result of the clays’ fine-grained size, identification by optical microscopy was difficult and clays are therefore named according to color (observed on thin sections) (i.e., brown clays and white clays). Other alteration minerals observed in the basaltic cores are pyrite and Fe oxyhydroxides. Pyrite is the only sulfide mineral observed throughout Hole U1347A, either disseminated in the groundmass or as a constituent of veins and vesicles (Fig. F34).

Alteration degree and mineralogy at Site U1347 will be compared with those of basaltic rocks recovered at Site U1346 (Shirshov Massif), previously well studied portions of ocean crust (Alt, 1995, 2004), and basalts recovered from the OJP (ODP Leg 192; Mahoney, Fitton, Wallace, et al., 2001; Banerjee et al., 2004).

Low-temperature pervasive alteration processes

Based on core descriptions and thin section observations, alteration of the basaltic rocks recovered from Hole U1347A is similar throughout the entire hole, with variations only in the degree of alteration (see

Figure F34 and 324ALT.XLS in LOGS in “[Supplementary material](#)”).

Primary phase replacement

Basalts recovered from Hole U1347A are dominated by plagioclase and pyroxene (as phenocrysts and in the groundmass) with minor olivine microphe-nocrysts and titanomagnetite in a cryptocrystalline to glassy groundmass (see “[Igneous petrology](#)” for detailed description). Plagioclases and pyroxenes are slightly to moderately altered to brown and white clays (typically, from ~5% to ~40%), phenocrysts being commonly less affected by alteration than minerals forming the groundmass (Fig. F35). Olivine phenocrysts are completely pseudomorphed by various proportions of calcite and brown clays (likely Mg saponite) (Fig. F36) throughout the basement lava flows. Only three occurrences of relics of fresh olivine were observed in Hole U1347A, all of which were present in glassy pillow margins (see “[Igneous petrology](#)”). Titanomagnetites, commonly present in the groundmass, are 5%–20% altered to fine-grained nonreflective opaque minerals, such as Fe oxyhydroxides.

Glassy mesostasis is commonly totally altered to brown clays in the basaltic rocks, whereas relics of interstitial glass have been observed in few samples (Fig. F37).

Alteration of chilled-margin glass

Glass at the margin of pillows and tops of sheet flows is commonly well preserved in Hole U1347A. Alteration of the glass consists of palagonite replacement along veins and vesicles (Fig. F38). Most pillow margins are rimmed by a black soft material, which is composed of a mixture of clays (i.e., montmorillonite and nontronite) (Fig. F39). This ~1 cm thick, dark, soft rim may either be a result of alteration of the pillow margins or clay-rich sediment that has been deposited between pillows or lava lobes.

Vesicles

Basaltic rocks recovered from Hole U1347A are all poorly vesicular. The vesicles are mainly filled with calcite and gray clay (most likely nontronite and saponite) (Fig. F40). Traces of pyrite are present in vesicles in all of the lava units described in “[Igneous petrology](#)” (Figs. F34, F41A, F41B). Vesicles commonly contain a rim of segregated melt that has been altered to dark brown clay minerals and fine-grained oxides (Fig. F41C). There is no systematic variation in mineral infilling vesicles with depth (Fig. F34), but variation occurs within lava flows and calcite vesicles are commonly observed close to lava flow

contacts. Occasionally calcite shows radial growth patterns in vesicles (Fig. F41D).

Veins

Three main vein types have been identified in Hole U1347A: (1) calcite veins, (2) green clay veins, and (3) calcite and green clay veins together (see Fig. F34 and 324VEIN.XLS in LOGS in “[Supplementary material](#)”), all with or without pyrite (Figs. F34, F42). Calcite veins are the dominant vein type ($N = 546$) and are found throughout Hole U1347A (Fig. F34). Calcite and green clay veins ($N = 152$ and $N = 108$, respectively) are also distributed throughout the hole (see Fig. F34 and 324VEIN.XLS in LOGS in “[Supplementary material](#)”). There is an average of ~3 veins/m in the basement lavas, and average vein thickness is ~1 mm (Fig. F34).

Interpretations of alteration

Basaltic rocks recovered from Hole U1347A have all undergone similar pervasive alteration throughout the hole, with variations only in alteration degree (from 5% to 50%). The predominance of clay minerals and calcite as secondary phases suggest relatively low temperature of alteration (<100°C) (Alt, 1995; Honnorez, 2003).

Alteration in Hole U1347A is clearly different from that encountered in Hole U1346A on Shirshov Massif in terms of fluid flux and/or fluid chemistry. On Shirshov Massif, three types of extensive pervasive low-temperature alteration were identified, suggesting chemically variable fluid flow (and maybe fluid flux). The predominant alteration type in Hole U1346A resulted from interaction of basalts with CO₂-rich seawater-derived hydrothermal fluids at relatively low temperature (<100°C) (Honnorez, 2003). In contrast, in Hole U1347A on Tamu Massif calcite replacement of the primary phases is less abundant and affects only olivine (micro-) phenocrysts and, rarely, the groundmass. This suggests that fluids circulating through the succession of lava units in Hole U1347A were compositionally different (less CO₂ rich) than those in Hole U1346A. The lower degree of alteration in Hole U1347A also suggests lower fluid fluxes and lower water-rock ratios.

Similar dark gray alteration has been described for the basalts of the OJP (Mahoney, Fitton, Wallace, et al., 2001; Banerjee et al., 2004) with replacement of olivine microphenocrysts and glassy mesostasis by clay minerals. This alteration type has been interpreted as a result of interaction between basalt and seawater-derived fluids under anoxic-suboxic conditions at low temperature and low water-rock ratios (Banerjee et al., 2004). Differences in alteration min-

erology in Hole U1347A are shown by the relative abundance of calcite replacing the olivine phenocrysts, the lack of celadonite, and the widespread occurrences of pyrite disseminated in the matrix or as a constituent of the veins and vesicles.

Structural geology

Cores recovered from the igneous basement in Hole U1347A between 157.4 mbsf in Core 324-U1347A-11R and 315.15 mbsf in Core 29R contain structures of magmatic, alteration, and deformational origins. Structures described here are solely within the basalt complex and exhibit wholly brittle and magmatic flow structures. The main structural features are represented by two types of magmatic flow structures, pillows and sheet flows. The details of these structures are characterized by distribution patterns of amygdules (or vesicles), veins, vein networks and fractures, and texture variation. All of these igneous structures include syn- to late magmatic structures that are linked to flow, cooling, and solidification of lava.

In the following sections, the characteristics of the major two types of structures are described, followed by a discussion of distribution, orientations, and relationships between structures and a short summary. Important observations and interpretations include

- Preferred orientations and contact relationships of planar and subplanar structures;
- Variation in structural morphology, such as pattern, size, shape (roundness or sphericity), and vesicles (vesicularity); and
- Crosscutting relationships, such as primary and secondary structures and structural sequence.

These are evidence for close linkages between extrusive processes, fluid flow, brittle deformation, and paleostress field.

Magmatic flow structures

Magmatic flow structures exhibit evidence of particle rotation or plastic strain imposed by the flow of viscous magma and provide clues to movement plane and direction (Davis, 1984; Passchier and Trouw, 1996).

Sheet flow structure

A sheet flow is generally composed of three parts: lava upper crust, lava core, and basal zone (Keszthelyi et al., 1999). The distinctive and typical structure of a sheet flow in Hole U1347A is displayed in Sections 324-U1347A-16R-1 through 16R-5 (Fig. F43).

The upper crust has relatively high vesicularity, irregular and hackly jointing, and hypocrystalline textures. At the top of the upper crust, some ropy folds were also observed (see “[Igneous petrology](#)”). Vesicularity decreases from top to bottom in the upper crust. Although many vesicles are filled by calcite, forming amygdules, several horizontal vesicle zones are not filled in Hole U1347A (Fig. F43). The size distribution and shape of the vesicles in the upper crust show that the horizontal zones of vesicles can be interpreted to form when the upward migrating gas bubbles become trapped against the downward growing solidification front of the upper crust of the flow. Irregular jointing is often related to jostling of the brittle, chilled lava that takes place during inflation (Fig. F43).

The lava core is generally characterized by <2% vesicles, pipe vesicles and regular jointing, fine- to medium-grained holocrystalline texture, and massive structure. Sometimes we also find several typical vesicle cylinders in the lava core, such as in interval 324-U1347A-18R-3 (Piece 1, 5–55 cm). Vesicle cylinders are the most characteristic structure of a vapor differentiation processes (Goff, 1977, 1996; Caroff et al., 2000). They are vertical tubes, 1–2 cm in diameter, filled with residual liquid and bubbles in Hole U1347A. The vesicle cylinder in interval 324-U1347A-18R-3 (Piece 1, 5–55 cm) extends from ~37 cm above the flow base (i.e., the top of interval 324-U1347A-18R-3 [Piece 3, 92–95 cm] to the bottom of the upper chilled crust).

The basal zone is usually 0.5–1 m thick but is often incompletely recovered (e.g., Sections 324-U1347A-16R-1 to 16R-5) (Fig. F43). This zone is characterized by being slightly vesicular, having little poorly developed jointing or subvertical or stretched pipe vesicles at the base. It usually comprises much less than 10% of the overall sheet flow thickness (Fig. F43).

Pillow structure

Amygdules in pillows are not common in Hole U1347A. Numerous pillow lavas in this hole have rounded chilled margins without radial cracking, concentric vesicular zones, or radially aligned vesicles. Chilled margins show that individual pillow sizes are from 10 to 50 cm (Fig. F44). Under the microscope, the chilled margins show flow banding and stretched spherulites. The other major identifiers of pillow structures include spheroidal or ellipsoidal shape, inner glassy skin, and flow banding (Thorpe and Brown, 1985). Several layers of pillow lavas, with typical chilled margins, are observed in Hole U1347A, such as at interval 324-U1347A-21R-4, 94–104 cm (Fig. F45).

Brittle fracturing

Fractures occur at discrete breaks in a rock mass where cohesion was lost, including four kinds of structures in Hole U1347A:

1. Microfaults and faults in which the two sides are displaced relative to each other,
2. Joints in which the two sides show no differential displacement (relative to the naked eye),
3. Healed or sealed joints in which fluids passing through the rock have partially or completely joined together the adjacent sides by the deposition of crystalline material, and
4. Veins in which a considerable thickness (>1 mm) of filling material occupies the region between the fracture walls (Ramsay and Huber, 1987).

In this report, we consider veins with >0.1 mm thickness of filling material.

Microfaults

A microfault is a hole-scale observable fracture with a small displacement or tiny offset, including microcracks fractions of a millimeter long seen in thin sections of rock under the microscope (Ramsay and Huber, 1987). Here we adopted the principle of Davis (1984) that a microfault is a fracture with an amount of shear separation <1 cm. In general, the displacement or offset is difficult to estimate because of core breakage. However, the slickenlines on the fault plane surfaces (slickenside) display some oriented fiber minerals in intervals 324-U1347A-29R-4, 110–124 cm (315.48–315.70 mbsf), and 29R-5, 46–56 cm (314.75–314.88 mbsf) (Fig. F46). The dip angles are very steep, >70°. When the striations plunge steeply on the slickenside surface, we can identify it as a normal microfault in combination with striation and congruous steps (Hancock, 1985), but their original orientations must be constrained with the help of FMS logging data.

Joints

Joints are common in Hole U1347A cores. Some joints are related to the cooling of lava and are represented by curved, concentric, and irregular veins filled with secondary minerals. However, most joints in the rocks of Hole U1347A are conjugate joints related to postmagmatic deformation rather than cooling. Generally, dips of joints in the middle and lower cores (324-U1347A-17R through 29R) are steeper than those in the upper cores (11R through 16R) (Fig. F47).

On a meter scale, moreover, it seems that the steeper joints in each unit are correlated with lower vesicularity and smaller groundmass grain size (Figs. F47,

F48). Joints are very useful in interpreting the stress and strain conditions of past deformational events (Davis, 1984).

Veins

Veins are defined as a sealed fracture by Ramsay and Huber (1987). Vein widths are generally <5 mm (most are ~0.1 or ~1 mm wide) in Hole U1347A. The density of veins in Hole U1347A is ~3 veins/m (also see “[Alteration and metamorphic petrology](#)”).

Veins are generally closely associated with joints. Conjugate joint planes are also generally shear veins at this site (e.g., interval 324-U1347A-27R-6, 70–95 cm) (Fig. F49). In general, dips of veins in the middle and lower cores (17R through 29R) are steeper than those in the upper cores (11R through 16R) (Fig. F47), as well as those of the joints in Hole U1347A. The steepness of veins in each unit or in Cores 17R, 18R, 20R, 21R, 24R, and 26R appears to be correlated with lower vesicularity and smaller groundmass grain size (Figs. F47, F48). In some samples, veins have splays and intersect others with Y- and T-shaped morphologies (Fig. F49). These intersections can be complex, with changes in mineralogy along the length of the vein. Furthermore, many veins that apparently merge in hand samples have crosscutting relationships when observed in thin section. Crosscutting relationships can also be found as displacements at vein intersections, even under the microscope, showing that jointing is a multiphase process.

In Hole U1347A many veins, except those with well-defined walls, have halos. The color of the alteration halos reflects secondary mineral contents. Vein-filling minerals change from pyrite and nontronite to calcite from edge to center of veins or vesicles in Hole U1347A. Calcite-rich veins commonly show polycrystalline fabrics and partly syntaxial or cross-fiber fabrics. Sulfides in the veins or vesicles are texturally late in many instances.

Geochemistry

Major and trace element analysis

Forty samples of lavas from Hole U1347A were analyzed by ICP-AES for concentrations of major and several trace elements (see “[Geochemistry](#)” in the “[Methods](#)” chapter for information on analytical procedures, instrumentation, and data quality). Samples of all the igneous units recovered (stratigraphic Units IV, V, VII, IX, X, XII, and XIV–XVI) were included. All were taken from holocrystalline portions of the cores, except for one specimen from a rind of highly altered glass rimming holocrystalline rock at the top of Unit V (see below).

As with Site U1346, total weight percentages of the major element oxides in the Site U1347 analyses are quite variable, between 96.53 and 101.52 wt%. This variation may again partly be a result of the inability of the muffle furnace to attain a temperature above 1000°C during the ignition step of sample preparation (see “**Geochemistry**” in the “**Methods**” chapter). Some of the variation also may be a result of errors during weighing of the sample or flux powders. In any case, we again normalized the raw major-element values to 100 wt% totals for use in the figures and in the discussion below; the normalized values are presented below the raw data in Table T7.

Alteration is much less severe overall in the Site U1347 lavas than in those recovered from Site U1346 (see “**Alteration and metamorphic petrology**”). Weight loss on ignition (LOI) is 0.07–3.57 wt%. In comparison, the LOI range for Site U1346 is 3.12–13.85 wt%. Alteration effects on the elements we measured are correspondingly much smaller, in general, than they are among the Site U1346 samples. For example, whereas data points for only four Site U1346 samples (the four with the lowest LOI values) lie in the field of tholeiitic basalt in a total alkalis versus SiO₂ diagram, values for all but two of the Site U1347 samples fall within this field in Figure F50A. The exceptions are the samples with the highest LOI value, Samples 324-U1347A-22R-1 (Piece 9, 55–58 cm) and 13R-6 (Piece 1, 80–83 cm), which are from a segregation of dark gray basalt within lighter gray basalt near the base of Unit IV. Values for Sample 22R-1 (Piece 9, 55–58 cm) place it (barely) above the tholeiitic-alkalic dividing line in the figure, whereas Sample 13R-6 (Piece 1, 80–83 cm) has the highest SiO₂ value measured for Site U1347 (52.29 versus 47.68–50.67 wt% for the other samples), putting it just within the field of basaltic andesite. Although total alkali contents remain relatively low in the Site U1347 samples, alteration nevertheless appears to have variably increased K₂O concentrations, as K₂O shows a rough positive correlation with LOI (Fig. F50B). Even so, the range in K₂O measured for Site U1347 (0.05–0.45 wt%) is far smaller than for Site U1346 (0.10–4.77 wt%). Several other elements (e.g., CaO) show relatively minor effects probably related to alteration. One of the most altered Site U1347 samples is the altered glass from the top of Unit V (interval 324-U1347A-13R-7 [Piece 6, 28–30 cm]). This sample has 3.40 wt% LOI and one of the highest K₂O values (0.34 wt%). It also exhibits the lowest concentrations of Sr, P, Zr, Ti, Y, and Sc (e.g., Fig. F51A; Table T7); the second lowest Ba concentration; the lowest CaO and Al₂O₃ (e.g., Fig. F52A); and the highest Fe₂O₃^T (total iron calculated as ferric oxide) and MgO contents.

Downhole variations in element concentrations and interelement ratios do not lend themselves to any single, simple generalization. However, variations from unit to unit are in some cases smaller than variability within a unit. For example, chemical differences between Units XII and XIV are smaller, overall, than the intraunit variation among the subunits of Unit X or those of Unit VII (Fig. F53).

As with the Site U1346 lavas, only limited overlap is seen between the Site U1347 data and the field of OJP basalts in most variation diagrams. Instead, the Site U1347 data again lie within the field of East Pacific Rise basalts in many diagrams (e.g., Fig. F52A–F52D) and extend from values near those of lavas from Site 1213 (southern Tamu Massif) toward higher TiO₂, Zr, P₂O₅, and Ba and lower Ni, Cr, and Mg# (Mg# = $100 \times \text{Mg}^{2+}/[\text{Mg}^{2+} + \text{Fe}^{2+}]$, assuming Fe₂O₃/FeO = 0.15). For example, Mg# ranges from 58.9 to 47.4 among the Site U1347 basalts versus 60.8 to 57.6 for Site 1213. These characteristics are consistent with the Site U1347 basalts representing more (and variably) evolved relatives of the Site 1213 lavas. The sample of the segregation near the bottom of Unit IV (Sample 324-U1347A-13R-6 [Piece 1, 80–83 cm]), in addition to having the highest SiO₂ content, is distinct in having higher Ba, P, Zr, and Y (Fig. F51A); lower V and Sc; and higher Zr/Ti than the other holocrystalline Site U1347 samples. These differences do not appear to be a result of alteration, as the sample (LOI = 2.53 wt%) is not visibly more altered than several others with similar LOI. We infer that these characteristics are related to details of the particular differentiation history of the material in this segregation.

Incompatible-element patterns of the Site U1347 basalts are also broadly ocean-ridge-like (Fig. F51B–F51F), with a marked relative depletion of Ba. However, the lavas exhibit notable differences from normal ocean-ridge basalts; in particular, they are slightly enriched in Ba, Sr, P, Zr, and Ti relative to Y, similar to so-called enriched (or E-type) ocean-ridge basalts. In this respect, they are similar to, and in some cases even slightly more enriched than, the Site 1213 lavas. The difference from normal ocean-ridge basalt patterns could reflect a difference in the chemical composition of the source mantle; that is, the source(s) of the Site U1347 basalts could have been slightly richer in the more incompatible elements than normal ocean-ridge mantle. Alternatively (or additionally), the Site U1347 lavas could represent smaller and/or deeper mean fractions of partial melting than do most ocean-ridge basalts; because Y is a compatible element in garnet (e.g., Salters and Longhi, 1999), low relative Y concentrations can be a sign of control by residual garnet during

melting. Unlike the Site 1213 or typical ocean-ridge basalts, many of the Site U1347 patterns display small peaks at P relative to Zr and Sr. Although this may be a primary characteristic of the lavas, we cannot rule out the possibility that it is an artifact of the onboard measurement of P_2O_5 (see “[Geochemistry](#)” in the “Methods” chapter). The P peaks seem unlikely to be a result solely of alteration, as most of the Site U1347 samples define a rough positive correlation of P_2O_5 with alteration-resistant elements like Ti and Zr. Additionally, like Zr, the combined Site U1347 and Site 1213 data also show a rough increase in Sr with decreasing Mg# and increasing TiO_2 (e.g., Fig. F52E), whereas the Sr/Zr ratio displays no correlation with Mg# and only limited variation (mean = 1.7, standard deviation = 0.2, excluding the altered glass and segregation). Because Sr is compatible in plagioclase (e.g., Bindeman and Davis, 2000), these characteristics could suggest that plagioclase removal during differentiation was not significant enough to obscure the effects of any earlier (preplagioclase) stages of differentiation and/or small variations in amount of partial melting. Resolution of the effects of variations in partial melting and magmatic differentiation on the Site U1347 lavas awaits detailed on-shore analysis of a larger set of elements.

Total carbon and carbonate carbon

Thirty-seven samples of sedimentary material from Cores 324-U1347A-3R through 17R were analyzed in replicate for carbonate content (percent carbonate). The carbonate values are baseline-corrected for CO_2 in equilibrium with acid and scaled to a 100% $CaCO_3$ standard (see “[Geochemistry](#)” in the “Methods” chapter for an explanation of analytical procedures and instrumentation used for carbonate, total carbon, and organic carbon measurement). The samples were also analyzed for total carbon, although not in replicate. The content of organic carbon was estimated by subtracting the percentage of measured carbonate from that of total carbon. Results are presented and discussed in “[Sedimentology](#).”

Physical properties

Igneous rock, sedimentary rock, and sediments from Hole U1347A were characterized for physical properties as described in “[Physical properties](#)” in the “Methods” chapter. Core sections with continuous intervals longer than 8 cm were run through the Whole-Round Multisensor Logger for measurement of gamma ray attenuation (GRA) density and magnetic susceptibility. Data from whole-round measurements were filtered by a MATLAB code to remove data associated with gaps and small pieces as

described in “[Physical properties](#)” in the “Methods” chapter. The filtered data were then visually double-checked against images of the core section halves. Sections longer than 50 cm were measured with the Natural Gamma Ray Logger. Fifty-nine measurements of thermal conductivity were performed. Fifty-five discrete oriented cubic samples of igneous material were cut from the working half of the cores for measurement of moisture and density (MAD) properties as well as compressional (*P*-wave) velocities in three directions.

Whole-Round Multisensor Logger measurements

Magnetic susceptibility

The results for whole-round magnetic susceptibility in Hole U1347A are summarized in Figure F33 and reported in 10^{-5} SI units. The raw data were corrected using a Bartington correction factor (Blum, 1997). The correction assumes that the core liner is filled. Because the liner is usually less than filled, the data should be treated as minima.

A first-order observation is that magnetic susceptibility in Hole U1347A is much higher than in Hole U1346A, which was subjected to pervasive alteration. Average values in igneous material in Hole U1347A range from $\sim 1500 \times 10^{-5}$ to $\sim 2400 \times 10^{-5}$ SI. Two exceptions occur in massive flow Units VII and XV, which show a two-fold increase in magnetic susceptibility, yielding values up to 3800×10^{-5} SI (Fig. F33).

Recovered sedimentary interbeds are characterized by markedly lower magnetic susceptibility values, generally $< 100 \times 10^{-5}$ SI, making them useful for correlative purposes (see also “[Downhole Logging](#)”).

Gamma ray attenuation density

The results for GRA bulk density measurements are summarized in Figure F33. Caution should be used when interpreting the absolute density values from the whole-round track because RCB drilling results in cores that generally do not fill the liners, thus underestimating density. As with magnetic susceptibility, values from Hole U1347A are higher than those at Site U1346. This is in agreement with the fresher nature of the material at Site U1347. Sedimentary interlayers are again easily distinguishable by their lower density relative to igneous material.

Natural Gamma Ray Logger

Natural gamma ray (NGR) measurements are summarized in Figure F33. NGR in Hole U1347A averaged 2–4 cps, in stark contrast to the 20–30 cps rou-

tinely measured at Site U1346. This observation is again in keeping with the fresher nature of the material in Hole U1347A versus Hole U1346A. With such low count rates, the spectra in Hole U1347A are not as well defined as in Hole U1346A. Geochemical shipboard analyses of igneous material confirm low K_2O content, with samples yielding values of 0.1–0.2 wt% (see “[Geochemistry](#)”). The sedimentary section in the bottom of Core 324-U1347A-16R to the top of 17R shows the only appreciable increase in total NGR counts, reaching values of almost 10 cps (Fig. [F33](#)).

Moisture and density

A summary of bulk density, dry density, grain density, void ratio, water content, and porosity measurements on discrete samples is listed in Table [T8](#). The densities and porosities are shown in Figure [F54](#). The bulk density of igneous material ranges from 2.49 to 2.94 g/cm³, with a porosity range of 2.36%–22.89%. When porosity is low, the bulk, dry, and grain densities converge. Porosity is low in the interiors of flows, where presumably there is less vesicularity. The recovered igneous material is relatively well preserved (see “[Igneous petrology](#)” and “[Alteration and metamorphic petrology](#)”), and porosity displays a tight negative correlation with bulk density (Fig. [F55](#)).

The MAD determinations are also correlated with identified stratigraphic units (see “[Igneous petrology](#)” and “[Sedimentology](#)”). Massive flows (stratigraphic Unit XV) and thick upper pillow basalts (Unit X) have the lowest porosity (<5%) and highest bulk densities measured at the site (Fig. [F54](#)).

Compressional (*P*-wave) velocity

Downhole variation of compressional wave velocity is summarized in Figure [F54](#) and listed in Table [T9](#). *P*-wave velocity shows several intervals of interest. In particular, there is a sharp increase in downhole velocity at ~220 mbsf. This corresponds to the beginning of a ~30 m thick pillow lava (stratigraphic Unit X; see “[Igneous petrology](#)”). The increase is accompanied by a drop in porosity and increase in bulk density. The other interval of note is the massive igneous flow (Unit XV) recovered below ~290 mbsf. This ~20 m thick unit has consistently high *P*-wave velocities, low porosities, and high bulk densities (as measured by discrete sampling).

Figure [F56](#) illustrates the relationship between the stratigraphic units with bulk density versus *P*-wave velocity. The massive flows appear to be distinguishable from one another by their physical properties. Massive flow Units IV–IX have lower *P*-wave veloci-

ties and bulk densities and display very little overlap with massive flow Unit XV, which has the highest measured bulk densities and *P*-wave velocities. The pillow basalts (stratigraphic Units X–XIV) span the entire range of bulk density and *P*-wave velocity. One outlier on Figure [F56](#) is from Section 324-U1347A-16R-5. This sample has an apparently low density for its *P*-wave velocity. This sample had a large vesicle in one corner of the discrete sample cube. This likely results in a lower density without affecting the *P*-wave velocity because the vesicle is not continuous throughout the cube and the *P*-wave measurement records the first (fastest) arrival time.

Thermal conductivity

Fifty-nine measurements of thermal conductivity were performed (58 igneous and 1 sedimentary sample). The results are summarized in Table [T10](#) and Figure [F57](#). The sedimentary measurement yielded 1.007 ± 0.017 W/(m·K) (2σ). The average of all igneous measurements was 1.59 ± 0.200 W/(m·K) (2σ). The massive flow Unit XV, recovered below ~290 mbsf, has consistently higher thermal conductivity than the rest of the hole (average = 1.733 ± 0.092 W/[m·K]; 2σ , $N = 11$). Unit XV also has the highest magnetic susceptibility (Fig. [F57](#)), indicating a greater proportion of magnetic, thermally conductive minerals (e.g., titanomagnetite).

Paleomagnetism

The major goals in paleomagnetism on the recovered cores were to characterize the paleomagnetic remanence and resolve paleolatitude from the magnetization components recorded in the igneous rocks. At Site U1347, we focused only on discrete sample measurements from the working halves of the igneous cores using the Molspin Minispin magnetometer and alternating-field (AF) demagnetizations using the DTech degausser. We also carried out thermal demagnetizations on discrete samples using the Schonstedt oven. Our use of discrete samples only was dictated by ongoing problems with the passthrough 2G cryogenic magnetometer (see “[Paleomagnetism](#)” in the “[Methods](#)” chapter).

Working-half discrete sample measurements

We measured and analyzed 61 discrete basalt samples (7 cm³) from various lithologies downhole (Table [T11](#)). Samples from this site are less altered compared to Hole U1346A. We preferred carrying out thermal demagnetization because this method is thought to be better for isolating magnetization

components in oceanic basalt samples that may contain self-reversed chemical remanent magnetization (e.g., Doubrovine and Tarduno, 2005). Twenty-three samples were AF demagnetized up to 140 mT in steps of 2, 5, or 10 mT, and thirty-nine were thermally demagnetized up to 600°C. Ten samples from Sections 324-U1347A-24R-1 through 29R-4, which were thermally demagnetized, were treated with a 5 mT AF demagnetization step prior to the 100°C heating step in an attempt to erase the drilling overprint. Magnetic susceptibility was measured after each heating step in order to detect possible mineralogical changes (for more details, see “Paleomagnetism” in the “Methods” chapter). Room temperature susceptibilities for basalts range between 2.0×10^{-2} and 9.2×10^{-2} SI. Most of the samples have a steep vertical component at natural remanent magnetization (NRM) and first demagnetization steps, typical of drilling overprint (e.g., Audunsson and Levi, 1989; Wilson, Teagle, Acton, et al., 2003), but this is usually erased at ~10 mT or 200°C (Fig. F58).

Alternating-field demagnetizations

Before the removal of the drilling overprint, samples carry a very strong NRM. However, the median destructive fields (MDF) are very low, from 1.2 to 13.9 mT with an arithmetic mean of 4.6 ± 3.0 mT (Fig. F58; Table T11). This low MDF often makes it more difficult to separate overprints from the characteristic remanent magnetization compared to samples from Site U1346. Nevertheless, it is usually possible to isolate a stable component that decays toward the origin of orthogonal vector plots for field steps between ~15 and 80–100 mT.

To further investigate the origin of the low-coercivity components in igneous rocks recovered from Hole U1347A, we carried out a simple anhysteretic remanent magnetization (ARM)-AF demagnetization test on a few samples after the completion of the AF demagnetization of the NRM. This test allows us to understand the coercivity of those samples and possible domain state of magnetic carriers. Three samples from massive flows (Samples 324-U1347A-27R-2, 23–25 cm; 28R-5, 16–18 cm; and 28R-8, 80–82 cm) were selected for this test. We first applied an ARM (with a peak AF of 100 mT superimposed on a direct current field of 0.1 mT) on the samples and then demagnetized them at 0, 5, 10, 20, 30, 40, and 50 mT using the DTech demagnetizer. Resulting MDF values from the ARM-AF demagnetization are 7.61 mT for Sample 324-U1347A-27R-2, 23–25 cm; 2.99 mT for Sample 28R-5, 16–18 cm; and 2.89 mT for Sample 28R-8, 80–82 cm (Fig. F59). These low values confirm that multidomain grains are most likely the magnetization carriers.

Inclinations and declinations were calculated using principal component analyses (Kirshvink, 1980) anchored to the origin for AF demagnetization steps between ~15 and 80–100 mT. Low values of maximum angular deviation show that these directional results are of high quality (Table T11). Three AF demagnetization results from Section 324-U1347A-12R-1 show very shallow negative inclinations, whereas all samples taken from Section 324-U1347A-12R-2 and deeper show positive inclinations.

Thermal demagnetizations

Compared to AF demagnetization results, most thermal demagnetizations poorly show the characterization of the magnetic remanence. The variation of the magnetization with temperature reveals that two unblocking temperatures are generally present, one at ~300°–400°C, corresponding to titanomagnetite (-maghemite) with an ulvospinel fraction x of ~0.4–0.5 (Hunt et al., 1995) and the other at ~575°C, indicating the presence of almost pure magnetite. Many thermal demagnetizations also show a large drop in magnetization after heating to 100°C, suggesting the presence of an overprint with a very low unblocking temperature.

Bulk magnetic susceptibilities measured at room temperature after each heating step stay more or less constant for heating steps up to ~300°C. At higher temperature, susceptibilities increase to 2–3 times the room temperature values and then decrease again. This could indicate that the primary magnetic carrier could be titanomaghemite that inverts to strongly magnetic magnetite as a result of heating (Özdemir and O’Reilly, 1982).

Two main behaviors were observed in the thermal demagnetizations. In the samples from Sections 324-U1347A-12R-1 to 26R-1 (stratigraphic igneous Units IV–XIV), the low-temperature part of the demagnetization (from room temperature to ~450°–500°C) behaves so erratically that it is impossible to define a stable direction. However, the high-temperature part (500°–600°C) often enables us to obtain a fairly stable direction with maximum angular deviation <8°. However, in this temperature range the carrier of magnetization is probably no longer the primary carrier, which has been oxidized by the heating, as indicated by large changes in bulk susceptibility. Nevertheless, it is likely that the alteration product, which might be the component with the high unblocking temperature, inherits its remanence direction from the original titanomaghemite (Marshall and Cox, 1971; Matzka and Krása, 2007). Furthermore, this high-temperature direction does point toward the origin on orthogonal vector plots indicating a stable, primary remanence.

The second behavior was observed in the lowermost part of the cored section (Sections 324-U1347A-26R-2 through 29R-4; stratigraphic igneous Unit XV). The low-temperature part of the demagnetization (up to $\sim 300^\circ\text{C}$) is stable enough in some cases to give a direction pointing toward the origin of orthogonal vector plots and with maximum angular deviation $<8^\circ$, whereas the high-temperature part is too weak to give a consistent direction. As a result, we could not extract a stable remanence direction from about half of these samples. The susceptibility variation with temperature is also different; no large increase in susceptibility with heating exists. Instead, the susceptibility decreases at $\sim 300^\circ\text{C}$, stays more or less constant, and then drops after 500°C . This suggests that the magnetic mineralogy is different from that observed in the samples measured from shallower cores. Also, it must be noted that the very last sample that we studied, which belongs to a different flow (Unit XVI; see “[Igneous petrology](#)”) shows a behavior similar to that from the shallow part of the section.

Overall, samples that exhibit simple univectorial decay are rare in thermal demagnetization results from the igneous section in Hole U1347A. Only eight samples show a consistent behavior with maximum angular deviation $<5^\circ$. We can classify the rest of the samples into three groups:

1. Samples with some erratic behavior steps in demagnetization results but whose characteristic remanence can still be determined (e.g., Sample 324-U1347A-23R-6, 96–98 cm; Fig. [F58](#)) with maximum angular deviation $<8^\circ$,
2. Samples with erratic behavior in demagnetization results and directions that cannot be determined and often contain possible self-reversals (e.g., Sample 324-U1347A-20R-3, 118–110 cm; Fig. [F58](#)), and
3. Samples with erratic behavior steps in demagnetization results and directions that cannot be determined (e.g., Sample 324-U1347A-18R-5, 82–84 cm; Fig. [F58](#)).

For the stratigraphic plot of inclination, we kept only samples for which maximum angular deviation is $<8^\circ$.

Downhole inclinations and tectonic implications

Slight changes in inclination correlating with the different stratigraphic units exist in Hole U1347A (Fig. [F60](#)). The averaged inclinations show four inclination groups:

1. The top igneous core section (324-U1347A-12R-1) with shallow negative inclination ($-6^\circ \pm 7^\circ$);

2. Sections 12R-2 through 16R-5 (lower part of the massive basalt Flows 1–3), with an average inclination of $28^\circ \pm 13^\circ$;
3. Sections 324-U1347A-17R-2 through 26R-1 (basalt Flow 4 and pillow lava section), with an average inclination of $20^\circ \pm 14^\circ$; and
4. Sections 324-U1347A-26R-2 through 29R-4 (basalt Flows 5 and 6), with an average inclination of $54^\circ \pm 27^\circ$.

The top negative polarity found in the upper massive basalt flow (Section 324-U1347A-12R-1) may suggest the existence of polarity reversals in Hole U1347A, indicative of a late-stage eruption with respect to underlying massive flow sections.

The massive basalt stratigraphic Units IV–VII show steeper inclinations than those of upper and middle pillow lava Units IX–XIV. A few explanations are possible for this discrepancy. First, geomagnetic secular variation may not be averaged throughout Hole U1347A because the series of eruptions happened over a short period of time. Second, the drilling overprint may be not completely erased because of abundant multidomain titanomagnetites formed by the relatively slow cooling of the massive flows. Third, steeper than expected inclinations may have resulted from block rotations of a stack of flows caused by lava loading and regional tectonics.

The averaged inclination for the lowermost section (lower pillow lava to lower massive basalt flow) should be interpreted with caution because most of the samples from this section gave unreliable results. Of the four AF demagnetized samples used, two have a steep inclination, whereas the other two have a shallow inclination. Magnetic susceptibility values suggest an abundance of magnetic minerals in the rocks from these sections. However, the slow cooling of the thick lava units probably formed multidomain titanomagnetite, which was chemically altered during low-temperature oxidation as this part of Shatsky Rise aged. As a result, the magnetic properties in this section might have become unstable for retaining NRM. We found that several samples are plagued with a large viscous remanent magnetization, sometimes on the timescale of the laboratory measurements, which is consistent with the suspected presence of large multidomain grains as carriers of the magnetization. Detailed rock magnetic measurements will be necessary on shore before we can interpret these directional results with certainty.

Downhole Logging

Downhole logging data obtained from Hole U1347A included natural and spectral gamma ray, density, neutron porosity, photoelectric factor, and electrical

resistivity measurements from three depths of investigation. Interpretations of gamma ray and electrical resistivity downhole logs were used to identify 15 logging units in Hole U1347A with 3 in the sediment sequences and 12 in the basaltic basement.

Operations

A wiper trip was completed throughout the open hole before the start of the wireline logging operations. The drill pipe was set at 130 m wireline matched depth below seafloor (WMSF), which is ~28 m above the sediment/basement interface. The hole was circulated with 83.5 bbl of 10.5 ppg barite mud. Downhole logging operations lasted 24 h beginning at 1955 h on 30 September 2009. Wireline logging operations consisted of two tool string deployments and testing of the wireline heave compensator (WHC). Logging operations in Hole U1347A took place in good sea conditions with ship heave of ~1 m. A planned third logging run with the Hostile Environment Natural Gamma Ray Sonde (HNGS)-General Purpose Inclinerometry Tool (GPIT)-UBI tool string had to be abandoned because of communication problems with the tool string. Troubleshooting on the rig floor revealed a bad digital telemetry adapter (DTA-A) and communication problems between the GPIT and the UBI. The logging personnel were unable to resolve the latter in a timely manner and the deployment was aborted.

Tool string deployment

HNGS-APS-HLDS-GPIT-DITE

The wireline tool string deployment consisted of a 30.2 m long triple combo tool string that included a logging equipment cable head (LEH-QT), digital telemetry cartridge (DTC-H), HNGS, Hostile Environment Natural Gamma Ray Cartridge (HNGC), Litho-Density Sonde Cartridge (LDSC), Accelerated Porosity Sonde (APS), Hostile Environment Litho-Density Sonde (HLDS), DTA-A, GPIT, and the Digital Dual Induction Tool model E (DITE). Downhole logs were recorded in two passes: (1) a downlog from seafloor to 287 m WMSF and (2) an uplog from 314 to 128 m WMSF.

After the downlog was stopped and prior to starting Pass 1, 30 min was spent assessing downhole tool motion and optimizing the efficiency of the WHC for the water depth at Hole U1347A and heave conditions at the time of the logging operations. Once the best possible WHC parameters were chosen for the prevailing heave conditions, the tool string was lowered to 314 m WMSF to begin the first uplog.

HNGS-DSI-GPIT-FMS

The second wireline tool string deployment consisted of a 34.39 m long FMS-sonic tool string that included a LEH-QT, DTC-H, HNGS, DSI, DTA-A, GPIT, and FMS. Downhole logs were recorded in three passes: (1) a downlog from seafloor to 287 m WMSF, (2) an uplog from 314 to 115.5 m WMSF, and (3) a second uplog from 314.6 m WMSF to seafloor.

After completion of the downlog the first upward pass was started and run from 314 to 115.5 m WMSF. The tool string was then lowered to ~314 m WMSF to begin the second upward pass through seafloor.

Data processing

Logging data were recorded onboard the *JOIDES Resolution* by Schlumberger and archived in DLIS format. Data were sent by satellite transfer to Lamont-Doherty Earth Observatory–Borehole Research Group, processed there, and transferred back to the ship for distributing to the shipboard scientific party and archiving in the shipboard database. Processing and data quality notes are given below.

Depth shifting

In general, depth shifts are applied to logging data by selecting a reference (base) log (usually the total gamma ray log from the run with the greatest vertical extent and no sudden changes in cable speed) and aligning features in equivalent logs from other passes by eye. Logging data seafloor depth could not be determined by the step in gamma ray values because the gamma ray signal was affected by the presence of the FFF and drill collars. As a result, the seafloor depth given by the drillers (3461 m DRF) was used for depth shift (Table T12). The depth-shifted logs were then depth matched to the gamma ray log from the main pass of the triple combo tool string.

Data quality

The quality of wireline logging data were assessed by evaluating whether logged values are reasonable for the lithologies encountered and by checking consistency between different passes of the same tool. Gamma ray logs recorded through the BHA should be used only qualitatively because of the attenuation of the incoming signal. The thick-walled BHA attenuates the signal more than the thinner walled drill pipe.

A wide (>30.5 cm) and/or irregular borehole affects most recordings, particularly those like the HLDS that require eccentricity and good contact with the borehole wall. The density log roughly correlates

with the resistivity logs, but it is largely affected by hole conditions. The hole diameter was recorded by the hydraulic caliper on the HLDS tool (LCAL) and shows a very irregular borehole with intervals exceeding the maximum caliper aperture. Good repeatability was observed between Pass 1 and 2, particularly for measurements of electrical resistivity, gamma ray, and density.

Bulk density (HLDS) data were recorded with a sampling rate of 2.54 cm, in addition to the standard sampling rate of 15.24 cm. The enhanced bulk density curve is the result of a Schlumberger enhanced processing technique performed on the MAXIS system onboard the *JOIDES Resolution*. In normal processing, short-spacing data are smoothed to match long-spacing data; in the enhanced processing this is reversed. In a situation where there is good contact between the HLDS pad and the borehole wall (low-density correction) the results are improved because the short spacing has better vertical resolution.

The FMS images are generally of good quality below 155 m WMSF as a result of the relatively good hole condition (hole size < 35.6 cm) and of intermediate quality above 155 m WMSF because of the large borehole size where it ranges from 35.6 to 48.3 cm. The irregular and possibly elliptical shape of the borehole occasionally prevents some FMS pads from being in direct contact with the formation, resulting in poor resolution or dark images. Hence, the FMS images (and the high-resolution resistivity logs) should be used with caution in this depth interval.

The sea state was relatively calm with a peak to peak heave of ~1.0 m or less. The WHC was used during the entire logging operation.

Preliminary results

Electrical resistivity measurements

Three electrical resistivity curves were obtained with the DITE. The spherically focused log (SFL), medium induction phasor-processed resistivity (IMPH), and deep induction phasor-processed resistivity (IDPH) profiles represent different depths of investigation into the formation (64, 76, and 152 cm) and different vertical resolutions (76, 152, and 213 cm). Downhole open hole electrical resistivity measurements covered 26.8 m of the bottommost sedimentary sequences and the uppermost 159.8 m the basement lithostratigraphic units (Fig. F61). The DITE was the only tool that reached the bottom of the logged interval in Hole U1347A because it was the bottommost tool in the logging tool string (see Fig. F19 in the “Methods” chapter).

In the bottommost sedimentary sequences IMPH values range from 1.1 to 2.0 Ωm , IDPH values range

from 1.1 to 2.3 Ωm , and SFLU values range from 0.85 to 2.0 Ωm . The interbedded layers of sediment within the basaltic basement have IMPH, IDPH, and SFLU values between 1.9 and 4.0 Ωm . In the basaltic basement units IMPH measurements range from 6.2 to 123.8 Ωm , IDPH measurements range from 7.9 to 186.5 Ωm , and SFLU measurements range from 3.8 to 1211 Ωm (Fig. F61).

Gamma ray measurements

Standard, computed, and individual spectral contributions from ^{40}K , ^{238}U , and ^{232}Th were part of the gamma ray measurements obtained in Hole U1347A with the HNGS. The total gamma ray measurements through the BHA show two anomalous peaks between 12.8 and 18.8 m WMSF and between 78.5 and 97.5 m WMSF (Fig. F61).

Downhole open hole gamma ray measurements covered 26.8 m of the bottommost sedimentary sequences and 160.6 m of the basement lithostratigraphic units. Total gamma ray measurements in the bottommost sediments of Hole U1347A are moderately variable, ranging from 11.0 to 40.7 gAPI with a mean of 23.4 gAPI. Potassium values are also relatively high with values between 0.46 and 1.45 wt% with a mean of 0.82 wt% (Fig. F62). Uranium values are mostly between 0.33 and 1.7 ppm with a mean of 2.84 ppm. In contrast, thorium values are relatively low, ranging from 0.01 to 0.55 ppm with a mean of 0.15 ppm.

Total gamma ray measurements in the basaltic basement are low with basement values between 5.31 and 10.86 gAPI. The sediment layers interbedded within the basement show higher values between 6.89 and 24.0 gAPI, highlighting the locations of the sediment layers (Fig. F61).

Potassium values are relatively low in the basaltic basement with values between 0.072 and 0.35 wt% (Fig. F62). The sediment interbeds, by contrast, show higher potassium values between 0.45 and 0.85 wt%. Uranium values are mostly between 0.0 and 2.45 ppm with a gradual increase from 250 m WMSF to the base of the hole (Fig. F62). The sediment interbeds within basement have low uranium values of <0.5 ppm. Thorium values range from 0.01 to 1.32 ppm with a mean of 0.64 ppm (Fig. F62). A significant gamma ray anomaly was recorded while in-pipe during FMS Pass 2, but it was not recorded during the deployment of the HNGS-APS-HLDS-GPIT-DITE tool string.

Density

Density values range from 1.2 to 1.8 g/cm^3 over the lowermost sediment section in Hole U1347A (Fig.

F63). In the basement section, density values are between 1.8 and 3.1 g/cm³. Sediment interbedded within basement has values between 1.5 and 1.9 g/cm³. A comparison between discrete physical property samples and the downhole density log shows that discrete sample data (MAD) are consistent with the downhole data (Fig. **F63**).

Sonic velocity measurements

Downhole velocity data were obtained for the open hole interval between 127.16 and 295 m WMSF (Fig. **F63**). In the sediment section average velocity is ~1.7 km/s. In the basement section velocities range between 3.6 and 6.8 km/s with an increasing trend with depth. A comparison with discrete sample measurements of *P*-wave velocity shows that the core data are consistently faster than the downhole measurements.

Neutron porosity measurements

Overall, downhole neutron porosity measurements show good agreement with physical property measurements obtained from core samples (Fig. **F63**). Most high-porosity values in the upper 250 m correspond to sections where the borehole was enlarged and therefore the log returns artificially high measurements. The bottommost section of Hole U1347A, where flows are massive, shows porosities slightly below 20% and good correlation with discrete physical property measurements.

Magnetic field measurements

Measurements of total magnetic moment, magnetic inclination, and magnetic intensity were obtained with the GPIT (Fig. **F64**). The mean magnetic inclination and total magnetic moment from 131.8 to 313.9 m WMSF are 44° and 0.43 Oe, respectively. The magnetic intensity is 0.29 Oe on the *z*-axis and varies between -0.46 to 0.43 Oe on the *x*- and *y*-axes.

Formation MicroScanner images

FMS images were obtained for the open hole interval between 134 and 315 m WMSF. The diameter of hole measured by the FMS calipers varied between 10.2 and 38.1 cm. High-quality FMS images were obtained in sections of the hole with a diameter <35.6 cm. FMS images from the basement section showed sections with high fracture density, well-defined pillow structures, and massive flow units in the basaltic sequences (Fig. **F65**). Large numbers of fractures and veins are clearly visible, which should allow reorientation of core pieces postcruise.

Lithostratigraphic correlations

Preliminary interpretation of the downhole log data divided Hole U1347A into 15 logging units within three main sections, the section covered by the BHA, the sedimentary sequences in open hole, and the basaltic basement (Figs. **F61**, **F62**, **F63**, **F65**). Logging units in the section covered by the BHA were interpreted on the basis of the gamma ray downhole logs, and only intervals that showed significant anomalies were characterized as logging units. Logging units within the open hole section that contained sedimentary sequences were also interpreted on the basis of the gamma ray fluctuations, whereas the basaltic basement was characterized using the resistivity logs.

Two logging units were qualitatively identified in the section covered by the BHA (Fig. **F61**):

- Logging Unit Ip shows a significant increase in total gamma ray measurements between 12.75 and 18.20 m WMSF. Spectral gamma data show a large contribution from thorium and uranium (Figs. **F61**, **F62**).
- Logging Unit Iip (80.2–97.5 m WMSF) shows an increase in gamma ray values with three distinct peaks (Fig. **F61**). Spectral gamma data show that the peak has a significant contribution from uranium (Fig. **F62**).

Only one logging unit was identified in the sedimentary sequence in open hole below the BHA based on gamma ray downhole logs (Fig. **F61**):

- Logging Unit Is (127.78–154.93 m WMSF) has gamma ray values between 11 and 41 gAPI.

The basement sequence below 154.93 m WMSF is divided into 12 logging units using the downhole resistivity and natural gamma logs (Fig. **F61**):

- Logging Unit Ib (154.93–167.9 m WMSF) resistivity shows a steady increase from the sediment/basement interface through the unit with maximum values of 60 Ωm. Caliper data show the borehole is larger than the bit size in the unit with a maximum diameter of 35.6 cm. Density averages 2.7 g/cm³.
- Logging Unit Iib (167.9–173.2 m WMSF) shows lower resistivity values of ~6.7 Ωm. Caliper data show the borehole has a consistent diameter of 27.3 cm within the unit. Total gamma shows a small peak up to 7.78 gAPI with spectral gamma showing that potassium makes the largest contribution to the peak (0.26 wt%).
- Logging Unit IIb (173.2–183.7 m WMSF) has resistivity values of ~20 Ωm with a peak of ~75 Ωm. Caliper data show the borehole in the unit

has a diameter of 27.3 cm. Natural gamma ray measurements are low in the unit and density has a mean value of 2.6 g/cm³.

- Logging Unit IVb (183.7–191.6 m WMSF) is characterized by low resistivity values of ~1.9 Ωm. Caliper data show a diameter of 32 cm. Potassium is high with a peak at 0.69 wt%.
- Logging Unit Vb (191.6–196.9 m WMSF) resistivity values range between 12.5 and 61.5 Ωm. Natural gamma and potassium measurements are low. Borehole diameter is ~32 cm.
- Logging Unit VIb (196.87–206.75 m WMSF) has resistivity values averaging ~2.9 Ωm. Borehole diameter ranges between 45.7 and 29.7 cm. Potassium peaks at 0.87 wt%.
- Logging Unit VIIb (206.75–237.07 m WMSF) resistivity values range between 10.6 and 175 Ωm. Natural gamma and potassium measurements are low. Borehole diameter averages 26.7 cm.
- Logging Unit VIIIb (237.07–242.30 m WMSF) resistivity values average 1.9 Ωm. Potassium peaks at 0.77 wt%. Borehole diameter is wide in this unit with a maximum of 44.5 cm.
- Logging Unit IXb (242.30–256.79 m WMSF) resistivity values show a peak of 1000 Ωm. Potassium ranges between 0.1 and 0.35 wt%. Borehole diameter is wide in this unit with a maximum of 42.4 cm.
- Logging Unit Xb (256.79–258.76 m WMSF) resistivity values average 5.75 Ωm. Potassium peaks at 0.86 wt%. Borehole diameter averages 29.7 cm.
- Logging Unit XIb (258.76–290.12 m WMSF) resistivity values range between 18.2 and 246 Ωm. Potassium and natural gamma measurements are low and show a decreasing trend through the unit. Borehole diameter averages 22.7 cm.
- Logging Unit XIIb (290.12–315.0 m WMSF) resistivity values are considerably higher than the upper logging units, ranging between 42.3 and 1153 Ωm. Borehole diameter is consistent throughout the unit with a diameter close to bit size of 25.9 cm.

Within the basement several highly altered sediment layers were recovered. These layers correspond with logging Units Iib, IVb, VIb, VIIb, and Xb, which show high natural gamma values. Elevated potassium concentrations in the sediment layers may be indicative of alteration of the sediment.

References

- Almeev, R., Holtz, F., Koepke, J., Haase, K., and Devey, C., 2008. Depths of partial crystallization of H₂O-bearing MORB: phase equilibria simulations of basalts at the MAR near Ascension Island (7–11°S). *J. Petrol.* 49(1):25–45. doi:10.1093/petrology/egm068
- Alt, J.C., 1995. Subseafloor processes in mid-ocean ridge hydrothermal systems. In Humphris, S.E., Zierenberg, R., Mullineaux, L., and Thomson, R. (Eds.), *Seafloor Hydrothermal Systems: Physical, Chemical, Biological and Geological Interactions within Hydrothermal Systems*. Geophys. Monogr., 91:85–114.
- Alt, J.C., 2004. Alteration of the upper oceanic crust: mineralogy, chemistry, and processes. In Elderfield, H., and Davis, E. (Eds.), *Hydrogeology of the Oceanic Lithosphere*. New York (Cambridge Univ. Press), 456–488.
- Audunsson, H., and Levi, S., 1989. Drilling-induced remanent magnetization in basalt drill cores. *Geophys. J. Int.*, 98(3):613–622. doi:10.1111/j.1365-246X.1989.tb02294.x
- Bach, W., Hegner, E., Erzinger, J., and Satir, M., 1994. Chemical and isotopic variations along the superfast spreading East Pacific Rise from 6 to 30°S. *Contrib. Mineral. Petrol.*, 116(4):365–380. doi:10.1007/BF00310905
- Banerjee, N.R., Honnorez, J., and Muehlenbachs, K., 2004. Low-temperature alteration of submarine basalts from the Ontong Java Plateau. In Fitton, J.G., Mahoney, J.J., Wallace, P.J., and Saunders, A.D. (Eds.), *Origin and Evolution of the Ontong Java Plateau*. Geol. Soc. Spec. Publ., 229(1):259–273. doi:10.1144/GSL.SP.2004.229.01.15
- Bindeman, I.N., and Davis, A.M., 2000. Trace element partitioning between plagioclase and melt: investigation of dopant influence on partition behavior. *Geochim. Cosmochim. Acta*, 64(16):2863–2878. doi:10.1016/S0016-7037(00)00389-6
- Blum, P., 1997. Physical properties handbook: a guide to the shipboard measurement of physical properties of deep-sea cores. *ODP Tech. Note*, 26. doi:10.2973/odp.tn.26.1997
- Bown, P.R., 2005. Early to mid-Cretaceous calcareous nanoplankton from the northwest Pacific Ocean, Leg 198, Shatsky Rise. In Bralower, T.J., Premoli Silva, I., and Malone, M.J. (Eds.) *Proc. ODP, Sci. Results*, 198: College Station, TX (Ocean Drilling Program), 1–82. doi:10.2973/odp.proc.sr.198.103.2005
- Bryan, W.B., 1983. Systematics of modal phenocryst assemblages in submarine basalts: petrologic implications. *Contrib. Mineral. Petrol.*, 83(1–2):62–74. doi:10.1007/BF00373080
- Caroff, M., Maury, R.C., Cotten, J., and Clément, J.-P., 2000. Segregation structures in vapor-differentiated basaltic flows. *Bull. Volcanol.*, 62(3):171–187. doi:10.1007/s004450000077
- Davis, G.H., 1984. *Structural Geology of Rocks and Regions*. New York (John Wiley and Sons, Inc.).
- Davis, R.A., Jr., 1985. Beach and nearshore zone. In Davis, R.A., Jr. (Ed.), *Coastal Sedimentary Environments* (2nd ed.): New York (Springer-Verlag), 379–444.
- Dubrovin, P.V., and Tarduno, J.A., 2005. On the compositional field of self-reversing titanomaghemite: constraints from Deep Sea Drilling Project Site 307. *J. Geophys. Res., [Solid Earth]*, 110(B11):B11104. doi:10.1029/2005JB003865

- Engel, C.G., and Fisher, R.L., 1975. Granitic to ultramafic rock complexes of the Indian Ocean Ridge system, western Indian Ocean. *Geol. Soc. Am. Bull.*, 86(11):1553–1578. doi:10.1130/0016-7606(1975)86<1553:GTURCO>2.0.CO;2
- Fitton, J.G., and Godard, M., 2004. Origin and evolution of magmas on the Ontong Java Plateau. In Fitton, J.G., Mahoney, J.J., Wallace, P.J., and Saunders, A.D. (Eds.), *Origin and Evolution of the Ontong Java Plateau*. Geol. Soc. Spec. Publ., 229(1):151–178. doi:10.1144/GSL.SP.2004.229.01.10
- Fisk, M.R., 1984. Depths and temperatures of mid-ocean ridge magma chambers and the composition of their source magmas. In Gass, I.G., Lippard, S.J., and Shelton, A.W. (Eds.), *Ophiolites and Oceanic Lithosphere*. Geol. Soc. Spec. Publ., 13(1):17–23. doi:10.1144/GSL.SP.1984.013.01.02
- Fontile, K., Marsaglia, K.M., and Dean, N., 2006. A petrological and geochemical study of Cretaceous siliceous rocks from Shatsky Rise. In Bralower, T.J., Premoli Silva, I., and Malone, M.J. (Eds.), *Proc. ODP, Sci. Results*, 198: College Station, TX (Ocean Drilling Program), 1–45. doi:10.2973/odp.proc.sr.198.107.2006
- Fujii, T., and Bougault, H., 1983. Melting relations of a magnesian abyssal tholeiite and the origin of MORBs. *Earth Planet. Sci. Lett.*, 62(2):283–295. doi:10.1016/0012-821X(83)90091-2
- Goff, F.E., 1977. Vesicle cylinders in vapor-differentiated basalt flows [Ph.D. thesis]. Univ. California, Santa Cruz.
- Goff, F., 1996. Vesicle cylinders in vapor-differentiated basalt flows. *J. Volcanol. Geotherm. Res.*, 71(2–4):167–185. doi:10.1016/0377-0273(95)00073-9
- Hall, L.S., Mahoney, J.J., Sinton, J.M., and Duncan, R.A., 2006. Spatial and temporal distribution of a C-like asthenospheric component in the Rano Rahi Seamount field, East Pacific Rise, 15°–19°S. *Geochem., Geophys., Geosyst.*, 7(3):Q03009. doi:10.1029/2005GC000994
- Hancock, P.L., 1985. Brittle microtectonics: principles and practice. *J. Struct. Geol.*, 7(3–4):437–457. doi:10.1016/0191-8141(85)90048-3
- Hartley, M.E., and Thordarson, T., 2009. Melt segregations in a Columbia River basalt lava flow: a possible mechanism for the formation of highly evolved mafic magmas. *Lithos*, 112(3–4):434–446. doi:10.1016/j.lithos.2009.04.003
- Hekinian, R., and Morel, J.M., 1980. Basement rocks from the East Pacific Rise near 9°N compared with other ocean-floor volcanic provinces. In Rosendahl, B.R., Hekinian, R., et al., *Init. Repts. DSDP*, 54: Washington, DC (U.S. Govt. Printing Office), 819–832. doi:10.2973/dsdp.proc.54.137.1980
- Holbourn, A., Kuhnt, W., and Soeding, E., 2001. Atlantic paleobathymetry, paleoproductivity and paleocirculation in the late Albian: the benthic foraminiferal record. *Palaeogeogr., Palaeoclimatol., Palaeoecol.*, 170(3–4):171–196. doi:10.1016/S0031-0182(01)00223-1
- Hon, K., Kauahikaua, J., Denlinger, R., and Mackay, K., 1994. Emplacement and inflation of pahoehoe sheet flows: observations and measurements of active lava flows on Kilauea Volcano, Hawaii. *Geol. Soc. Am. Bull.*, 106(3):351–370. doi:10.1130/0016-7606(1994)106<0351:EAIOPS>2.3.CO;2
- Honnorez, J., 2003. Hydrothermal alteration vs. ocean-floor metamorphism. A comparison between two case histories: the TAG hydrothermal mound (Mid-Atlantic Ridge) vs. DSDP/ODP Hole 504B (equatorial East Pacific). *Comp. Rendus Geosci.*, 335(10–11):781–824. doi:10.1016/j.crte.2003.08.009
- Hunt, C.P., Moskowitz, B.M., and Banerjee, S.K., 1995. Magnetic properties of rocks and minerals. In Ahrens, T.J. (Ed.), *Rock Physics and Phase Relations: A Handbook of Physical Constants*. Am. Geophys. Union Ref. Shelf, 3:189–204.
- Jerram, D.A., Cheadle, M.J., and Philpotts, A.R., 2003. Quantifying the building blocks of igneous rocks: are clustered crystal frameworks the foundation? *J. Petrol.*, 44(11):2033–2051. doi:10.1093/petrology/egg069
- Jerram, D.A., and Widdowson, M., 2005. The anatomy of continental flood basalt provinces: geological constraints on the processes and products of flood volcanism. *Lithos*, 79(3–4):385–405. doi:10.1016/j.lithos.2004.09.009
- Jones, R.W., and Wonders, A.A.H., 1992. Benthic foraminifers and paleobathymetry of Barrow Group (Berriasian–Valanginian) deltaic sequences, Sites 762 and 763, northwest shelf, Australia. In von Rad, U., Haq, B.U., et al., *Proc. ODP, Sci. Results*, 122: College Station, TX (Ocean Drilling Program), 557–568. doi:10.2973/odp.proc.sr.122.174.1992
- Keszthelyi, L., Self, S., and Thordarson, T., 1999. Application of recent studies on the emplacement of basaltic lava flows to the Deccan traps. In Subbarao, K.V. (Ed.), *Deccan Volcanic Province*. Mem. Geol. Soc. India, 1:485–520.
- Kinzler, R.J., and Grove, T.L., 1992. Primary magmas of mid-ocean ridge basalts, 1. Experiments and methods. *J. Geophys. Res., [Solid Earth]*, 97(B5):6885–6906. doi:10.1029/91JB02840
- Kirkpatrick, R.J., 1975. Crystal growth from the melt: a review. *Am. Mineral.*, 60(9–10):798–814.
- Kirkpatrick, R.J., 1979. Processes of crystallization in pillow basalts, Hole 396B, DSDP Leg 46. In Dmitriev, L., Heirtzler, et al., 1979. *Init. Repts. DSDP*, 46: Washington, DC (U.S. Govt. Printing Office), 271–282. doi:10.2973/dsdp.proc.46.117.1979
- Kirkpatrick, R.J., and Hodges, F.N., 1978. Crystallization of the Core 15 basalt cooling unit, Hole 396B. DSDP Leg 46. In Heirtzler, J.R., Dmitriev, L.V., et al., *Init. Repts. DSDP*, 46: Washington (U.S. Govt. Printing Office), 259–269. doi:10.2973/dsdp.proc.46.116.1979
- Kirschvink, J.L., 1980. The least-squares line and plane and the analysis of palaeomagnetic data. *Geophys. J. R. Astron. Soc.*, 62(3):699–718. doi:10.1111/j.1365-246X.1980.tb02601.x
- Klaus, A., and Sager, W.W., 2002. Data report: high-resolution site survey seismic reflection data for ODP Leg 198 drilling on Shatsky Rise, northwest Pacific. In Bralower, T.J., Premoli Silva, I., Malone, M.J., et al., *Proc. ODP, Init.*

- Repts.*, 198: College Station, TX (Ocean Drilling Program), 1–21. doi:10.2973/odp.proc.ir.198.111.2002
- Koutsoukos, E.A.M., and Hart, M.B., 1990. Cretaceous foraminiferal morphogroup distribution patterns, palaeo-communities and trophic structures: a case study from the Sergipe Basin, Brazil. *Trans. R. Soc. Edinburgh: Earth Sci.*, 81:221–246.
- Kushiro, I., and Thompson, R.N., 1972. Origin of some abyssal tholeiites from the Mid-Atlantic Ridge. *Yearb.—Carnegie Inst. Washington*, 71:403–406.
- Le Maitre, R.W., Bateman, P., Dudek, A., Keller, J., Lameyre, J., Le Bas, M.J., Sabine, P.A., Schmid, R., Sorensen, H., Streckeisen, A., Woolley, A.R., and Zanettin, B., 1989. *A Classification of Igneous Rocks and Glossary of Terms*: Oxford (Blackwell).
- Lyubetskaya, T., and Korenaga, J., 2007. Chemical composition of Earth's primitive mantle and its variance, 1. Method and results. *J. Geophys. Res., [Solid Earth]*, 112(B3):B03211. doi:10.1029/2005JB004223
- Macdonald, G.A., 1968. Composition and origin of Hawaiian lavas. In Coats, R.R., Hay, R.L., and Anderson, C.A. (Eds.), *Studies in Volcanology: A Memoir in Honor of Howel Williams*. Mem.—Geol. Soc. Am., 116:477–522.
- Macdonald, G.A., and Katsura, T., 1964. Chemical composition of Hawaiian lavas. *J. Petrol.*, 5(1):82–133.
- Mahoney, J.J., Duncan, R.A., Tejada, M.L.G., Sager, W.W., and Bralower, T.J., 2005. Jurassic–Cretaceous boundary age and mid-ocean-ridge–type mantle source for Shatsky Rise. *Geology*, 33(3):185–188. doi:10.1130/G21378.1
- Mahoney, J.J., Fitton, J.G., Wallace, P.J., et al., 2001. *Proc. ODP, Init. Repts.*, 192: College Station, TX (Ocean Drilling Program). doi:10.2973/odp.proc.ir.192.2001
- Mahoney, J.J., Sinton, J.M., Kurz, M.D., Macdougall, J.D., Spencer, K.J., and Lugmair, G.W., 1994. Isotope and trace element characteristics of a super-fast spreading ridge: East Pacific Rise 13–23°S. *Earth Planet. Sci. Lett.*, 121(1–2):173–193. doi:10.1016/0012-821X(94)90039-6
- Marshall, M., and Cox, A., 1971. Effect of oxidation on the natural remanent magnetization of titanomagnetite in suboceanic basalt. *Nature (London, U. K.)*, 230(5288):28–31. doi:10.1038/230028a0
- Matzka, J., and Krása, D., 2007. Oceanic basalt continuous thermal demagnetization curves. *Geophys. J. Int.*, 169(3):941–950. doi:10.1111/j.1365-246X.2007.03378.x
- Nakanishi, M., Sager, W.W., and Klaus, A., 1999. Magnetic lineations within Shatsky Rise, northwest Pacific Ocean: implications for hot spot–triple junction interaction and oceanic plateau formation. *J. Geophys. Res., [Solid Earth]*, 104(B4):7539–7556. doi:10.1029/1999JB900002
- Natland, J.H., 1979. Crystal morphologies in basalts from DSDP Site 395, 23°N, 46°W, Mid-Atlantic Ridge. In Melson, W.G., Rabinowitz, P.D., et al., *Init. Repts. DSDP*, 45: Washington, DC (U.S. Govt. Printing Office), 423–445. doi:10.2973/dsdp.proc.45.118.1979
- Natland, J.H., Adamson, A.C., Laverne, C., Melson, W.G., and O'Hearn, T., 1983. A compositionally nearly steady-state magma chamber at the Costa Rica Rift: evidence from basalt glass and mineral data, Deep Sea Drilling Project Sites 501, 504, and 505. In Cann, J.R., Langseth, M.G., Honnorez, J., Von Herzen, R.P., White, S.M., et al., *Init. Repts. DSDP*, 69: Washington, DC (U.S. Govt. Printing Office), 811–858. doi:10.2973/dsdp.proc.69.154.1983
- Natland, J.H., and Dick, H.J.B., 2009. Paired melt lenses at the East Pacific Rise and the pattern of melt flow through the gabbroic layer at a fast-spreading ridge. *Lithos*, 112(1–2):73–86. doi:10.1016/j.lithos.2009.06.017
- Ogg, J.G., Ogg, G., and Gradstein, F.M., 2008. *The Concise Geologic Time Scale*: Cambridge (Cambridge Univ. Press). <http://www.cambridge.org/catalogue/catalogue.asp?isbn=9780521898492>
- Özdemir, Ö., and O'Reilly, W., 1982. Magnetic hysteresis properties of synthetic monodomain titanomagnetites. *Earth Planet. Sci. Lett.*, 57(2):437–447. doi:10.1016/0012-821X(82)90162-5
- Passchier, C.W., and Trouw, R.A.J., 1996. *Microtectonics*: Berlin (Springer-Verlag).
- Ramsay, J.G., and Huber, M.I., 1987. *The Techniques of Modern Structural Geology* (Vol. 2): *Folds and Fractures*: New York (Acad. Press).
- Sager, W.W., 2005. What built Shatsky Rise, a mantle plume or ridge processes? In Foulger, G.R., Natland, J.H., Presnall, D.C., and Anderson, D.L. (Eds.), *Plates, Plumes, and Paradigms*. Spec. Pap.—Geol. Soc. Am., 388:721–733. doi:10.1130/0-8137-2388-4.721
- Sager, W.W., and Han, H.-C., 1993. Rapid formation of the Shatsky Rise oceanic plateau inferred from its magnetic anomaly. *Nature (London, U. K.)*, 364(6438):610–613. doi:10.1038/364610a0
- Sager, W.W., Handschumacher, D.W., Hilde, T.W.C., and Bracey, D.R., 1988. Tectonic evolution of the northern Pacific plate and Pacific-Farallon Izanagi triple junction in the Late Jurassic and Early Cretaceous (M21–M10). *Tectonophysics*, 155(1–4):345–364. doi:10.1016/0040-1951(88)90274-0
- Sager, W.W., Kim, J., Klaus, A., Nakanishi, M., and Khankishieva, L.M., 1999. Bathymetry of Shatsky Rise, north-west Pacific Ocean: implications for ocean plateau development at a triple junction. *J. Geophys. Res., [Solid Earth]*, 104(4):7557–7576. doi:10.1029/1998JB900009
- Salters, V.J.M., and Longhi, J., 1999. Trace element partitioning during the initial stages of melting beneath mid-ocean ridges. *Earth Planet. Sci. Lett.*, 166(1–2):15–30. doi:10.1016/S0012-821X(98)00271-4
- Sandwell, D.T., and MacKenzie, K.R., 1989. Geoid height versus topography for oceanic plateaus and swells. *J. Geophys. Res., [Solid Earth]*, 94:7403–7418. doi:10.1029/JB094iB06p07403
- Sano, T., and Yamashita, S., 2004. Experimental petrology of basement lavas from Ocean Drilling Program Leg 192: implications for differentiation processes in Ontong Java Plateau magmas. In Fitton, J.G., Mahoney, J.J., Wallace, P.J., and Saunders, A.D. (Eds.), *Origin and Evolution of the Ontong Java Plateau*. Geol. Soc. Spec. Publ., 229(1):185–218. doi:10.1144/GSL.SP.2004.229.01.12

- Self, S., Thordarson, T., and Keszthelyi, L., 1997. Emplacement of continental flood basalt lava flows. In Mahoney, J.J., and Coffin, M. (Eds.), *Large Igneous Provinces: Continental, Oceanic, and Planetary Flood Volcanism*. Geophys. Monogr., 100:381–410.
- Shipboard Scientific Party, 2001. Leg 192 summary. In Mahoney, J.J., Fitton, J.G., Wallace, P.J., et al., *Proc. ODP, Init. Repts.*, 192: College Station, TX (Ocean Drilling Program), 1–75. doi:10.2973/odp.proc.ir.192.101.2001
- Shipboard Scientific Party, 2002a. Leg 197 summary. In Tarduno, J.A., Duncan, R.A., Scholl, D.W., et al., *Proc. ODP, Init. Repts.*, 197: College Station, TX (Ocean Drilling Program), 1–92. doi:10.2973/odp.proc.ir.197.101.2002
- Shipboard Scientific Party, 2002b. Leg 198 summary. In Bralower, T.J., Premoli Silva, I., Malone, M.J., et al., *Proc. ODP, Init. Repts.*, 198: College Station, TX (Ocean Drilling Program), 1–148. doi:10.2973/odp.proc.ir.198.101.2002
- Shipboard Scientific Party, 2002c. Site 1213. In Bralower, T.J., Premoli Silva, I., Malone, M.J., et al., *Proc. ODP, Init. Repts.*, 198: College Station, TX (Ocean Drilling Program), 1–110. doi:10.2973/odp.proc.ir.198.109.2002
- Sinton, J.M., and Detrick, R.S., 1992. Mid-ocean ridge magma chambers. *J. Geophys. Res., [Solid Earth]*, 97(B1):197–216. doi:10.1029/91JB02508
- Sinton, J.M., Smaglik, S.M., Mahoney, J.J., and Macdonald, K.C., 1991. Magmatic processes at superfast spreading mid-ocean ridges: glass compositional variations along the East Pacific Rise 13°–23°S. *J. Geophys. Res., [Solid Earth]*, 96:6133–6155. doi:10.1029/90JB02454
- Sliter, W.V., and Baker, R.A., 1972. Cretaceous bathymetric distribution of benthic foraminifers. *J. Foraminiferal Res.*, 2(4):167–183. doi:10.2113/gsjfr.2.4.167
- Sliter, W.V., and Brown, G.R., 1993. Shatsky Rise: seismic stratigraphy and sedimentary record of Pacific paleoceanography since the Early Cretaceous. In Natland, J.H., Storms, M.A., et al., *Proc. ODP, Sci. Results*, 132: College Station, TX (Ocean Drilling Program), 3–13. doi:10.2973/odp.proc.sr.132.302.1993
- Smith, W.H.F., and Sandwell, D.T., 1997. Global sea floor topography from satellite altimetry and ship depth soundings. *Science*, 277(5334):1956–1962. doi:10.1126/science.277.5334.1956
- Stolper, E., 1980. A phase diagram for mid-ocean ridge basalts: preliminary results and implications for petrogenesis. *Contrib. Mineral. Petrol.*, 74(1):13–27. doi:10.1007/BF00375485
- Tejada, M.L.G., Mahoney, J.J., Duncan, R.A., and Hawkins, M.P., 1996. Age and geochemistry of basement and alkalic rocks of Malaita and Santa Isabel, Solomon Islands, southern margin of Ontong Java Plateau. *J. Petrol.* 37(2):361–394. doi:10.1093/petrology/37.2.361
- Tejada, M.L.G., Mahoney, J.J., Neal, C.R., Duncan, R.A., and Petterson, M.G., 2002. Basement geochemistry and geochronology of central Malaita, Solomon Islands, with implications for the origin and evolution of the Ontong Java Plateau. *J. Petrol.*, 43(3):449–484. doi:10.1093/petrology/43.3.449
- Thordarson, T., and Self, S., 1998. The Roza Member, Columbia River Basalt Group: a gigantic pahoehoe lava flow field formed by endogenous processes. *J. Geophys. Res., [Solid Earth]*, 103(B11):27411–27445. doi:10.1029/98JB01355
- Thorpe, R.S., and Brown, G.C., 1985. *Geological Society of London Handbook: The Field Description of Igneous Rocks*: Milton Keynes, U.K. (Open Univ. Press)
- Wilson, D.S., Teagle, D.A.H., Acton, G.D., et al., 2003. *Proc. ODP, Init. Repts.*, 206: College Station, TX (Ocean Drilling Program). doi:10.2973/odp.proc.ir.206.2003
- Winterer, E.L., and Sager, W.W., 1995. Synthesis of drilling results from the Mid-Pacific Mountains: regional context and implications. In Winterer, E.L., Sager, W.W., Firth, J.V., and Sinton, J.M. (Eds.), *Proc. ODP, Sci. Results*, 143: College Station, TX (Ocean Drilling Program), 497–535. doi:10.2973/odp.proc.sr.143.245.1995

Publication: 3 November 2010

MS 324-104

Figure F1. Bathymetry of Tamu Massif and location of Sites U1347 and U1348. Contours and colors indicate bathymetric depths predicted by satellite altimetry (Smith and Sandwell, 1997). Contours shown at 200 m intervals; dark contours shown for kilometer multiples. Red line = track of Cruise TN037 site survey (Klaus and Sager, 2002), open circles = prior drill sites, blue circle = location of Site 1213.

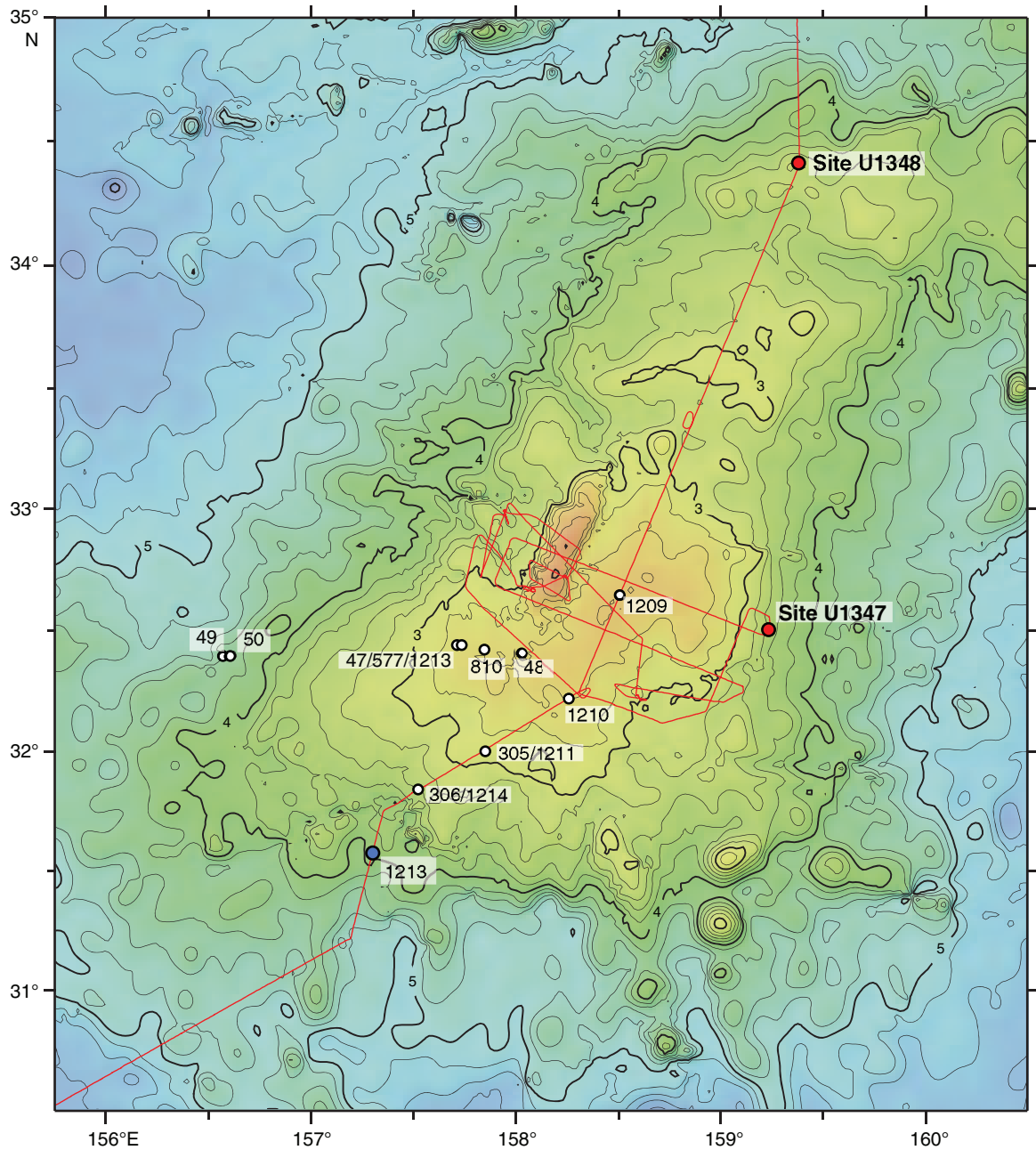


Figure F2. Seismic section and precruise layer interpretation (color overlay), Site U1347 (Klaus and Sager, 2002). Dashed yellow lines = coherent reflections within igneous basement. UTC = Universal Time Coordinated, c/c = course change.

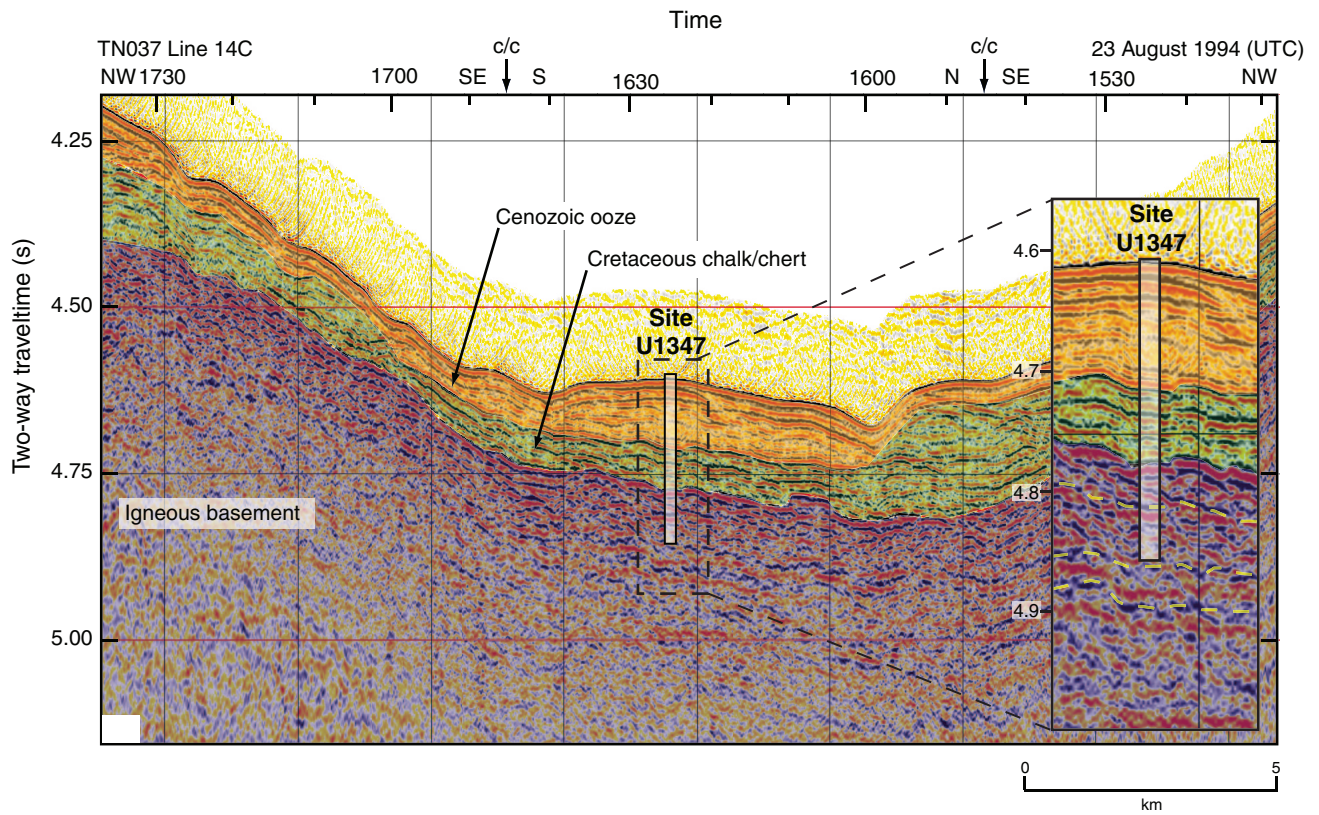


Figure F3. Plot of operation time vs. penetration depth, Hole U1347A. Dashed line = planned penetration progress, solid blue line = actual depth achieved. RCB = rotary core barrel, CW = core winch.

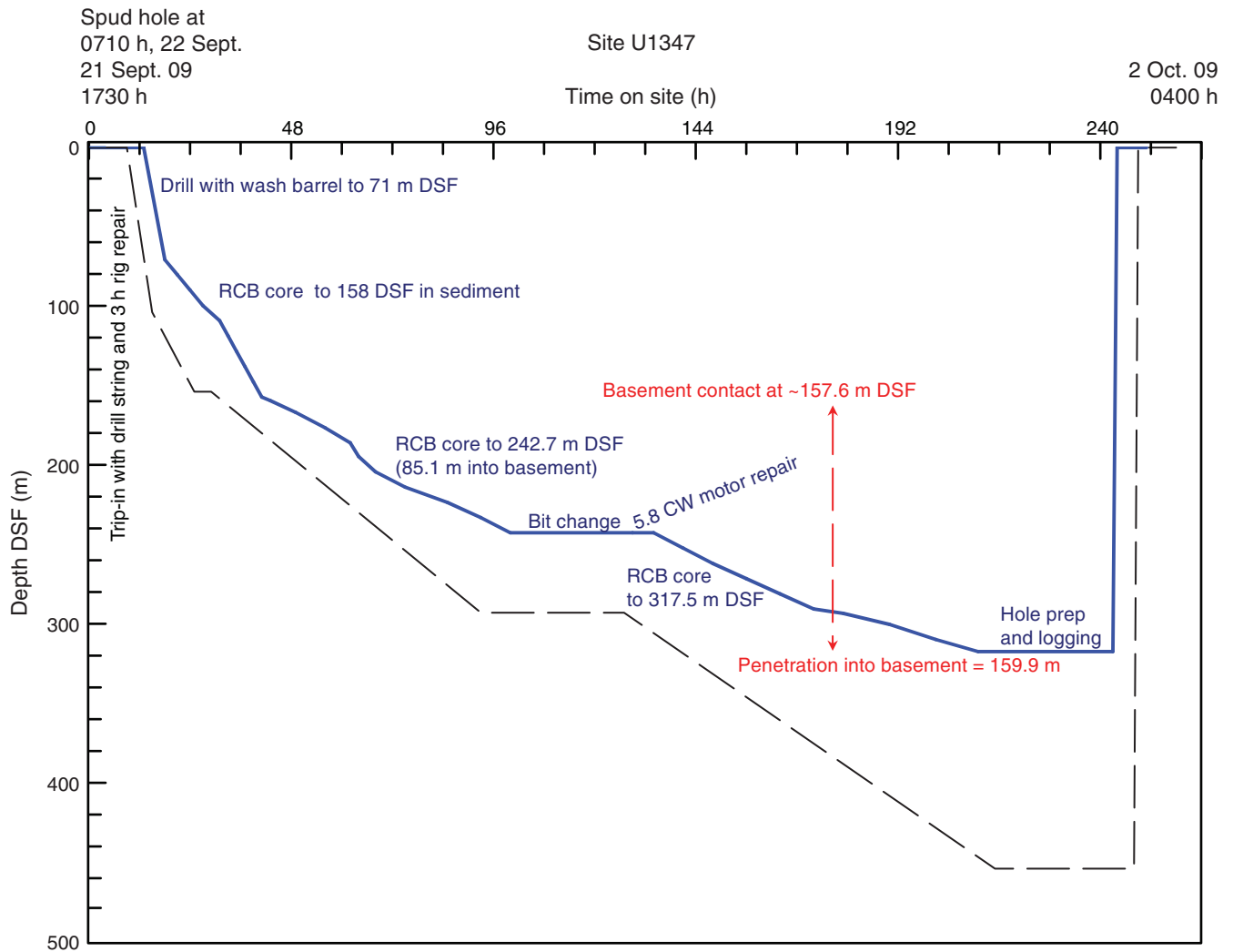


Figure F4. Lithostratigraphy, Site U1347. See "Igneous petrology" for descriptions of basaltic units.

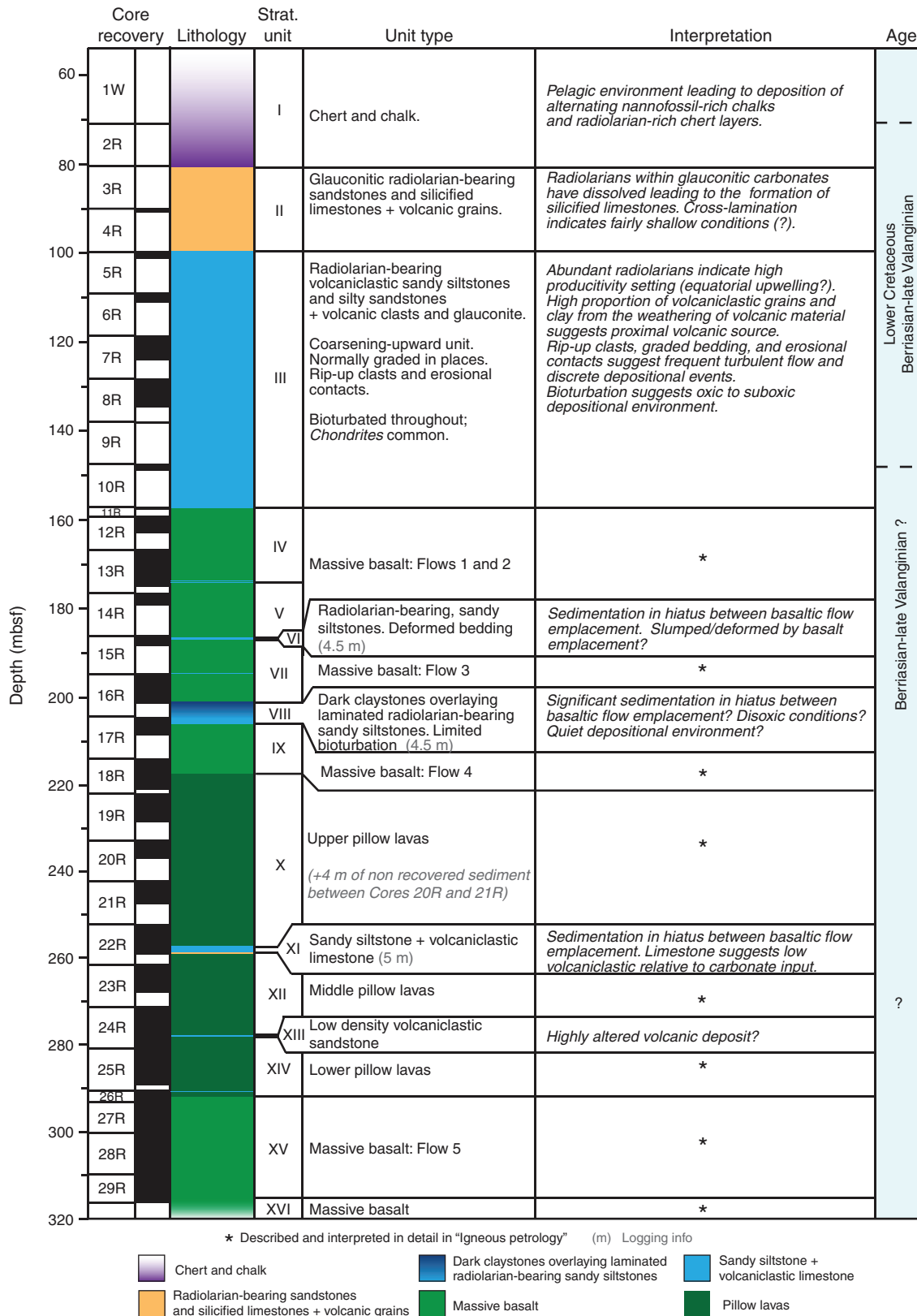


Figure F5. Lithostratigraphy of stratigraphic Units I–III, Site U1347.

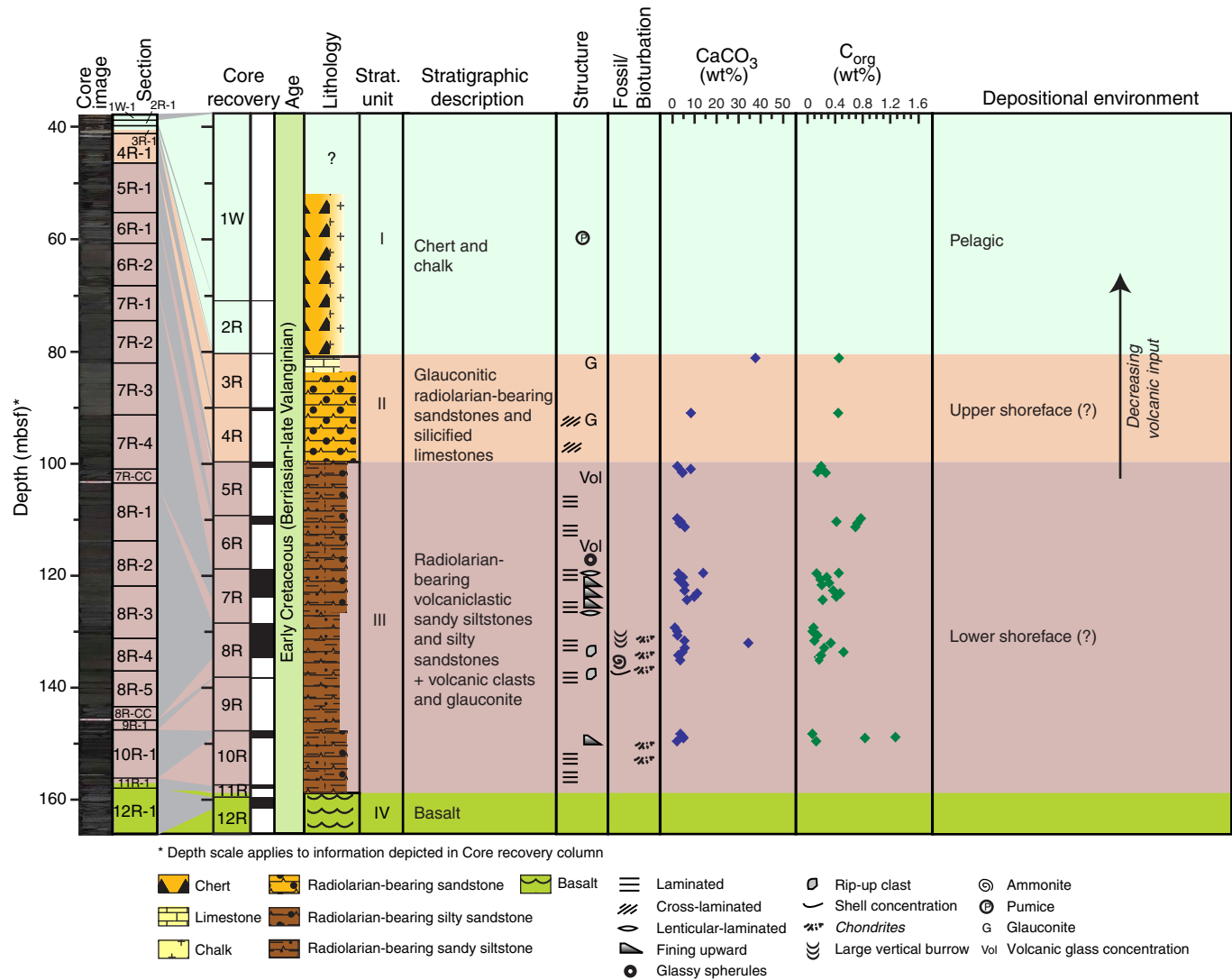


Figure F6. Thin section photomicrographs of radiolarians replaced by glauconite in stratigraphic Unit II, Hole U1347A (Core 324-U1347A-4R). Many delicate primary biogenic structures, such as chambers and occasionally spines, can be seen preserved by the secondary glauconite. Fine micritic matrix with secondary silica cement is visible surrounding the radiolarians. **A.** Conical radiolarians (Sample 324-U1347A-4R-1, 7–9 cm). Plane-polarized light. **B.** Spherical radiolarian (Sample 324-U1347A-4R-1, 7–9 cm). Cross-polarized light. **C.** Spherical radiolarians (Sample 324-U1347A-4R-1, 38–44 cm). Plane-polarized light. **D.** Intact and fractured spherical radiolarians (Sample 324-U1347A-4R-1, 38–44 cm). Plane-polarized light.

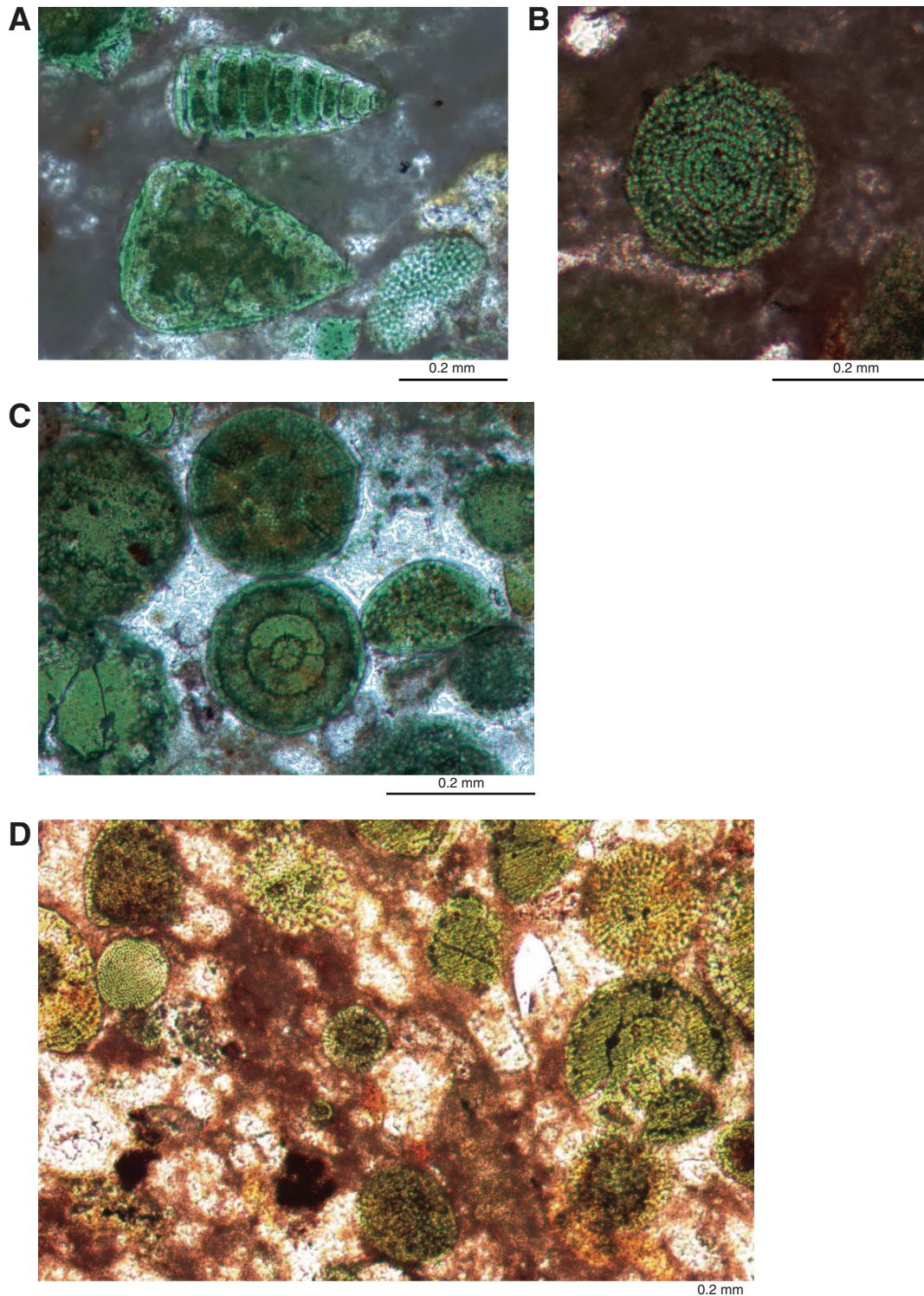
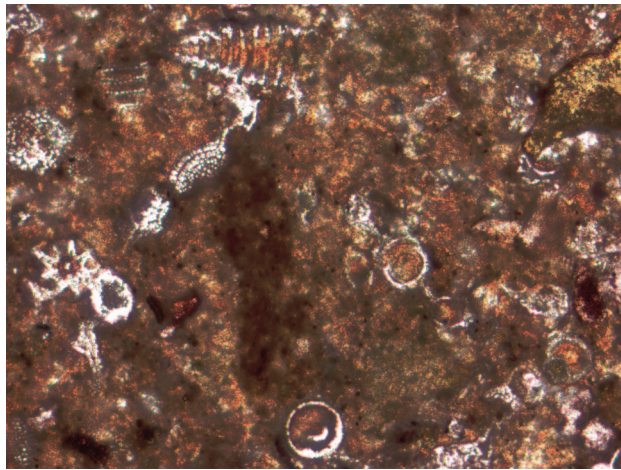


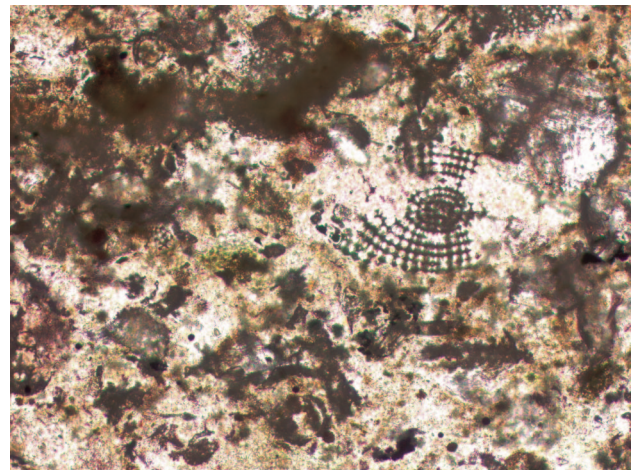
Figure F7. Cross-bedding in silicified sandstones in Unit II, Hole U1347A (interval 324-U1347A-4R-1, 31–53 cm). White lines = most prominent bedding planes.



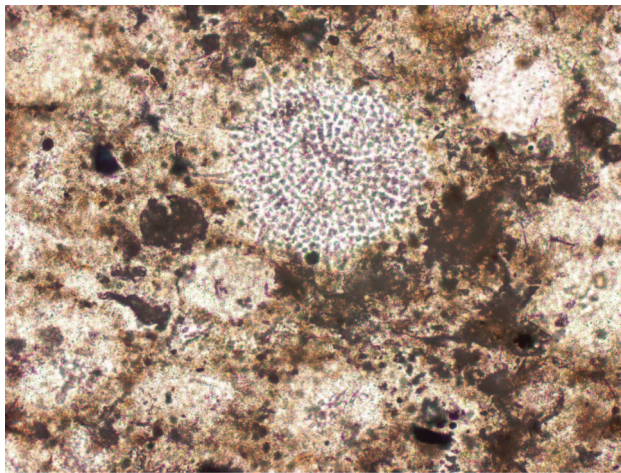
Figure F8. Thin section photomicrographs of radiolarians (and diatoms?) in sandy siltstones from Unit III, Hole U1347A (Sample 324-U1347A-6R-2, 59–62 cm). Plane-polarized light.



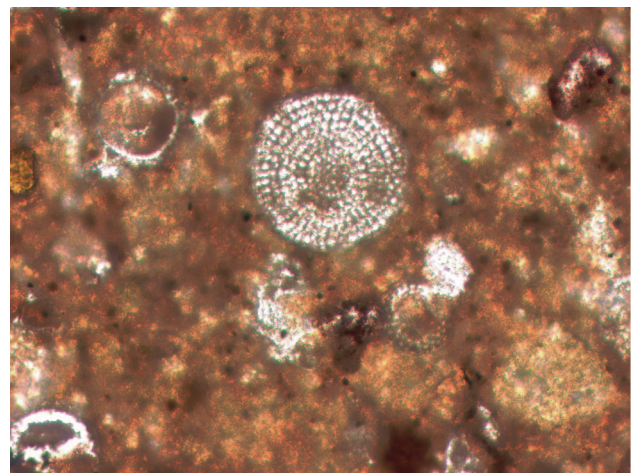
0.2 mm



0.1 mm



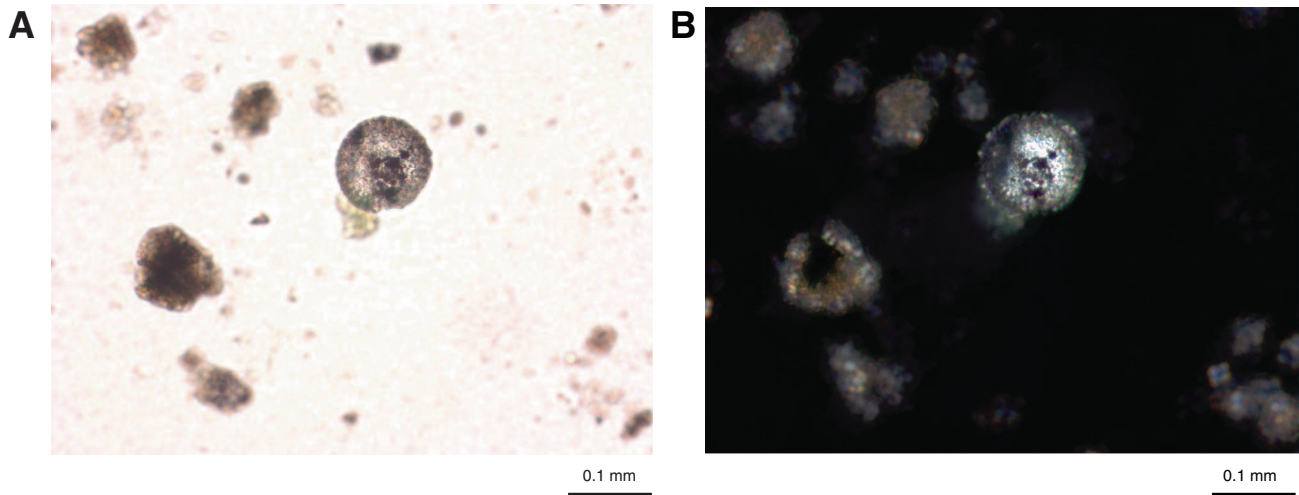
0.2 mm



0.1 mm

Figure F9. Smear slide photomicrographs of well-preserved radiolarians present in Unit III sandy siltstones, Hole U1347A. **A, B.** Spherical radiolarian under (A) plane-polarized light and (B) cross-polarized light. **C, D.** Conical chambered radiolarian under (C) plane-polarized light and (D) cross-polarized light.

Sample 324-U1347A-8R-4, 67-68 cm



Sample 324-U1347A-8R-2, 41-42 cm

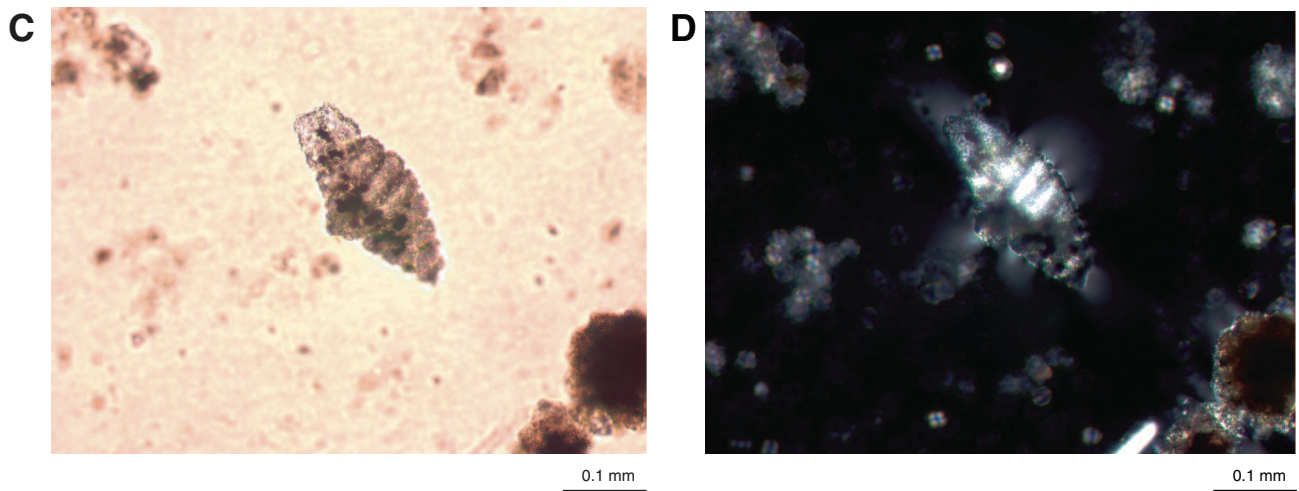
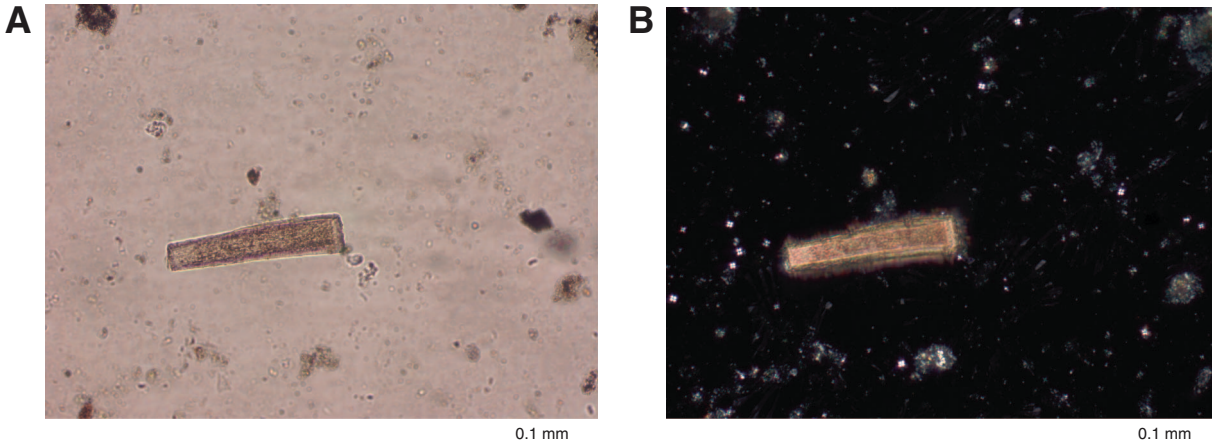
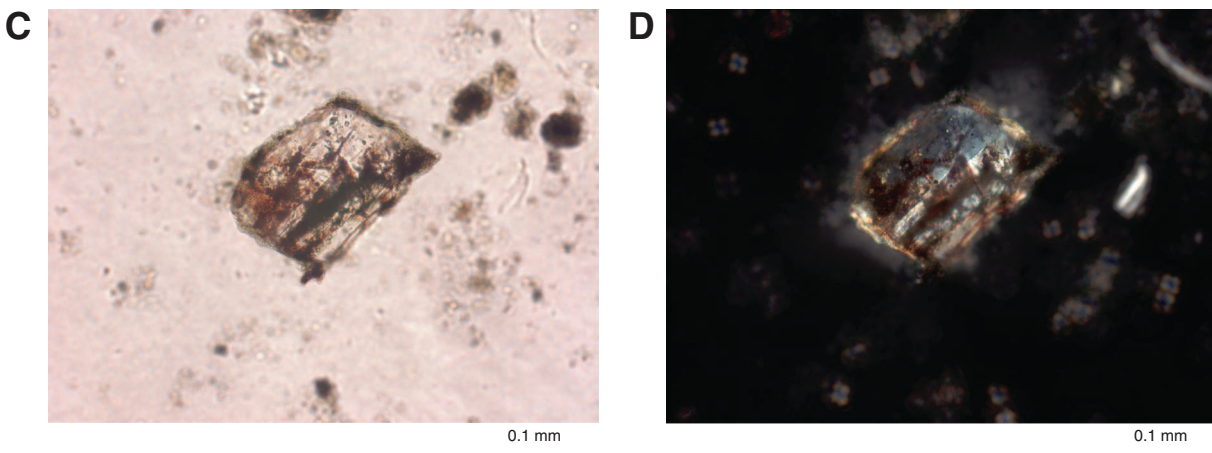


Figure F10. Photomicrographs of minerals in stratigraphic Unit III, Hole U1347A. **A, B.** Phillipsite (zeolite) crystal under (A) plane-polarized light and (B) cross-polarized light. **C, D.** Altered plagioclase crystal under (C) plane-polarized light and (D) cross-polarized light. **E, F.** High-relief, high-birefringence mineral (pyroxene?) under (E) plane-polarized light and (F) cross-polarized light.

Sample 324-U1347A-8R-CC, 4-5 cm



Sample 324-U1347A-8R-CC, 4-5 cm



Sample 324-U1347A-8R-2, 113-114 cm

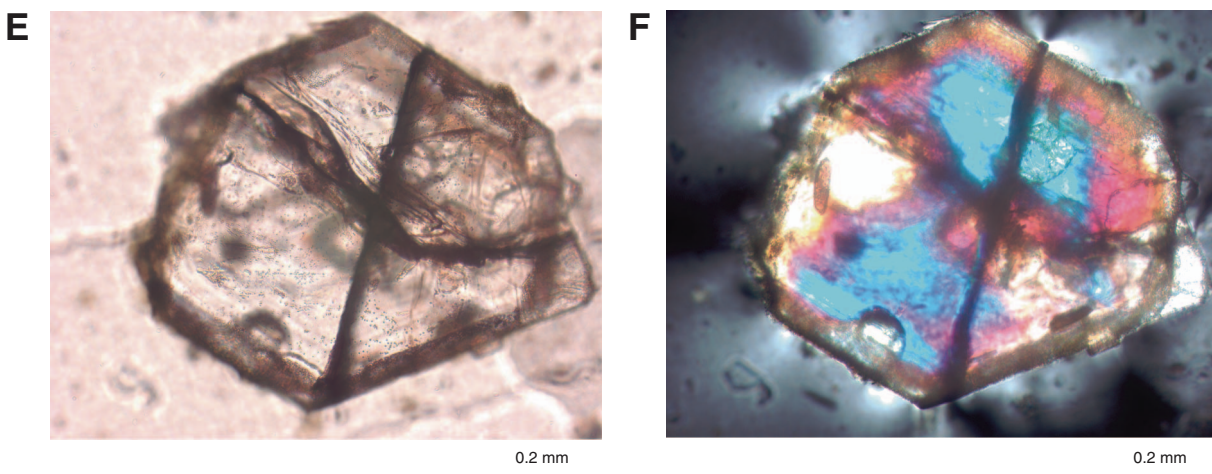


Figure F11. Photographs of large glassy spherules concentrated in a coarse layer in Core 324-U1347A-6R (stratigraphic Unit III), Hole U1347A. A coarse glassy core with a fine (quenched?) outer rim is visible in the larger clasts.



1 cm



0.5 cm

Figure F12. Core photographs of sedimentary structures in Core 324-U1347A-8R (stratigraphic Unit III), Hole U1347A. **A.** Coarse radiolarian-rich band at base, with finer bioturbated sandy siltstone above. Chaotic churned strata indicate rapid lateral transport of material. **B.** Dark irregular claystone bleb in greenish gray sandy siltstone matrix. **C.** Dark claystone blebs, probably rip-up clasts from rapid lateral emplacement of sediments, in greenish siltstone matrix. Bioturbation also visible. **D.** Graded sequence showing fining upward from coarse sandy siltstone to fine dark claystone. Lower beds are laminated. *Chondrites* trace fossils visible at top of sequence truncated by erosional contact with next coarse layer above.

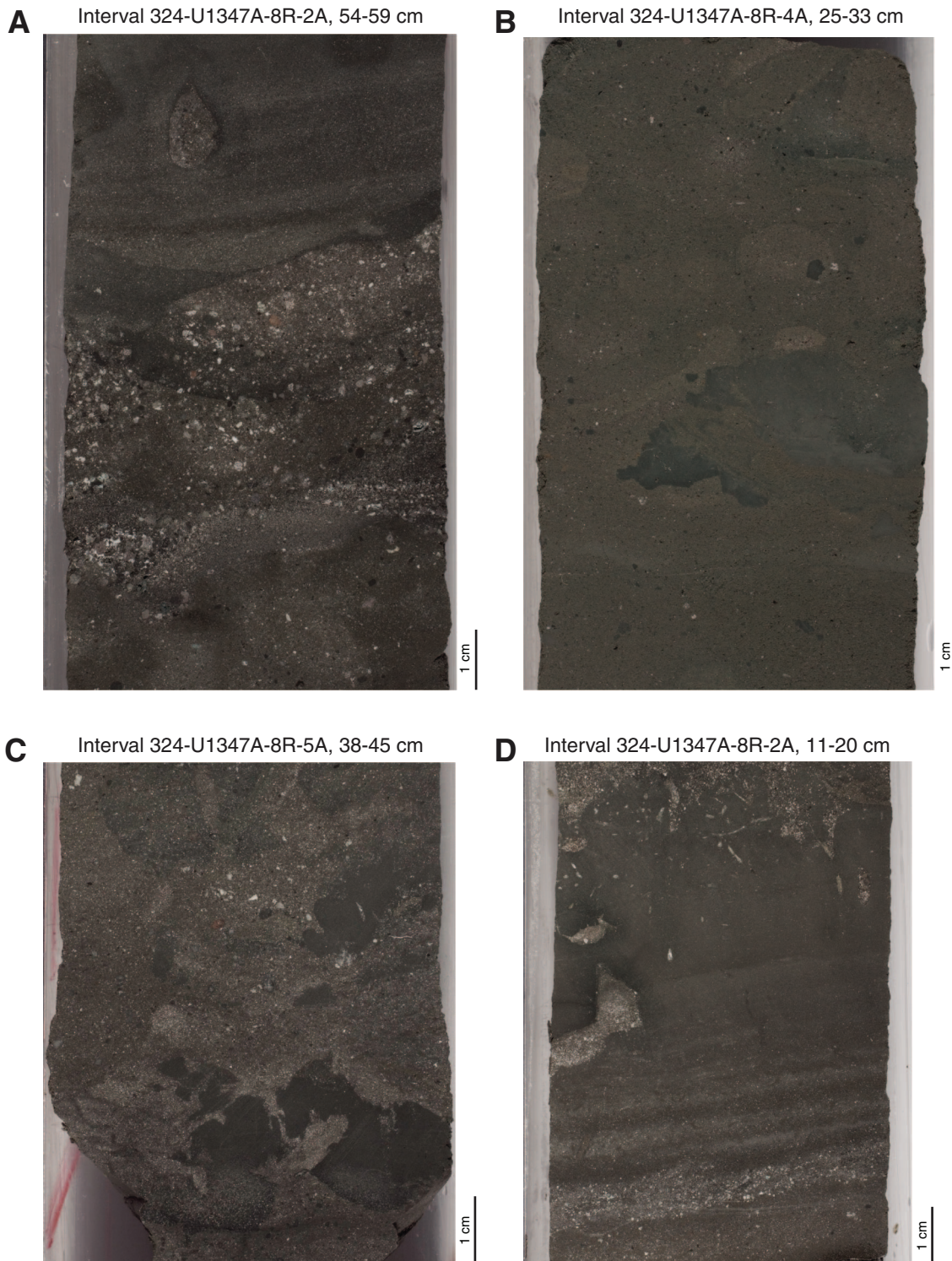


Figure F13. Photographs of bioturbation and ichnofossils in Core 324-U1347A-8R (stratigraphic Unit III), Hole U1347A. **A.** Long, vertical, U-shaped burrow. **B.** *Planolites* trace fossils (circled). **C.** *Chondrites* ichnofossils in the fine clay layer at the top of a graded sequence.

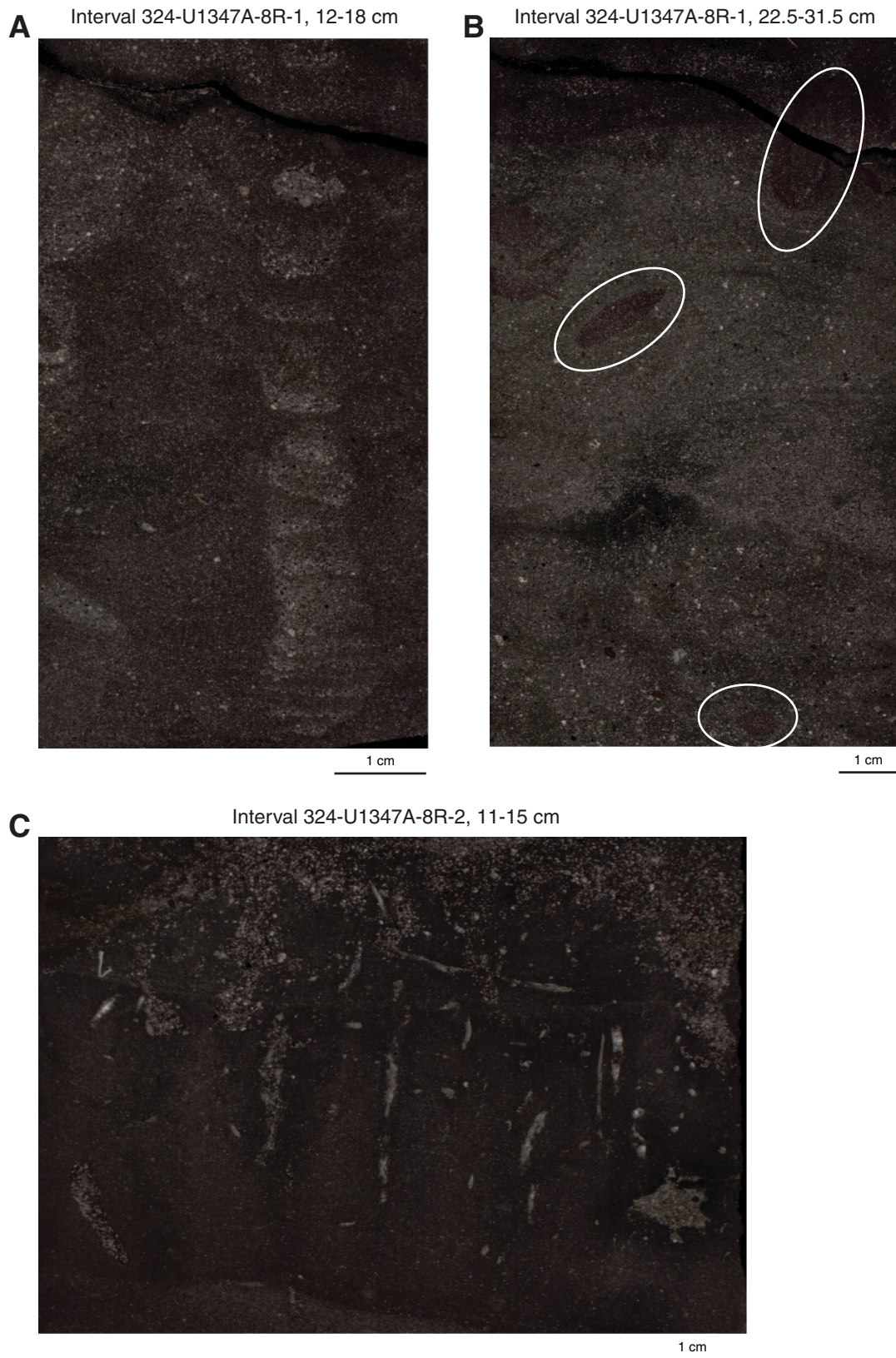


Figure F14. Stereomicroscopic image of Sample 324-U1347A-13R-7, 19.5–21.5 cm, showing exceptionally high radiolarian abundance (>125 μm fraction of washed foraminifer sample), Hole U1347A.

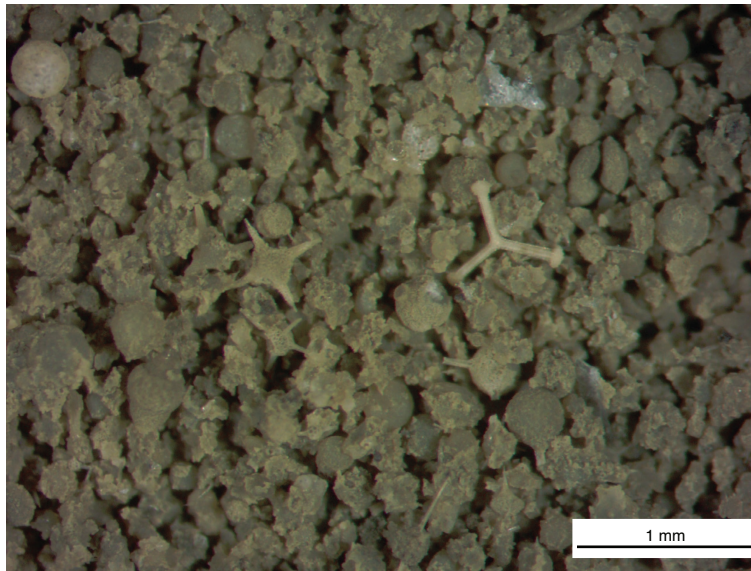


Figure F15. Overview of recovery, Hole U1347A. Inflation unit thicknesses are minimal estimates based on the measured upper and lower contacts identified in the core (see 324UNIT.XLS in LOGS in “**Supplementary material**” for data). Stratigraphic unit thicknesses are given based on available coring data (black) and downhole logging measurements (gray).

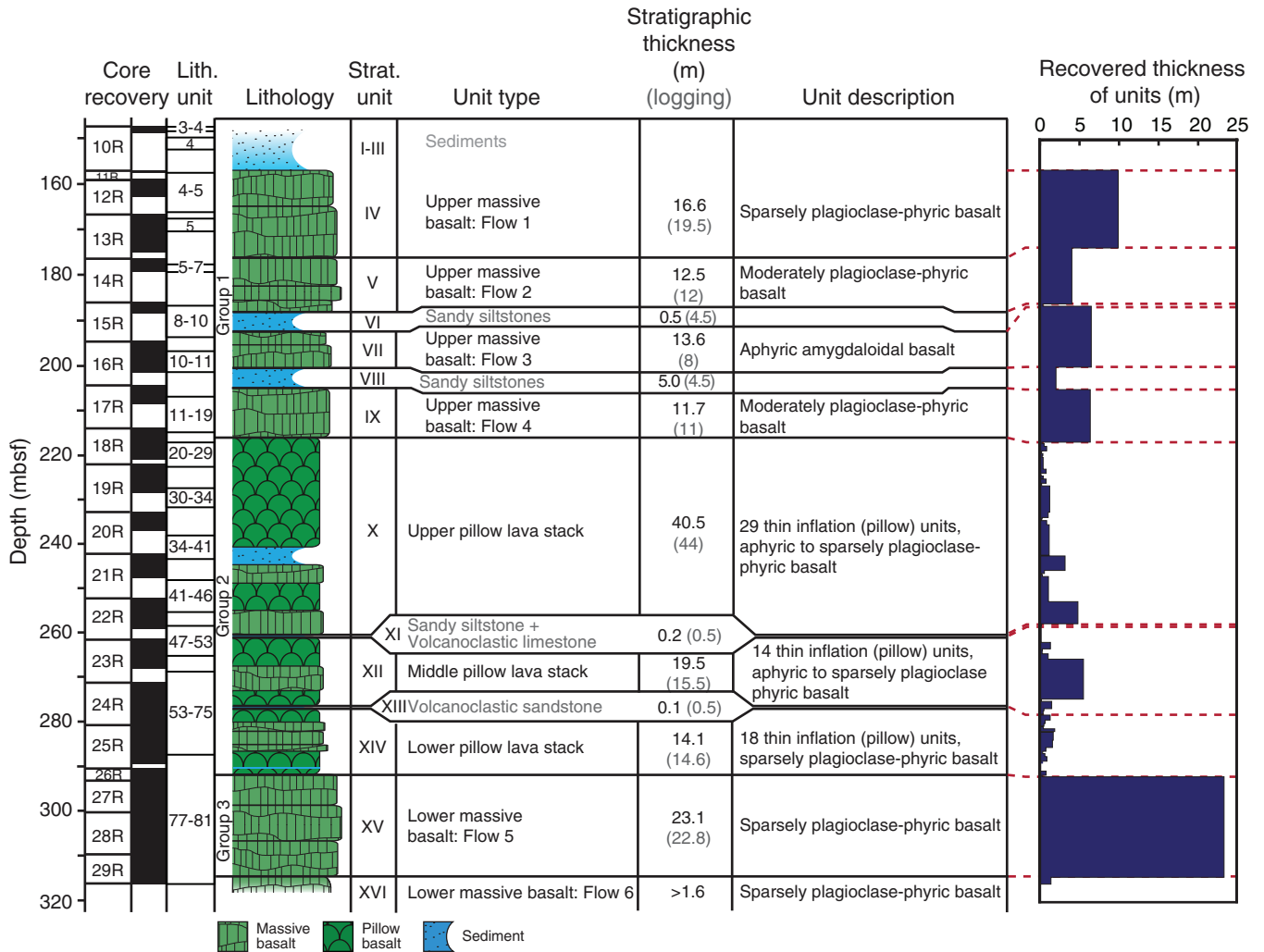


Figure F16. Overview of Cores 324-U1347A-10R through 29R, Hole U1347A. NGR = natural gamma radiation, GRA = gamma ray attenuation density, MS = whole-round and point-source magnetic susceptibility (see “Physical properties” for more details).

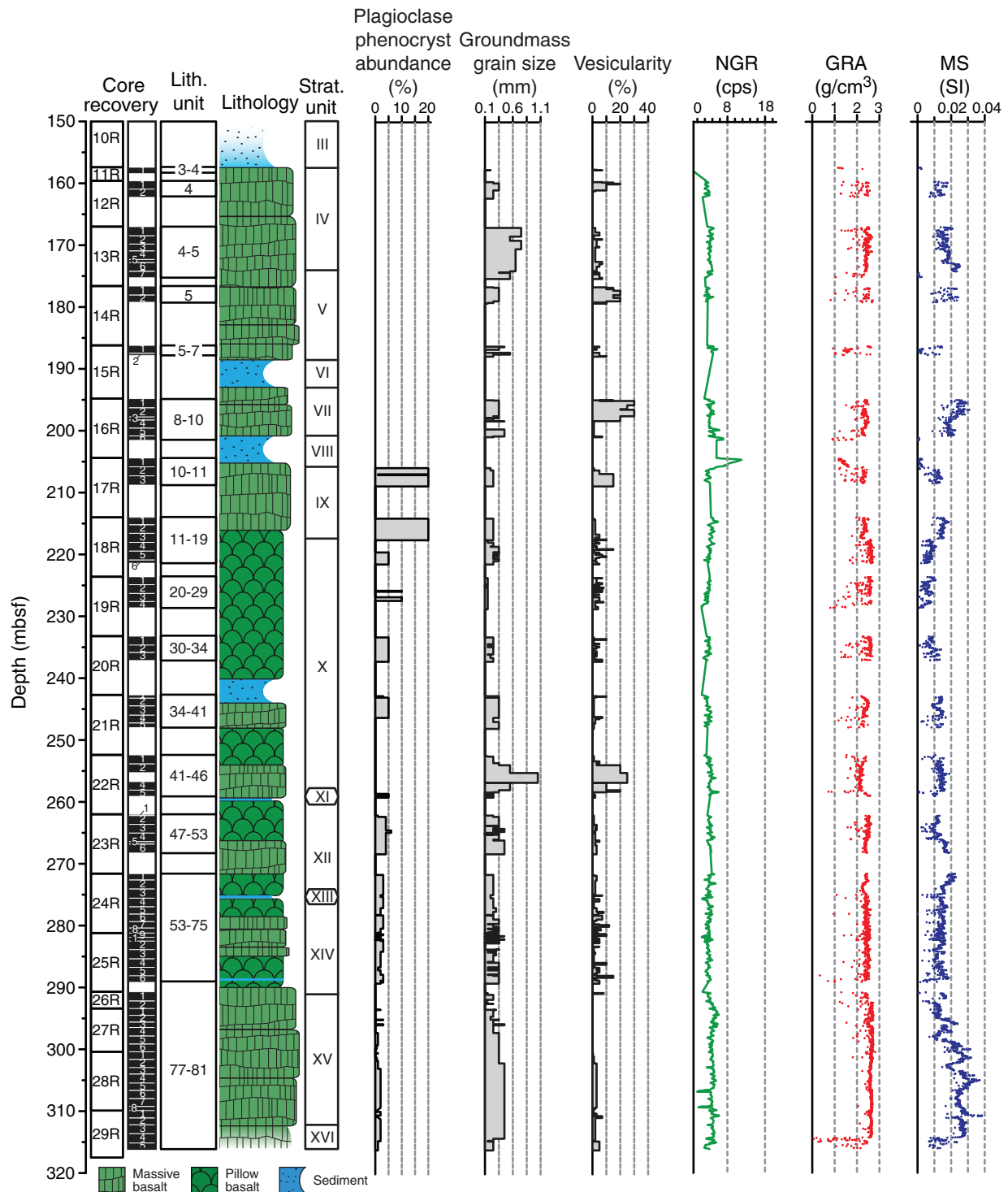


Figure F17. Core section images annotated with volcanological features for a massive submarine basalt flow (Unit V) from Sections 324-U1347A-13R-7 through 15R-1, Hole U1347A. These core sections exhibit primary magmatic features including folded glassy crusts and vesicular zones. Interflow sediment occurs between the massive flows in Section 324-U1347A-15R-1 and appears to be ~5 m thick in downhole logging measurements. Red dashed lines = upper and lower bounds of sections.

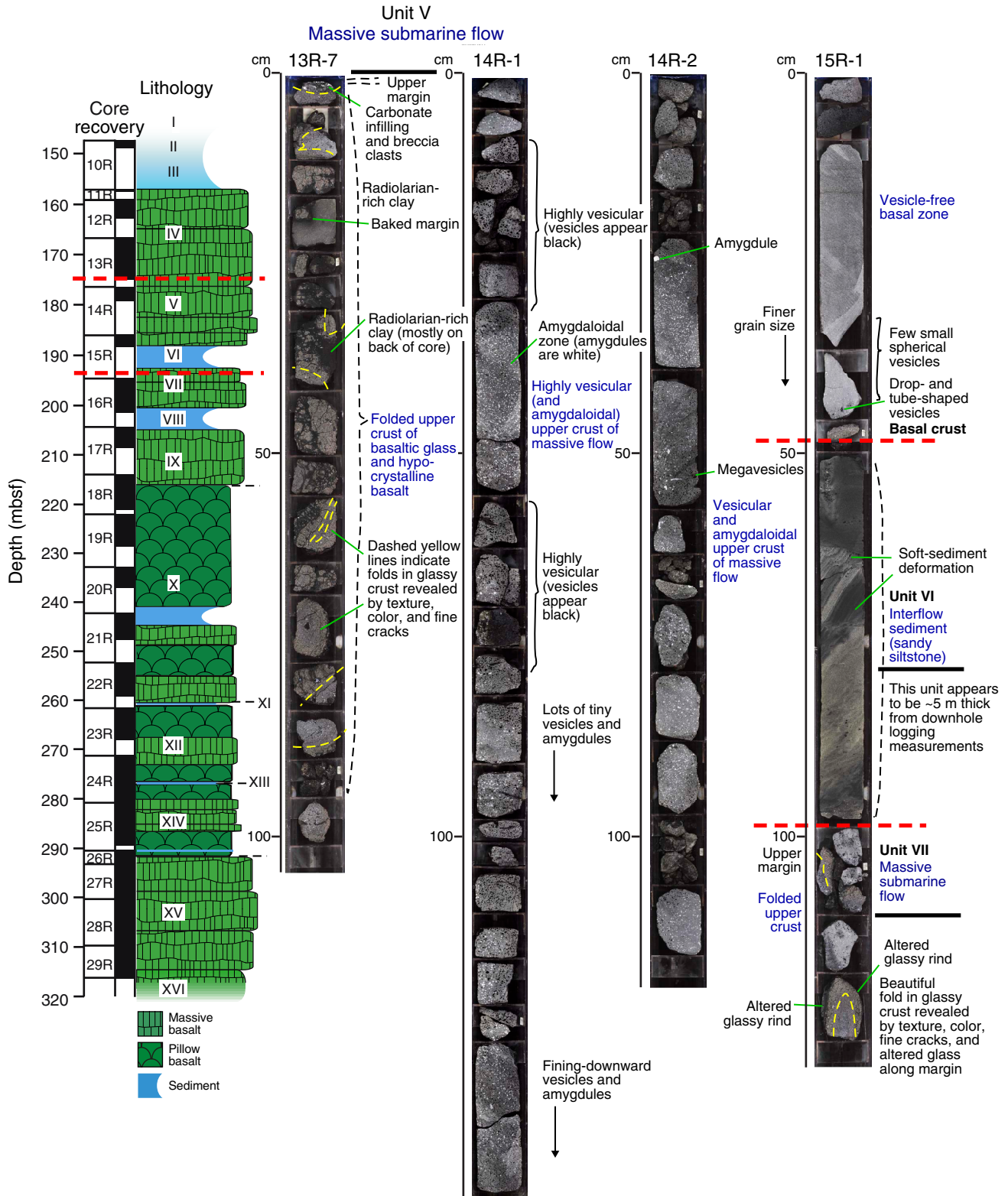


Figure F18. Core section images of Sections (A) 324-U1347A-13R-7 and (B) 15R-1, (C, D, E) close-up photographs, and (F, G, H, I) photomicrographs of the upper and lower crusts of a massive submarine flow in Unit V, Hole U1347A. The core scan shows folded upper crust of basaltic glass and hypocrySTALLINE basalt. The folded crust in C is sideromelane with plagioclase and clinopyroxene, with increasing amounts of plagioclase and Fe-Ti oxide spherulites moving out of the glassy margin. Dashed yellow lines indicate folds in the glassy crust revealed by texture, color, and fine cracks. The rock in D contains a good example of a fold in glassy crust. Close-up photograph locations of C, D, and E are indicated by red boxes in A and B. Red box in E indicates photomicrograph location in F, G, H, and I. Width of the field of view in photomicrographs is ~2.5 mm. All photomicrographs are under plane-polarized light. cpx = clinopyroxene, plag = plagioclase.

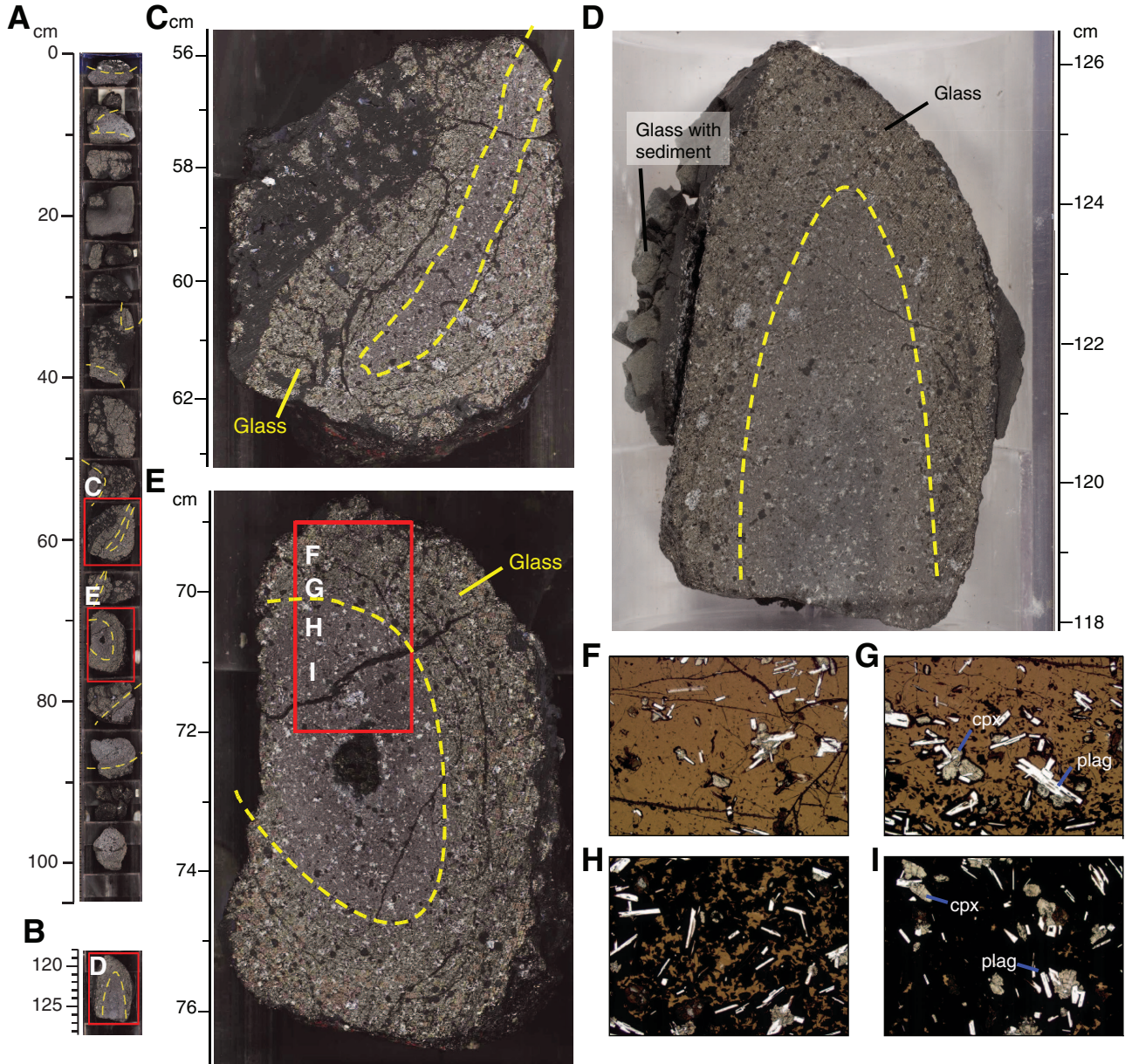


Figure F19. Core images of Sections (A) 324-U1347A-17R-2 (Unit IX) and (B) 13R-7 (Unit V), (C) thin section scan, and (D, E, F, G) photomicrographs (plane-polarized light) of chilled lava/sediment contacts within the glassy upper crust of massive submarine flow in Unit V, Hole U1347A. Thin section scan location of C (made from bottom of billet on working half of core and so is not identical to image in A) is indicated by the red box in A. Red boxes in C indicate photomicrograph locations. Dashed yellow lines in D, E, and G outline part of the fine-grained sediment/glass contact. Height of field of view of D, E, and G is ~6 mm (2.5×). Height of field of view of F is ~1 mm (20×).

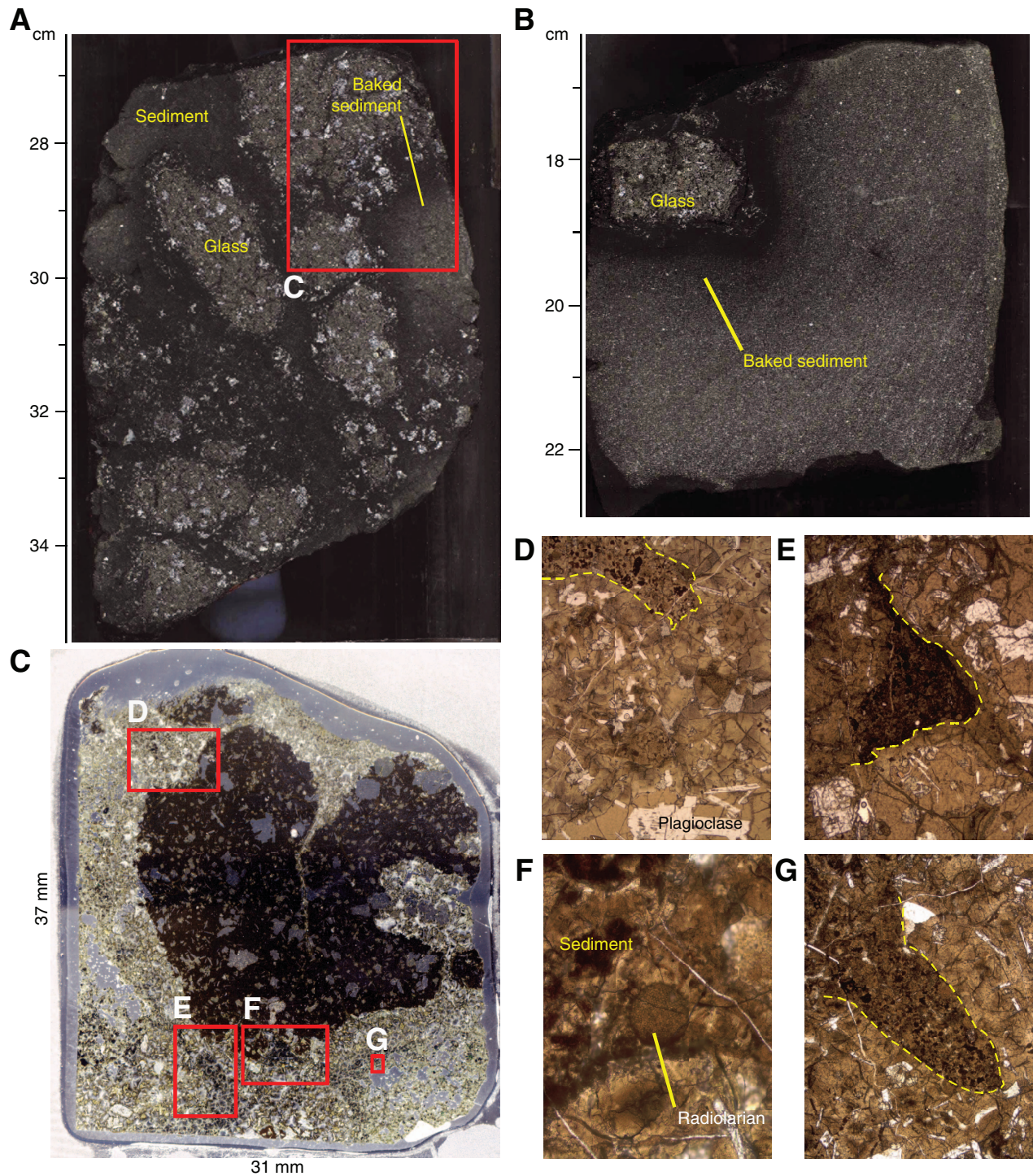


Figure F20. Core images annotated with volcanological features for a section of the lower pillow basalts (Unit XIV) and upper part of a massive basalt flow (Unit XV) from Sections 324-U1347A-25R-3 through 26R-2, Hole U1347A. Red dashed lines = upper and lower bounds of sections, red text = top and bottom of pillow lobes, dashed green lines = glassy chilled margins.

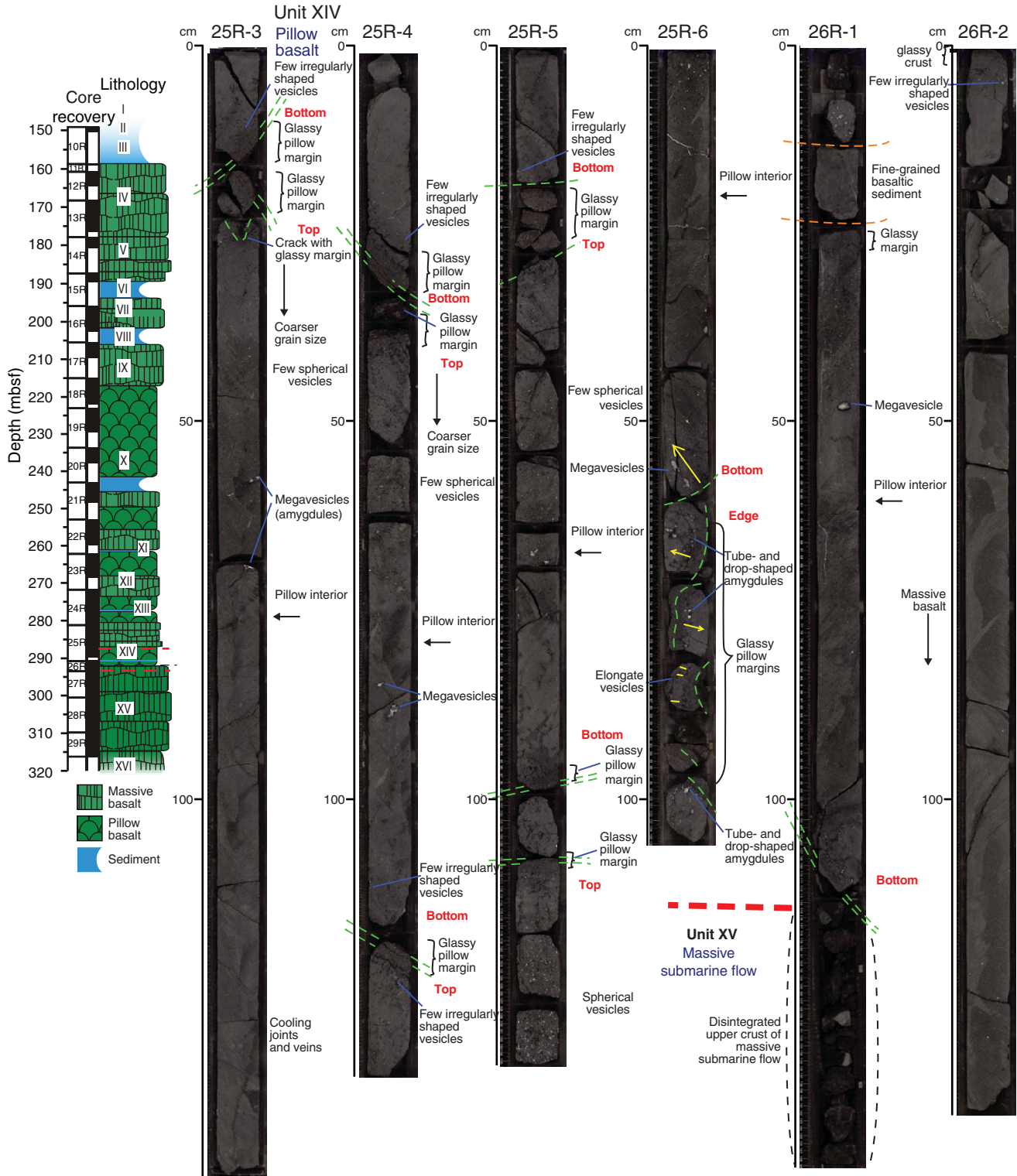


Figure F21. Core section images of Sections (A) 324-U1347A-18R-5 (Unit X) and (B) 23R-3 (Unit XII), (C, D) thin section scans, and (E, F, G, H) photomicrographs of the glassy margins of pillow basalt, Hole U1347A. Chilled glassy rinds (yellow dashed lines) show a transition zone with increasing amounts of plagioclase and Fe-Ti oxide spherulites inward of the glassy margin. Thin section scan locations of C and D are indicated with red boxes in A and B. Red boxes in C and D indicate photomicrograph locations. Width of field of view in photomicrographs is 2.5 mm. E and G are under plane-polarized transmitted light; F and H are under crossed nicols. cpx = clinopyroxene, plag = plagioclase.

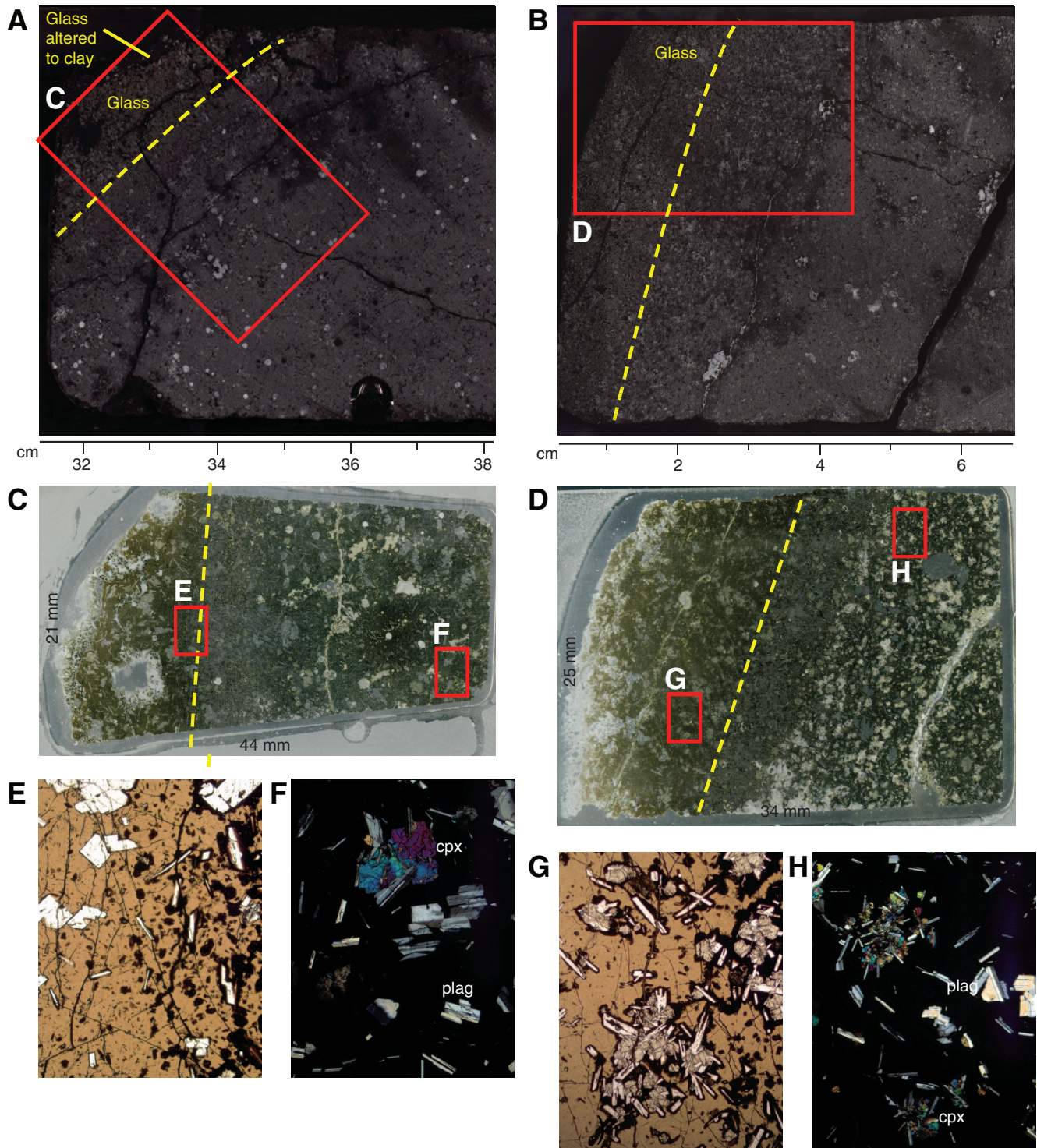


Figure F22. Histogram of inflation unit size distribution as measured by the difference in recovered (or estimated) depths of upper and lower contacts. Complete flows are defined as these inflation units with a recovered top and bottom contact in core of Hole U1347A.

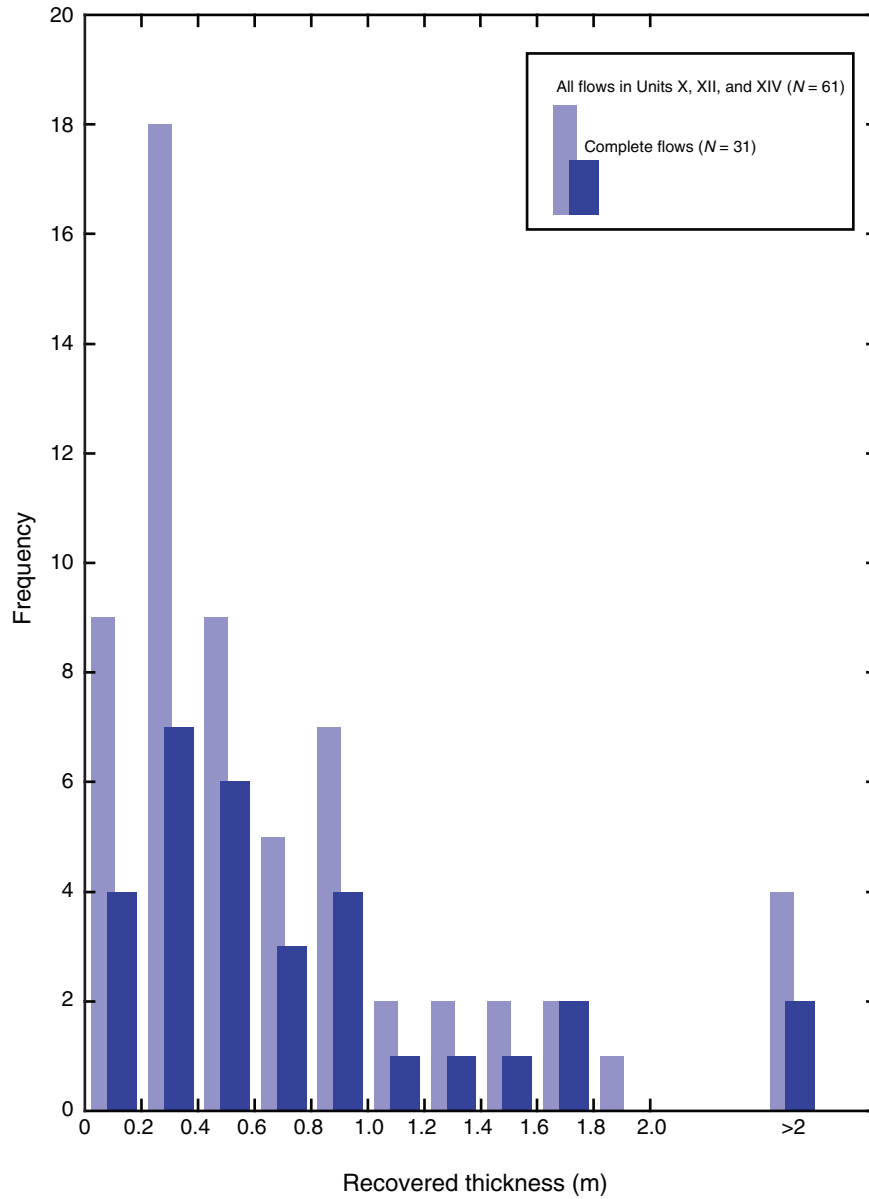


Figure F23. Depth profiles of modal abundances of olivine, clinopyroxene, and plagioclase occurring as either phenocrysts or microphenocrysts, Hole U1347A. Red dotted lines = recovered depths of unit boundaries. Tr = trace of phenocryst phases only, displayed for convenience as -0.5%.

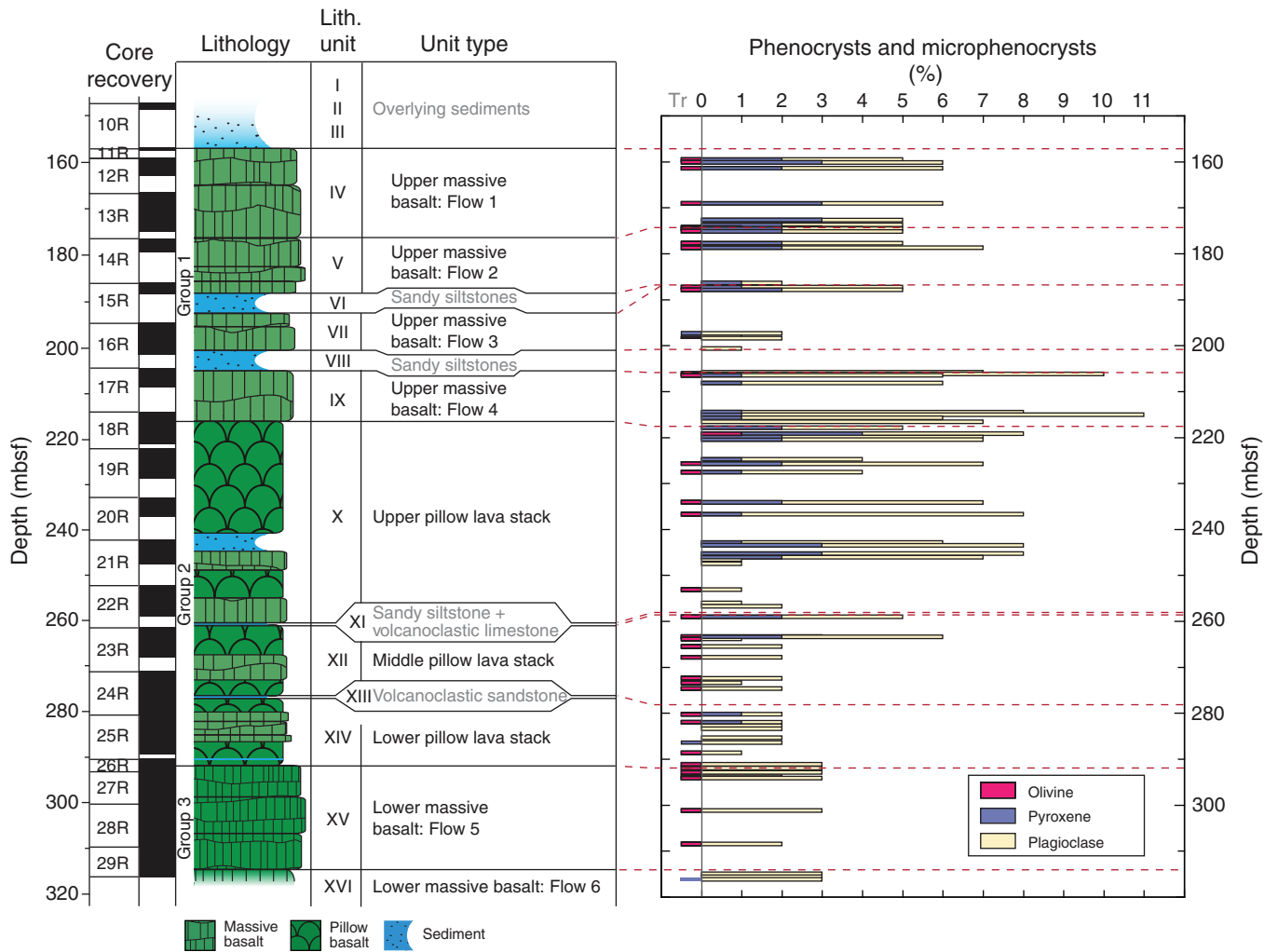


Figure F24. Photomicrographs of thin sections from Flow 3, Hole U1347A. Depths are at tops of thin section intervals. **A.** 187.27 mbsf (Thin Section 84; Sample [324-U1347A-15R-1, 107–109 cm](#)). **B.** 187.71 mbsf (Thin Section 85; Sample [324-U1347A-15R-2, 24–26 cm](#)). **C.** 197.30 mbsf (Thin Section 86; Sample [324-U1347A-16R-2, 100–104 cm](#)). **D.** 198.17 mbsf (Thin Section 87; Sample [324-U1347A-16R-3, 39–42 cm](#)). **E.** 198.31 mbsf (Thin Section 88; Sample [324-U1347A-16R-4, 4–8 cm](#)). **F.** 200.57 mbsf (Thin Section 89; Sample [324-U1347A-16R-5, 99–102 cm](#)). **G.** 201.40 mbsf (Thin Section 90; Sample [324-U1347A-16R-6, 57–60 cm](#)). Plane-polarized light.

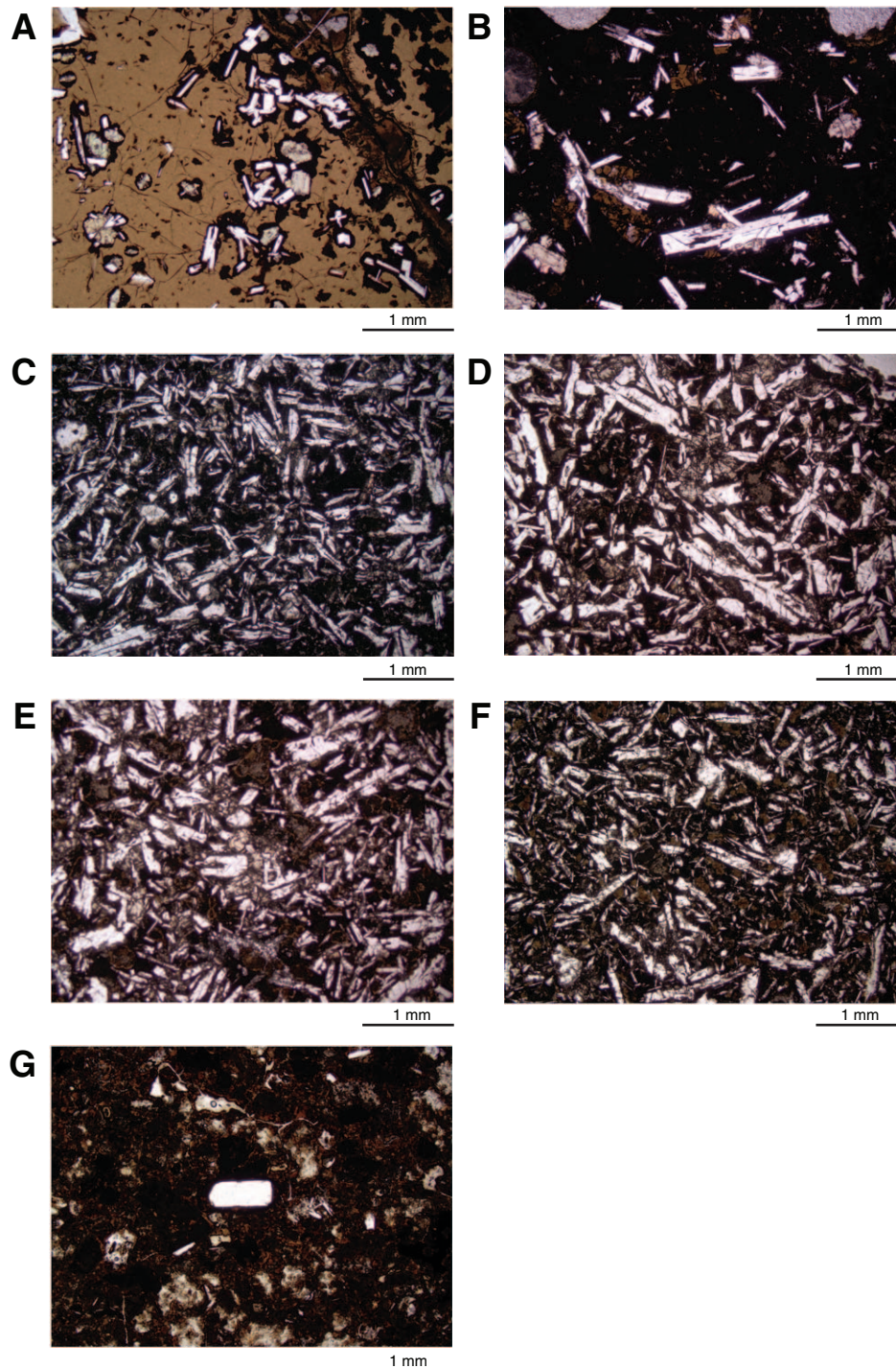


Figure F25. Photomicrographs of thin sections from Flow 5, Hole U1347A. Depths are at tops of thin section intervals. A. 291.78 mbsf (Thin Section 143; Sample [324-U1347A-26R-1, 108–111 cm](#)). B. 292.96 mbsf (Thin Section 144; Sample [324-U1347A-26R-2, 77–78 cm](#)). C. 293.85 mbsf (Thin Section 145; Sample [324-U1347A-27R-1, 45–48 cm](#)). D, E. 294.05 mbsf (Thin Section 146; Sample [324-U1347A-27R-1, 65–67 cm](#)). F. 301.12 mbsf (Thin Section 147; Sample [324-U1347A-28R-1, 72–73 cm](#)). G. 308.48 mbsf (Thin Section 148; Sample [324-U1347A-28R-7, 50–52 cm](#)). Plane-polarized light.

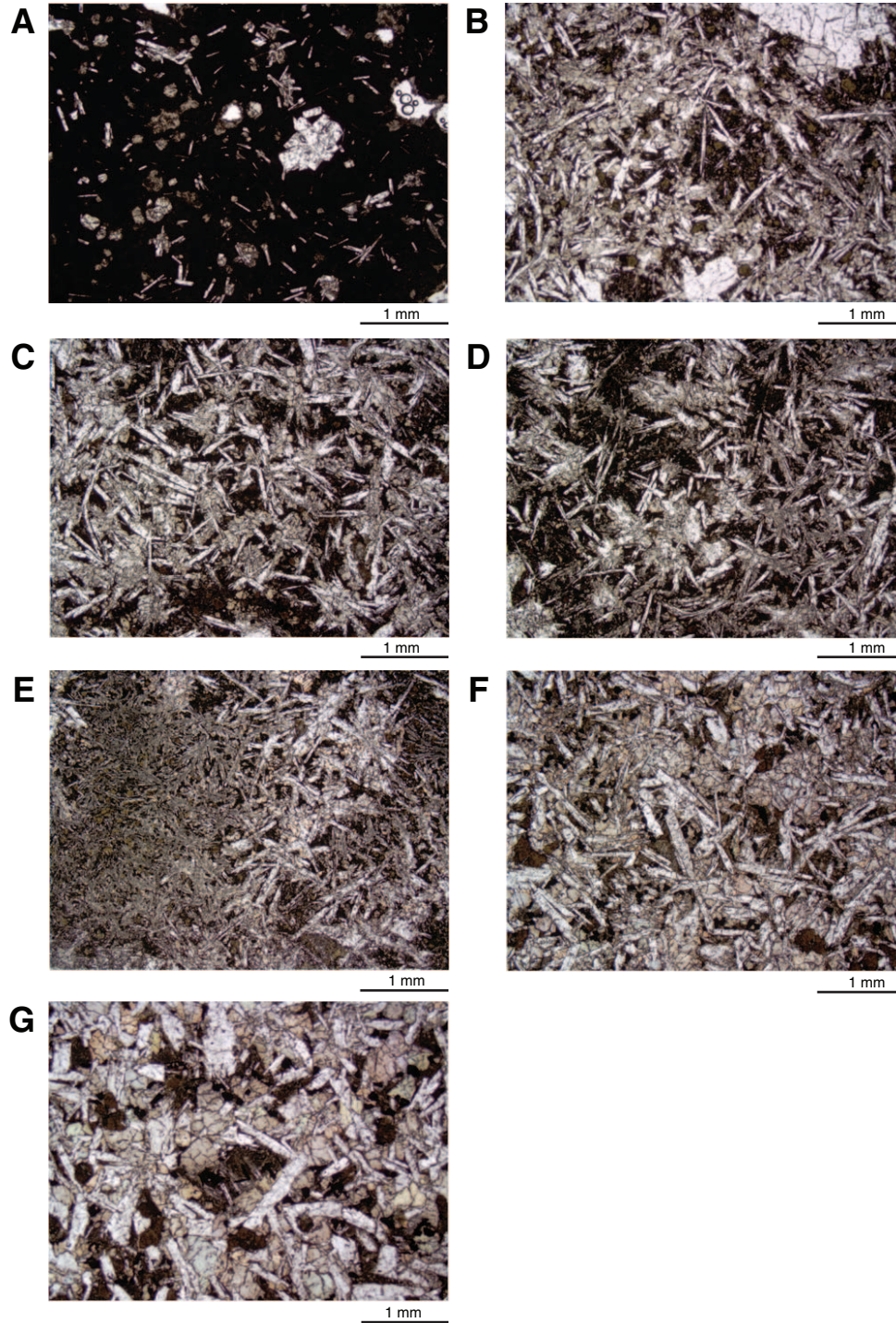


Figure F26. Photomicrographs of glass margins of lava flows showing development of tabular elongate plagioclase and plagioclase-clinopyroxene intergrowths, Hole U1347A. Note development of dark spherulitic coatings to the minerals. Depths are at top of thin section interval. **A.** Top of Flow 2; 174.93 mbsf (Thin Section 78; Sample [324-U1347A-13R-7](#), 69–72 cm). **B.** Top of Flow 4; 206.1 mbsf (Thin Section 93; Sample [324-U1347A-17R-2](#), 27–30 cm). **C.** Near top of the middle pillow stack of Unit XII; 263.64 mbsf (Thin Section 124; Sample [324-U1347A-23R-3](#), 1–4 cm). **D.** Near base of the lower pillow stack of Unit XIV; 291.78 mbsf (Thin Section 143; Sample [324-U1347A-26R-1](#), 108–111 cm). Plane-polarized light.

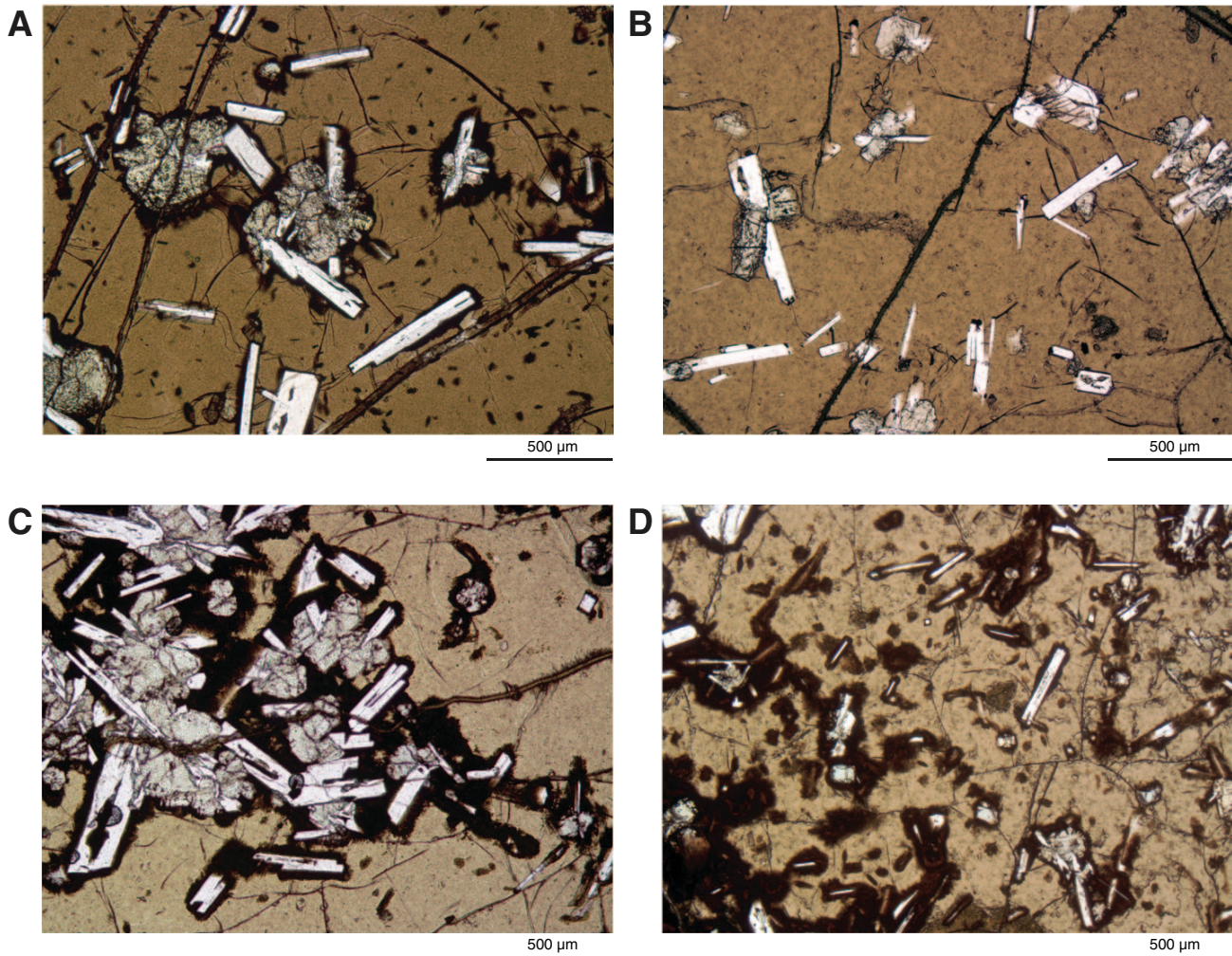


Figure F27. Photomicrographs of olivine pseudomorphs, Hole U1347A. **A.** Pseudomorph located in a spherulitic portion near the margin of Flow 2 and replaced by clays but still showing skeletal morphology; 174.21 mbsf (Thin Section 75; Sample [324-U1347A-13R-6](#), [139–142 cm](#)). **B, C, D.** Flow 2; 187.71 mbsf. In **B**, pseudomorphs are replaced by clays but still show altered glass inclusions (dark circular spots). In **C**, they are intergrown with euhedral plagioclase, partly skeletal, and contain plagioclase in elliptical interior inclusion. In **D**, a broken crystal is replaced by both clay and calcite (white) (Thin Section 85; Sample [324-U1347A-15R-2](#), [24–26 cm](#)). **E.** Relict fresh olivine with single spinel grain. Top of Flow 2; 174.93 mbsf (Thin Section 78; Sample [324-U1347A-13R-7](#), [69–72 cm](#)). Plane-polarized light.

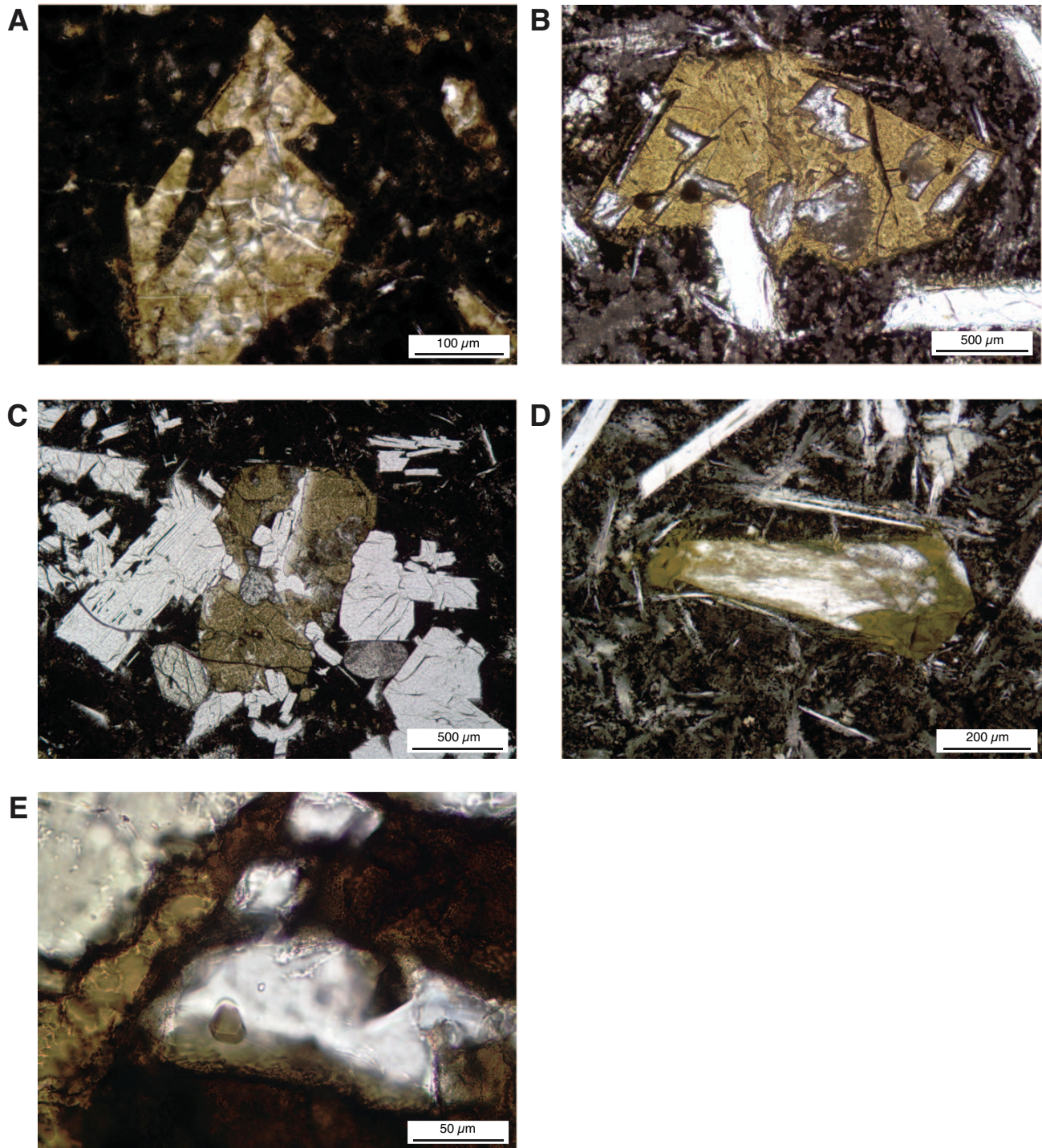


Figure F28. Photomicrographs of plagioclase phenocrysts and glomerocrysts, Hole U1347A. Depths are at tops of thin section intervals. **A.** Tabular plagioclase with devitrified inclusions parallel to C-axis that is broken on the lower side of the crystal. Flow 3; 198.31 mbsf (Thin Section 88; Sample [324-U1347A-16R-4, 4–8 cm](#)). **B.** Plagioclase synneusis-twin aggregate. Flow 1; 169.05 mbsf (Thin Section 72; Sample [324-U1347A-13R-2, 56–59 cm](#)). **C, E, F.** In **C**, a multicrystal aggregate has devitrified inclusions and oscillatory and normal zoning. In **E**, large plagioclase glomerocryst can be seen. **F** contains a detail of plagioclase with interior skeletal inclusions and oscillatory zoning in the lower right corner of **E**. Flow 4; 214.42 mbsf (Thin Sample 96; Sample [324-U1347A-18R-1, 42–43 cm](#)). **D.** Large irregular multicrystal plagioclase glomerocryst with devitrified inclusions occurring in volcanic glass. Top of Flow 4; 205.92 mbsf (Thin Section 92; Sample [324-U1347A-17R-2, 9–11 cm](#)). **D** is under plane-polarized light; all others are under cross-polarized light.

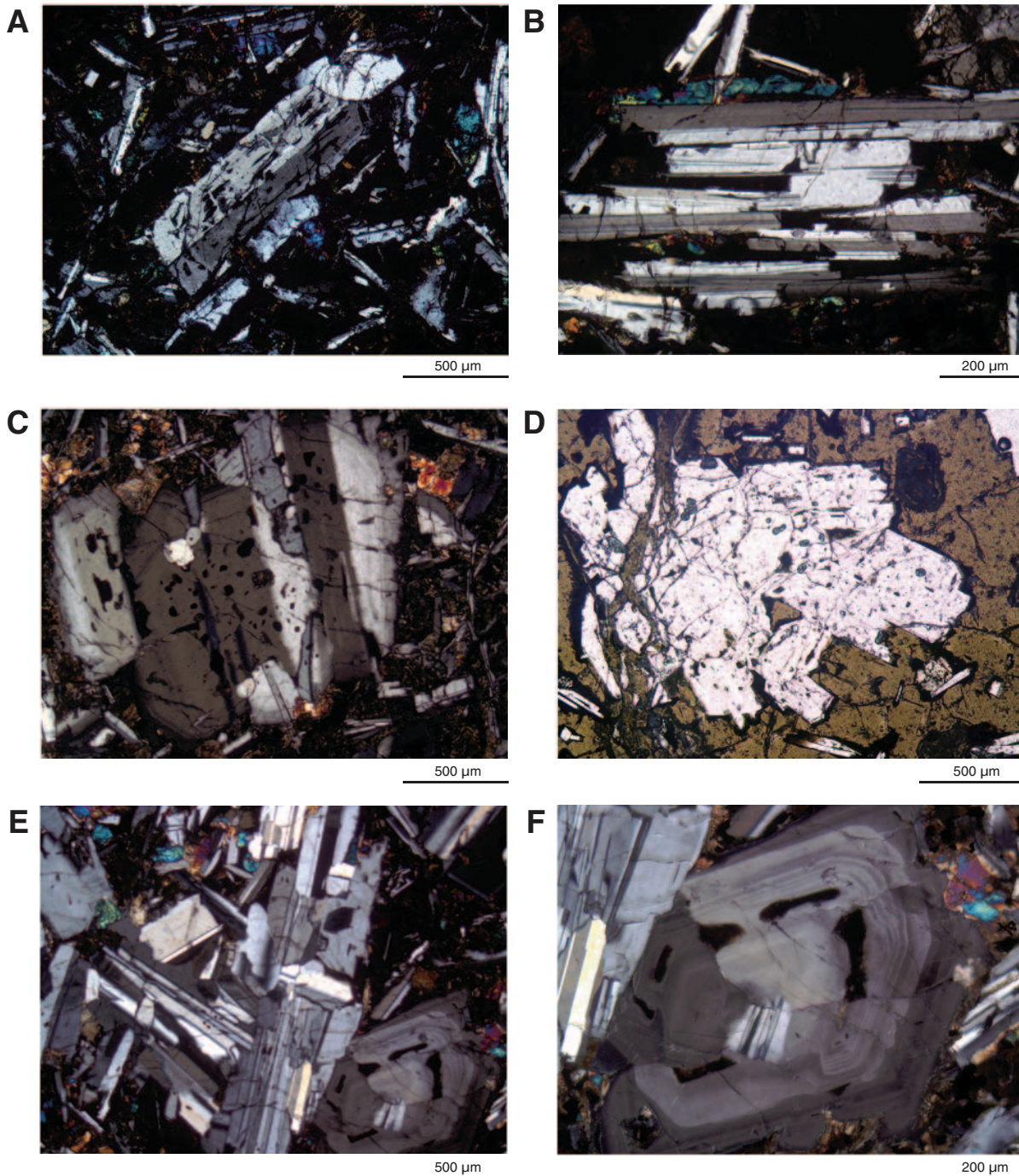


Figure F29. Composite photomicrograph of large plagioclase glomerocryst with a complex history of tabular crystal growth, attachment of other crystals, formation of a mantle with devitrified inclusions, and oscillatory and normal zoning surrounding the entire aggregate, Hole U1347A. Flow 4; 214.93 mbsf (top of the thin section interval) (Thin Section 99; Sample [324-U1347A-18R-1, 93–96 cm](#)).

500 μm

Figure F30. Photomicrographs of melt inclusions in a single large plagioclase glomerocryst, itself occurring in volcanic glass, Hole U1347A. Top of Flow 4; 206.10 mbsf (top of the thin section interval) (Thin Section 93; Sample [324-U1347A-17R-2, 27–30 cm](#)). **A.** Distribution of pale brown glass inclusions in glomerocryst. Plane-polarized light. **B.** Same view as A, but in cross-polarized light to show the full aggregate of crystals. **C.** Detail of the central portion of the glomerocryst, showing crystal-parallel and crystal-edge glass inclusions. **D.** Same as C, but in reflected light, to show polished surfaces of unaltered glass inclusions.

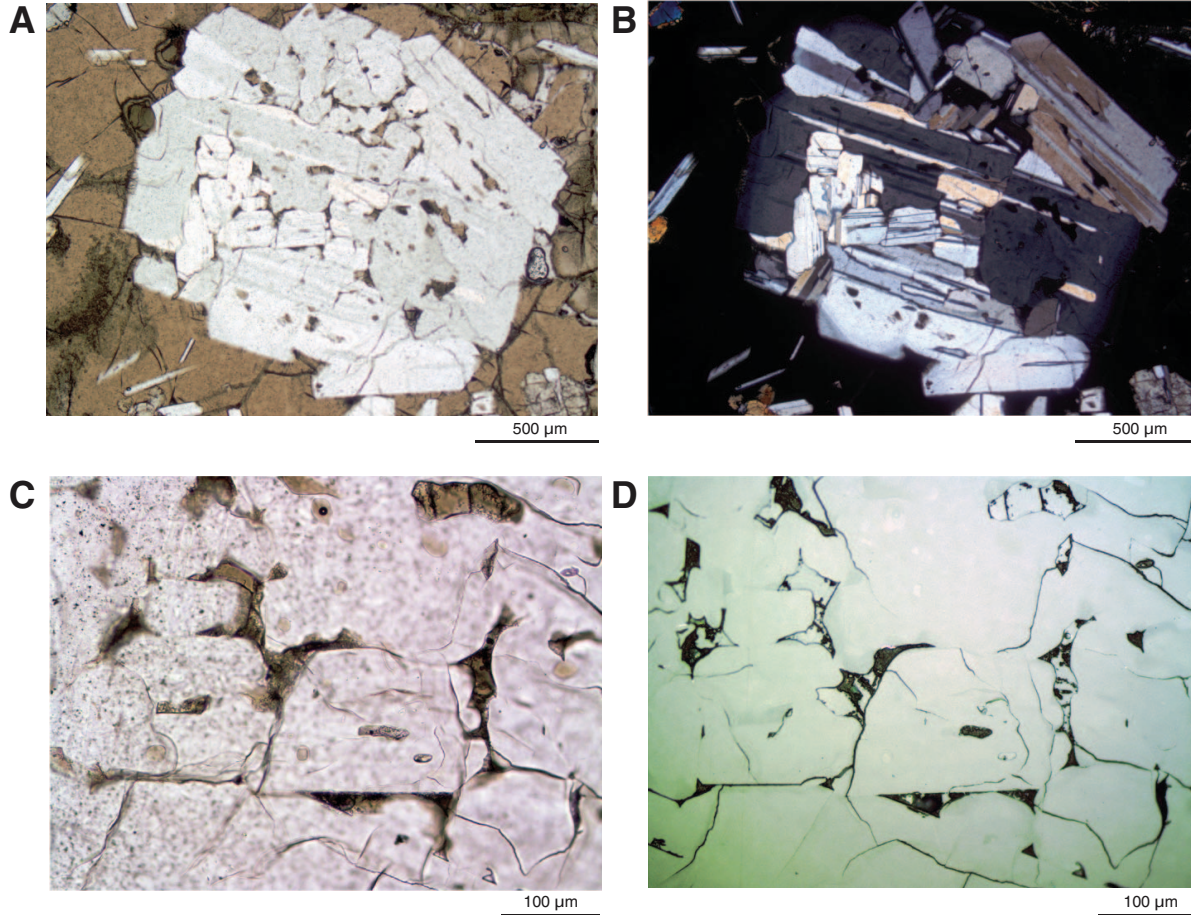


Figure F31. Photomicrographs of crystal morphologies of clinopyroxene, Hole U1347A. Depths are at tops of thin section intervals. **A.** Typical plagioclase-clinopyroxene intergrowth set in glass. Flow 2; 174.58 mbsf (Thin Section 81; Sample [324-U1347A-13R-7, 34–37 cm](#)). **B.** Clinopyroxene (blue~green) intergrown with skeletal plagioclase (white and gray) in glass. Top of Flow 4; 205.92 mbsf (Thin Section 92; Sample [324-U1347A-17R-2, 9–11 cm](#)). **C.** Incipient network of intergrown plagioclase and clinopyroxene set in the spherulitic portion of a pillow margin. Base of lower pillow stack of Unit XIV; 291.78 mbsf (Thin Section 143; Sample [324-U1347A-26R-1, 106–111 cm](#)). **D.** Somewhat coarser plagioclase-clinopyroxene intergrowth from a pillow interior. Middle pillow stack of Unit XII; 272.37 mbsf (Thin Section 128; Sample [324-U1347A-24R-1, 77–79 cm](#)). **E.** Plagioclase-clinopyroxene glomerocryst containing broken plagioclase crystals. Middle of Flow 1; 169.05 mbsf (Thin Section 72; Sample [324-U1347A-13R-2, 56–59 cm](#)). **F.** Euhedral clinopyroxene phenocryst wrapping around plagioclase. Top of Flow 4; 206.10 mbsf (Thin Section 93; Sample [324-U1347A-17R-2, 27–30 cm](#)). **G.** Euhedral clinopyroxene intergrown with another clinopyroxene set in glass. Top of Flow 2; 174.58 mbsf (Thin Section 81; Sample [324-U1347A-13R-7, 34–37 cm](#)). A, C, and D are under plane-polarized light; B and E–G are under cross-polarized light. (**Figure shown on next page.**)

Figure F31 (continued). (Caption shown on previous page.)

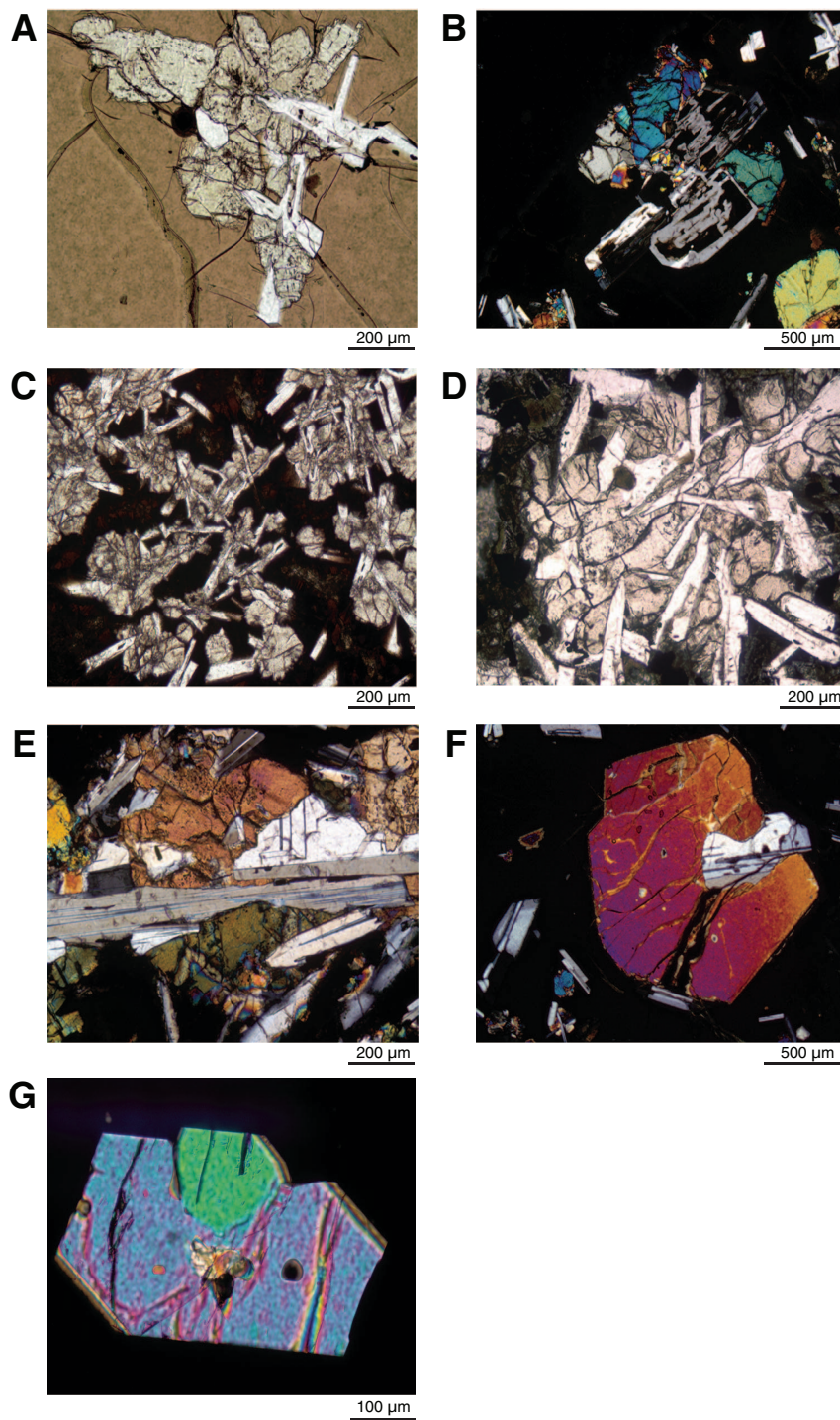


Figure F32. Photomicrographs of crystallization of titanomagnetite, Hole U1347A. Depths are at tops of thin section intervals. **A, B.** Different spherulitic portions of the pillow margin, both showing details of fibrous spherulites that nucleated on tabular and acicular plagioclase crystals (gray). Light-colored needles are clinopyroxene dendrites; darker curving or branching needles are plagioclase. Strongly reflective specks of titanomagnetite are visible in B, which has larger fibrous needles (further into flow interior) but not in A. Top of Flow 2; 174.93 mbsf (Thin Section 78; Sample [324-U1347A-13R-7, 69–72 cm](#)). **C.** Very fine grained matrix, dotted with titanomagnetite. Orange-colored species are altered interstitial glass with no titanomagnetite. Bottom of Flow 1; 174.21 mbsf (Thin Section 75; Sample [324-U1347A-13R-6, 139–142 cm](#)). **D.** Reflective titanomagnetite (white) in a segregation vesicle. Gray crystals are plagioclase. Dark area is altered and nonreflective. Lower pillow stack of Unit XIV; 281.25 mbsf (Thin Section 135; Sample [324-U1347A-25R-1, 5–9 cm](#)). **E.** Elongate skeletal titanomagnetite (white) projecting from intergrown plagioclase and clinopyroxene (light gray), at upper left, toward intersertal patches (nonreflective, dark gray), at lower right. Flow 3; 197.3 mbsf (Thin Section 86; Sample [324-U1347A-16R-2, 100–104 cm](#)). **F.** Skeletal titanomagnetite (white), mainly at edges of intergrowths of clinopyroxene (light gray) and acicular plagioclase (darker gray), next to altered intersertal patches (dark brown and black and nonreflective). Interior of Flow 1; 161.34 mbsf (Thin Section 71; Sample [324-U1347A-12R-2, 40–42 cm](#)). **G.** High-magnification image of skeletal titanomagnetite, partly altered and pitted and intergrown with plagioclase. Interior of Flow 3; 200.57 mbsf (Thin Section 89; Sample [324-U1347A-16R-5, 99–108 cm](#)). **H.** Thin lens of an unaltered glass inclusion dished out against plagioclase lying beneath and thinned to enable viewing of trellislike titanomagnetite (black) and dendritic clinopyroxene (sprays of smaller crystals). Top of Flow 1; 159.62 mbsf (Thin Section 69; Sample [324-U1347A-12R-1, 2–5 cm](#)). C and H are under transmitted light; A, B, and D–G are under reflected light. (**Figure shown on next page.**)

Figure F32 (continued). (Caption shown on previous page.)

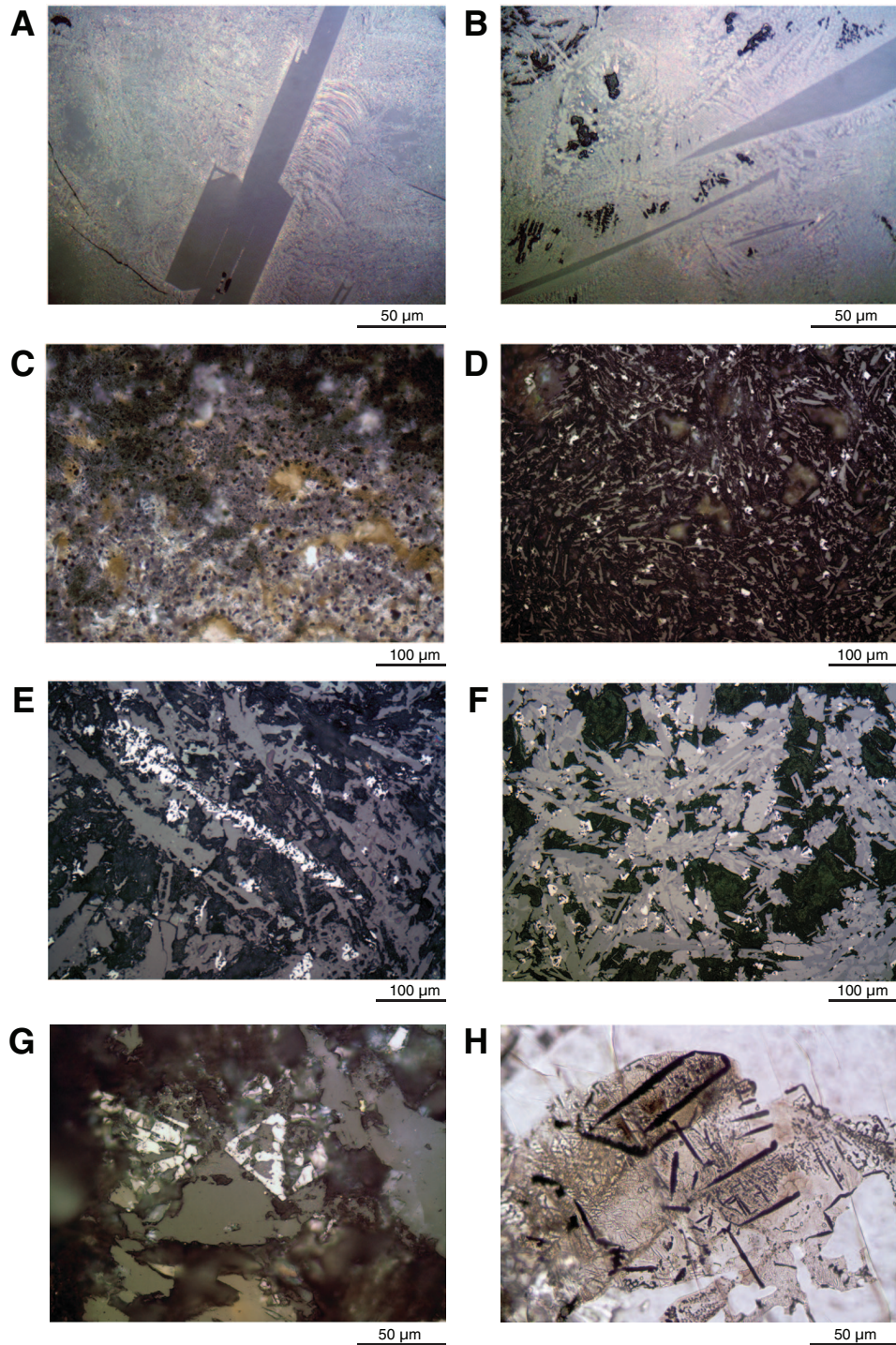


Figure F33. Whole-round physical property data summary, Hole U1347A. Light blue areas = sedimentary intervals, light green areas = pillow lava units, unshaded areas = massive igneous flows. Note the offset between data and lithologic column. This is because the log is based on downhole logging data, resulting in offsets with recovered core, which corresponds to the curated depths (see “[Igneous petrology](#)” and “[Downhole Logging](#)”). For example, the recovered length of sedimentary Unit VI is only 0.5 m, whereas the logging data shows that the unit is 4.5 m thick. For detailed treatment of lithologic units and their relationship to logging data, see Figure F15. For details of filtering protocols, see “[Physical properties](#)” in the “Methods” chapter. MS = magnetic susceptibility, GRA = gamma ray attenuation, NGR = natural gamma radiation.

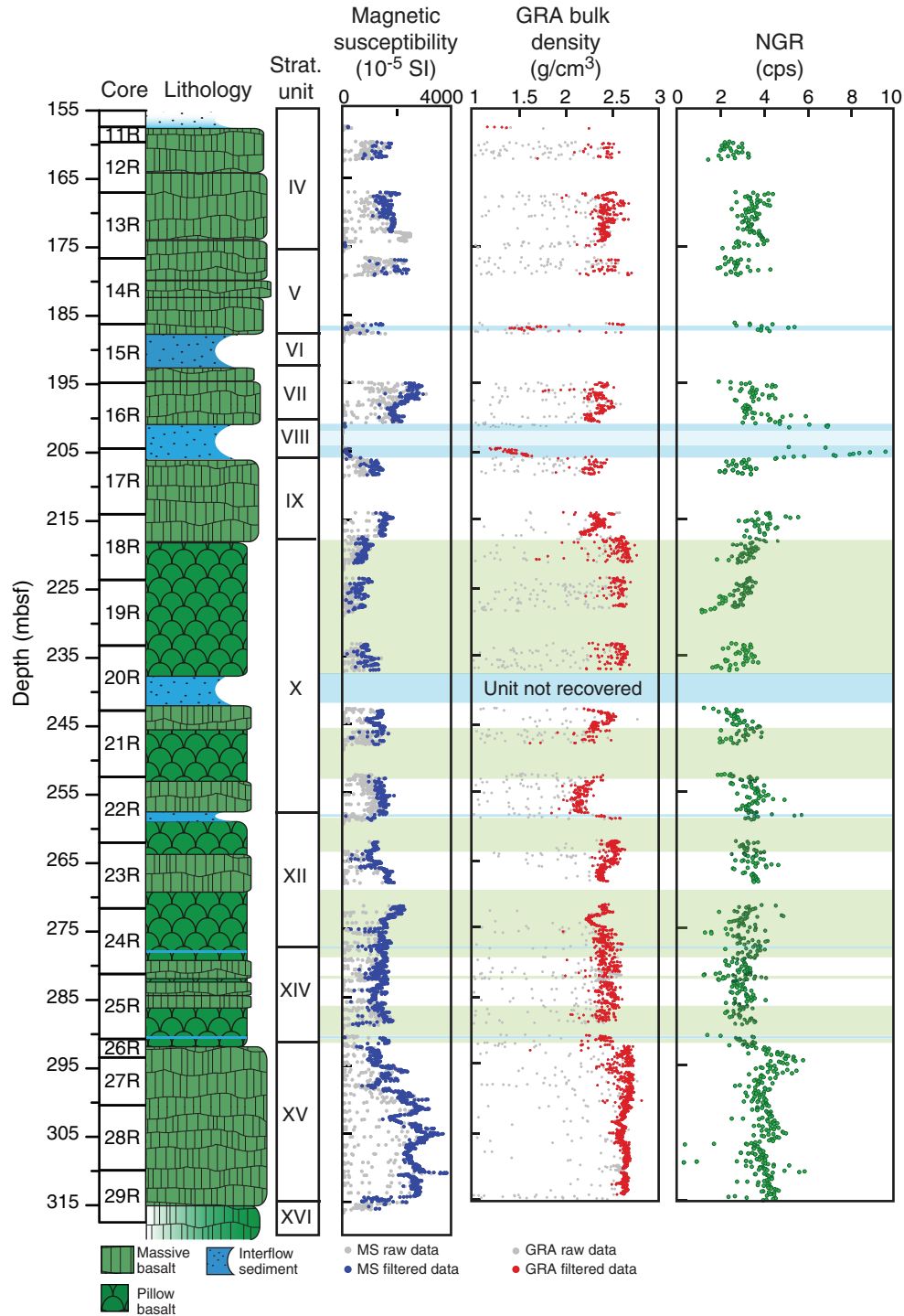


Figure F34. Downhole variations of alteration degree, presence of fresh glass, vein thickness, vein mineralogy, and pyrite occurrences, Hole U1347A. Lithology is from “**Igneous petrology**” and is a schematic representation of stratigraphic units based on a compilation of visual core descriptions and logging data. In the alteration intensity column, gaps are representative of intervals where cores were not recovered. Percentage of glass preserved indicates fresh glass at pillow and sheet flow margins. Pyrite occurrences in

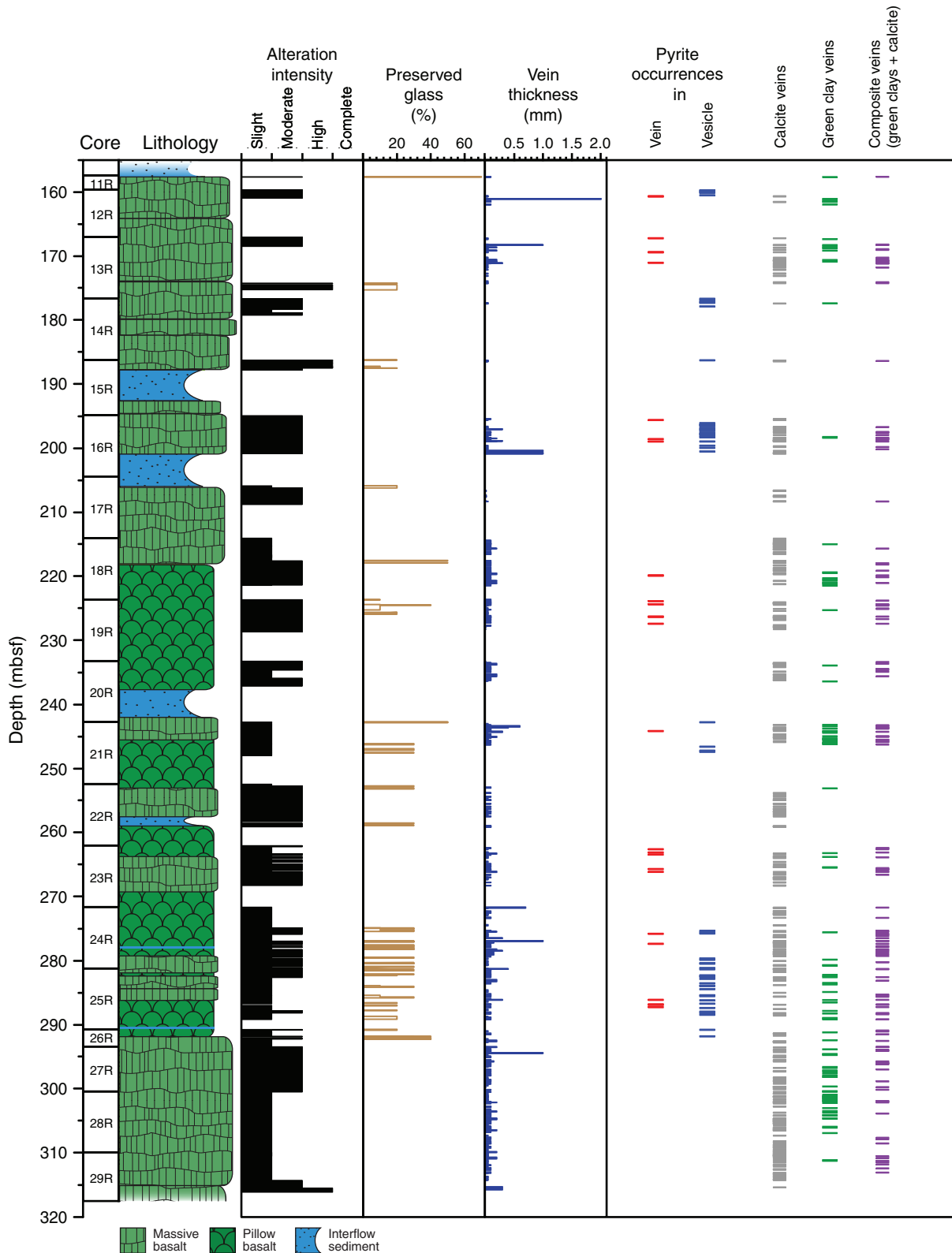


Figure F35. Photomicrograph of altered plagioclase (30%) and altered pyroxene (40%) surrounded by nonreflective altered glass in (A) plane-polarized light, (B) crossed-polarized light, and (C) reflected light, Hole U1347A (Thin Section 94; Sample [324-U1347A-17R-2](#), 48–50 cm). Plagioclase and pyroxene crystals have been partially altered to nonreflective clays.

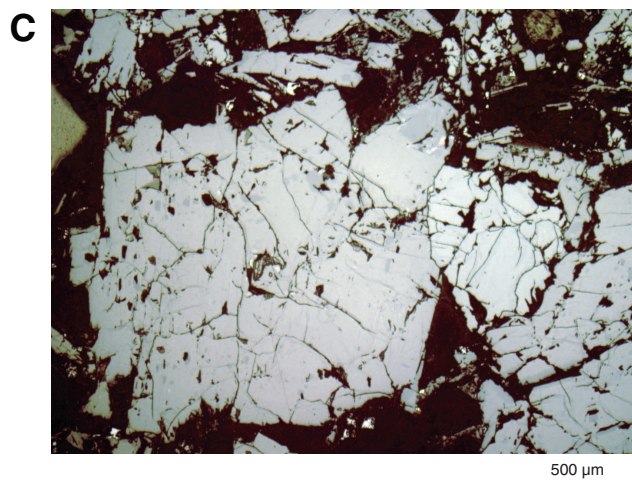
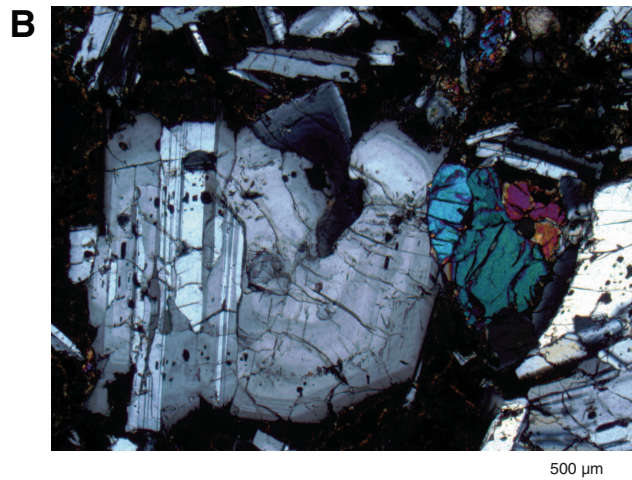


Figure F36. Photomicrograph of olivine phenocryst pseudomorphed by calcite and brown clays, Hole U1347A (Thin Section 72; Sample 324-U1347A-13R-2, 56–59 cm). Cross-polarized light.

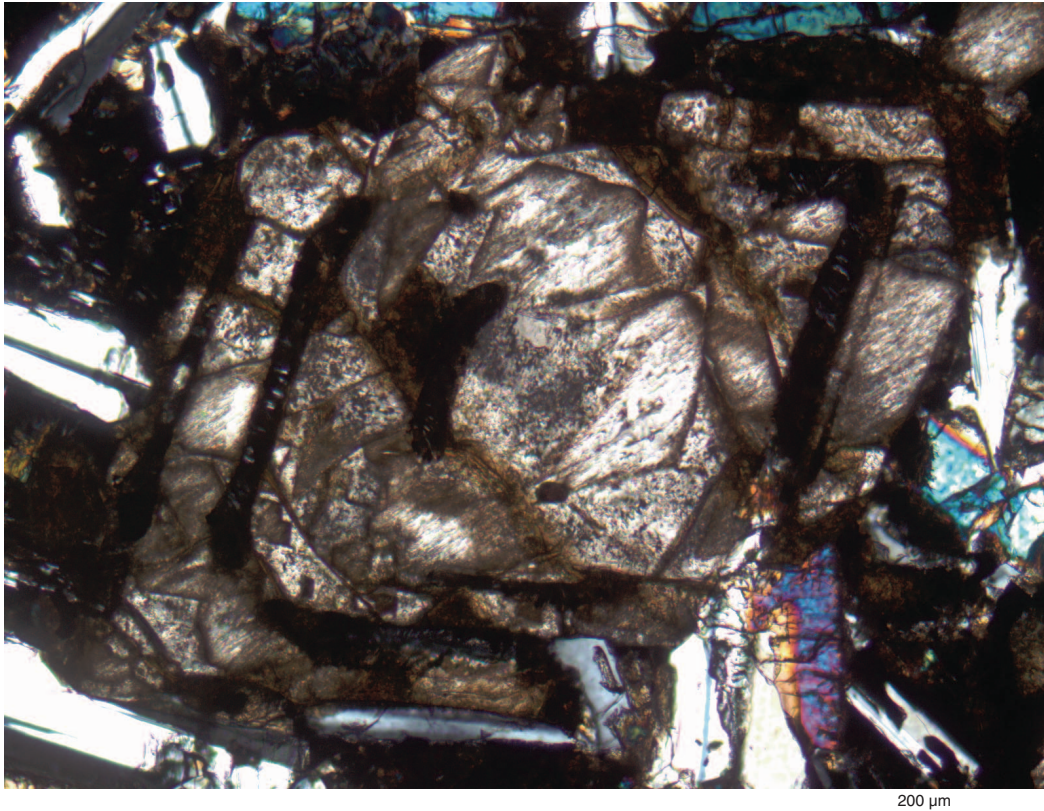
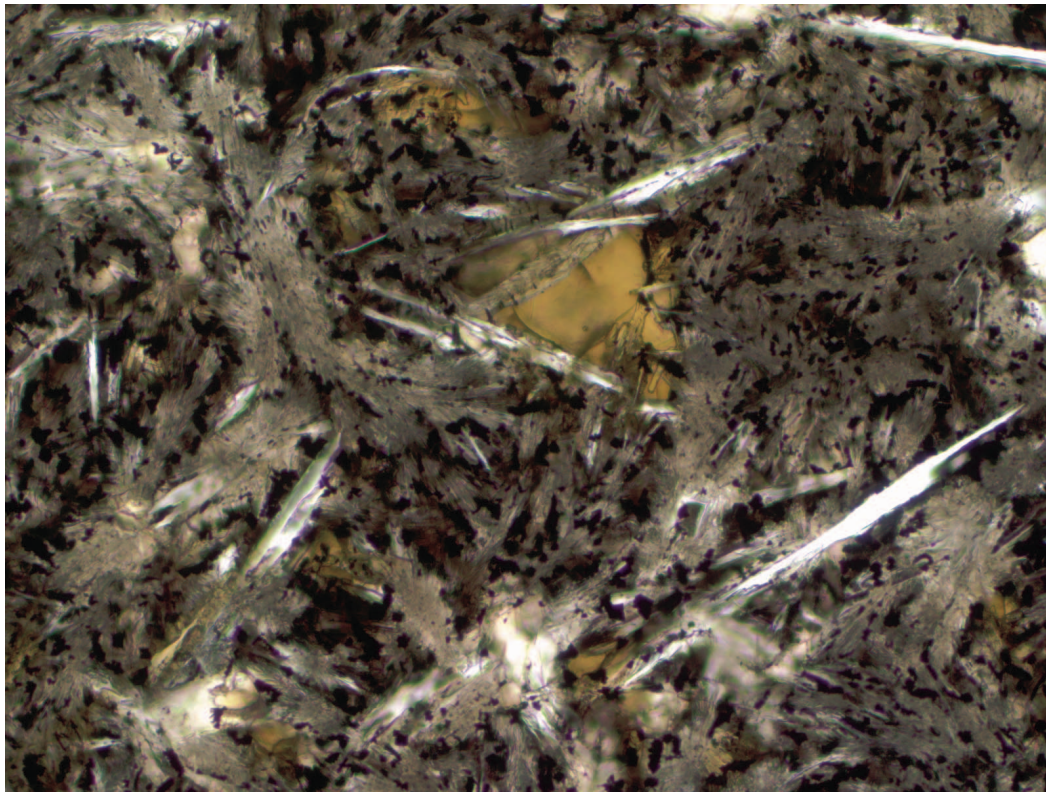


Figure F37. Photomicrograph of relics of brown glass in basalt now altered to nonreflective clays, Hole U1347A (Thin Section 85; Sample 324-U1347A-15R-2, 24–26 cm). Plane-polarized light.



100 μ m

Figure F38. Photomicrograph of light brown fresh glass altered to dark brown palagonite along veins and vesicles at pillow margin, Hole U1347A (Thin Section 124; Sample 324-U1347A-23R-3, 1–4 cm). Plane-polarized light.

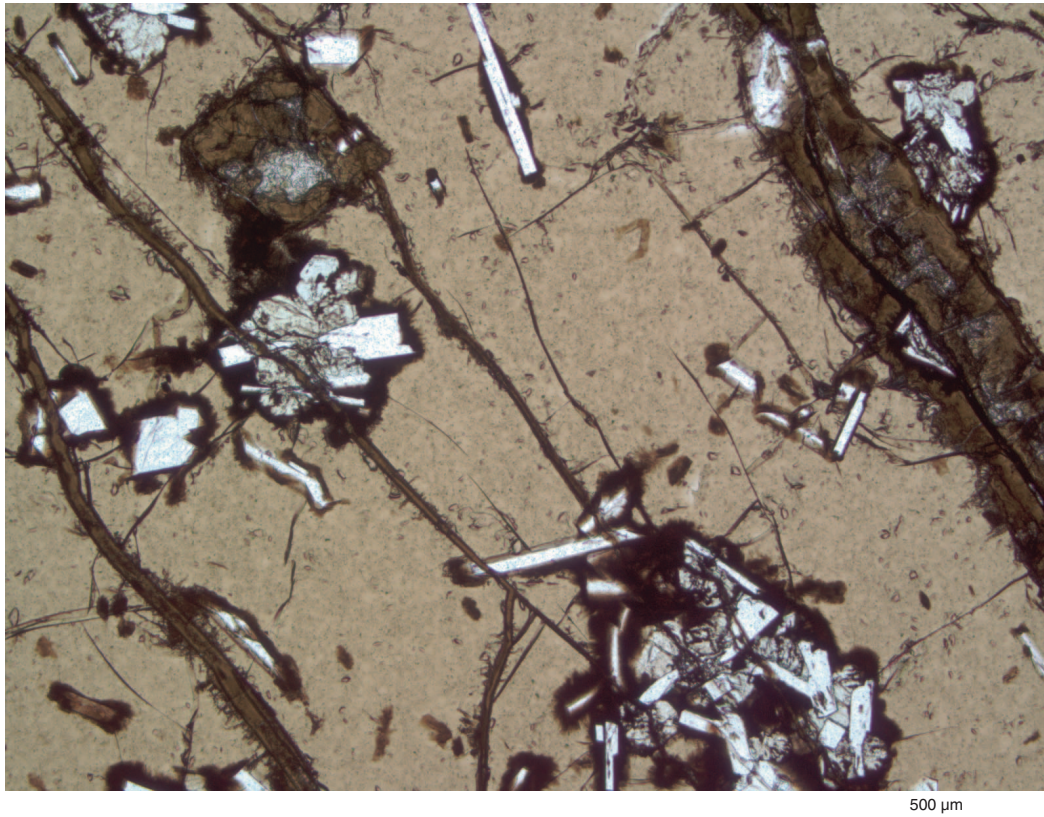


Figure F39. A. Photograph of black soft rind along the margin of a pillow (red box), Hole U1347A (Sample 324-U1347A-15R-1, 122–127 cm). B. X-ray diffraction pattern indicating that the black soft rind is composed of a mixture of clays (i.e., montmorillonite and nontronite).

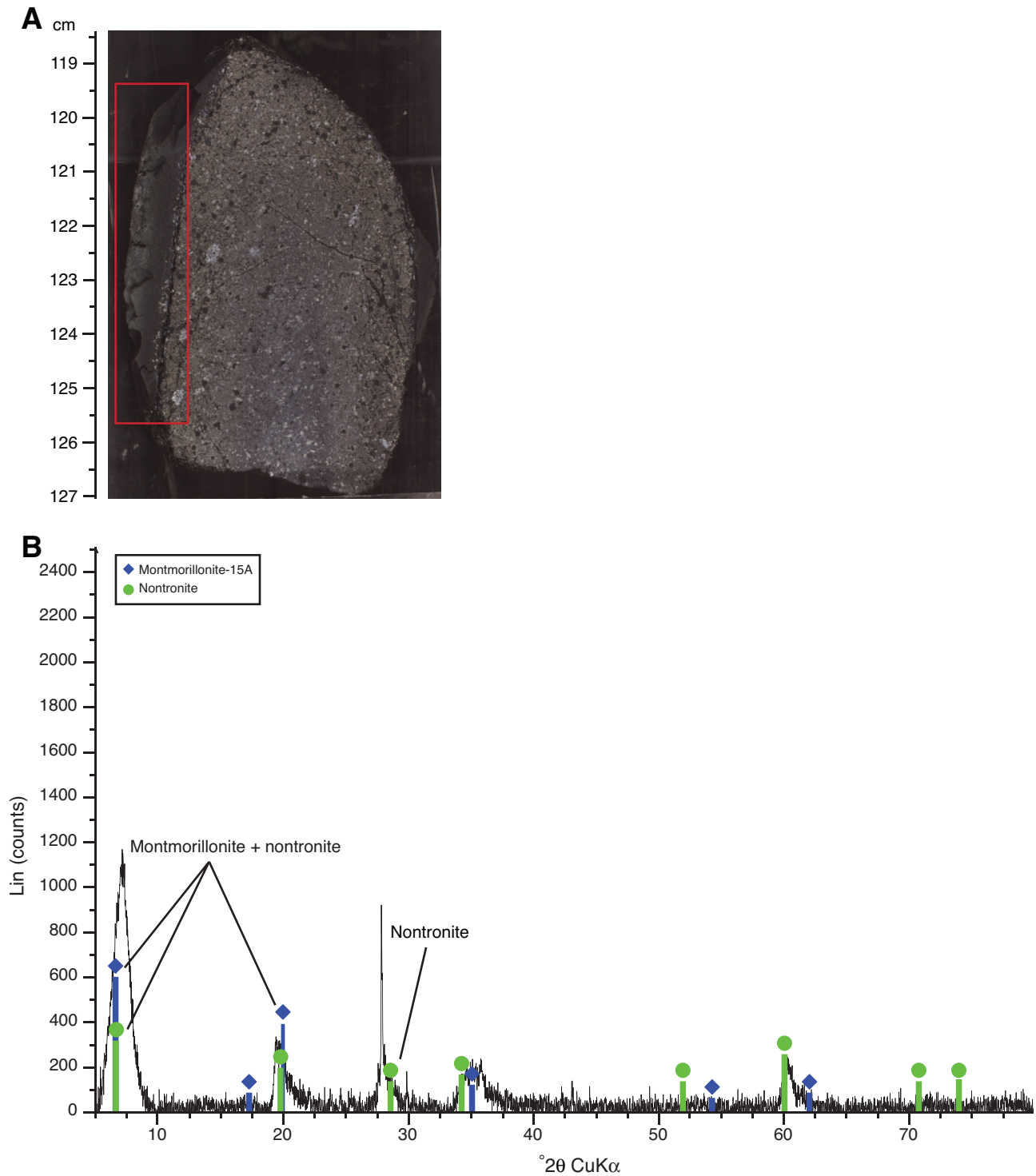


Figure F40. X-ray diffraction (XRD) pattern for clay minerals separated from vesicles, Hole U1347A (Sample 324-U1347A-23R-5, 12–16 cm). The peak, ranging from $26^{\circ}2\theta$ to $28^{\circ}2\theta$, corresponds to anorthite. The remaining peaks fit the XRD patterns for both saponite and nontronite. Based on thin section observations, clay mineral is most likely saponite.

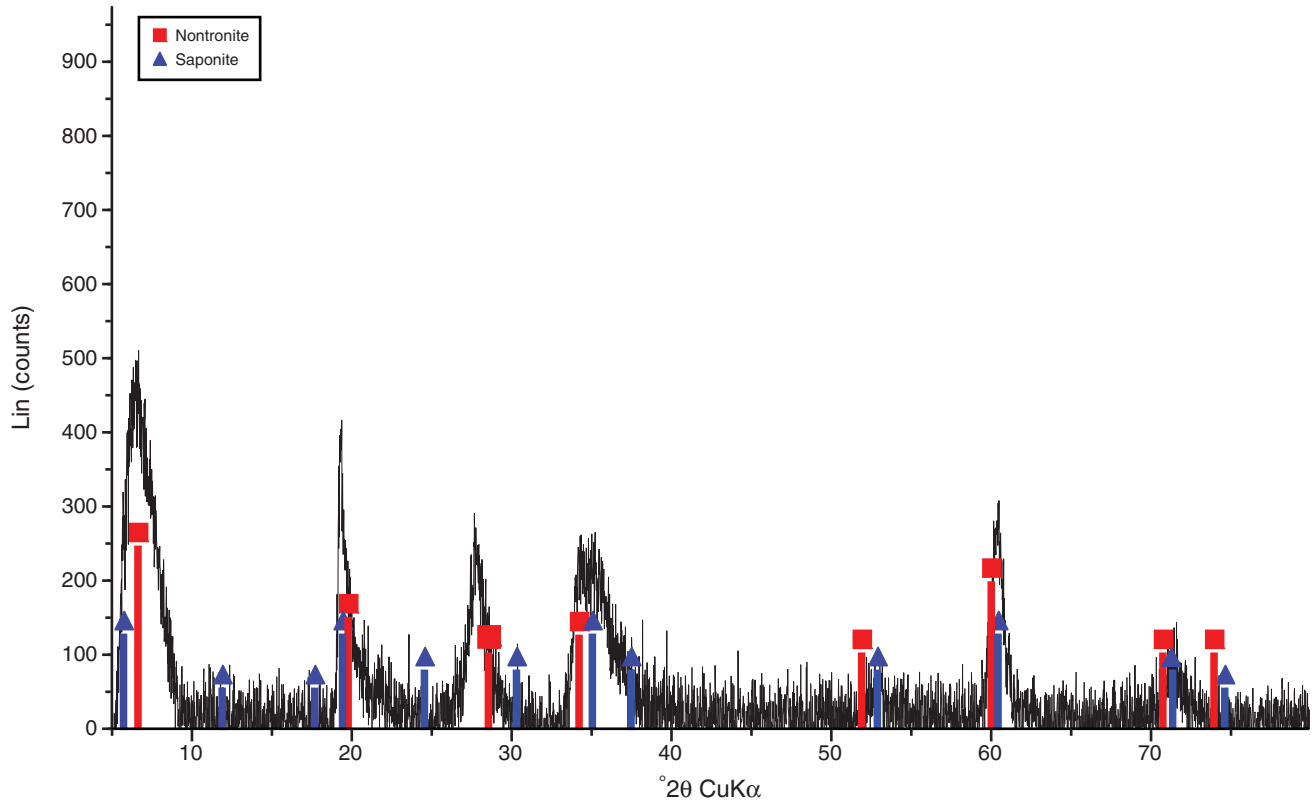


Figure F41. A. Photomicrograph of grayish green clay and golden brown pyrite partially filling a vesicle, Hole U1347A (Thin Section 79; Sample [324-U1347A-14R-1, 108–110 cm](#)). Combined plane-polarized and reflected light. B. Close-up photograph of a vesicle lined with dark green clay and pyrite and filled with calcite (Sample [324-U1347A-12R-1, 30–31 cm](#)). C. Segregation melt altered to dark brown clays and opaques around a brown clay vesicle (Thin Section 127; Sample [324-U1347A-23R-6, 95–96 cm](#)). Plane-polarized light. D. Calcite with radial growth patterns in a vesicle (Thin Section 95; Sample [324-U1347A-17R-3, 65–67 cm](#)). Cross-polarized light.

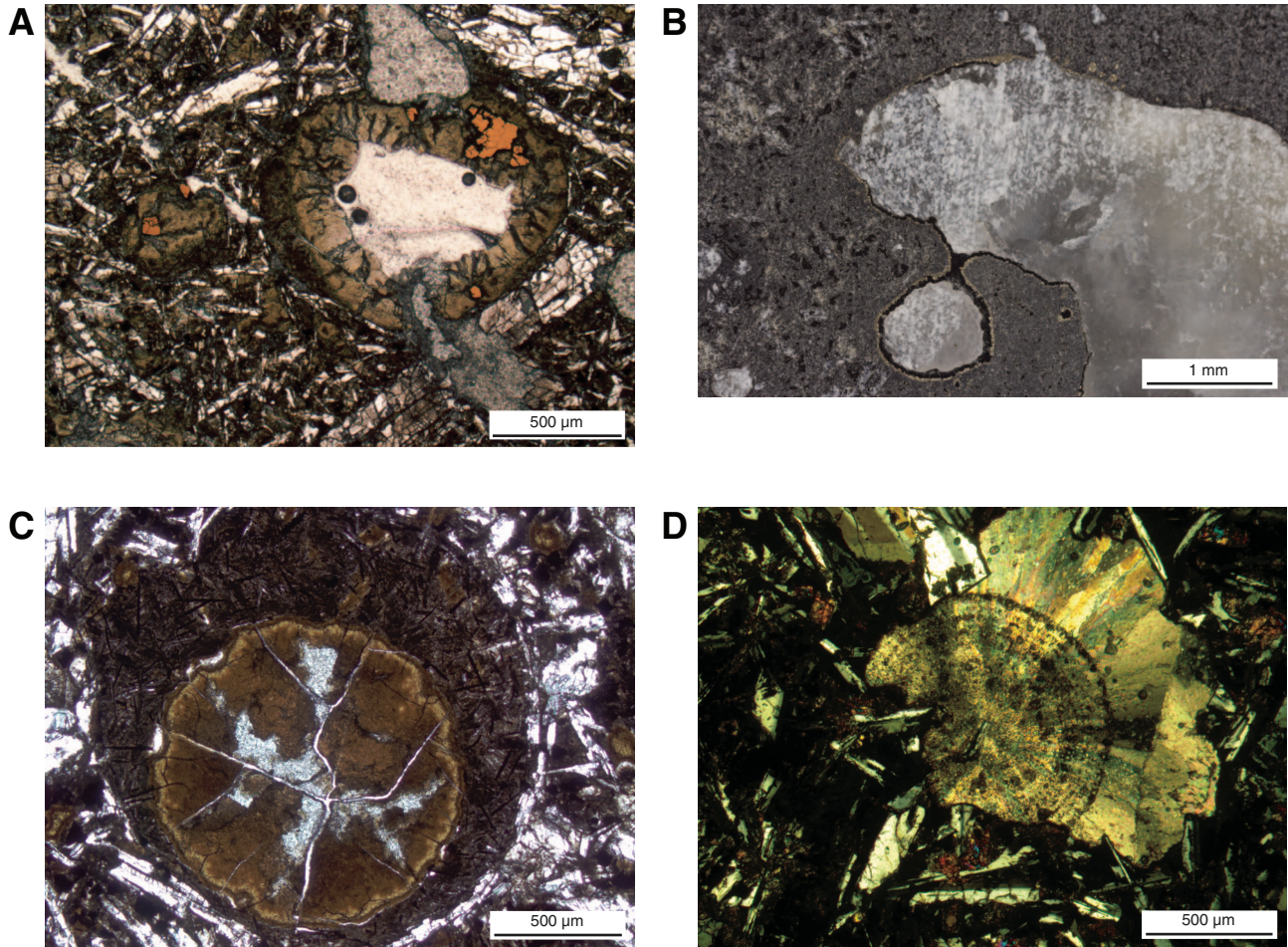


Figure F42. Photomicrograph of a vein containing pyrite, Hole U1347A (Thin Section 104; Sample 324-U1347A-18R-4, 106–107 cm). Continuation of vein contains calcite and gray clay. Reflected light.

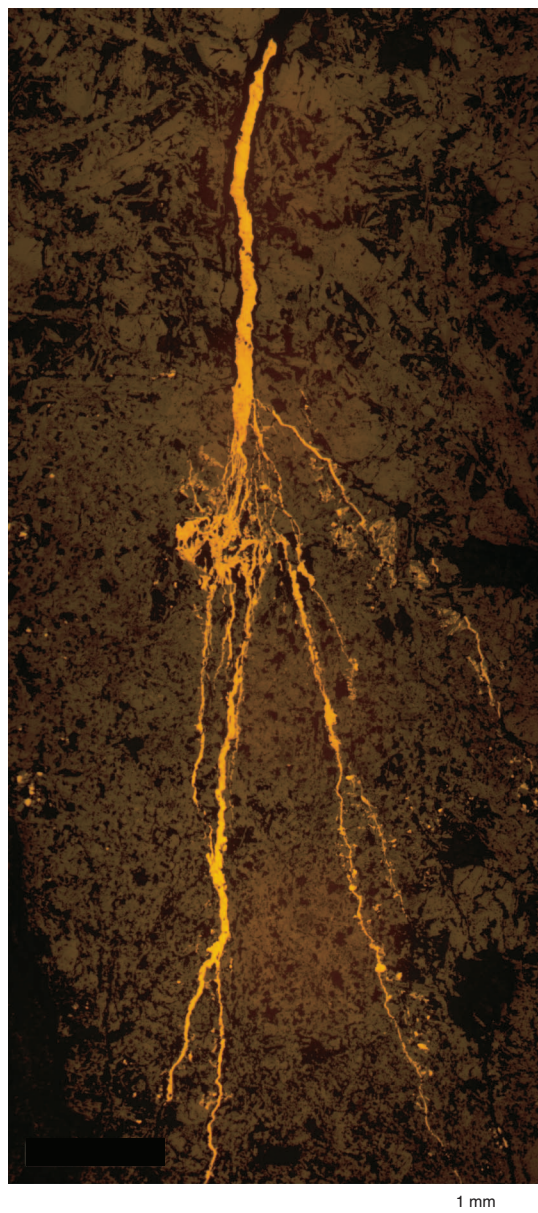


Figure F43. Description and core photographs of sheet flow three-part structure, Hole U1347 (Sections 324-U1347A-16R-1 through 16R-5).

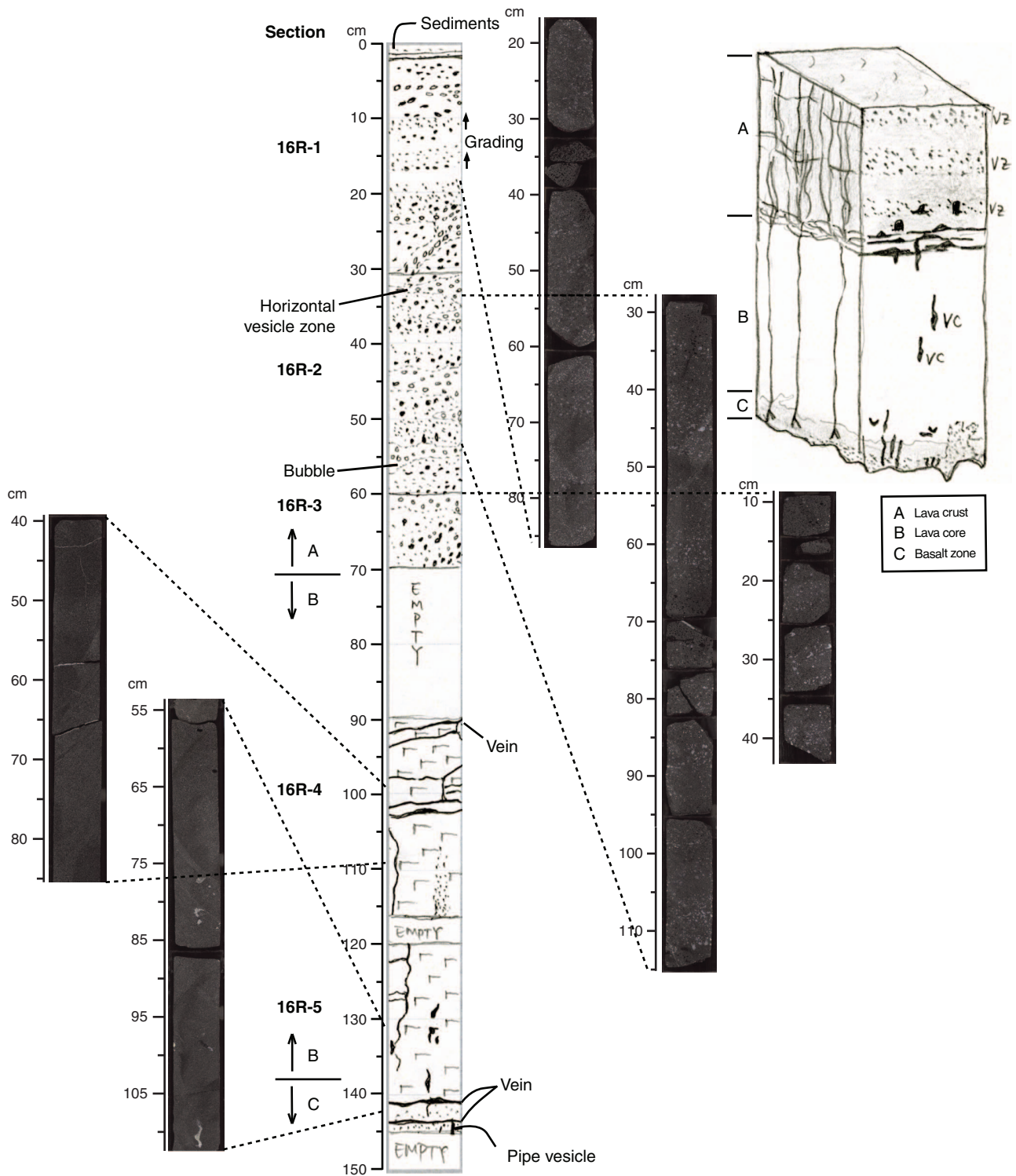


Figure F44. Description and core photographs of pillow lava structures showing stacked pillow lavas (10–50 cm in diameter) and concentric chilled margins with no radial cracking, no concentric vesicular zones, and no radially aligned vesicles, Hole U1347A (Sections 324-U1347A-19R-1 through 20R-1).

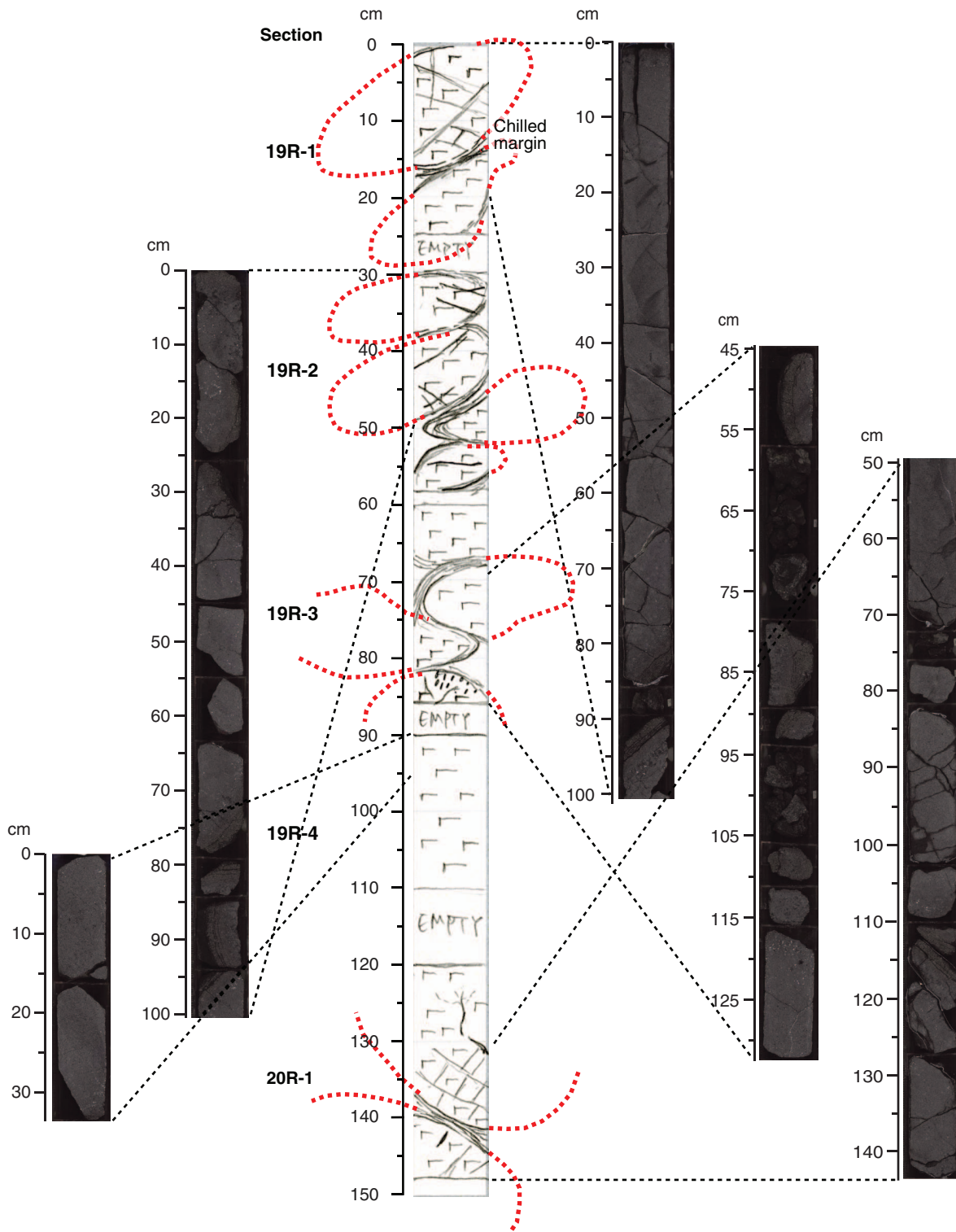


Figure F45. Core image of pillow lava with typical chilled margin, Hole U1347A (interval 324-U1347A-21R-4, 94–104 cm).

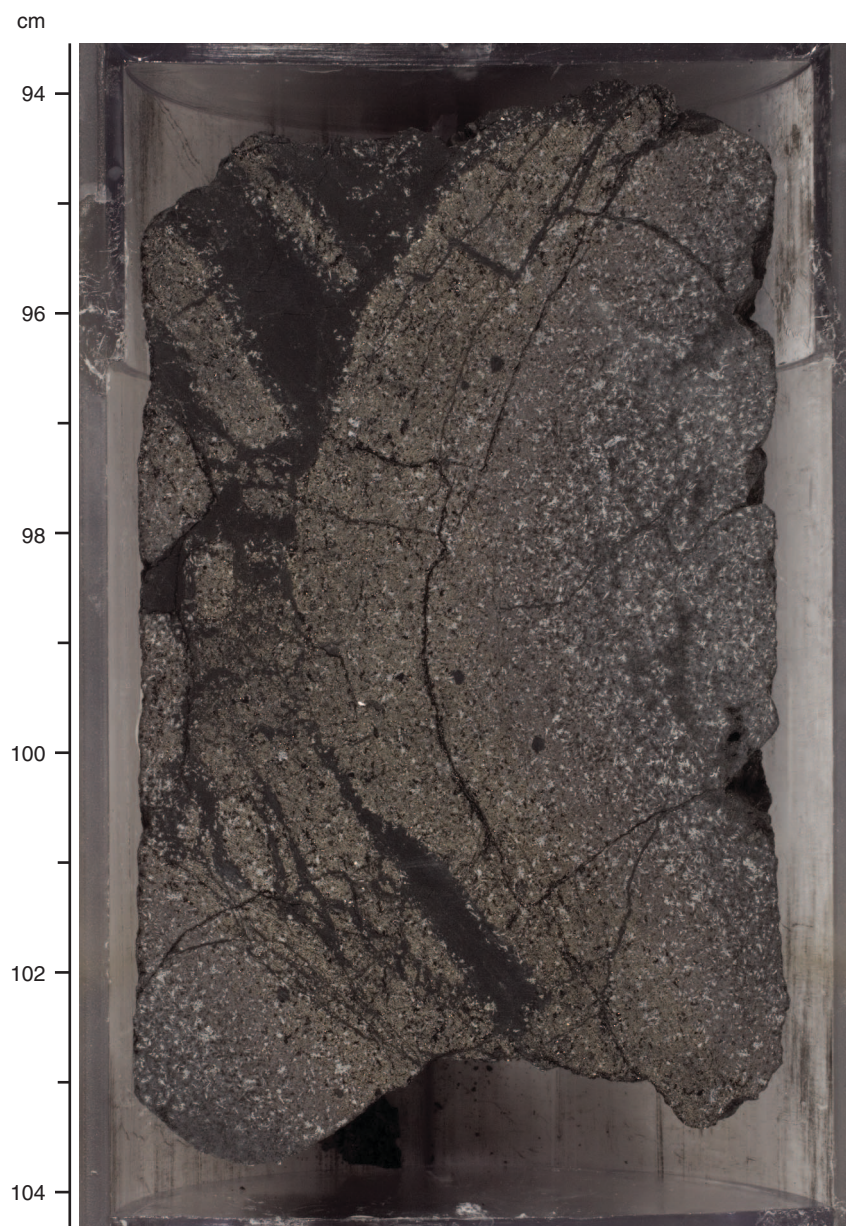


Figure F46. Core image of slickenlines on fault plane surfaces (slickenside) with observed, oriented fiber minerals, Hole U1347A. **A.** Interval 324-U1347A-29R-4, 110–124 cm. **B.** Interval 324-U1347A-29R-5, 46–56 cm.



Figure F47. Comparison of vein and joint dips, vesicularity, and groundmass grain size, Hole U1347A.

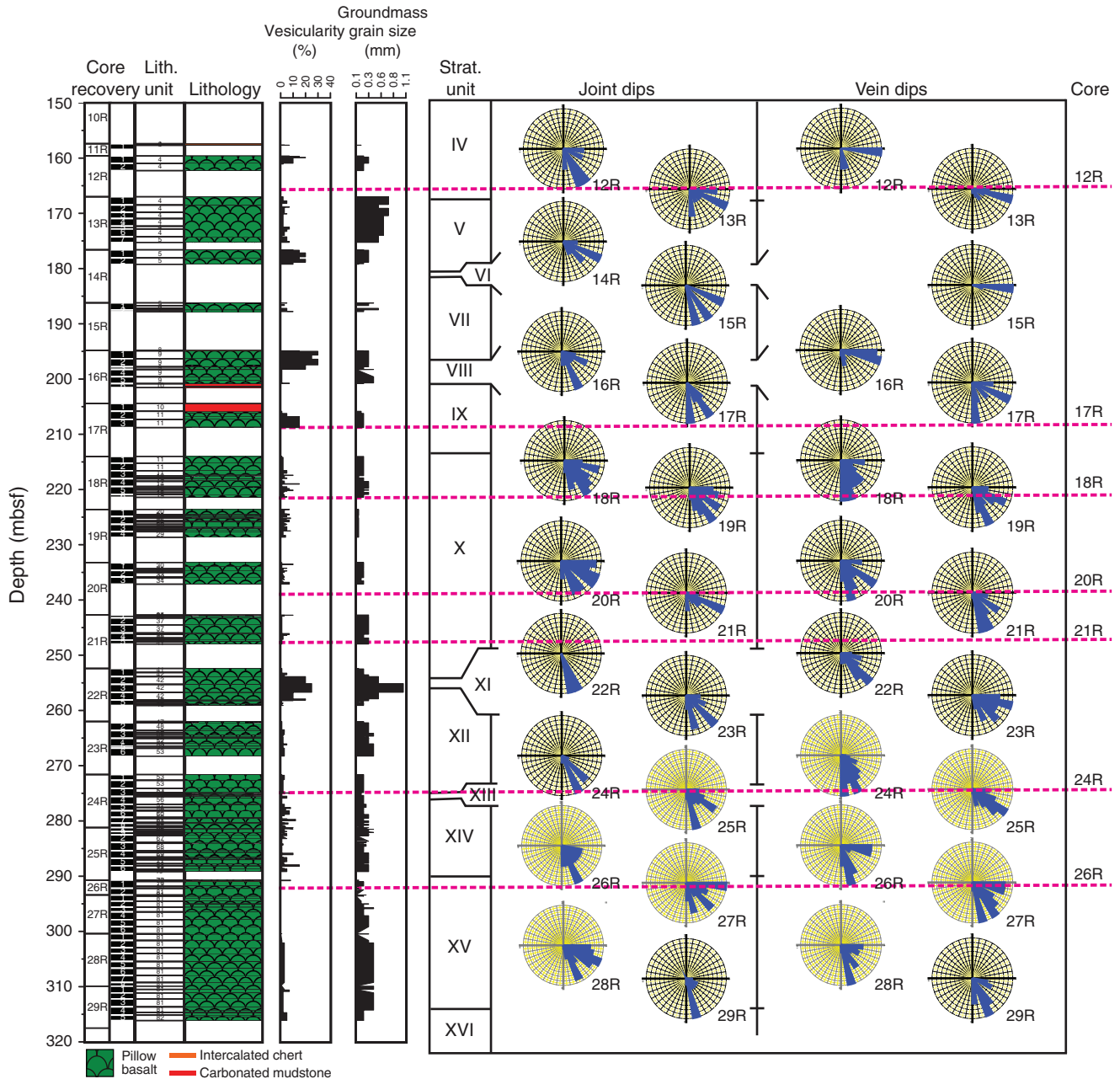


Figure F48. Relationships among vesicularity, groundmass grain size, joints, and veins, Hole U1347A.

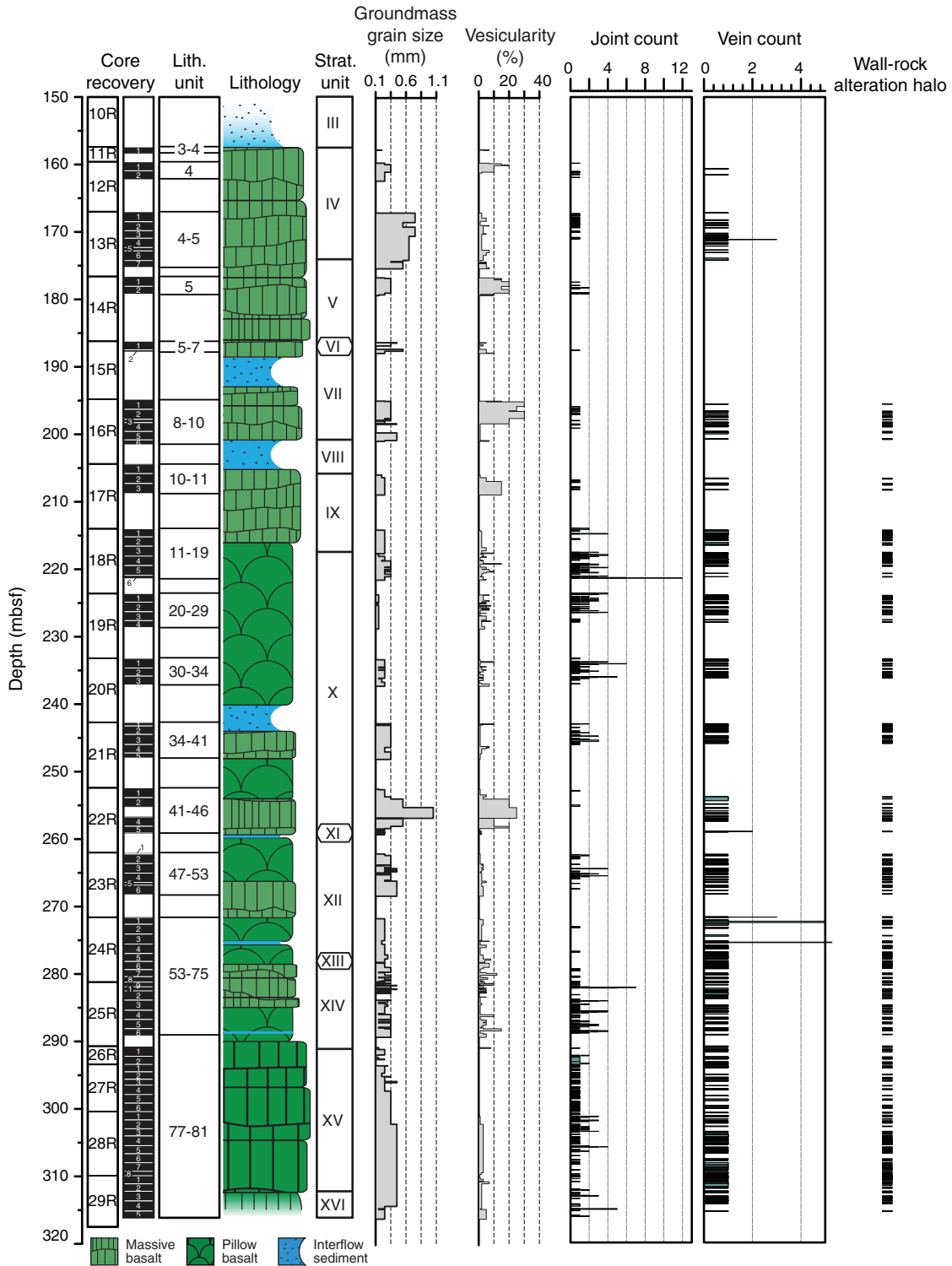


Figure F49. Sketch and core image of one set of conjugate joint planes, Hole U1347A (interval 324-U1347A-27R-6, 70–95 cm).

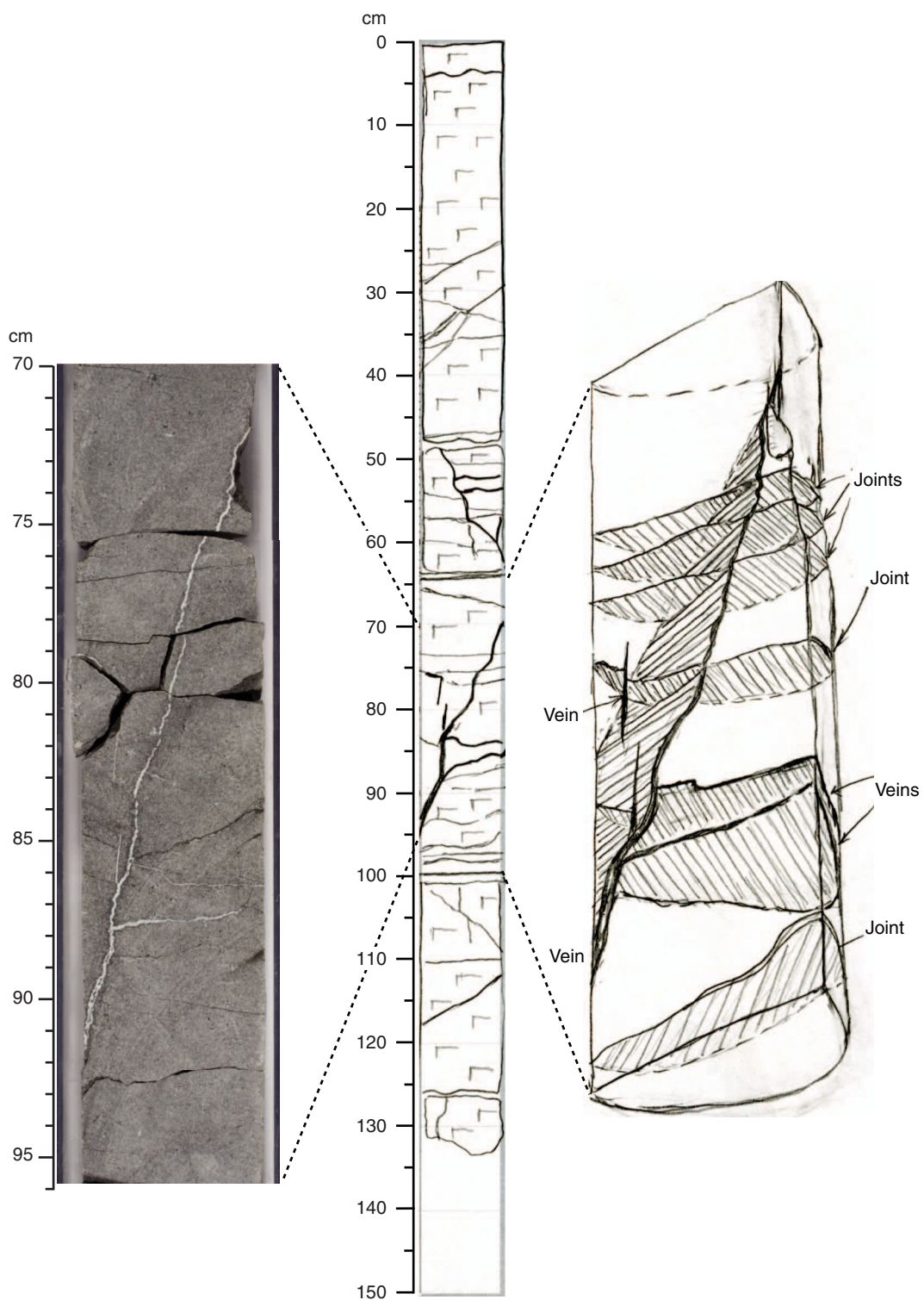


Figure F50. A. Total alkalis vs. SiO₂ plot with Le Maitre et al.'s (1989) classification of volcanic rock types. Heavy dashed line = division of data for tholeiitic and alkalic lavas of Hawaii (Macdonald and Katsura, 1964; Macdonald, 1968). Values normalized to 100 wt% totals. OJP = Ontong Java Plateau (data of Tejada et al., 1996, 2002; Fitton and Godard, 2004), EPR = East Pacific Rise (data of Sinton et al., 1991; Bach et al., 1994; Mahoney et al., 1994), Nazca-ESC = Nazca Ridge and Easter seamount chain (Ray et al., unpubl. data). **B.** K₂O vs. loss on ignition (LOI). Data for the two carbonate-rich vein samples from Site U1346 are not included in either A or B.

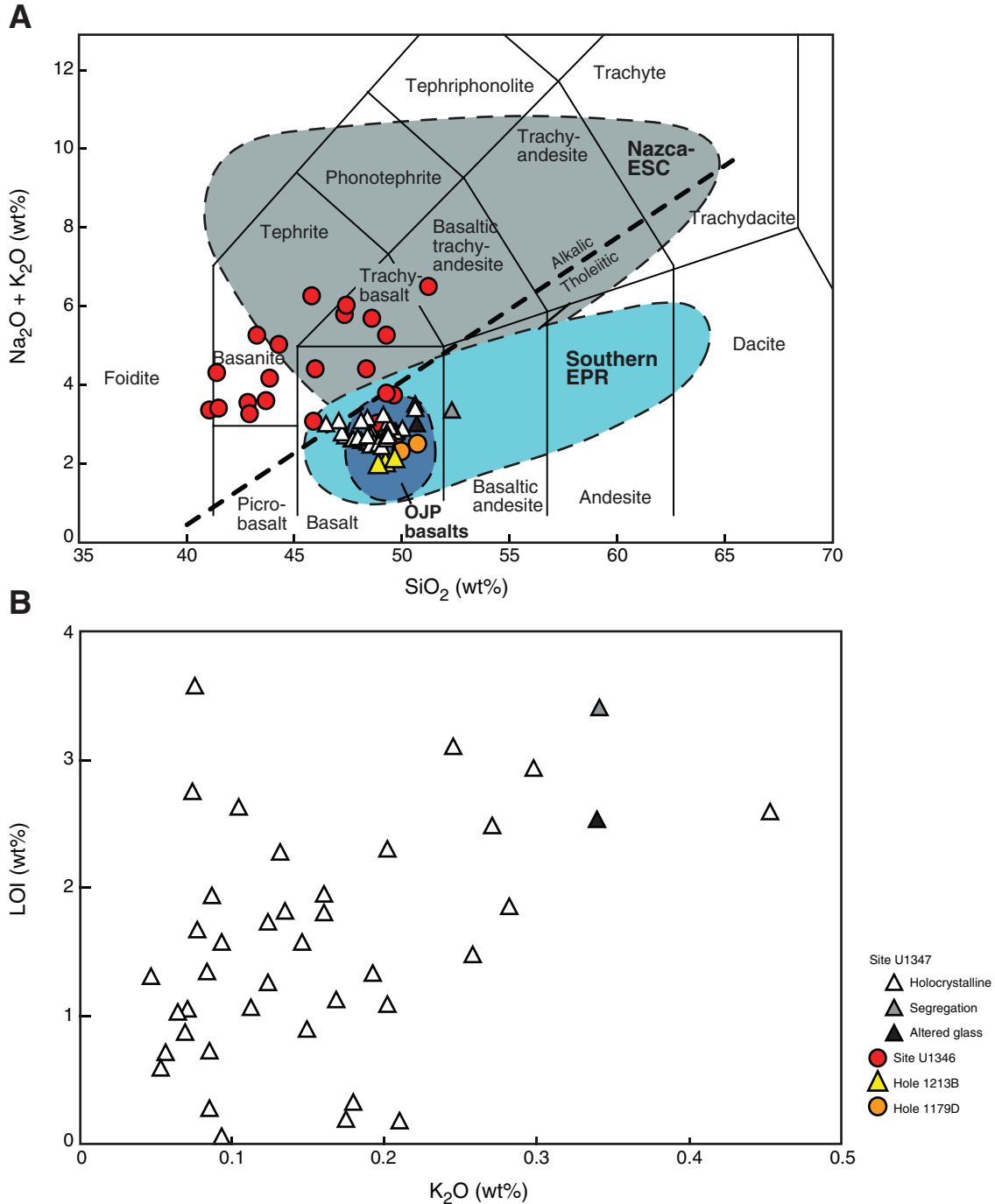


Figure F51. Patterns of Ba, Sr, P, Zr, Ti, and Y for the Site U1347 basement samples compared with patterns of ODP Leg 198 Site 1213 basalts (Mahoney et al., 2005), Ontong Java Plateau (OJP) basalts (Kwaimbaita magma type; Tejada et al., 2002; Fitton and Godard, 2004), and normal mid-ocean-ridge basalts (N-MORB) of the southern East Pacific Rise (Hall et al., 2006, and references therein; data adjusted to 8 wt% MgO). Element concentrations are normalized to estimated primitive-mantle (PM) concentrations of Lyubetskaya and Korenaga (2007). Gray band = total range of compositions measured for the Site U1347 holocrystalline samples. **A.** Pattern of stratigraphic Unit IV holocrystalline basalt (Sample 324-U1347-13R-2 [Piece 3, 52–55 cm]) compared with that of the segregation near the bottom of Unit IV (Sample 324-U1347-13R-6 [Piece 1, 80–83 cm]) and the altered glass from the top of Unit V (Sample 324-U1347-13R-7 [Piece 6, 28–30 cm]). **B–F.** Patterns of Site U1347 holocrystalline basalts by stratigraphic unit.

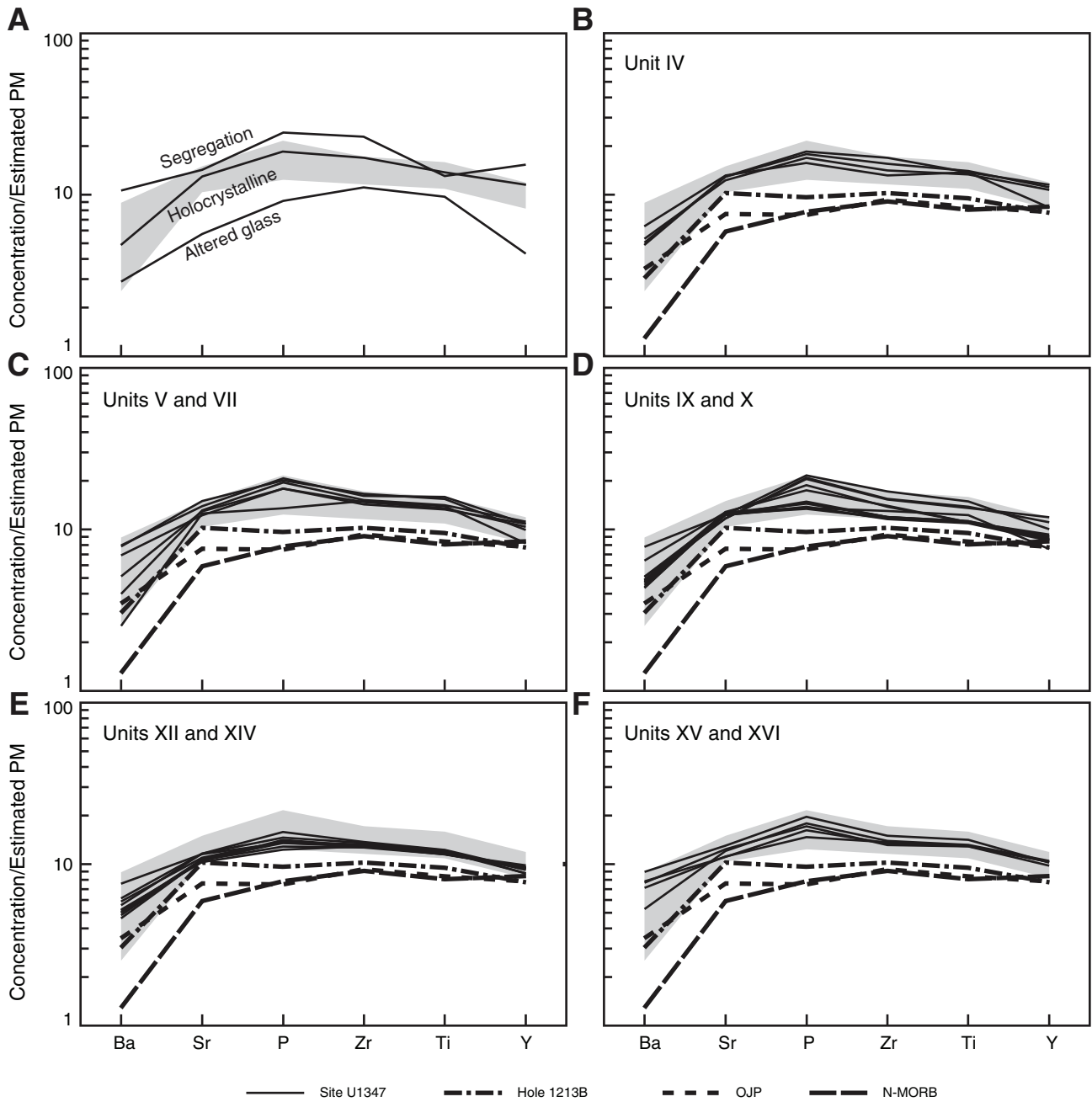


Figure F52. Plots of TiO_2 vs. (A) Al_2O_3 , (B) Mg#, (C) Ni, (D) Cr, and (E) Sr. Major element values normalized to 100 wt% totals. $Mg\# = 100 \times Mg^{2+}/(Mg^{2+} + Fe^{2+})$, assuming that $Fe_2O_3/FeO = 0.15$. Data for two carbonate-rich vein samples from Site U1346 are not shown. OJP = Ontong Java Plateau (data of Tejada et al., 1996, 2002; Fitton and Godard, 2004), EPR = East Pacific Rise (data of Sinton et al., 1991; Bach et al., 1994; Mahoney et al., 1994), Nazca-ESC = Nazca Ridge and Easter seamount chain (data of Ray et al., submitted).

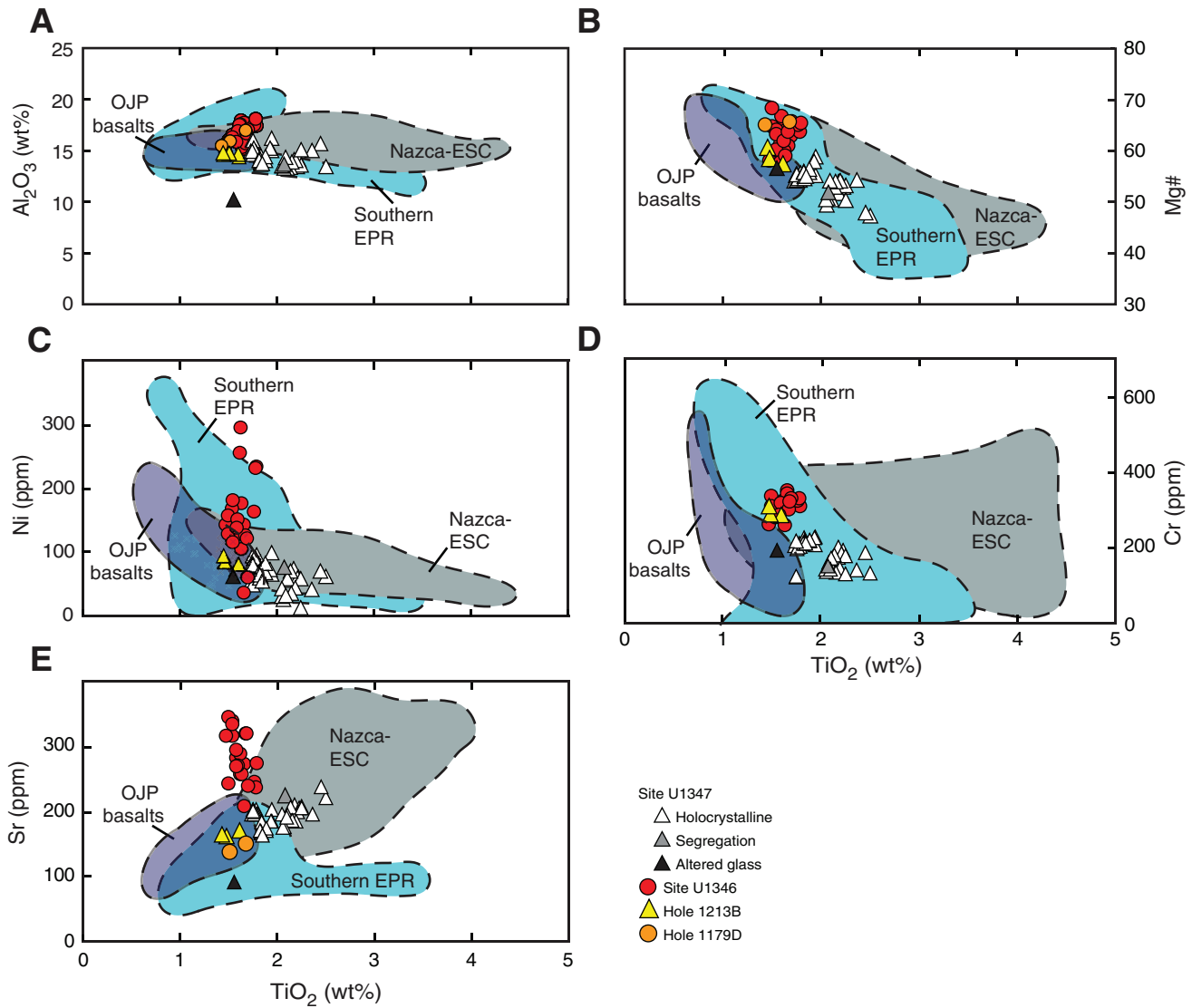


Figure F53. Downhole variation of (A) TiO₂, (B) Mg#, (C) Cr, and (D) Ni in Site U1347 basement. Dashed lines = unit boundaries. See “Sedimentology” and “Igneous petrology” for definition and description of stratigraphic units.

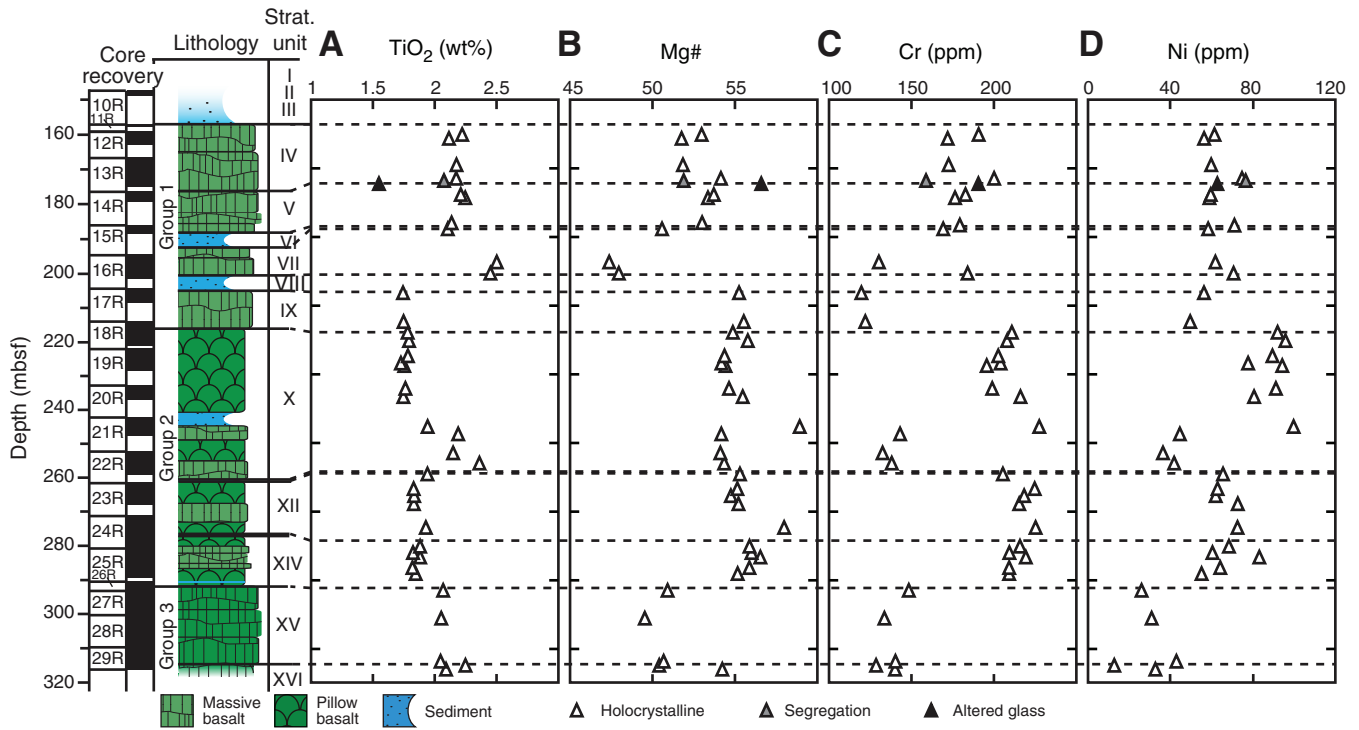


Figure F54. Plots of selected discrete sample measurements, Hole U1347A. The discrepancy in logged and recovered unit thicknesses is the same as in Figure F33.

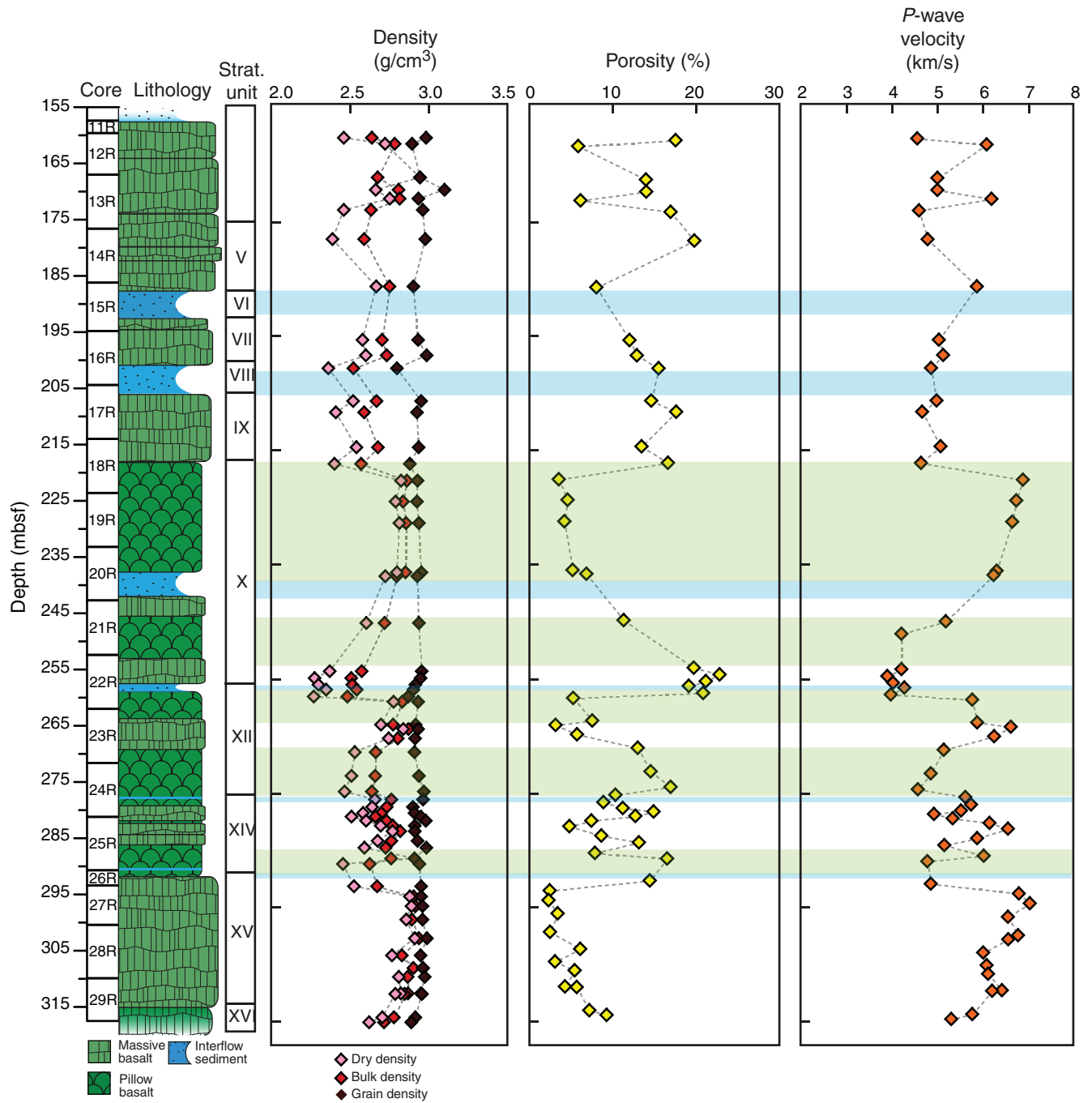


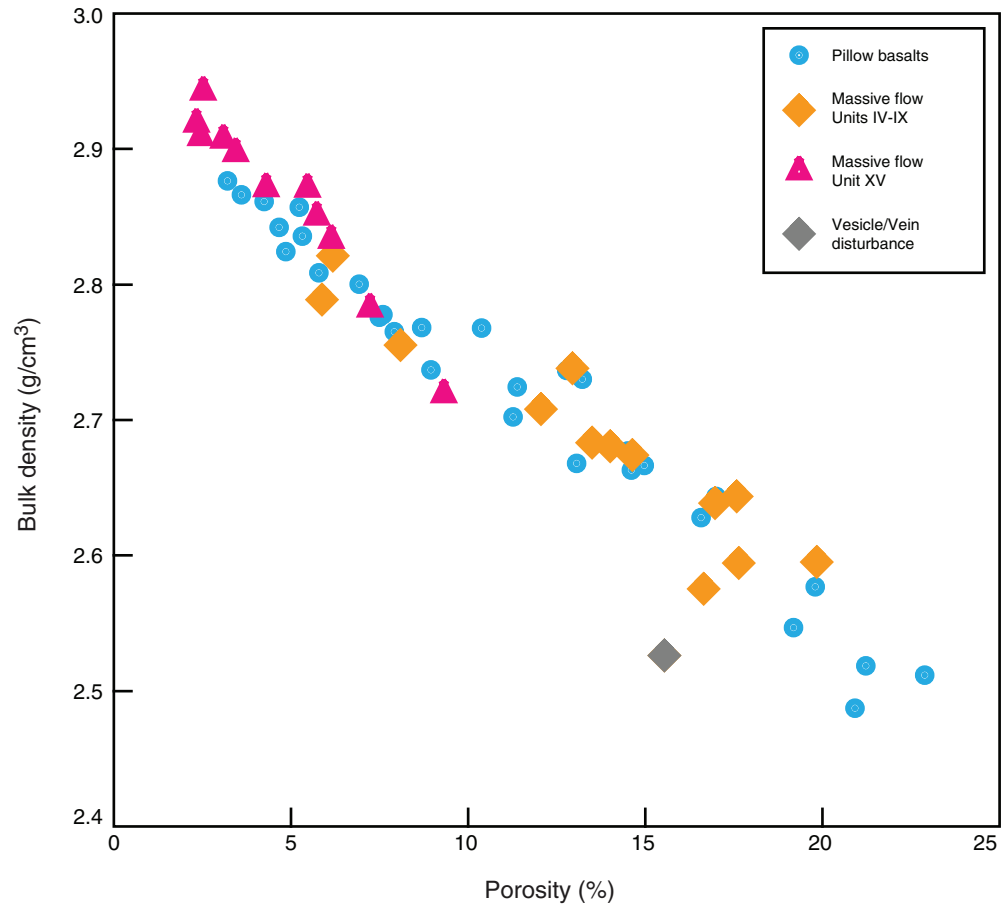
Figure F55. Plot of porosity vs. bulk density measurements on discrete samples, Hole U1347A.

Figure F56. Plot of bulk density vs. *P*-wave velocity measurements on discrete samples, Hole U1347A.

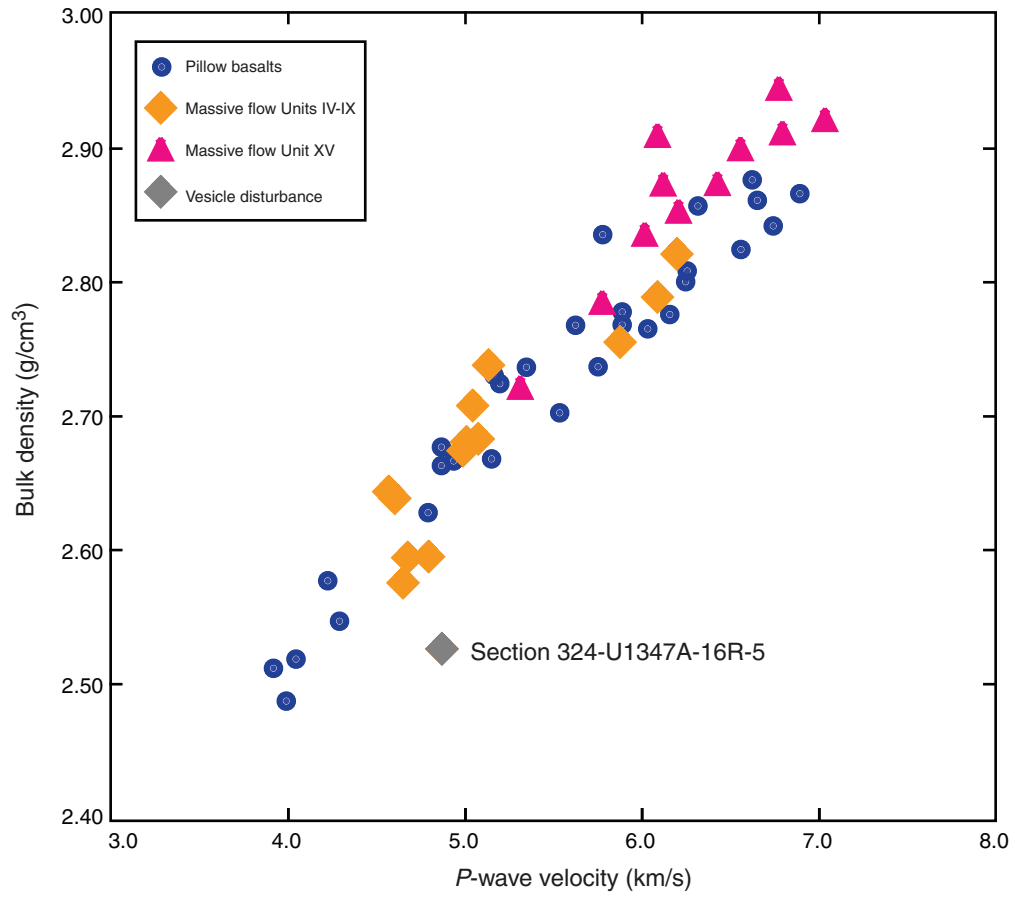


Figure F57. Plots of thermal conductivity and magnetic susceptibility (MS) vs. depth, Hole U1347A. Measurements performed on homogeneous vein- and crack-free split-half pieces at least 8 cm long from both the working and archive halves of the core, depending on availability.

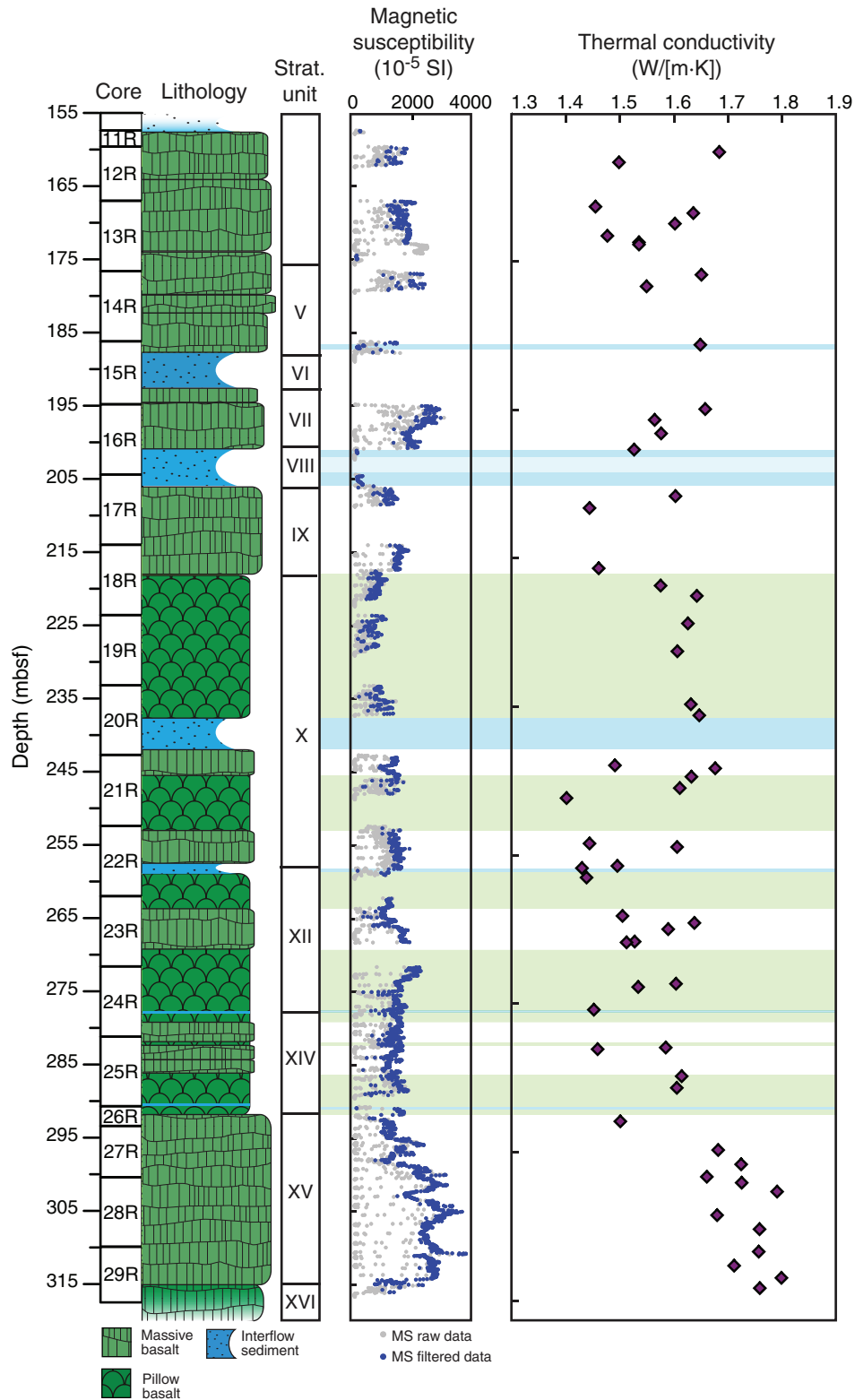


Figure F58. Example orthogonal vector plots of (A, B) alternating-field and (C–E) thermal demagnetization results, Hole U1347A. Open circles = inclinations, solid circles = declinations, NRM = natural remanent magnetization.

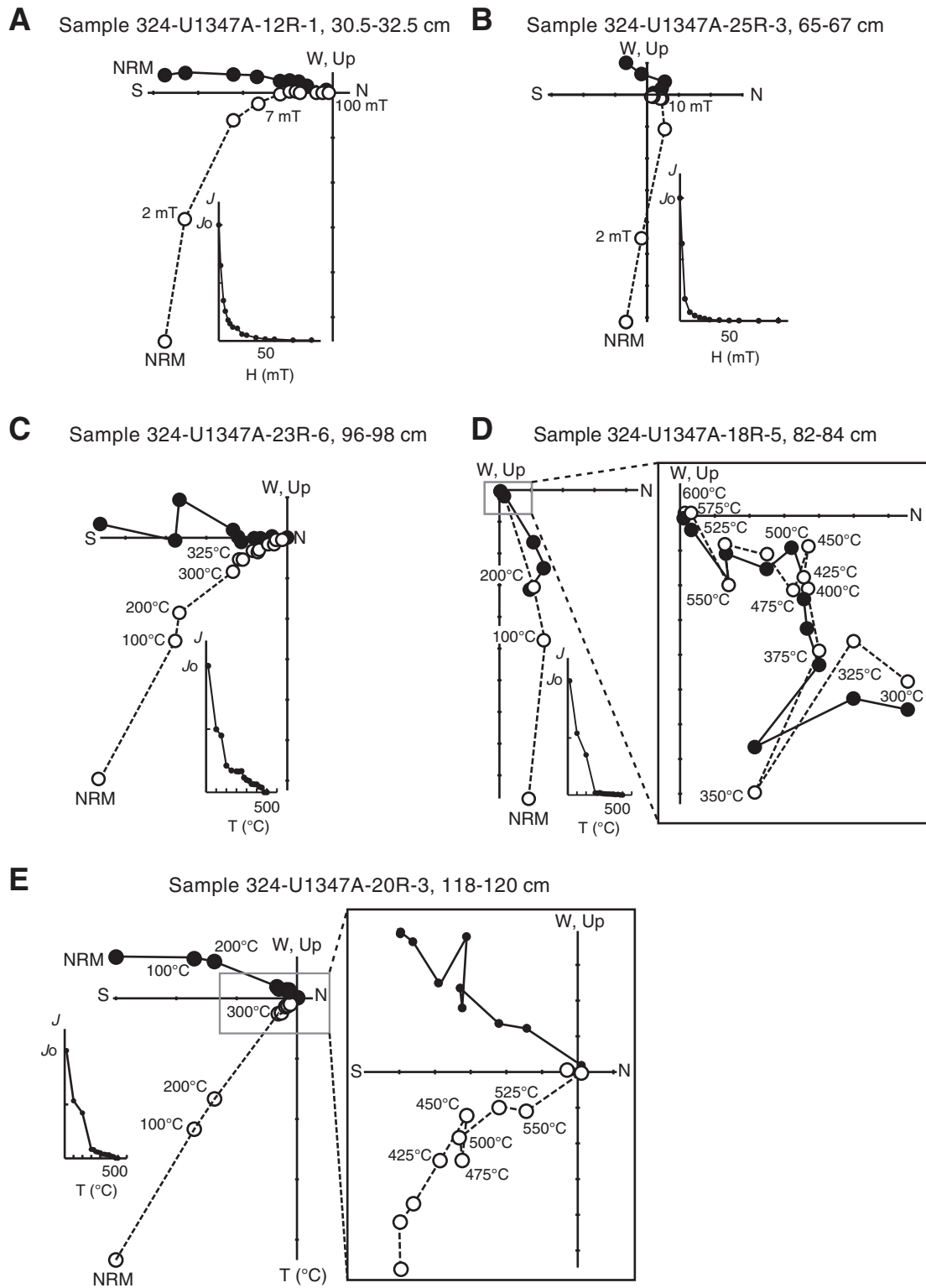


Figure F59. Alternating-field demagnetization of anhysteretic remanent magnetization (ARM), Hole U1347A. Green diamond = Sample 324-U1347A-27R-2, 23–25 cm; orange circle = Sample 324-U1347A-28R-5, 16–18 cm; blue plus = Sample 324-U1347A-28R-8, 80–82 cm.

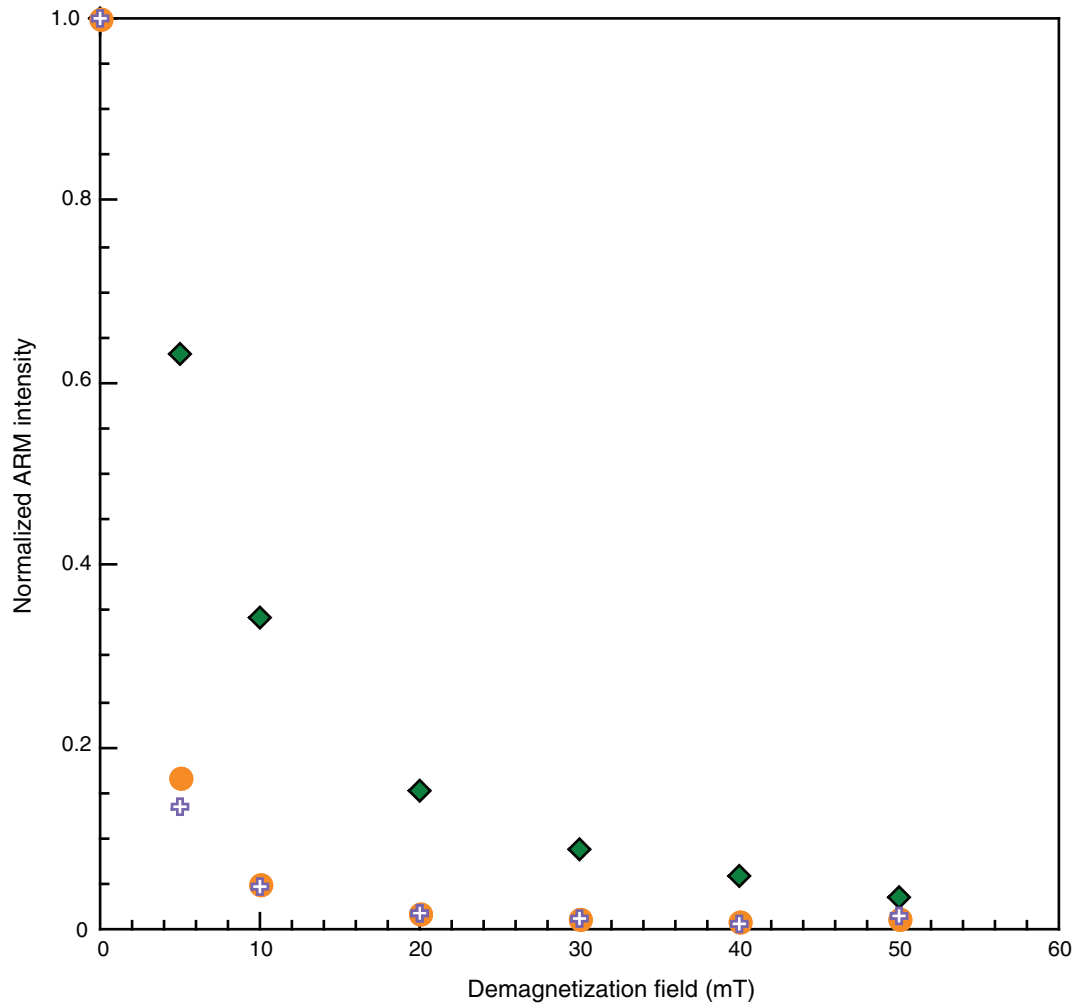


Figure F60. A. Plot of characteristic remanence inclination vs. depth, Hole U1347A. AF demag = alternating-field demagnetization, TH demag = thermal demagnetization. Rejected data points have maximum angular deviation >8°. See “**Igneous petrology**” for stratigraphic unit details. Circled numbers = four groups of inclinations. Dotted lines = limits between inclination groups. B. Downhole magnetic susceptibility (filtered by Physical Properties Specialists, see “**Physical properties**” in the “Methods” chapter). Orange lines = sediments.

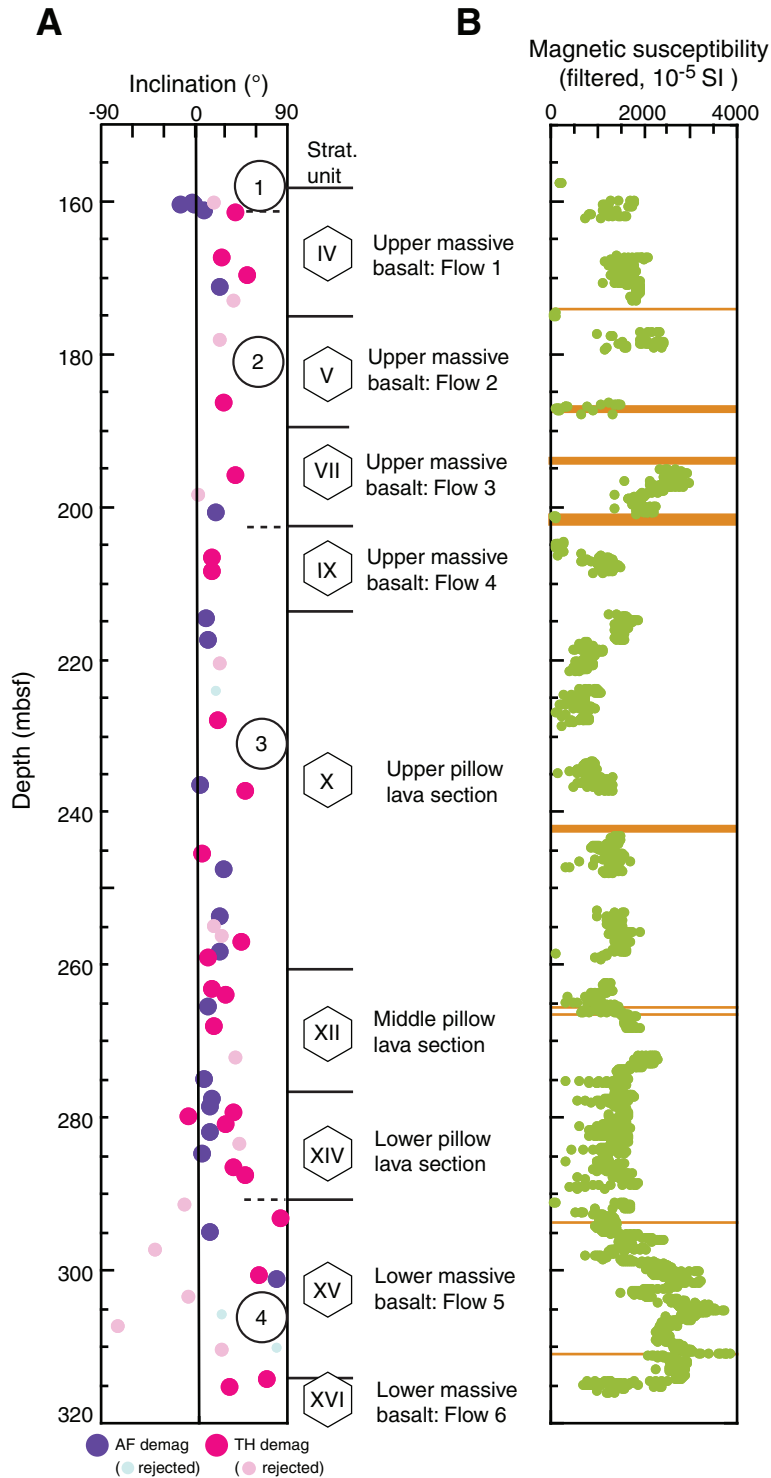


Figure F61. Downhole caliper, electrical resistivity, and gamma ray logs from the basement section of Hole U1347A. IDPH = deep induction phasor-processed resistivity, IMPH = medium induction phasor-processed resistivity, SFLU = spherically focused resistivity, HSGR = gamma ray log, HCGR = computed gamma radiation, NGR = natural gamma radiation.

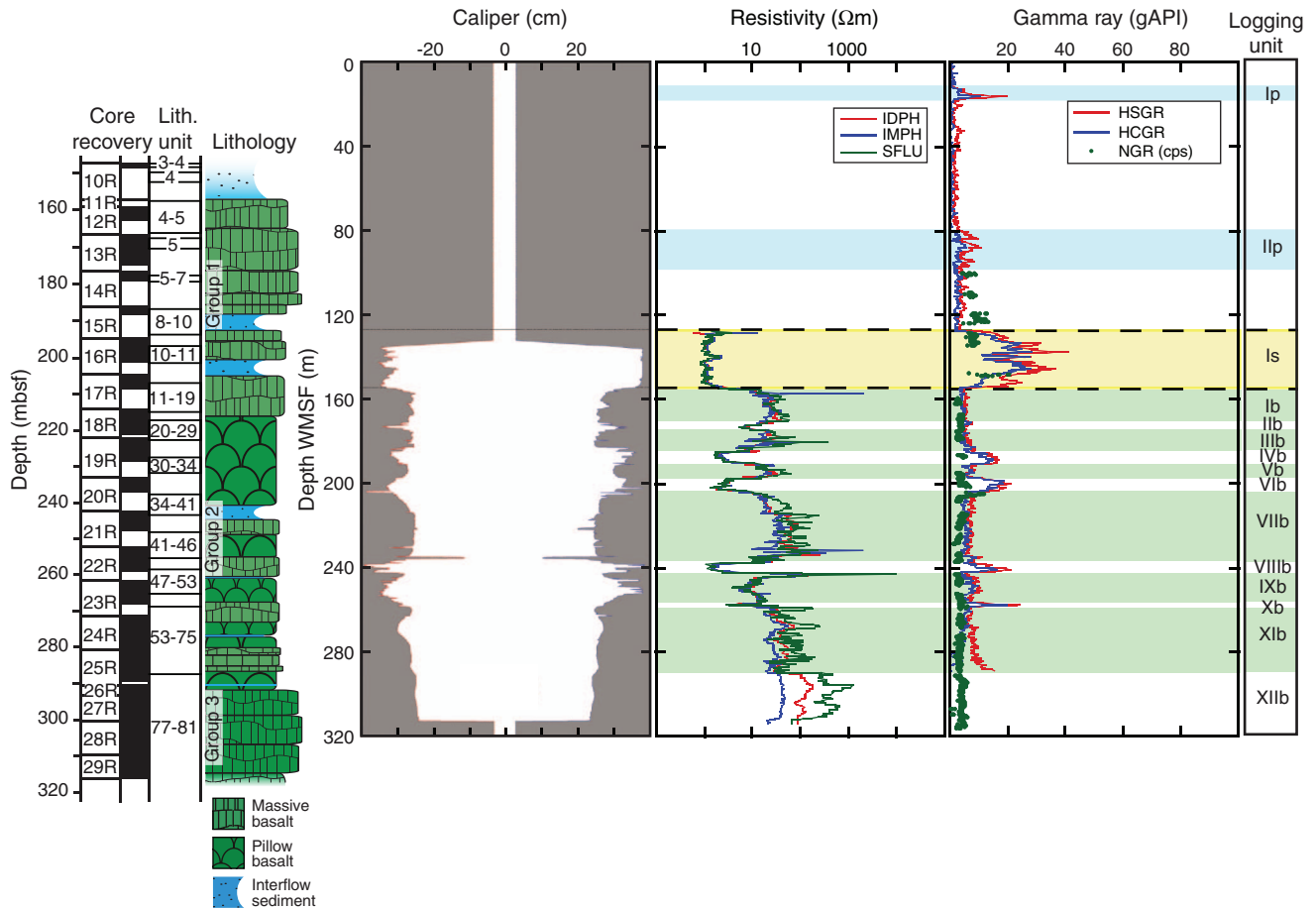


Figure F62. Whole-rock K₂O elemental concentrations and downhole spectral gamma ray logs of uranium, potassium, and thorium, Hole U1347A. Solid circles = whole-rock K₂O elemental concentrations from ICP-AES measurements on cores. HFK = gamma ray log potassium measurement.

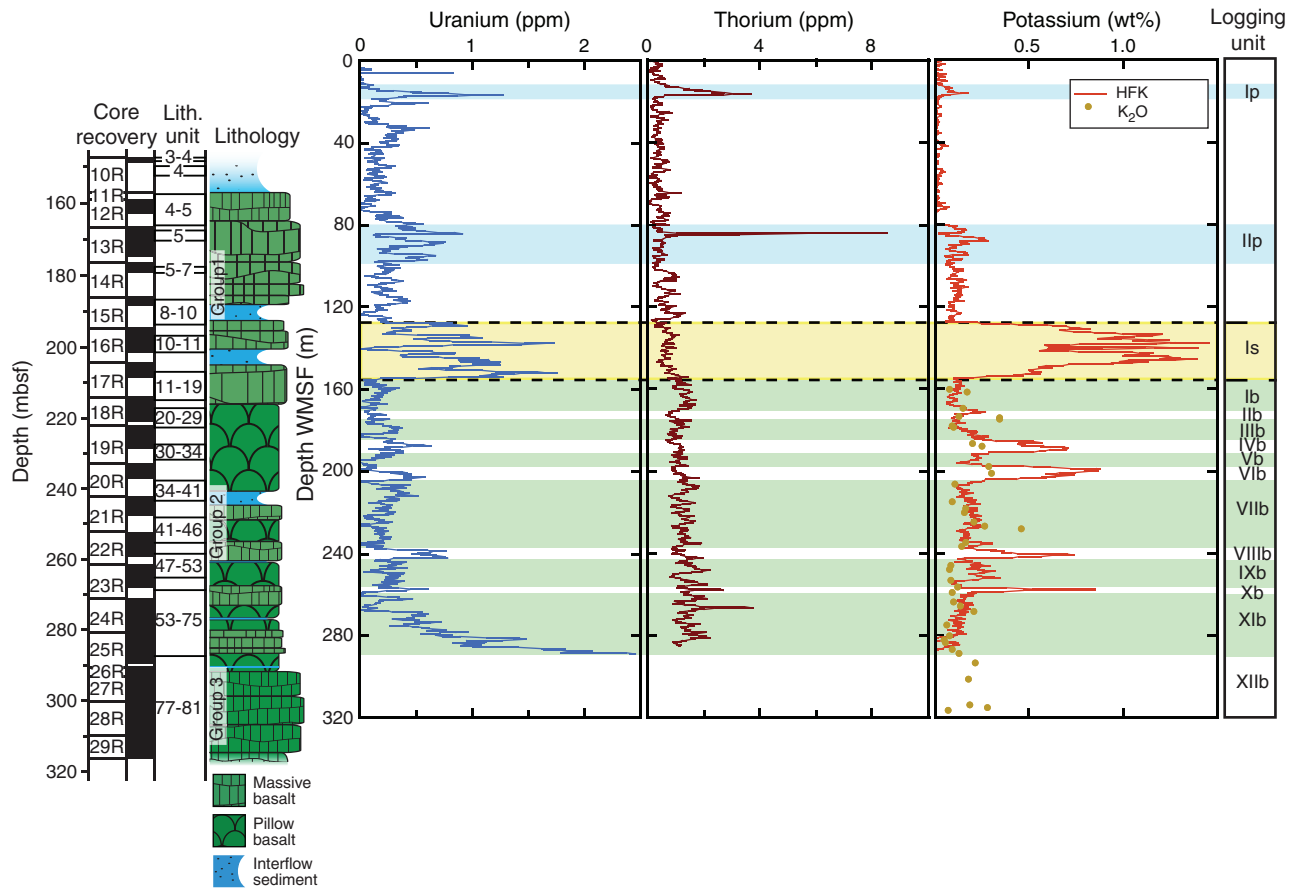




Figure F63. Downhole caliper, density, *P*-wave velocity, and neutron porosity, Hole U1347A. Solid circles = physical property measurements made on core samples. HROM = high-resolution corrected bulk density, MAD = moisture and density, VCO = compressional velocity, HALC = high-resolution near-array limestone porosity corrected.

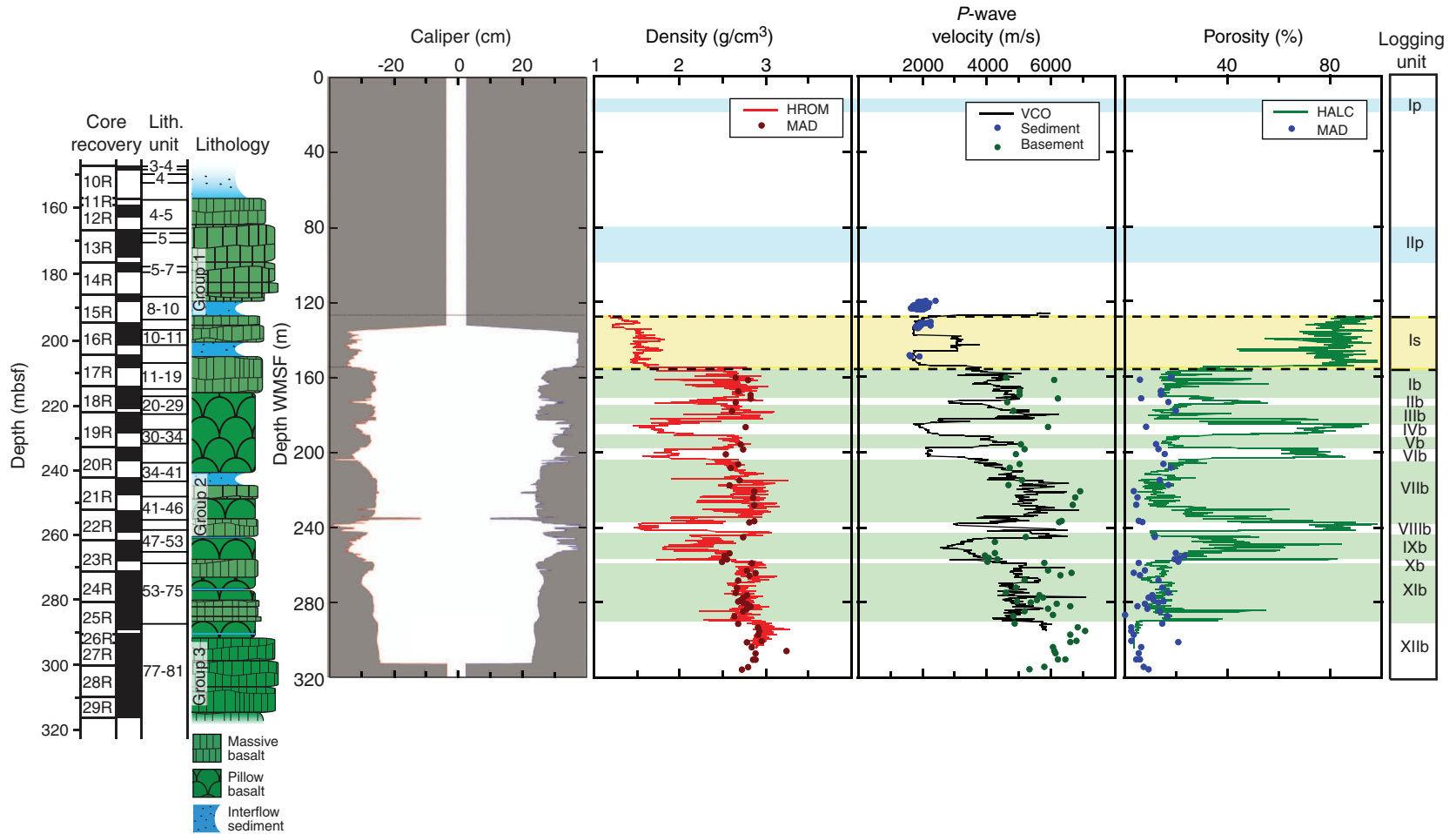


Figure F64. Downhole magnetic inclination, total magnetic field moment, and magnetic intensity, Hole U1347A. F_x , F_y , F_z = x-, y-, and z-axis measurements. FINC = magnetic field inclination, FNOR = magnetic field total moment.

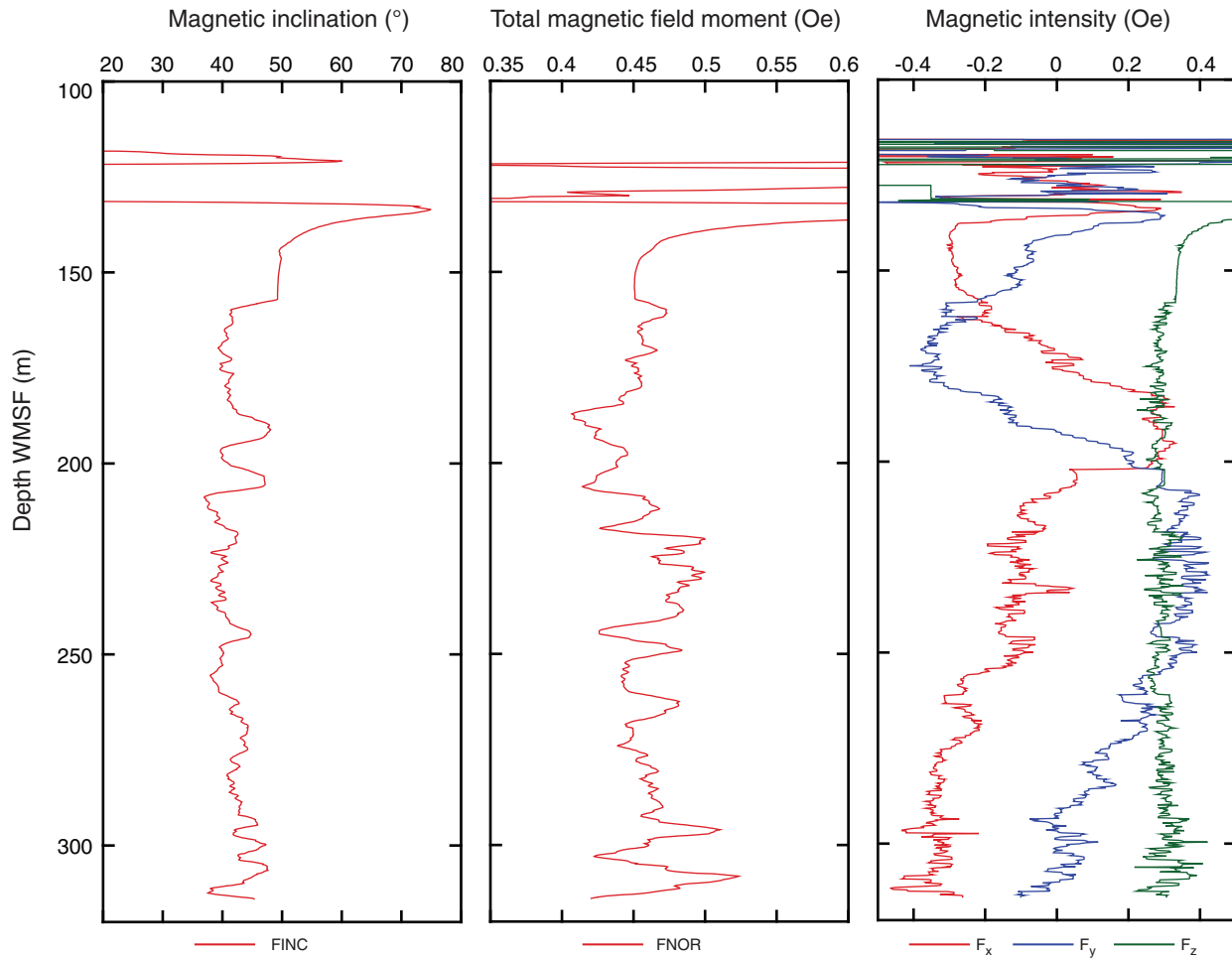


Figure F65. FMS images of high-angle fractures in the shallow basement and pillow lavas and massive lavas flows from the lower section of Hole U1347A.

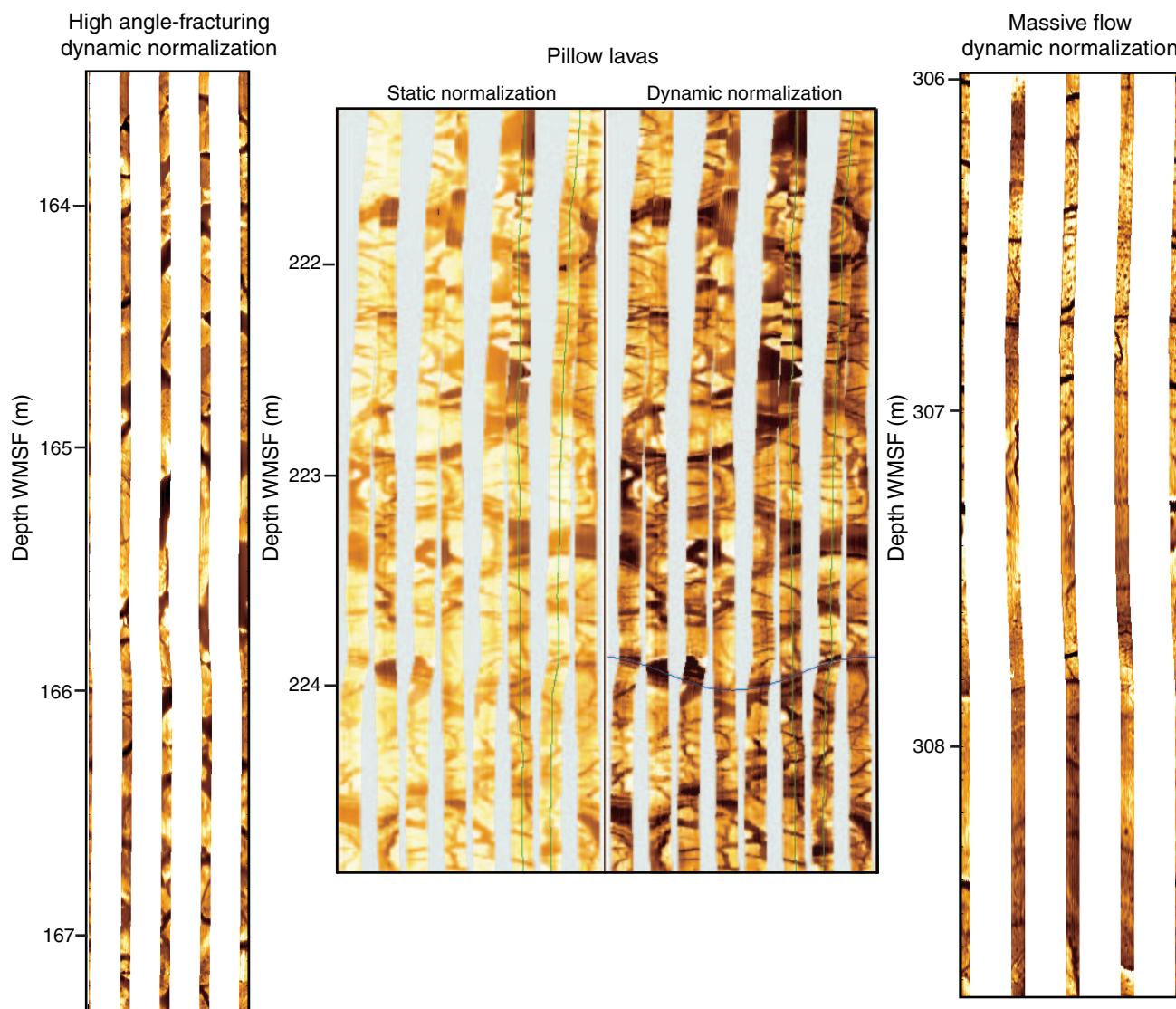


Table T1. Coring summary, Site U1347. (See table notes.)

Site U1347					
Time on site (h): 250.5 (1730 h, 21 September–0400 h, 2 October 2009)					
Hole U1347A					
Latitude: 32°30.475'N					
Longitude: 159°14.078'E					
Time on hole (h): 250.5 (1730 h, 21 September–0400 h, 2 October 2009)					
Seafloor (drill pipe measured below rig floor, m DRF): 3461.0					
Distance between rig floor and sea level (m): 11.0					
Water depth (drill pipe measured from sea level, mbsl): 3450.0					
Total depth (drill pipe measured from rig floor, m DRF): 3778.5					
Total penetration (drilling depth below seafloor, m DSF): 317.5					
Total length of cored section (m): 246.5 (159.9 in igneous basement)					
Total core recovered (m): 116.6					
Core recovery (%): 47.1 (64.2 in igneous basement)					
Total number of cores: 29					
Core	Depth DSF (m)		Interval advanced (m)	Length of core recovered (m)	Recovery (%)
	Top of cored interval	Bottom of cored interval			
324-U1347A-					
1W	0.0	71.0	71.0	0.17	0
2R	71.0	80.5	9.5	0.11	1
3R	80.5	90.1	9.6	0.15	2
4R	90.1	99.8	9.7	0.65	7
5R	99.8	109.3	9.5	1.04	11
6R	109.3	118.9	9.6	1.78	19
7R	118.9	128.6	9.7	5.20	54
8R	128.6	138.2	9.6	6.20	65
9R	138.2	147.8	9.6	0.27	3
10R	147.8	157.4	9.6	1.34	14
11R	157.4	159.6	2.2	0.84	38
12R	159.6	167.0	7.4	2.17	29
13R	167.0	176.6	9.6	7.71	80
14R	176.6	186.2	9.6	2.30	24
15R	186.2	194.8	8.6	1.47	17
16R	194.8	204.4	9.6	6.05	63
17R	204.4	214.0	9.6	3.87	40
18R	214.0	223.6	9.6	7.07	74
19R	223.6	233.2	9.6	4.10	43
20R	233.2	242.7	9.5	3.90	41
21R	242.7	252.4	9.7	4.65	48
22R	252.4	262.0	9.6	5.61	58
23R	262.0	271.6	9.6	6.05	63
24R	271.6	281.2	9.6	10.47	109
25R	281.2	290.7	9.5	7.61	80
26R	290.7	293.4	2.7	2.84	105
27R	293.4	300.4	7.0	6.62	95
28R	300.4	309.9	9.5	9.83	103
29R	309.9	317.5	7.6	6.11	80
Totals:			317.5	116.8	37
Totals without wash barrel:			246.5	116.6	47

Notes: DRF = drilling depth below rig floor, DSF = drilling depth below seafloor. Local time = UTC + 10 h.

Table T2. X-ray diffraction analysis result summary, Hole U1347A. (See table notes.)

Core, section, interval (cm)	Sample name*	Stratigraphic unit	Unit description	Mineral composition
324-U1347A-7R-1, 23–25	CUTS1556791	III	Radiolarian-bearing sandy siltstones	Glaucosite Anorthite Magnesium calcite Heulandite Montmorillonite Saponite
7R-1, 90–92	CUTS1556801	III	Radiolarian-bearing sandy siltstones	Glaucosite Anorthite Calcite Heulandite Saponite Orthoclase Sanidine Nontronite
7R-3, 4–6	CUTS1556811	III	Radiolarian-bearing sandy siltstones	Glaucosite Anorthite Magnesium calcite Heulandite Montmorillonite Nontronite Talc
8R-1, 32–34	CUTS1556821	III	Radiolarian-bearing sandy siltstones	Montmorillonite Clinopyroxene Albite Fedotovite Talc Pseudomalachite
24R-5, 115–118	CUTS1556831	XIII	Low-density volcaniclastic sandstone	Quartz Cristobalite

Notes: * = LIMS sample name. For original data, see LIMS at iodp.tamu.edu/database/index.html.

Table T3. Carbon concentrations, Hole U1347A. (See table notes.)

Core, section, interval (cm)	Depth (mbsf)	Total carbon (wt%)	Organic carbon (wt%)	Carbonate (wt%)
324-U1347A-				
3R-1, 15–16	80.65	4.97	0.46	37.65
4R-1, 36–37	90.46	1.45	0.45	8.34
5R-1, 19–21	99.98	0.47	0.20	2.25
5R-1, 70–72	100.50	1.19	0.20	8.27
5R-1, 117–119	100.97	0.66	0.14	4.31
5R-1, 135–138	101.15	0.81	0.26	4.56
6R-1, 0–2	109.30	1.03	0.78	2.08
6R-1, 0–2 (R)	109.30	—	—	2.13
6R-1, 58–60	109.88	0.87	0.42	3.76
6R-1, 58–60 (R)	109.88	—	—	3.72
6R-2, 1–4	110.17	1.12	0.72	3.27
6R-2, 66–68	110.82	1.36	0.70	5.56
7R-1, 17–19	119.07	2.13	0.45	13.94
7R-1, 20–22	119.10	0.45	0.13	2.66
7R-1, 90–92	119.80	0.85	0.28	4.71
7R-2, 37–39	120.23	0.54	0.19	2.79
7R-2, 37–39 (R)	120.23	—	—	3.07
7R-2, 99–101	120.85	0.87	0.32	4.63
7R-3, 20–22	121.21	0.85	0.21	5.35
7R-3, 20–22 (R)	121.21	—	—	5.37
7R-3, 117–119	122.18	1.03	0.37	5.48
7R-4, 26–28	122.68	1.83	0.47	11.27
7R-4, 83–85	123.25	1.59	0.42	9.80
7R-4, 143–145	123.85	1.00	0.22	6.52
8R-1, 22–24	128.82	0.22	0.09	1.09
8R-1, 89–91	129.49	0.34	0.07	2.22
8R-2, 8–10	130.18	0.43	0.15	2.32
8R-2, 106–108	131.16	0.75	0.10	5.39
8R-3, 30–32	131.55	4.47	0.34	34.42
8R-3, 116–118	132.41	0.92	0.24	5.59
8R-4, 52–54	133.16	1.08	0.53	4.61
8R-5, 26–28	133.73	0.51	0.20	2.62
8R-CC, 21–23	134.61	0.59	0.17	3.53
10R-1, 0–2	147.80	0.49	0.07	3.54
10R-1, 53–55	148.33	1.85	1.28	4.82
10R-1, 70–72	148.50	1.43	0.83	4.98
10R-CC, 20–24	149.07	0.37	0.13	2.00
15R-1, 74–75	186.94	0.37	0.19	1.45
16R-6, 33–35	201.16	0.31	0.19	0.98
17R-1, 26–28	204.66	1.12	0.53	4.90
17R-1-90–91	205.30	0.30	0.10	1.63

Notes: R = repeated analysis. — = no data.

Table T4. Calcareous nannofossil age assignments, Site U1347. (See table notes.)

Core, section, interval (cm)	Age-diagnostic species (Abundance)	Stratigraphic range (Zone)	Age (Ma)
324-U1347A-1W-1, 15	<i>Axopodorhabdus cylindratus</i> (F)	Berriasian–Valanginian (NK1–NK3b)	142.3–101.7
	<i>Cretarhabdus striatus</i> (F)	Aptian–Cenomanian (?–UC4)	
	<i>Cruciellipsis cuvillieri</i> (R)	Tithonian–Hauterivian (NJ18–NC5)	
	<i>Rotelapillius laffittei</i> (R)	Berriasian–Turonian (NJKd–UC9)	
2R-1, 9	<i>Axopodorhabdus cylindratus</i> (R)	Berriasian–Valanginian (NK1–NK3b)	140–133.1
	<i>Cretarhabdus striatus</i> (R)	Aptian–Cenomanian (?–UC4)	
	<i>Cruciellipsis cuvillieri</i> (R)	Tithonian–Hauterivian (NJ18–NC5)	
	<i>Speetonia</i> sp. (R)	Berriasian–Hauterivian (NK3–NC5)	
6R-2, 97–98	<i>Axopodorhabdus cylindratus</i> (R)	Berriasian–Valanginian (NK1–NK3b)	140–133.1
	<i>Cruciellipsis cuvillieri</i> (R)	Tithonian–Hauterivian (NJ18–NC5)	
7R-3, 65	<i>Axopodorhabdus cylindratus</i> (R)	Berriasian–Valanginian (NK1–NK3b)	140–133.1
10R-1, 66	<i>Axopodorhabdus cylindratus</i> (R)	Berriasian–Valanginian (NK1–NK3b)	140–133.1

Notes: Abundance: F = frequent, R = rare. Zone ranges are only given for properly defined taxa.

Table T5. Benthic foraminifer preservation and abundance, Site U1347. (See table notes.)

Core, section, interval (cm)	Depth (mbsf)	Preservation	Agglutinated		Calcareous			
			<i>Glomospirella</i>	<i>Dorothia</i>	<i>Dentalina</i>	<i>Lenticulina</i>	<i>Planularia</i>	<i>Conorboides</i>
324-U1347A-1W-1, 9–16	0.13	P		T				
2R-1, 8.5–8.5	71.08	P	T					T
5R-1, 81–83	100.62	B*						
6R-1, 16–18	109.47	M–G				T	T	
6R-1, 34–36	109.65	B						
6R-2, 97–98	111.14	G				R		
7R-4, 50–52	122.93	G			R	F	T	
7R-CC, 19–21	124.09	G				T		
8R-1, 22–25	128.84	B						
8R-2, 49–51	130.60	VG						T
8R-3, 39–41	131.65	G					T	
8R-5, 42–44	133.90	B						
8R-CC, 35–37	134.76	G					T	
9R-1, 18.5–19	138.39	M				T		
10R-CC, 17–18	149.03	M				F		
10R-1, 51–53	148.32	B*						
11R-1, 14–16	157.55	B						
13R-7, 19.5–21.5	174.45	B						
15R-1 (Piece 6, 70–72)	186.91	G					T	
16R-6, 6–8	200.90	B						
17R-1, 41.5–43.5	204.83	M–G				R		
22R-5, 28–30	258.39	B						

Notes: * = indurated and/or disaggregation not completed. Preservation: VG = very good, G = good, M = moderate, P = poor, B = barren. Abundance: F = few, R = rare, T = trace. See “Paleontology” in the “Methods” chapter for preservation and abundance descriptions. For all samples, >125 μ m fractions were examined.

Table T6. Original microphenocryst and/or phenocryst abundances, Site U1347. (See table notes.) (Continued on next page.)

Thin section number	Core, section, interval (cm)	Unit in VCD	Recovered thickness (m)	Original modal abundance										Stratigraphic unit
				Plagioclase			Olivine			Pyroxene			Fresh glass	
				R	P	A	R	P	A	R	P	A		
324-U1347A-														
69	12R-1, 2-5	4	16.6	██████████			██████			██████████			Fresh glass	IV
70	12R-1, 57-59			██████████			██████			██████████				
71	12R-2, 40-42			██████████			██████			██████████				
72	13R-2, 56-59			██████████			██████			██████████				
73	13R-5, 38-40			██████████			██████			██████████				
74	13R-6, 84-86	5	12.5	██████████			██████			██████████			Fresh glass	V
75	13R-6, 139-142			██████████			██████			██████████				
76	13R-7, 17-20			██████████			██████			██████████				
81	13R-7, 34-37			██████████			██████			██████████				
78	13R-7, 69-72			██████████			██████			██████████				
79	14R-1, 108-110	7 and 9	13.6	██████████			██████			██████████			Fresh glass	VII
80	14R-2, 52-54			██████████			██████			██████████				
83	15R-1, 9-11			██████████			██████			██████████				
84	15R-1, 107-109			██████████			██████			██████████				
85	15R-2, 24-26			██████████			██████			██████████				
86	16R-2, 100-104	11	11.7	██████████			██████			██████████			Fresh glass	IX
87	16R-3, 39-42			██████████			██████			██████████				
88	16R-4, 4-8			██████████			██████			██████████				
89	16R-5, 99-102			██████████			██████			██████████				
92	17R-2, 9-11			██████████			██████			██████████				
93	17R-2, 27-30	14	1	██████████			██████			██████████			Fresh glass	X
94	17R-2, 48-50			██████████			██████			██████████				
95	17R-3, 65-67			██████████			██████			██████████				
96	18R-1, 42-43			██████████			██████			██████████				
97	18R-1, 93-96			██████████			██████			██████████				
98	18R-2, 41-44	16	0	██████████			██████			██████████			Fresh glass	XII
99	18R-2, 122-126			██████████			██████			██████████				
100	18R-3, 122-123			██████████			██████			██████████				
101	18R-4, 104-108			██████████			██████			██████████				
102	18R-5, 32-36			██████████			██████			██████████				
103	18R-5, 80-81	17	0	██████████			██████			██████████			Fresh glass	XII
104	19R-1, 106-107	21	0	██████████			██████			██████████				
105	19R-2, 74-77	24	1	██████████			██████			██████████				
106	19R-3, 49-52	27	0	██████████			██████			██████████				
107	19R-3, 122-124	29	1	██████████			██████			██████████				
108	20R-1, 96-97	30	1	██████████			██████			██████████			Fresh glass	XII
109	20R-3, 74-76	34	1	██████████			██████			██████████				
110	21R-1, 14-16	35	0	██████████			██████			██████████				
111	21R-2, 8-11	37	3	██████████			██████			██████████				
112	21R-3, 76-77	37	3	██████████			██████			██████████				
113	21R-4, 16-19	37	3	██████████			██████			██████████			Fresh glass	XII
114	21R-4, 39-43	38	1	██████████			██████			██████████				
115	21R-5, 16-18	40	0	██████████			██████			██████████				
117	22R-1, 59-61	41	0	██████████			██████			██████████				
118	22R-3, 69-71	42	1	██████████			██████			██████████				
119	22R-4, 1-2	42	0	██████████			██████			██████████			Fresh glass	XII
122	22R-5, 96-98	46	0	██████████			██████			██████████				
123	23R-2, 115-118	48	0	██████████			██████			██████████				
125	23R-2, 100-103	48	1	██████████			██████			██████████				
124	23R-3, 1-4	49	0	██████████			██████			██████████				
126	23R-4, 39-41	52	1	██████████			██████			██████████			Fresh glass	XII
127	23R-6, 95-96	53	6	██████████			██████			██████████				
128	24R-1, 77-79	53	6	██████████			██████			██████████				
129	24R-2, 64-67	53	6	██████████			██████			██████████				
130	24R-3, 57-58	53	6	██████████			██████			██████████				



Table T6 (continued).

Thin section number	Core, section, interval (cm)	Unit in VCD	Recovered thickness (m)	Original modal abundance										Stratigraphic unit
				Plagioclase			Olivine			Pyroxene			Fresh glass	
				R	P	A	R	P	A	R	P	A		
132	24R-7, 19-22	60	1	■			■			■	■	■	XIV	
133	24R-7, 79-80	61	1	■							■			
134	24R-9, 8-9	65	2	■										
135	25R-1, 5-9	65	2	■										
136	25R-2, 26-28	67	2	■										
137	25R-2, 78-79	67	2	■										
138	25R-3, 138-142	68	2	■										
139	25R-4, 98-99	68	1	■						■				
140	25R-6, 41-42	72	1	■			■							
141	25R-6, 82-86	74	0	■						■				
143	26R-1, 108-111	79	1	■						■				
144	26R-2, 77-78	80	23.1	■										
145	27R-1, 45-48			■										
146	27R-1, 65-67			■							XV			
147	28R-1, 72-73			■										
148	28R-7, 50-52			■										
149	29R-4, 119-120	81	1.6	■							XVI			
150	29R-5, 51-53			■										
151	29R-5, 83-84			■						■				

Notes: VCD = visual core description. R = rare (<1%), P = present (1%–5%), A = abundant (>5%).





Table T7. Whole-rock major and trace element compositions, Hole U1347A. (See table notes.) (Continued on next page.)

Stratigraphic unit:	324-U1347A-																			
	IV					V				VII			IX		X					
Core:	12R	12R	13R	13R	13R*	13R†	14R	14R	15R	15R	16R	16R	17R	18R	18R	18R	19R	19R	19R	20R
Section:	1	2	2	6	6	7	1	2	1	2	2	5	2	1	3	5	1	3	3	1
Piece:	9	5	3	1	1	6	15	5	3	4	8	4A	7	2	6	4	3	8	15	5
Interval (cm):	59–62	39–42	53–55	15–18	80–83	28–30	108–111	55–57	9–11	21–23	104–106	102–105	48–51	43–46	124–126	78–80	107–110	51–52	123–125	96–98
Top depth (mbsf):	160.19	161.33	169.02	172.97	173.62	174.52	177.68	178.62	186.28	187.68	197.34	200.60	206.30	214.43	217.82	220.24	224.67	226.80	227.52	234.16
Major element oxide (wt%):																				
SiO ₂	49.34	49.02	47.00	49.13	50.70	50.26	47.09	46.17	48.64	48.19	45.43	49.84	46.87	49.26	49.62	47.94	47.16	46.78	47.66	47.99
TiO ₂	2.26	2.14	2.14	2.15	2.01	1.54	2.20	2.20	2.13	2.11	2.41	2.41	1.69	1.75	1.81	1.76	1.74	1.68	1.72	1.73
Al ₂ O ₃	14.55	13.96	13.57	14.14	13.43	10.12	13.60	13.50	13.56	13.55	13.21	15.67	15.76	16.14	15.27	14.51	14.53	14.77	14.58	15.19
Fe ₂ O ₃ ^T	14.82	14.67	14.50	13.73	12.42	19.51	15.98	14.94	14.10	13.94	13.69	12.47	12.12	12.23	12.58	12.36	12.16	12.29	12.39	12.07
MnO	0.16	0.22	0.22	0.15	0.16	0.09	0.17	0.19	0.22	0.26	0.24	0.15	0.15	0.14	0.22	0.21	0.22	0.21	0.21	0.20
MgO	7.17	6.76	6.71	6.97	5.76	10.93	7.97	7.34	6.84	6.13	5.29	4.94	6.43	6.56	6.57	6.70	6.22	6.24	6.36	6.25
CaO	10.12	11.65	11.57	9.57	8.88	3.63	9.60	10.39	11.37	13.11	12.97	9.18	10.50	10.47	12.51	12.03	12.62	12.79	12.46	11.95
Na ₂ O	2.75	2.42	2.45	2.68	2.92	2.63	2.59	2.63	2.41	2.34	2.70	3.17	2.96	2.97	2.41	2.31	2.28	2.36	2.22	2.40
K ₂ O	0.07	0.17	0.14	0.12	0.33	0.34	0.08	0.09	0.19	0.25	0.27	0.29	0.10	0.09	0.16	0.15	0.20	0.25	0.45	0.16
P ₂ O ₅	0.27	0.26	0.28	0.24	0.35	0.14	0.20	0.29	0.27	0.27	0.30	0.30	0.27	0.26	0.24	0.22	0.22	0.20	0.20	0.20
Totals:	101.52	101.28	98.58	98.87	96.96	99.18	99.48	97.74	99.72	100.14	96.53	98.42	96.86	99.87	101.37	98.18	97.33	97.58	98.24	98.13
LOI	0.87	1.13	1.58	1.26	2.53	3.40	0.73	1.57	1.34	3.10	1.86	2.93	2.64	1.94	1.81	0.90	1.10	1.48	2.59	1.95
Major element oxide (wt%) normalized to 100 wt%:																				
SiO ₂	48.60	48.40	47.68	49.69	52.29	50.67	47.33	47.23	48.77	48.12	47.06	50.64	48.39	49.33	48.94	48.83	48.45	47.94	48.51	48.90
TiO ₂	2.22	2.12	2.18	2.17	2.07	1.55	2.21	2.25	2.14	2.11	2.50	2.45	1.74	1.75	1.78	1.79	1.78	1.73	1.75	1.76
Al ₂ O ₃	14.34	13.79	13.76	14.30	13.85	10.20	13.67	13.81	13.60	13.53	13.69	15.92	16.27	16.16	15.06	14.78	14.93	15.14	14.84	15.48
Fe ₂ O ₃ ^T	14.59	14.49	14.71	13.89	12.81	19.68	16.06	15.28	14.14	13.92	14.18	12.67	12.52	12.24	12.41	12.59	12.49	12.59	12.61	12.30
MnO	0.16	0.21	0.22	0.15	0.16	0.09	0.17	0.20	0.22	0.26	0.25	0.15	0.16	0.14	0.21	0.21	0.22	0.21	0.22	0.20
MgO	7.07	6.68	6.80	7.05	5.94	11.02	8.01	7.51	6.86	6.12	5.48	5.02	6.64	6.57	6.48	6.82	6.39	6.40	6.47	6.37
CaO	9.97	11.51	11.74	9.67	9.16	3.66	9.65	10.63	11.40	13.10	13.44	9.32	10.84	10.49	12.34	12.26	12.96	13.11	12.68	12.18
Na ₂ O	2.71	2.39	2.49	2.71	3.01	2.66	2.61	2.69	2.41	2.33	2.80	3.22	3.05	2.98	2.38	2.35	2.34	2.42	2.26	2.44
K ₂ O	0.07	0.17	0.15	0.12	0.34	0.34	0.09	0.09	0.19	0.25	0.28	0.30	0.10	0.09	0.16	0.15	0.20	0.26	0.45	0.16
P ₂ O ₅	0.27	0.26	0.28	0.24	0.37	0.14	0.20	0.29	0.27	0.27	0.32	0.30	0.28	0.26	0.23	0.22	0.23	0.21	0.21	0.20
Totals:	100.00	100.00	100.00	100.00	100.00	100.00	100.00	100.00	100.00	100.00	100.00	100.00	100.00	100.00	100.00	100.00	100.00	100.00	100.00	100.00
Mg#	53.0	51.8	51.8	54.1	51.9	56.6	53.7	53.4	53.0	50.6	47.4	48.0	55.2	55.5	54.9	55.8	54.4	54.2	54.4	54.6
Trace element (ppm):																				
Ba	26	27	25	32	54	15	13	20	26	35	40	40	22	25	23	24	25	26	24	22
Sr	204	194	206	209	224	90	198	207	205	193	220	237	199	202	201	195	194	195	195	198
Zr	131	119	142	112	193	93	126	128	125	120	136	139	116	117	105	101	101	98	99	100
Y	37	36	39	28	51	14	28	38	35	36	37	33	31	30	33	29	31	29	29	30
V	468	450	432	470	272	316	454	451	439	450	511	508	373	389	375	361	357	350	356	360
Sc	47	44	42	46	36	31	45	44	44	43	44	49	41	42	43	41	41	40	41	42
Cu	251	234	249	251	221	154	249	256	238	240	289	295	215	217	207	203	200	203	177	197
Zn	115	107	114	111	125	59	114	113	115	108	124	129	109	101	104	99	98	96	100	97
Co	72	66	77	60	56	46	64	50	70	65	67	72	44	47	61	56	55	47	54	53
Cr	191	172	173	200	159	191	183	176	179	169	130	184	120	122	211	208	203	204	196	199
Ni	61	56	60	75	76	63	60	59	71	58	62	71	56	50	92	96	89	78	94	91

Notes: * = segregation of dark gray basalt within lighter gray basalt. † = altered glass. All analyses were conducted on samples ignited to 975°C. Fe₂O₃^T = total iron expressed as Fe₂O₃. LOI = weight loss on ignition. Mg# = 100 × (Mg²⁺/[Mg²⁺ + Fe²⁺]), assuming that Fe₂O₃/FeO = 0.15.



Table T7 (continued).

Stratigraphic unit:	324-U1347A-																			
	X					XII					XIV					XV			XVI	
Core:	20R	21R	21R	22R	22R	22R	23R	23R	23R	24R	24R	24R	25R	25R	25R	26R	28R	29R	29R	29R
Section:	3	3	5	1	3	5	2	4	6	3	7	9	2	4	6	2	1	4	4	5
Piece:	5	2	3	9	3	10	10	1	1	1	6	1	1	6	1	4B	1	1A	9	9
Interval (cm):	71-73	78-80	17-19	55-58	66-68	99-100	114-116	37-39	96-97	58-61	78-80	9-11	79-81	99-102	38-40	78-80	70-73	0-2	117-119	81-83
Top depth (mbsf):	236.56	245.27	247.42	252.95	255.93	259.09	263.36	265.41	267.76	274.67	280.14	281.99	283.29	286.36	288.48	292.98	301.10	313.65	314.82	315.96
Major element oxide (wt%):																				
SiO ₂	48.37	50.29	48.09	46.40	50.60	49.94	49.53	48.60	50.06	49.27	48.49	48.24	48.89	49.35	48.74	49.06	48.93	48.70	48.49	48.07
TiO ₂	1.74	1.95	2.19	2.15	2.36	1.95	1.85	1.84	1.86	1.92	1.88	1.81	1.86	1.84	1.83	2.06	2.04	2.02	2.22	2.08
Al ₂ O ₃	15.04	16.48	14.29	14.11	15.20	15.30	14.21	13.88	14.89	15.38	14.18	14.33	14.50	14.39	13.84	13.47	13.63	13.55	15.09	14.45
Fe ₂ O ₃ ^T	12.11	11.31	14.28	14.05	13.39	12.30	13.89	13.61	12.79	12.79	13.63	13.48	13.08	13.60	13.61	14.35	14.57	13.93	12.21	13.88
MnO	0.22	0.12	0.19	0.21	0.11	0.15	0.20	0.22	0.19	0.11	0.18	0.18	0.15	0.19	0.19	0.23	0.20	0.18	0.17	0.18
MgO	6.48	6.97	7.25	7.12	6.85	6.54	7.34	7.08	6.78	7.58	7.42	7.37	7.31	7.40	7.19	6.39	6.15	6.15	5.33	7.07
CaO	12.71	10.35	10.35	12.58	7.80	11.25	11.52	12.18	11.72	9.48	11.15	11.33	10.35	11.45	11.26	11.20	10.91	11.28	11.62	10.61
Na ₂ O	2.37	2.85	3.01	2.92	3.26	2.75	2.39	2.36	2.66	2.85	2.45	2.41	2.65	2.43	2.31	2.40	2.49	2.48	2.95	2.62
K ₂ O	0.13	0.08	0.07	0.08	0.11	0.08	0.09	0.13	0.20	0.06	0.07	0.05	0.05	0.09	0.12	0.21	0.17	0.18	0.27	0.06
P ₂ O ₅	0.22	0.21	0.32	0.31	0.33	0.24	0.22	0.21	0.21	0.22	0.21	0.19	0.21	0.21	0.18	0.22	0.24	0.26	0.29	0.27
Totals:	99.38	100.61	100.04	99.93	100.02	100.51	101.23	100.09	101.35	99.66	99.65	99.40	99.05	100.93	99.28	99.60	99.33	98.73	98.64	99.28
LOI	1.81	1.67	2.75	3.57	1.06	1.34	0.07	2.28	2.30	0.72	1.06	1.31	0.60	0.27	1.74	0.19	0.20	0.33	2.49	1.03
Major element oxide (wt%) normalized to 100 wt%:																				
SiO ₂	48.67	49.99	48.07	46.44	50.59	49.69	48.92	48.56	49.39	49.44	48.66	48.54	49.36	48.90	49.09	49.25	49.26	49.33	49.16	48.42
TiO ₂	1.75	1.94	2.19	2.15	2.36	1.94	1.83	1.83	1.83	1.93	1.88	1.82	1.88	1.82	1.85	2.07	2.05	2.05	2.25	2.09
Al ₂ O ₃	15.14	16.38	14.29	14.12	15.20	15.23	14.04	13.87	14.69	15.44	14.23	14.41	14.64	14.26	13.94	13.53	13.72	13.73	15.30	14.55
Fe ₂ O ₃ ^T	12.18	11.24	14.27	14.06	13.39	12.24	13.72	13.60	12.62	12.83	13.67	13.56	13.20	13.47	13.71	14.40	14.67	14.11	12.38	13.98
MnO	0.22	0.11	0.19	0.21	0.11	0.15	0.20	0.22	0.19	0.11	0.18	0.18	0.15	0.19	0.19	0.23	0.20	0.19	0.17	0.18
MgO	6.52	6.93	7.25	7.13	6.85	6.51	7.25	7.07	6.69	7.61	7.44	7.42	7.38	7.33	7.25	6.42	6.19	6.23	5.41	7.12
CaO	12.78	10.28	10.34	12.59	7.80	11.19	11.38	12.16	11.56	9.51	11.19	11.40	10.45	11.34	11.34	11.25	10.98	11.42	11.78	10.69
Na ₂ O	2.39	2.83	3.01	2.92	3.26	2.74	2.36	2.35	2.63	2.86	2.46	2.43	2.68	2.40	2.32	2.41	2.51	2.51	2.99	2.64
K ₂ O	0.13	0.08	0.07	0.08	0.11	0.08	0.09	0.13	0.20	0.06	0.07	0.05	0.05	0.08	0.12	0.21	0.17	0.18	0.27	0.06
P ₂ O ₅	0.22	0.21	0.32	0.31	0.33	0.24	0.21	0.21	0.20	0.22	0.21	0.19	0.21	0.20	0.19	0.22	0.24	0.26	0.30	0.27
Totals:	100.00	100.00	100.00	100.00	100.00	100.00	100.00	100.00	100.00	100.00	100.00	100.00	100.00	100.00	100.00	100.00	100.00	100.00	100.00	100.00
Mg#	55.5	58.93	54.17	54.12	54.35	55.30	55.15	54.75	55.21	57.98	55.88	56.01	56.54	55.88	55.16	50.92	49.53	50.68	50.41	54.23
Trace element (ppm):																				
Ba	23	33	26	25	40	31	25	26	38	28	23	25	30	26	27	36	40	39	45	27
Sr	199	202	184	185	194	183	166	166	182	184	169	168	173	169	163	175	175	195	205	190
Zr	100	110	130	129	145	116	109	108	110	114	112	107	109	108	109	115	113	111	126	117
Y	31	25	37	40	34	31	33	32	32	29	31	32	30	32	32	35	35	33	35	36
V	361	430	467	459	485	440	409	400	411	421	406	386	415	401	406	456	451	443	488	452
Sc	42	49	48	47	50	49	47	46	47	48	46	46	47	46	44	46	45	45	49	47
Cu	203	242	278	281	322	247	224	227	237	242	234	228	247	229	228	250	242	252	304	260
Zn	97	105	119	115	123	94	110	100	104	105	101	107	107	101	103	107	110	103	133	104
Co	61	59	55	51	58	52	81	51	58	55	73	61	62	51	53	54	54	61	49	47
Cr	216	227	143	132	138	205	225	218	215	225	216	209	219	209	209	148	134	140	129	140
Ni	81	100	45	36	42	66	63	62	73	73	68	60	83	64	55	26	31	43	13	33

Table T8. Moisture and density measurements, Site U1347. (See table notes.)

Core, section, interval (cm)	Top depth (mbsf)	Density (g/cm ³)			Void ratio	Water content (%)	Porosity (%)
		Bulk	Dry	Grain			
324-U1347A-							
12R-1, 69-71	160.29	2.643	2.463	2.989	0.214	6.823	17.611
12R-2, 42-44	161.36	2.788	2.728	2.899	0.063	2.166	5.898
13R-1, 24-26	167.24	2.680	2.950	2.950	0.163	5.365	14.041
13R-2, 90-92	169.39	2.813	2.668	3.106	0.164	5.130	14.092
13R-4, 2-4	170.96	2.820	2.757	2.939	0.066	2.253	6.204
13R-6, 13-15	172.95	2.638	2.464	2.968	0.205	6.596	16.991
14R-1, 145-147	178.05	2.594	2.391	2.984	0.248	7.842	19.869
15R-1, 13-15	186.33	2.755	2.672	2.907	0.088	3.016	8.112
16R-1, 89-91	195.69	2.707	2.583	2.938	0.137	4.570	12.082
16R-4, 10-12	198.37	2.737	2.604	2.993	0.149	4.853	12.972
16R-5, 107-109	200.65	2.525	2.366	2.802	0.184	6.314	15.573
17R-2, 54-56	206.37	2.673	2.523	2.957	0.172	5.618	14.668
17R-3, 107-109	208.36	2.593	2.413	2.930	0.215	6.978	17.673
18R-1, 44-46	214.46	2.682	2.544	2.942	0.156	5.165	13.530
18R-3, 75-77	217.36	2.575	2.404	2.885	0.200	6.632	16.676
18R-5, 82-84	220.28	2.866	2.829	2.935	0.037	1.286	3.600
19R-1, 32-34	223.94	2.842	2.794	2.931	0.049	1.679	4.659
19R-4, 8-10	227.72	2.861	2.818	2.943	0.044	1.520	4.247
20R-3, 46-48	236.33	2.857	2.803	2.958	0.055	1.877	5.236
20R-3, 118-120	237.03	2.800	2.730	2.932	0.074	2.529	6.917
21R-3, 72-74	245.23	2.724	2.608	2.943	0.128	4.278	11.383
22R-1, 121-123	253.63	2.577	2.374	2.960	0.247	7.868	19.800
22R-2, 95-97	254.83	2.512	2.277	2.953	0.297	9.331	22.886
22R-3, 70-72	255.99	2.519	2.301	2.921	0.269	8.629	21.223
22R-4, 12-14	256.86	2.547	2.351	2.908	0.237	7.711	19.178
22R-4, 135-137	258.08	2.487	2.273	2.874	0.264	8.610	20.912
22R-5, 86-88	258.98	2.836	2.781	2.937	0.056	1.921	5.320
23R-2, 76-78	263.00	2.778	2.700	2.922	0.082	2.799	7.594
23R-3, 9-11	263.74	2.877	2.844	2.938	0.033	1.140	3.202
23R-4, 34-36	265.40	2.809	2.749	2.918	0.061	2.109	5.784
23R-6, 96-98	267.81	2.668	2.534	2.915	0.150	5.013	13.062
24R-1, 34-36	271.96	2.663	2.514	2.944	0.171	5.618	14.610
24R-3, 61-63	274.72	2.644	2.470	2.975	0.205	6.585	17.001
24R-4, 51-53	276.10	2.768	2.662	2.970	0.116	3.838	10.374
24R-5, 41-43	277.40	2.737	2.645	2.905	0.098	3.350	8.954
24R-6, 30-32	278.47	2.702	2.587	2.916	0.127	4.269	11.265
24R-6, 90-92	279.07	2.666	2.513	2.956	0.176	5.748	14.968
24R-7, 45-47	279.83	2.737	2.606	2.988	0.147	4.783	12.782
24R-8, 24-26	280.66	2.776	2.699	2.918	0.081	2.761	7.486
25R-1, 44-46	281.66	2.824	2.775	2.916	0.051	1.761	4.856
25R-2, 81-83	283.33	2.768	2.679	2.934	0.095	3.214	8.690
25R-3, 65-67	284.55	2.730	2.595	2.990	0.152	4.959	13.221
25R-4, 102-104	286.42	2.765	2.915	2.915	0.086	2.931	7.915
25R-5, 59-61	287.36	2.628	2.458	2.947	0.199	6.460	16.579
26R-1, 58-60	291.28	2.677	2.528	2.958	0.170	5.551	14.512
26R-2, 84-86	293.04	2.910	2.885	2.958	0.025	0.874	2.483
27R-2, 23-25	294.74	2.920	2.896	2.966	0.024	0.828	2.360
27R-4, 63-65	297.10	2.898	2.863	2.966	0.036	1.224	3.464
27R-6, 123-125	300.38	2.944	2.917	2.994	0.026	0.886	2.546
28R-1, 67-69	301.07	2.779*	2.568*	3.236*	0.260*	7.601*	20.630*
28R-3, 44-46	303.39	2.834	2.771	2.953	0.066	2.225	6.159
28R-5, 16-18	305.61	2.908	2.969	2.969	0.032	1.098	3.118
28R-6, 49-51	307.15	2.872	2.816	2.980	0.058	1.961	5.499
28R-8, 80-82	310.04	2.872	2.828	2.956	0.045	1.546	4.336
29R-1, 23-25	310.13	2.851	2.793	2.963	0.061	2.066	5.754
29R-4, 57-59	314.22	2.783	2.709	2.921	0.078	2.672	7.264
29R-4, 142-144	315.07	2.720	2.624	2.895	0.103	3.515	9.337

Notes: * = broken/cracked sample. Water content is relative to the wet mass.

Table T9. Compressional wave velocity measurements, Site U1347. (See table notes.)

Core, section, interval (cm)	Top depth (mbsf)	Velocity (km/s)		
		x-direction	y-direction	z-direction
324-U1347A-				
12R-1, 69–71	160.29	4.541	4.563	4.573
12R-2, 42–44	161.36	6.118	6.179	6.093
13R-1, 24–26	167.24	4.86	4.863	5.012
13R-2, 90–92	169.39	4.988	4.92	5.013
13R-4, 2–4	170.96	6.159	6.186	6.202
13R-6, 13–15	172.95	4.652	4.691	4.608
14R-1, 145–147	178.05	4.835	4.82	4.798
15R-1, 13–15	186.33	5.795	5.861	5.881
16R-1, 89–91	195.69	5.024	5.034	5.047
16R-4, 10–12	198.37	5.105	5.178	5.137
16R-5, 107–109	200.65	4.822	4.89	4.873
17R-2, 54–56	206.37	5.022	5.048	4.993
17R-3, 107–109	208.36	4.621	4.583	4.679
18R-1, 44–46	214.44	4.962	5.070	5.080
18R-3, 75–77	217.34	4.607	4.591	4.653
18R-5, 82–84	220.28	6.776	6.740	6.890
19R-1, 32–34	223.92	6.600	6.545	6.742
19R-4, 8–10	227.70	6.680	6.652	6.652
20R-3, 46–48	236.31	6.308	6.286	6.315
20R-3, 118–120	237.03	6.159	6.259	6.245
21R-3, 72–74	245.21	5.052	5.118	5.194
21R-5, 121–123	247.39	4.262*	4.181*	4.225*
22R-1, 95–97	253.61	4.194	4.230	4.221
22R-2, 70–72	254.81	3.911	3.909	3.916
22R-3, 12–14	255.97	4.042	4.008	4.042
22R-4, 135–137	256.83	4.272	4.240	4.289
22R-4, 86–88	258.07	3.961	3.981	3.988
22R-5, 76–78	258.96	5.934	6.039	5.777
23R-2, 9–11	262.98	5.936	5.965	5.887
23R-3, 34–36	263.73	6.796	6.624	6.623
23R-4, 96–98	265.39	6.223	6.166	6.255
23R-6, 34–36	267.79	5.159	5.141	5.149
24R-1, 61–63	271.94	4.801	4.842	4.866
24R-3, 51–53	274.70	4.559	4.553	4.586
24R-4, 41–43	276.08	5.562	5.553	5.623
24R-5, 30–32	277.38	5.784	5.647	5.750
24R-6, 90–92	278.45	5.499	5.491	5.533
24R-6, 45–47	279.05	4.887	4.981	4.935
24R-7, 24–26	279.81	5.346	5.323	5.346
24R-8, 44–46	280.64	6.043	6.014	6.155
25R-1, 81–83	281.64	6.687	6.577	6.559
25R-2, 65–67	283.31	5.814	5.934	5.886
25R-3, 102–104	284.53	5.201	5.176	5.162
25R-4, 59–61	286.40	6.008	5.991	6.031
25R-5, 58–60	287.33	4.817	4.778	4.789
26R-1, 84–86	291.28	4.804	4.909	4.865
26R-2, 23–25	293.04	6.777	6.687	6.797
27R-2, 63–65	294.74	6.950	6.982	7.039
27R-4, 123–125	297.10	6.742	6.667	6.560
27R-6, 67–69	300.38	6.930	6.791	6.778
28R-1, 44–46	301.07	6.623*	6.717*	6.566*
28R-3, 16–18	303.39	6.132	6.063	6.019
28R-5, 49–51	305.61	5.964	6.051	6.092
28R-6, 80–82	307.15	6.189	6.148	6.123
28R-8, 23–25	310.04	6.350	6.446	6.430
29R-1, 69–71	310.13	6.293	6.294	6.210
29R-4, 42–44	314.22	5.664	5.822	5.779
29R-4, 24–26	315.07	5.402	5.280	5.317

Notes: * = broken/cracked samples. Values are accurate to ± 20 m/s.

Table T10. Thermal conductivity measurements, Site U1347.

Core, section, interval (cm)	Top depth (mbsf)	Thermal conductivity (W/[m·K])	2 σ	Material
324-U1347A-				
12R-1, 76–97	160.36	1.685	0.013	Igneous
12R-2, 78.5–92	161.73	1.499	0.008	Igneous
13R-1, 71.5–105	167.72	1.455	0.019	Igneous
13R-2, 11–30	168.60	1.637	0.018	Igneous
13R-3, 19.5–59.5	170.02	1.603	0.015	Igneous
13R-4, 70–85	171.64	1.477	0.015	Igneous
13R-5, 18–50.5	172.50	1.536	0.009	Igneous
13R-6, 0–20	172.82	1.536	0.009	Igneous
14R-1, 29–55	176.89	1.652	0.039	Igneous
14R-2, 38–57	178.45	1.550	0.014	Igneous
15R-1, 13–36	186.33	1.650	0.012	Igneous
16R-1, 17–32.5	194.97	1.659	0.014	Igneous
16R-2, 13–27.5	196.43	1.565	0.009	Igneous
16R-4, 0–39	198.27	1.577	0.016	Igneous
16R-5, 87–114	200.45	1.527	0.053	Igneous
17R-1, 120–138	204.46	1.007	0.017	Sediment
17R-2, 16.5–25.5	206.70	1.604	0.013	Igneous
17R-3, 102–119.5	208.31	1.444	0.014	Igneous
18R-2, 121–137	216.43	1.461	0.015	Igneous
18R-4, 71–85.5	218.76	1.576	0.017	Igneous
18R-5, 68.5–87	220.16	1.644	0.010	Igneous
19R-1, 25–38	223.85	1.627	0.018	Igneous
19R-4, 0–16.5	227.62	1.607	0.011	Igneous
20R-2, 12–37.5	234.76	1.632	0.017	Igneous
20R-3, 37–62	236.22	1.648	0.023	Igneous
21R-1, 27–54	242.97	1.491	0.019	Igneous
21R-2, 15–30	243.39	1.678	0.025	Igneous
21R-3, 0–30.5	244.49	1.633	0.013	Igneous
21R-4, 4.5–21	246.04	1.612	0.018	Igneous
21R-5, 11.5–29	247.37	1.402	0.010	Igneous
22R-1, 108.5–127	253.49	1.444	0.013	Igneous
22R-2, 10.5–26	253.97	1.607	0.040	Igneous
22R-3, 124–137.5	256.51	1.496	0.030	Igneous
22R-4, 10.5–25.5	256.82	1.430	0.015	Igneous
22R-5, 0–19	258.10	1.439	0.008	Igneous
23R-2, 103–114	263.25	1.506	0.023	Igneous
23R-3, 57.5–72	264.21	1.639	0.011	Igneous
23R-4, 0–20	265.05	1.590	0.040	Igneous
23R-5, 27–39.5	266.71	1.528	0.014	Igneous
23R-6, 0–16	266.83	1.513	0.017	Igneous
24R-1, 80–92	272.40	1.605	0.028	Igneous
24R-2, 20–36	272.83	1.535	0.022	Igneous
24R-4, 30.5–47.5	275.88	1.452	0.008	Igneous
24R-8, 59–74	280.99	1.586	0.012	Igneous
25R-1, 0–19	281.20	1.459	0.020	Igneous
25R-3, 96–112	284.84	1.616	0.011	Igneous
25R-4, 105–118	286.43	1.606	0.008	Igneous
26R-1, 24–44	290.94	1.501	0.015	Igneous
27R-2, 29–42	294.80	1.683	0.018	Igneous
27R-4, 25–43	296.72	1.726	0.010	Igneous
27R-5, 53–68	298.39	1.662	0.021	Igneous
27R-6, 4–24	299.19	1.727	0.009	Igneous
28R-1, 0–14	300.40	1.793	0.053	Igneous
28R-3, 60–75	303.55	1.681	0.015	Igneous
28R-5, 0–20	305.45	1.760	0.032	Igneous
28R-7, 52–70	308.50	1.758	0.020	Igneous
29R-1, 48–63	310.38	1.713	0.022	Igneous
29R-2, 90–109	312.01	1.801	0.031	Igneous
29R-3, 120–143	313.41	1.760	0.009	Igneous



Table T11. Demagnetization results, Site U1347. (See table notes.) (Continued on next page.)

Core, section, interval (cm)	Depth (mbsf)		Demagnetization	Fit			Inclination (°)	Declination (°)	MAD (°)	Inclination group	Average inclination (°)	Average standard deviation (°)	NRM intensity (mA/m)	NRM _χ (SI)	MDF (mT)
	Top	Bottom		°C	mT	N									
324-U1347A-															
12R-1, 20.5–22.5	159.90	159.92	AF		12–100	10	–2.3	–166.6	4.9				1.34E+04	4.04E–02	3.50
12R-1, 33–35	159.93	159.95	TH	475–600		6	18.8	–160.2	12.3				1.42E+04	3.96E–02	
12R-1, 69–71	160.29	160.31	AF		12–100	10	–14.2	–133.4	1.2	1			2.01E+04	3.23E–02	3.49
12R-1, 78–80	160.38	160.40	AF		25–100	7	–1.4	–109.3	3.7		–6	7	2.86E+04	3.78E–02	3.01
12R-2, 9–11	161.03	161.05	AF		10–100	11	7.9	68.9	3.3				1.78E+04	3.88E–02	3.00
12R-2, 42–44	161.36	161.38	TH	400–600		10	34.0	–175.1	4.7				3.74E+04	3.37E–02	
13R-1, 24–26	167.24	167.26	TH	500–600		5	26.1	50.9	5.8				8.20E+03	4.72E–02	
13R-2, 90–92	169.39	169.41	TH	500–600		5	50.2	–120.9	5.7				2.17E+04	4.12E–02	
13R-4, 2–4	170.96	170.98	AF		15–120	11	23.0	29.7	2.5				2.34E+04	5.30E–02	1.17
13R-6, 13–15	172.95	172.97	TH	500–600		5	37.5	108.1	8.8				2.49E+04	5.06E–02	
14R-1, 145–147	178.05	178.07	TH	350–600		10	23.3	15.2	11	2			1.01E+04	4.10E–02	
15R-1, 13–15	186.33	186.35	TH	500–600		5	26.7	121.0	5.5				2.49E+04	3.87E–02	
16R-1, 89–91	195.69	195.71	TH	500–600		5	39.1	59.7	7.3				1.56E+04	6.00E–02	
16R-4, 10–12	198.37	198.39	TH	475–600		6	3.2	–91.2	27.1				1.12E+04	4.73E–02	
16R-5, 107–109	200.65	200.67	AF		20–100	8	19.3	–29.0	1.4		28	13	2.01E+04	4.88E–02	
17R-2, 54–56	206.37	206.39	TH	425–600		8	15.6	176.6	4.5				1.37E+04	3.40E–02	
17R-3, 107–109	208.36	208.38	TH	500–600		5	16.0	22.0	4.7	3			9.85E+03	3.38E–02	
18R-1, 44–46	214.44	214.46	AF		10–100	11	10.2	–136.1	4.3				1.95E+04	4.30E–02	4.22
18R-3, 75–77	217.34	217.26	AF		10–100	11	12.9	140.8	1.1				1.23E+04	4.52E–02	4.31
18R-5, 82–84	220.28	220.30	TH	400–550		7	24.2	34.2	11.8				2.57E+04	2.05E–02	
19R-1, 32–34	223.92	223.94	AF		15–80	8	20.8	–135.8	9				4.86E+04	2.62E–02	3.59
19R-4, 8–10	227.70	227.72	TH	375–600		10	22.3	113.8	8.3				3.15E+04	2.04E–02	
20R-3, 46–48	236.31	236.33	AF		25–100	7	3.8	137.9	3.9				4.69E+04	3.12E–02	3.33
20R-3, 118–120	237.03	237.05	TH	200–600		14	46.3	–154.4	6.1				2.66E+04	2.54E–02	
21R-3, 14–16	247.39	247.41	AF		10–100	11	26.6	–73.5	1.5				4.75E+02	3.40E–02	7.52
21R-3, 72–74	245.21	245.23	TH	300–500		9	5.9	138.8	5.9				1.42E+04	3.28E–02	
21R-1, 121–123	253.61	253.63	AF		12–60	8	24.3	–173.5	1.2				6.11E+03	3.83E–02	6.07
22R-2, 95–97	254.81	254.83	TH	475–600		6	17.5	94.5	12.2				2.53E+03	2.77E–02	
22R-3, 70–72	255.97	255.99	TH	475–600		6	25.0	–80.4	17.9				7.31E+03	3.02E–02	
22R-4, 12–14	256.84	256.86	TH	150–600		10	43.8	–77.9	5.6				1.01E+04	3.22E–02	10.76
22R-4, 135–137	258.06	258.08	AF		10–80	10	24.2	–33.7	0.9				3.26E+03	4.89E–02	
22R-5, 86–88	258.96	258.98	TH	200–600		13	9.7	97.3	6.2				1.41E+04	2.12E–02	
23R-2, 76–78	262.98	263.00	TH	425–600		8	15.9	26.4	7				1.89E+04	3.36E–02	
23R-3, 9–11	263.72	263.74	TH	200–600		13	29.3	–168.7	3				2.46E+04	1.98E–02	
23R-3, 34–36	265.38	265.40	AF		20–120	9	13.0	–42.8	3.5				2.45E+04	2.97E–02	4.14
23R-6, 96–98	267.79	267.81	TH	450–600		7	18.7	–178.9	5.7				1.51E+04	3.78E–02	
24R-1, 34–36	271.94	271.96	TH	350–600		11	39.7	–102.3	19				1.71E+04	3.99E–02	
24R-3, 61–63	274.70	274.72	AF		10–100	11	8.0	–125.0	1.6				8.85E+03	4.48E–02	3.23
24R-5, 41–43	277.38	277.40	AF		20–140	9	16.4	27.5	2.5				1.65E+04	3.22E–02	4.12
24R-6, 30–32	278.45	278.47	AF		15–100	9	13.6	–63.5	1.7				8.44E+03	3.42E–02	5.79
24R-6, 90–92	279.05	279.07	TH	200–600		10	32.3	–135.2	6.4				1.09E+04	2.87E–02	
24R-7, 45–47	279.81	279.83	TH	450–600		7	–7.1	4.4	0.7				6.22E+03	2.88E–02	
24R-8, 24–26	280.64	280.66	TH	400–600		9	30.2	–56.3	5.2				2.35E+04	2.35E–02	
25R-1, 44–46	281.64	281.66	AF		15–100	9	13.9	165.7	2.9				3.08E+04	2.62E–02	5.05
25R-2, 81–83	283.31	283.33	TH	350–575		10	43.2	169.7	8.6				2.78E+04	2.86E–02	
25R-3, 65–67	284.53	284.55	AF		20–80	7	6.2	–17.7	4.3				1.81E+04	4.06E–02	13.95
25R-4, 102–104	286.40	286.42	TH	450–600		9	35.3	11.0	3.9				2.21E+04	2.48E–02	

Table T11 (continued).

Core, section, interval (cm)	Depth (mbsf)		Demagnetization	Fit		N	Inclination (°)	Declination (°)	MAD (°)	Inclination group	Average inclination (°)	Average standard deviation (°)	NRM intensity (mA/m)	NRM _χ (SI)	MDF (mT)
	Top	Bottom		°C	mT										
25R-5, 59–61	287.34	287.36	TH	300–600		13	48.9	–146.2	4.6				1.70E+04	2.84E–02	
26R-1, 58–60	291.28	291.30	TH	475–600		6	–10.4	158.6	12.8		20	14	8.07E+03	3.13E–02	
26R-2, 84–86	293.04	293.06	TH	150–350		6	80.4	–30.5	4.6				3.35E+04	3.09E–02	
27R-2, 23–25	294.74	294.76	AF		20–80	7	14.1	179.0	5.1				3.97E+04	2.88E–02	5.01
27R-4, 63–65	297.10	297.12	TH	450–600		9	–38.7	–143.0	44.8				3.67E+04	4.13E–02	
27R-6, 123–125	300.38	300.40	TH	150–325		5	55.6	107.9	7.2				1.73E+04	6.88E–02	
28R-1, 67–69	301.07	301.09	AF		12–60	8	79.3	–137.5	4.5				5.52E+04	9.04E–02	1.81
28R-3, 44–46	303.39	303.41	TH	450–550		7	–6.9	42.3	14.1	4			1.77E+04	4.69E–02	
28R-5, 16–18	305.61	305.63	AF		20–50	5	26.5	125.9	9.5				4.43E+04	8.09E–02	1.84
28R-6, 49–51	307.15	307.17	TH	425–600		8	–75.7	57.8	22.6				4.55E+04	8.57E–02	
28R-8, 80–82	310.04	310.06	AF		7–60	10	77.8	–34.4	10.2				4.07E+04	9.20E–02	1.59
29R-1, 23–25	310.13	310.15	TH	350–600		11	25.4	–82.1	25.1				4.27E+04	8.37E–02	
29R-4, 57–59	314.22	314.24	TH	150–325		5	63.4	–116.8	4.1				3.61E+04	5.50E–02	
29R-4, 142–144	315.07	315.09	TH	350–600		11	30.7	138.7	2.6		54	27	1.49E+04	4.12E–02	

Notes: For all samples, principal component analysis (PCA) anchored to origin. *N* = number of points used for PCA, MAD = maximum angular deviation (Kirshvink, 1980), NRM = natural remanent magnetization, NRM_χ = bulk susceptibility of NRM, MDF = median destructive field. AF = alternating-field demagnetization, TH = thermal demagnetization.



Table T12. Logging operations, Hole U1347A. (See table notes.)

Tool string	Direction	Interval logged WMSF (m)		Pipe depth DRF (m)	Depth shift (m)	Logging speed (m/h)
		Top	Bottom			
HNCS-HLDS-GPIT-DITE	Downlog	0	287	3461.5	-3461	550
	Uplog Pass 1	128	314	3461.5	-3461	275
HNCS-DSI-FMS	Downlog	0	277	3461.5	-3461	550
	Uplog Pass 1	115.5	314	3461.5	-3461	550
	Pass 2	0	315	3461.5	-3461	550

Notes: Seafloor depth = 3461 m DRF, 3592.5 m WRF. HNCS = Hostile Environment Natural Gamma Ray Sonde, HLDS = Hostile Environment Litho-Density Sonde, GPIT = General Purpose Inclometry Tool, DITE = Dual Induction Tool model E, DSI = Dipole Sonic Imager, FMS = Formation MicroScanner.